

GROWTH OF 1.5 μm GaInNAsSb VERTICAL CAVITY
SURFACE EMITTING LASERS BY MOLECULAR BEAM
EPITAXY

A DISSERTATION
SUBMITTED TO THE DEPARTMENT OF ELECTRICAL
ENGINEERING
AND THE COMMITTEE ON GRADUATE STUDIES
OF STANFORD UNIVERSITY
IN PARTIAL FULFILLMENT OF THE REQUIREMENTS
FOR THE DEGREE OF
DOCTOR OF PHILOSOPHY

Mark Allan Wistey

March 2005

© Copyright by Mark Allan Wistey 2005
All Rights Reserved

Soli Deo Gloria

I certify that I have read this dissertation and that, in my opinion, it is fully adequate in scope and quality as a dissertation for the degree of Doctor of Philosophy.

James S. Harris Principal Adviser

I certify that I have read this dissertation and that, in my opinion, it is fully adequate in scope and quality as a dissertation for the degree of Doctor of Philosophy.

David A. B. Miller

I certify that I have read this dissertation and that, in my opinion, it is fully adequate in scope and quality as a dissertation for the degree of Doctor of Philosophy.

Olav Solgaard

Approved for the University Committee on Graduate Studies.

Abstract

Fiber optics has revolutionized long distance communication and long haul networks, allowing unimaginable data speeds and noise-free telephone calls around the world for mere pennies per hour at the trunk level. But the high speeds of optical fiber generally do not extend to individual workstations or to the home, in large part because it has been difficult and expensive to produce lasers which emitted light at wavelengths which could take advantage of optical fiber.

One of the most promising solutions to this problem is the development of a new class of semiconductors known as dilute nitrides. Dilute nitrides such as GaInNAs can be grown directly on gallium arsenide, which allows well-established processing techniques. More important, gallium arsenide allows the growth of vertical-cavity surface-emitting lasers (VCSELs), which can be grown in dense, 2D arrays on each wafer, providing tremendous economies of scale for manufacturing, testing, and packaging. Unfortunately, GaInNAs lasers have suffered from what has been dubbed the “nitrogen penalty,” with high thresholds and low efficiency as the fraction of nitrogen in the semiconductor was increased.

This thesis describes the steps taken to identify and essentially eliminate the nitrogen penalty. Protecting the wafer surface from plasma ignition, using an arsenic cap, greatly improved material quality. Using a Langmuir probe, we further found that the nitrogen plasma source produced a large number of ions which damaged the wafer during growth. The ions were dramatically reduced using deflection plates. Low voltage deflection plates were found to be preferable to high voltages, and simulations showed low voltages to be adequate for ion removal. The long wavelengths from dilute nitrides can be partly explained by wafer damage during growth. As a

result of these studies, we demonstrated the first CW, room temperature lasers at wavelengths beyond $1.5\mu\text{m}$ on gallium arsenide, and the first GaInNAs(Sb) VCSELs beyond $1.31\mu\text{m}$: $1.46\mu\text{m}$. These techniques offer the promise of inexpensive, high speed fiber networking.

Acknowledgements

The list of people who contributed to this work would take a volume in itself. There are doubtless people who contributed who have been overlooked below. If so, I offer sincere apologies and ask for corrections.

The most vital member of our research team is my advisor, Prof. James Harris, known within the group as “Coach.” As the moniker implies, Coach is known and respected for treating his students fairly, always giving credit to the folks in the trenches. He provides the most flexible and collaborative research environment one could hope for, and offers many insights from multiple perspectives, and a broad research program which defies categorization. He gives us the freedom to go off and work miracles. I hope, in some small way, to have fulfilled this charge.

Professors David Miller and Olav Solgaard, in addition to serving on my committee, have both taught me tremendously about optoelectronics and device physics, both in and out of class, and were endlessly patient with the occasional oddball question. I hope to emulate their high standards in the classroom. I also owe a special debt of gratitude to Professor David Goldhaber-Gordon for agreeing to serve as my orals chair when my scheduled chair proved unavailable at the last minute.

I can hardly give enough thanks to my present coworkers in the MBE lab, Homan Yuen and Seth Bank, who have proven to be nitride demigods and late-night MBE daemons. Homan and Seth are not only hard workers, but are humble (go state schools!), remarkably sharp, and amazingly well-read. Better still, they have provided an enjoyable atmosphere in the office and MBE lab, even on those endless growth campaigns. I am also grateful to have inherited the pioneering nitride work by Sylvia Spruytte and Chris Coldren, and followed it with subsequent work with

Vincent Gambin and Wonill Ha. Chris in particular gave me some key advice when I hit the end of my rut as a third-year graduate student. I have also had countless fruitful discussions with Vincenzo Lordi, Lynford Goddard, and Alireza Khalili on semiconductor physics and characterization, Xian Liu and especially Chien-Chung Lin on MBE, Rafael Aldaz and Evan Thrush on device design and processing, Wayne Martin on electronics both large and small (nano), as well as Hopil Bae, Ofer Levi, and Dan Grupp. Seth, Homan, and Evan Pickett proofread this manuscript. I hope I have helped others as much as these and others have helped me.

I have been deeply moved by the unwavering support and dearest care from Sarah Hall, Amy Norton, John Greenup, Caleb Kemere, Kevin Ross, Walter Ogburn, the “519” crowd, Isaac Lee, Sam Wong, the “Romans” small group, Olaf and Christy Hall-Holt, Mark and Bonnie Smith, Charis Quay, Chris and Carrie Jones, Jack McShea, Dave and Jennie Lockie, and of course, my family, Mom and Dad, Chad, and Eric. Graduate school is a lighter burden with friends such as these.

Bob Wheeler provided invaluable skill in welding several cracks on inside surfaces of the MBE machine, when we could find no one else who could or would do ultra-clean welding. Our laser machine would not be running today without his assistance. I am also grateful to the staff of SNF for help not only in the fab, but also lending us knowledge and equipment when things broke in the MBE lab. Mike Oye and Prof. Mark Cappelli explained basic plasma physics to the poor EE.

Gail Chun-Creech shields our research group from the burden of administrivia, working miracles behind the scenes so we can concentrate on our research, and cheerfully rescuing us even from our own disorder.

I would also like to thank the National Science Foundation and Mustard Seed Foundation for support for research and travel, and Steven Bond at the Lawrence Livermore National Lab for collaboration and support for characterizing early devices. Charles Evans Associates helped with SIMS and NRA-RBS measurements.

Finally, I would like to express my deepest gratitude to my lord and savior, Jesus Christ, who has given me more than I could ever hope to deserve, and who surprises me with the news that the gospel is for ragamuffins.

Errata

1. Several additional minor grammatical errors have been corrected in this version of the thesis. In particular, *which* had frequently been used in place of *that* in restrictive clauses. The British usage of *which* for some restrictive clauses can avoid confusion with finite noun component clauses (e.g. “*That no one was hurt* is a miracle.”) but I have yielded to strict American usage. (The confusion is avoided in common speech by emphasis and a subtle change in pronunciation—at least in the U.S. midwest: *Thăť dog* vs. *The dog thət...*) In any event, these changes do not affect any technical content.

2. In Section 4.8, the text referring to Figure 4.27 (PL with & without arsenic capping) has the two samples reversed. This measurement has been repeated for verification, and the figure and caption are actually correct. The discrepancy between PL and other results was explained upon re-examination of the growth logs for these particular samples. The sample with the arsenic cap was subjected to a prolonged exposure to the plasma after the cap was removed, but before the beginning of GaAs growth. The damage from this prolonged exposure outweighed the benefits of the arsenic cap, leading to a decrease in photoluminescence. The uncapped sample had a very short exposure. Thus it can be argued that the arsenic capped sample is, in fact, the more heavily damaged of the two, which explains the lower PL intensity. This does seem to detract from the main theme of the section (i.e. that an arsenic cap promotes better material), but we believe the subsequent laser results are conclusive. All of the laser growths had the shortest exposure possible, and the laser results are directly comparable. If anything, this serves to reinforce the discovery that early damage to the wafer before the QWs can still affect the QWs.

Contents

Abstract	v
Acknowledgements	vii
Errata	ix
1 Introduction	1
2 Background	4
2.1 Motivation for Dilute Nitrides	4
2.2 The Motivation for VCSELs	7
2.3 Competing Technologies	9
2.4 Alphabet soup: GaAs, InGaAs, GaNAs, GaInNAs, GaInNAsSb . . .	13
2.5 Bands and Bandgaps	15
2.6 Characterization Techniques: PL, CL, XRD.	16
2.7 Laser Fundamentals	18
2.7.1 Basic Lasers	18
2.7.2 Gain	19
2.7.3 Feedback and Phase	22
2.8 Growth Technique: Molecular Beam Epitaxy (MBE)	26
2.9 Conclusion	29
3 Intrinsic Properties of GaInNAs(Sb)	30
3.1 Overview of the Properties of Dilute Nitrides	30

3.2	Band Alignment in GaNAs and GaInNAs(Sb)	32
3.3	Effects on Growth from N, In, and Sb	36
3.3.1	Nitrogen	36
3.3.2	Indium	37
3.3.3	Antimony	38
3.4	Reduced Bandgap in Dilute Nitrides	40
3.4.1	Band Anticrossing	40
3.5	Effects from Annealing	42
3.5.1	Various Defects and Improved Luminescence with Anneal	42
3.5.2	Blueshift with Anneal due to Ga-In Rearrangement	43
3.5.3	Other Causes of Blueshift with Anneal	44
3.6	Other Defects in Dilute Nitrides	47
3.6.1	Background Contamination	47
3.6.2	Oxygen	48
3.6.3	Carbon	50
3.6.4	Hydrogen	50
3.6.5	Aluminum	51
3.6.6	AsN	52
3.7	Conclusions for GaInNAs for Optoelectronics	53
4	Advances in Growth of Dilute Nitrides by MBE	55
4.1	Motivation for Growth Improvement	55
4.2	Basic Plasma Physics	58
4.3	Implementation of Plasma-Assisted MBE	61
4.4	Plasma Optical Emission Spectra	66
4.5	Radio Frequency Impedance Matching & Cell Stability	71
4.5.1	RF Circuit Model of Plasma and Matching Network	71
4.5.2	Effects of Cell Drift and Impedance Mismatch	74
4.6	Using Beam Flux Gauge as Langmuir Probe	79
4.6.1	Measuring Ion Flux from Plasma	79
4.6.2	Langmuir Probe Results	82

4.6.3	Do Not Vary Nitrogen	84
4.6.4	Discussion	86
4.7	Low-voltage Ion Deflection Plates	89
4.7.1	Improved Material with Deflection Plates	89
4.7.2	Deflection Model and Verification	91
4.8	Protecting Wafer using an Arsenic Cap	97
4.8.1	Damage Below the Quantum Well	97
4.8.2	Arsenic Capping Procedure	99
4.8.3	Arsenic Capping Results	100
4.9	Redshift Induced by Plasma Damage	104
4.9.1	Defects Induced by Ion Damage	104
4.9.2	Damage Preceding the Quantum Well	108
4.9.3	Comparison of Wafer Damage	110
4.10	Substrate Temperature & Bandgap Thermometry	112
4.10.1	Importance and Difficulties of Temperature Calibration in MBE	112
4.10.2	Bandgap Thermometry using Direct Reflection	115
4.11	High Quality Material at Low Temperatures	122
4.12	Care and Feeding of an MBE Plasma Source	124
4.13	Summary	131
4.13.1	Major Contributions	131
4.13.2	Minor contributions	132
5	Long Wavelength VCSEL Design & Fabrication	134
5.1	GaInNAs Laser Properties	134
5.2	Edge Emitting lasers	135
5.2.1	Growth of Edge Emitting Lasers	135
5.2.2	Edge Emitting Laser Results	137
5.3	VCSELs: Vertical Cavity Surface Emitting Lasers	141
5.4	Introduction to VCSEL Design	143
5.4.1	What makes a great VCSEL	143
5.4.2	AlGaAs refractive index	145

5.4.3	GaInNAs refractive index	147
5.4.4	Electrical and Thermal Impedance of DBRs	149
5.5	Growth Considerations	153
5.6	Growth of VCSELs for 1.5 μ m Emission	155
5.7	VCSEL Processing	158
5.7.1	Lift-off process	158
5.7.2	Dry Etching with PlasmaQuest	160
5.7.3	Recovery from a failed lift-off process	162
5.7.4	Oxide aperture by selective oxidation	163
5.8	VCSEL Results	165
5.9	Analysis and Summary of VCSEL Results	171
6	Conclusion	172
6.1	Summary	172
6.2	Future Work	173
6.3	Other Contributions	175
A	Glossary:	177
B	Reloading Arm and Electropolishing	179
B.1	Reloading Sources in MBE	179
B.2	Electropolishing	182
C	Publication List	185
	Bibliography	189

List of Tables

2.1	Milestones in dilute nitride growth	10
4.1	Comparison of bandgap thermometry from various wafers and MBE chambers	120
5.1	VCSEL Threshold Currents with Temperature	170

List of Figures

2.1	Absorption in optical fiber vs. wavelength of light.	6
2.2	Eye safety limits for laser exposure for Class 1 and Class 3 lasers. . .	6
2.3	Edge emitting laser and VCSEL cross sections.	8
2.4	Bandgap vs. lattice constant for common semiconductors and their alloys.	14
2.5	Bandgap vs. lattice constant for GaNAs, InGaAs, and GaInNAs. . . .	15
2.6	Semiconductor band diagram with luminescence.	17
2.7	Amplified feedback, with a stereo or in a laser.	19
2.8	Stimulated emission: one photon in, two photons out.	20
2.9	Laser cavity in and out of resonance.	23
2.10	Stable oscillation is possible at several wavelengths, known as modes.	23
2.11	Longitudinal vs. transverse modes	24
2.12	Gain vs. modes for (a) edge emitting laser, or (b) VCSEL.	26
2.13	MBE chamber showing three source cells, two with open shutters. . .	27
3.1	Possible band lineups at a heterostructure interface.	33
3.2	Band lineup of GaInNAsSb, GaNAs, and GaAs as determined by spon- taneous emission and photoreflectance.	34
3.3	Unity (or constant) sticking coefficient leads to linear dependence on growth rate	36
3.4	Compositions from MOCVD growth with mixed Group V elements. . .	39
3.5	Band anticrossing.	41
3.6	Nitrogen outdiffusion in SIMS.	45
3.7	SIMS shows very low contamination unless intentionally doped (e.g. C or Si).	49

4.1	Adding nitrogen decreases photoluminescence, increases laser threshold	57
4.2	Excited energy levels of atomic and molecular nitrogen	60
4.3	Nitrogen plasma cell with matching network and gas handling system.	63
4.4	Nitrogen foreline pressure vs. leak valve setting.	67
4.5	Relative emission from several nitrogen spectral lines, taken from the front PBN aperture and from the rear viewport.	68
4.6	Emission intensities for several settings of the matching capacitor . .	69
4.7	Optical emission spectra collected from front and rear of plasma source.	70
4.8	Current captured through grounded deflection plates vs. matching ca- pacitor position.	72
4.9	Lumped, linear circuit model of inductive RF plasma cell	73
4.10	Circuit simulation of plasma cell with no parasitic losses.	75
4.11	Circuit simulation of plasma cell with a lossy shunt capacitor.	77
4.12	Ion current as captured by ion deflection plates. From Reifsnider [1].	80
4.13	Photoluminescence intensity vs. wavelength, with and without deflec- tion plates	81
4.14	Beam flux gauge as Langmuir probe.	83
4.15	Langmuir probe measurement at beam flux gauge filaments.	84
4.16	Langmuir probe current using various wires on beam flux gauge. . . .	85
4.17	Current through grounded collector wire vs. voltage applied to grid .	85
4.18	Langmuir probe measurement at several flow rates.	86
4.19	Transient in ion flux upon plasma ignition	89
4.20	Ion deflection plates prevent wafer damage. After Kovsh [2].	90
4.21	Peak PL intensity increases 3–5x with moderate deflection plate bias.	91
4.22	Simplified model of ion trajectory calculation.	91
4.23	Simulated particle trajectories due to deflection plates.	93
4.24	Deflection to different angles vs. deflection plate voltage	95
4.25	Optical emission spectra with –1000V and 0V deflection bias.	96
4.26	SIMS depth profile shows excess nitrogen incorporated when the plasma is ignited.	98
4.27	PL intensity with or without extended damage before the QW.	101

4.28	TEM of GaInNAsSb QW without (left) or with (right) arsenic cap. . .	102
4.29	Threshold current densities for lasers grown with no tricks, with arsenic cap, and with deflection plates	102
4.30	GaInNAsSb/GaNAs quantum well band structure, plus defect levels from DLTS and theory	105
4.31	Effects of ion deflection plates on PL and XRD	107
4.32	XRD of GaInNAsSb/GaNAs QWs with long or short plasma exposure before the QW	109
4.33	PL spectra from GaInNAsSb QWs, with and without plasma damage before the QW	110
4.34	Oxide blowoff temperatures, measured by thermocouple.	115
4.35	Specular reflection from semi-insulating GaAs vs. temperature.	117
4.36	Bandgap thermometry results for semi-insulating GaAs.	119
4.37	Bandgap thermometry vs. number of QWs.	122
5.1	L-I curve and lasing emission spectrum for GaInNAsSb edge emitting laser.	138
5.2	Laser threshold current density vs. wavelength for long-wavelength lasers on GaAs.	139
5.3	Edge emitting laser gain spectrum and gain parameters	139
5.4	Simplified structure of a top-emitting VCSEL	142
5.5	VCSEL oxide aperture increases current density, leading to higher power output.	145
5.6	DBR reflectivity fits refractive indices from Gehrsitz.	146
5.7	Refractive index and absorption coefficients for GaNAs and GaInNAs	148
5.8	Arsenic cap leads to reflectivity error	149
5.9	Graded DBR profile.	151
5.10	Stable fluxes from Ga SUMO, base and tip 150°C apart.	154
5.11	VCSEL cavity reflectivity spectrum and fit.	157
5.12	Lift-off metallization and its failure for thick metal	158
5.13	Vertical sidewalls after dry etch.	161

5.14	Simulated reflectivity vs. depth of dry etch (or time)	162
5.15	Selective oxidation rates of AlGaAs.	164
5.16	Aqua regia damage and oxidation front.	165
5.17	VCSEL spectrum at 500mA and 800mA	167
5.18	Current vs. voltage for VCSELs in pulsed mode.	168
5.19	VCSEL output power vs. setpoint current and measured current.	169
5.20	Impedance mismatch and limits of pulse driver produce soft turn-on and overshoot.	170
6.1	Test setup for optically-pumped VCSELs.	175
B.1	A retractable reloading arm for refilling MBE cells.	181

Chapter 1

Introduction

Optical fiber communication requires lasers with wavelengths in the near infrared, from 1.2-1.6 μm . Wavelengths near 1.31 μm and 1.55 μm are particularly important, since they represent the low-dispersion and low-loss regions, respectively, of optical fiber. Dilute nitrides such as GaInNAs have been developed for 1.31 μm applications, but lasers at the longer wavelengths have been elusive due to the destructive effects of nitrogen in the alloy. Vertical cavity surface emitting lasers (VCSELs) are particularly important due to their single-mode operation and wavelength stability without the need for e-beam lithography. VCSELs also benefit from wafer-scale fabrication and testing, the ability to create dense arrays of lasers, and the ease of fiber coupling. Creation of VCSELs at wavelengths near 1.55 μm is a driving interest. This thesis presents the longest wavelength VCSELs ever demonstrated on GaAs. VCSELs will be shown with a pulsed wavelength of 1.46 μm at 0°C, a significant step beyond existing lasers at 1.31 μm .

To reach this result, several improvements have been made to the growth and understanding of dilute nitrides. The output from our nitrogen plasma had long been assumed to be ion-free, but a detailed measurement that used the beam flux monitor as a Langmuir probe indicated that a significant number of ions were reaching the wafer, at energies up to 35eV. The Langmuir probe also showed that moderate voltages were sufficient to deflect ions from the plasma output, and photoluminescence showed that moderate voltages were in fact preferable to high voltages. In addition,

it was discovered that the ignition of the plasma caused damage to the wafer, and that the plasma was unstable for up to 20 minutes, so an arsenic capping technique was developed to protect the wafer surface during plasma ignition and stabilization. By comparing these two forms of wafer damage, it was found that damage itself contributes to the long wavelength emitted by dilute nitrides, and changes the incorporation of nitrogen into the semiconductor during growth, which helps to explain the role of antimony during growth and several inconsistencies among published reports. Improvements were also made to VCSEL structural simulation and to control of elemental sources during growth. These steps also significantly contributed to the development of the first CW, room temperature lasers on GaAs beyond $1.5\mu\text{m}$, with threshold current densities lower than any other published reports beyond $1.38\mu\text{m}$. Record low photoluminescence linewidths for this range, and the first reported room temperature exciton in GaInNAs were also demonstrated. These indicate the high material quality and suitability for long wavelength modulators based on the quantum confined Stark effect.

Throughout this thesis, units of microns (μm) refer to wavelength of light unless otherwise noted. Measurements in nanometers (nm) generally refer to physical dimensions. For mixed alloys, the element(s) in parentheses are optional: in other words, GaInNAs(Sb) refers to both GaInNAs and GaInNAsSb. Also, although international standards call for the chemical formula of the material to be written as “InGaAsN,” for consistency with prior publications from this group, this thesis refers to the material as GaInNAs. Finally, as a matter of notation, “redshift” is used to refer to a change in wavelength toward longer wavelengths, even if those wavelengths are already well beyond the red portion of the visible spectrum. “Blueshift” refers to a shift to shorter wavelengths.

The form of this thesis is in two parts: materials/growth, and devices/fabrication. Chapter 2 provides a brief overview of the motivation and requirements for optical fiber communication lasers. It will also present the method by which dilute nitride lasers are grown, a technique called molecular beam epitaxy (MBE).¹ Chapter 3 gives a detailed background of the intrinsic properties of dilute nitrides, a review of the

¹Or “mostly broken equipment.”

state of the art in Ga(In)NAs(Sb). Chapter 4 details how actually to grow high quality material, with discussion of the properties that are under human control. The major contributions to dilute nitride growth are presented here. As the first device chapter, Chapter 5 will cover additional background material regarding lasers, and then describe the growth and processing of record long wavelength vertical cavity surface-emitting lasers with GaInNAsSb. Chapter 6 closes with a summary of the work accomplished and suggestions for further work.

It is the nature of human endeavor that errors are made; it is the nature of science to question and correct those errors. Just as this thesis shall attempt to correct the errors of previous generations, others shall correct this work in time, although it is naturally hoped that the errors here are less significant and fewer in number.

Chapter 2

Background

2.1 Motivation for Dilute Nitrides

The introduction of nitrogen into semiconductor materials has opened up some of the most exciting developments in compound semiconductors in several decades. Although pure nitrides such as gallium nitride and indium nitride have found widespread use for blue and ultraviolet diode lasers, another revolution has been quietly brewing at the other end of the visible spectrum, in the infrared. It had long been expected that adding nitrogen to gallium arsenide would lead to GaN-like properties, including light emission in the visible. In an unexpected twist, Weyers, Sato, and Ando discovered that adding a small amount of nitrogen to GaAs actually pushes the wavelength of emitted light in the other direction, further into the infrared (IR)—contrary to decades of experience in III-V semiconductors [3, 4]. These “dilute nitrides,” with nitrogen concentrations less than 5%, have opened the door for several key technologies in the near-infrared, particularly for optical fiber communication.

Modern optical fiber is remarkably transparent, with losses less than 0.2dB/km. In other words, light can travel ten miles in an optical fiber and still have half its original intensity. But this is true only for certain wavelengths, or colors, of light. As shown in Figure 2.1, absorption losses in the fiber are extremely low for wavelengths from 1.2–1.7 μm . These wavelengths are beyond the range of conventional GaAs-based diode lasers, which can only cover wavelengths from 0.700–1.1 μm . There is a

tradeoff between wavelength and speed or distance: longer wavelengths, near $1.55\mu\text{m}$, can travel longer distances and still have sufficient power to overcome noise at the receiver. Optical fiber has historically had a strong absorption peak near $1.4\mu\text{m}$ due to OH bonds in the glass, so most commercial implementations of fiber networks have focused at either $1.31\mu\text{m}$ or $1.55\mu\text{m}$. However, Corning has developed low absorption fiber that provides a low-loss window over the full $1.2\text{--}1.7\mu\text{m}$ range. Thus there are applications waiting to use the $1.4\mu\text{m}$ window, but without adequate lasers.

The existing state of the art for lasers at these wavelengths is to use indium phosphide-based materials. These lasers tend to be sensitive to changes in temperature (a small characteristic temperature T_0), and processing is somewhat more difficult, with lower yield and smaller wafers. More importantly, InP-based lasers for fiber communication are expensive, because they require electron beam lithography to create distributed feedback (DFB) for stable, single-mode output at a single wavelength.

And yet the demand for optical networking is strong. There is even an IEEE task force (802.3sh, Ethernet in the First Mile) dedicated to bringing optical networking to the home. Optical fiber networks are up to 1000 times faster than 10-base-T ethernet, and fiber networks are already in use in local area networks (LANs), but the limitations due to the use of short wavelengths (or expensive lasers) prevent the deployment of optical networking beyond a relatively few, high-end servers. To solve the “last mile” problem and bring fiber networking to end users requires not only solving the oft-cited cost of laying fiber, but also the development of inexpensive lasers.

There are two additional motivations for pushing to these longer wavelengths. First, the human eye cannot focus these long wavelengths onto the retina, so there is a greater margin of eye safety. This is the basis for the relaxed set of limits on Class I laser power shown in Figure 2.2. Lasers can safely operate at higher powers without risk of eye damage. This allows for faster data rates, longer distances, and/or more wavelengths to be used in a fiber communication system. It also allows the laser to be used in free-space optics, for gas sensing or point-to-point optical communication links.

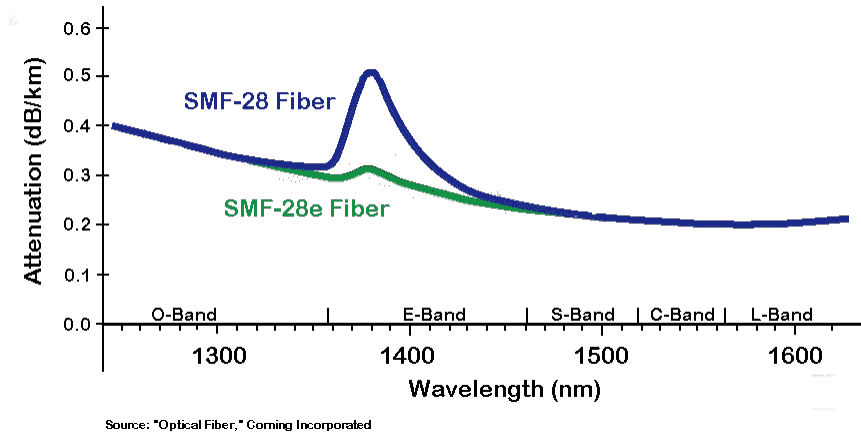


Figure 2.1: Absorption in optical fiber vs. wavelength of light. Modern SMF-28e (and LEAF fiber, not shown) have low attenuation even at the OH peak near 1400nm.

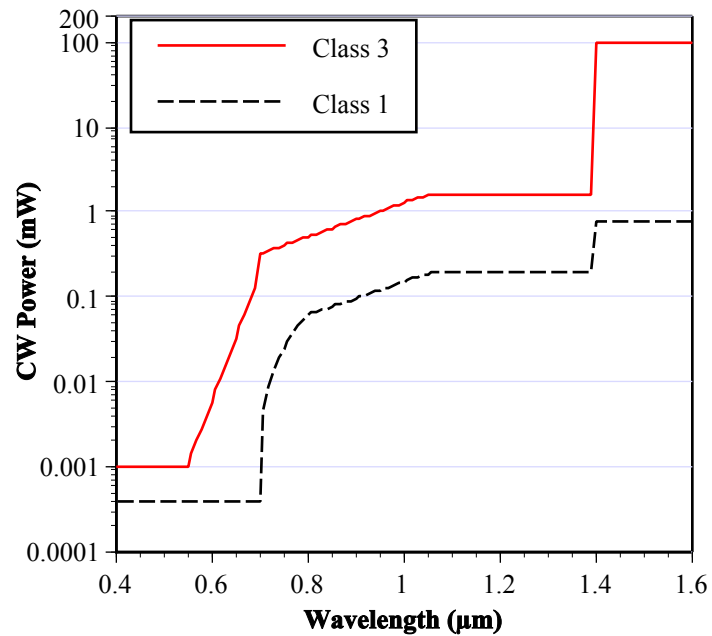


Figure 2.2: Eye safety limits for laser exposure for Class 1 and Class 3 lasers. From ANSI standard Z136.1.

The other motivation for long wavelength diode lasers is the operating voltage of the laser. The voltage across the laser is roughly equal to the bandgap,¹ which is inversely proportional to the wavelength of light emitted. Longer wavelengths correspond to lower voltages. Conventional GaAs-based lasers emitting at $0.98\mu\text{m}$ have a bandgap of 1.26V. High voltages are a nuisance if these lasers are to be incorporated with standard silicon CMOS, which is predicted to be operating at 0.8V within the next three years. On the other hand, a semiconductor emitting at $1.55\mu\text{m}$ has a bandgap of exactly 0.8V, so integration with CMOS becomes much simpler.

With these advantages in optical fiber and integration with CMOS, the development of an inexpensive laser material at $1.55\mu\text{m}$ would be a boon to long distance and high speed optical networking. The ultimate vision of this project, therefore, was to develop a laser material that could be used for optical fiber networking as simple and inexpensive as ethernet is today, and to offer an alternative to indium phosphide lasers up to $1.6\mu\text{m}$.

The problem with dilute nitrides has historically been poor gain due to poor material quality. Extensive theoretical and experimental studies have been performed on the nature of the defects in dilute nitride materials, but the original causes of these defects are uncertain.[5, 6, 7] It is difficult to grow good material with very reactive species such as atomic nitrogen. Several important contributions of this thesis are the identification and removal of the major types of defects in GaInNAs(Sb), such as plasma damage early in the growth, as well as ion damage, which occurs during the growth of actual GaInNAs(Sb) layers.

2.2 The Motivation for VCSELS

There are two major categories of semiconductor lasers: edge emitting lasers and VCSELS, shown schematically in Figure 2.3. The edge emitters presented in Section 5.2 are simple ridge waveguides: easy to grow, and easy to process a few devices

¹The forward diode voltage is slightly less than the bandgap, but resistance usually makes up more than the difference.

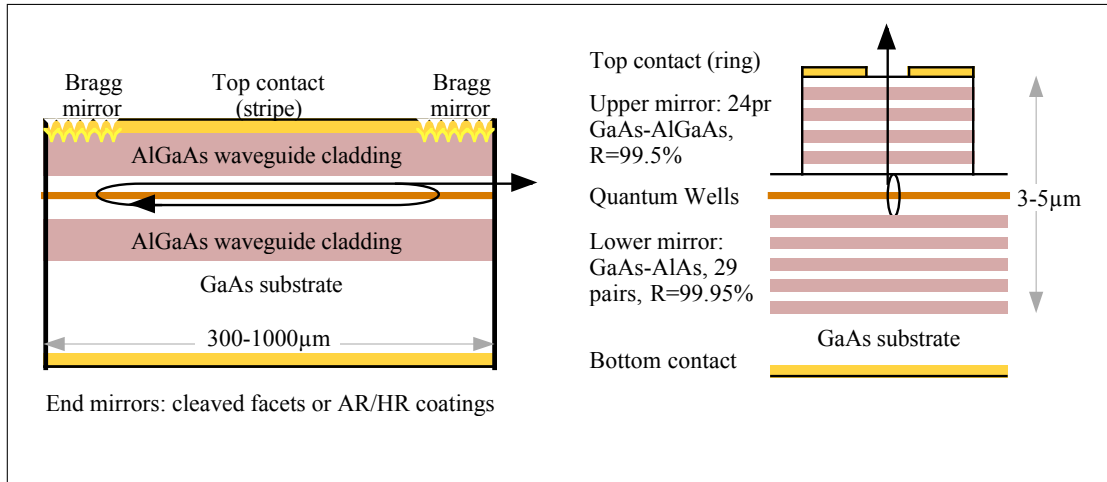


Figure 2.3: Edge emitting laser (left) and VCSEL (right) cross sections. Not to scale. For edge emitting lasers, the Bragg mirrors shown may extend over most of the top surface (e.g. DFB lasers) or be absent completely (simple ridge waveguides).

for research purposes. The edge emitters that are used for fiber communication, however, are more difficult to process, because they require e-beam lithography to define the $\lambda/4$ features for the Bragg mirror that makes a distributed feedback (DFB) laser.

The focus on low-cost lasers entails a focus on devices that can be grown, fabricated, and tested in a large scale. Dilute nitrides are particularly attractive because they can be grown on gallium arsenide, which allows the use of AlGaAs for distributed Bragg reflector (DBR) mirrors for vertical-cavity, surface-emitting lasers (VCSELs). VCSELs can be fabricated and tested on a large scale (wafer scale, with 6" or larger GaAs wafers). Unlike the expensive electron beam lithography required for InP-based DFB lasers, VCSELs have no lithographically-defined critical dimensions, so processing is significantly easier. Also, the testing of VCSELs is much simpler because the entire wafer full of devices can be tested by an automated probe station, and only good, working devices need be packaged. For edge emitting lasers, the wafer must be thinned, cleaved, and devices packaged before they can be tested, increasing overhead costs. Most importantly, because VCSELs emit light vertically from the top surface of the wafer, they are much easier to package and align to an optical fiber. Packaging represents a significant fraction of the cost for a diode communication laser.

But VCSELs at long wavelengths have been slow in coming. InP-based lasers at $1.5\mu\text{m}$ lacked compatible materials for making good DBR mirrors, while GaAs-based lasers, which have excellent DBR mirrors, lacked a compatible light emitting material for the longer wavelengths. Even after Kondow developed the four-element alloy GaInNAs [8], which emitted light at unprecedented long wavelengths, the bottleneck to VCSEL development has been the lack of gain at long wavelengths. As a result, the majority of this thesis represents efforts to understand and improve the poor optical quality of dilute nitrides, and to further improve the growth of GaInNAs(Sb) for application to lasers and other optoelectronic devices. This work culminated in demonstrations showing that GaInNAs(Sb) has a higher oscillator strength (and therefore more gain) than InP-based lasers. The first edge-emitting, room temperature, continuous-wave (CW) lasers on GaAs beyond $1.5\mu\text{m}$ were demonstrated, and ultimately the first VCSELs on GaAs at $1.46\mu\text{m}$, a step well beyond the best published reports to date.

Table 2.1 shows the major milestones in the development of dilute nitrides, from the first demonstration of GaNAs and GaInNAs (by Weyers and Kondow, respectively) to the longest wavelength lasers to date, near $1.5\mu\text{m}$.

2.3 Competing Technologies

A number of other solutions have been proposed for lasers at $1.3\text{--}1.6\mu\text{m}$. These include the predominant arsenide-phosphide alloys such as InGaAsP on InP, InGaAs quantum wells double-wafer-bonded between GaAs/AlAs DBR mirrors, InGaAlAs/InP quantum wells wafer-bonded to one AlGaAs DBR with a dielectric mirror on the other side, InAs or GaAsSb quantum dots on GaAs with GaAs/AlAs DBR mirrors, InGaAs/InP quantum wells on InP with quaternary bottom DBRs and lattice-mismatched GaAs/AlAs top mirrors, InGaAs/InP quantum wells with lattice matched AlGaAsSb mirrors, high-indium InGaAs, antimony-based DBRs on InP, InGaAlAs with GaAs/AlAs mirrors, or InGaAsP with air gap mirrors. The InGaAs and InGaAsP alloys on InP have already been discussed.

An extreme variant of long-wavelength InGaAs is to grow it on GaAs rather

Table 2.1: Milestones in dilute nitride growth

- 1992 Weyers, Sato, and Ando grow GaNAs by low-pressure MOVPE with NH_3 plasma, report decreased bandgap.[3]
- 1993 Sakai et al. predict large bandgap bowing parameter, negative bandgap.[4]
- 1994 Bharatan reports first GaNAs by MOMBE using ECR plasma.[9]
Kondow reports first GaNAs by GSMBE.[10]
- 1995 Kondow reports first GaInNAs. [8]
- 1997 Kondow demonstrates pulsed $1.22\mu\text{m}$ optically pumped edge emitting laser.[11] Sato at Ricoh demonstrates $1.3\mu\text{m}$ optically pumped edge emitter.[12] Larson, Kondow, et al. demonstrate $1.27\mu\text{m}$ optically pumped VCSEL.[13]
- 1999 Wang (at Columbia) and Harmand (at CNRS) simultaneously started growing with Sb. Wang reports surfactant effect but not incorporation.[14]
- 2000 Stanford reports first electrically-pumped VCSEL and first use of GaNAs barriers. [15] Cielo/Sandia report first $1.3\mu\text{m}$ VCSEL, with Infineon soon afterward. Many others follow. Shimizu (at Furukawa) reports incorporation of Sb in GaInNAsSb [16, 17]. Forchel (at Würzburg) reports laser at $1.52\mu\text{m}$, but this is not repeated [18].
- 2002 Stanford breaks $1.4\mu\text{m}$ for the first time repeatably on GaAs [19]. Takeuchi, Tan, et al. (at Agilent) report first MOCVD $1.3\mu\text{m}$ VCSEL [20].
- 2003 Würzburg and CNRS break $1.5\mu\text{m}$ nearly simultaneously. Stanford demonstrates CW lasing at $1.51\mu\text{m}$ [21] and VCSEL at $1.46\mu\text{m}$ at 0°C [22].
- 2004 Infineon demonstrates lasing at $1.49\mu\text{m}$ [23]. Stanford demonstrates $360\text{A}/\text{cm}^2$ at 15°C pulsed and $>1\text{W}$ at 25°C CW.

than InP, and use a very high concentration of indium to reach long wavelengths. If quantum dot formation can be suppressed, 40–50% InGaAs quantum wells could be made with a simple and reproducible growth, and they would operate at higher temperatures; 90°C has been demonstrated [24]. However, the lifetime of devices made with such extremely strained material is questionable, and it will not be possible to reach wavelengths beyond 1.3 μm with this technique.

Techniques that use GaAs/AlAs mirrors generally do so for two reasons. First, unlike other materials grown on InP, GaAs and AlAs have very different refractive indices, which is important for making DBR mirrors. The lack of a refractive index contrast on InP means that phosphide-alloy DBRs must be grown very thick, even 60 mirror pairs, leading to substantial electrical resistance, as well as optical losses due to sidewall scattering and diffraction. The other reason for GaAs-based DBRs is because they have higher conductivity, both electrical and thermal.

The use of relaxed or metamorphic AlGaAs mirrors allows their growth on InP, since the different lattice constants are matched by misfit dislocations along the interface. However, dislocations also promote dark line defects, which limit device lifetime. AlGaAsSb mirrors require extremely careful control over the mixed Group V fluxes. They also suffer from high band offsets, leading to high electrical resistance [25].

The double-bonded wafer approach is surprisingly effective for producing low threshold lasers, despite having two interfaces next to the quantum well that had been exposed to air or etching. Thresholds as low as 4.2kA/cm² have been demonstrated, but this comes at significant fabrication cost: 3 growths on different substrates, 2 wafer bonds, and the etch removal of 1–2 entire substrates, stopping at very critical layers. Also, current injection across the interface leads to local heating and leakage current. There is also no high-temperature processing available, and yield is an issue [26, 27]. The single-bonded approach with a single dielectric deposited mirror suffers from the same difficulties, plus it must be driven through intracavity contacts. Dielectric DBRs have very poor thermal conductivity. But the advantages include a top emitting device and planar surface topology [28].

Self-assembled quantum dot (QD) lasers have been demonstrated with low threshold currents [29, 30]. They offer the advantages of a simple growth (although initially

calibrating the fluxes and growth pauses is nontrivial), and good optical and mechanical properties. The first $1.3\mu\text{m}$ VCSEL on GaAs was based on QDs [31]. In principle, the threshold of quantum dot lasers could be made entirely insensitive to temperature, with exceptionally high gain on a single, narrow wavelength. In practice, quantum dots suffer from low gain [2], poor thermal characteristics (carrier confinement), and severe gain saturation. Stacks of QDs must be grown in order to provide sufficient gain for a reasonably powered laser, otherwise the laser simply begins to operate from the excited states in the QD. InGaSb QDs on GaAs have recently been demonstrated [32] and share many of the same characteristics as InGaAs QDs, both good and bad. Self-assembled quantum dots have been grown using dilute nitrides [33, 34], but these appear to inherit the worst characteristics of both approaches. Dilute nitrides tend to segregate when allowed to go to thermal equilibrium, but quantum dots are designed to do just that.

Little is known about the proposed InGaAlAs/InP lasers for $1.3\mu\text{m}$ that have been reported by the company E2O. This company has made promising claims regarding an improvement in reliability and thermal stability with this material system, but these results have not been published to the best of the author's knowledge.

The prospects of VCSELs based on air gap DBRs appear to be poor, except as a research tool, due to current crowding and a tunnel junction that limits the device due to a voltage drop and heating. Heating is especially problematic for air gap DBRs, which are almost ideal thermal insulators. This technique also requires InP growth, and leaves an unterminated surface immediately above and below the quantum well, which introduces device lifetime issues. On the other hand, the huge contrast in refractive index between GaAs (or InP) and air allows devices to be designed for any wavelength of interest from $1.3\text{--}1.55\mu\text{m}$. Also, the thicknesses of the DBR layers are not critical, for the same reason.

In contrast to these difficulties, GaInNAs(Sb) offers a number of advantages. These will be described in more depth in Chapter 3, but are summarized here. There is good electrical and thermal conductivity through the DBRs, allowing good device operation without intracavity contacts or tunnel junctions. GaInNAs is built on mature GaAs growth and processing methodologies. It can be grown monolithically

on GaAs, with no special fabrication or processing tricks. There are no inherent restrictions on wafer size, unlike thinning/bonding techniques. The high temperature anneal used for dilute nitrides is brief, making it potentially compatible with electronics (metal wiring) and MEMs. The growth is straightforward, with nitrogen displaying a “unity sticking coefficient.”² Finally, it simply works: CW lasers have been demonstrated at room temperature, and VCSELs at $1.46\mu\text{m}$.

2.4 Alphabet soup: GaAs, InGaAs, GaNAs, GaInNAs, GaInNAsSb

The choice of materials is determined primarily by the desired wavelength and the choice of substrates, i.e. the starting point for growth. Figure 2.4 plots the bandgap of the various semiconductors and their alloys vs. lattice constant. The vertical axis is bandgap (or $1/\text{wavelength}$). The target wavelengths for fiber communication are shown crosshatched. The major available substrates Si, GaAs, InP, InAs, and InSb are shown in bold. To maintain good quality growth, all alloys need to have very similar lattice constants to one of these substrates, so they need to fall on or near the corresponding vertical, dashed lines. There are several alloys that can reach the desired range of fiber wavelengths shown in the crosshatched box. For example, InGaAs is a very common and well-understood material for growing quantum wells, particularly for lasers at wavelengths from $0.85\text{--}1.1\mu\text{m}$. Growing InGaAs on GaAs would mean finding a point on the alloy line between GaAs and InAs within the crosshatched box. However, this composition of InGaAs, like any of the other ternary alloys—GaNAs, GaAsP, InGaP, etc.—would require a very different lattice constant from either GaAs, GaP, or InP. Because of the requirement that growth must follow same lattice constant as the substrate (i.e. material must lie on or near one of the dashed lines in the figure), it is difficult to reach wavelengths beyond $1.1\mu\text{m}$ using only GaNAs in the quantum well, or beyond $1.2\mu\text{m}$ using only InGaAs.

Figure 2.5 shows a blowup of the region near GaAs, with alloys for GaNAs and

²A later section discusses sticking coefficients apparently greater than 1.

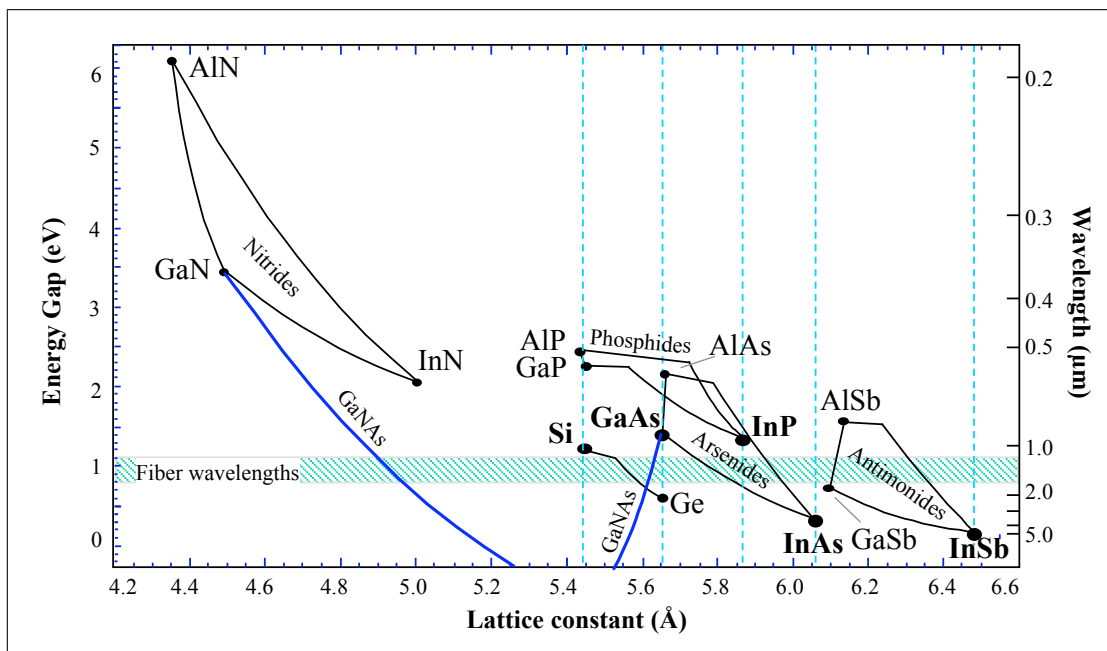


Figure 2.4: Bandgap vs. lattice constant for common semiconductors and their alloys. The major available substrates are shown in bold. Note the bowing (nonmonotonic) in the GaNAs alloy line between GaAs and GaN.

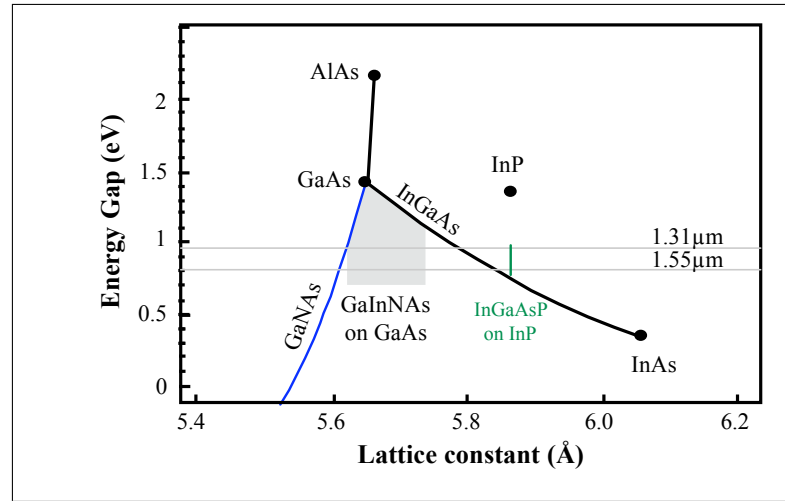


Figure 2.5: Bandgap vs. lattice constant for GaNAs, InGaAs, and GaInNAs grown on GaAs. GaInNAs can be grown in the shaded region below the GaNAs and InGaAs alloy lines. For comparison, InGaAs(P) on InP is also shown.

InGaAs. The remarkable property of GaNAs is visible from Figure 2.5: the GaNAs alloy line, which starts at GaAs, descends to the lower left. All other conventional III–V, II–VI, and Group IV semiconductors generally follow a rule known as Vegard’s Law, which says that the properties of any ternary alloy may be approximated by a linear interpolation of the two binaries on either end. The figure does show this general trend, with most alloy lines running diagonally from the upper left to the lower right, in approximately straight lines. GaNAs, however, runs in the opposite direction. This will be discussed in more detail in the following chapter. Also, adding Sb is similar to adding In: it moves the alloy down and to the right on the figure, toward GaSb.

2.5 Bands and Bandgaps

In a bulk semiconductor at near absolute zero temperature, every electron has a bond, and every bond has an electron. Every electron is therefore in its ground state and cannot move. Even at room temperature, although thermal energy will excite some electrons to higher energies, the vast number of electrons are still in the ground state.

In order to produce optical emission from excited electrons, additional energy must be provided. This is typically done with either electrical or optical pumping. For optical pumping, a bright light is focused on the semiconductor at a wavelength that the semiconductor will absorb. The light breaks valence electrons from their bonds. These electrons are then free to move through the semiconductor, and are said to be in the conduction band. The empty bonds that are left behind are known as holes. Holes are also free to move, in the same way as an empty space on a packed, rush-hour street appears to “move” backward through traffic. When an electron meets a hole, they will recombine, emitting a photon. The holes are in the valence band, which is the ground state of the valence electrons.

Electrical pumping also creates electrons and holes. Electrical current is applied through a junction of two semiconductors, one with excess electrons (n-doped), and the other with excess holes (p-doped). At the junction, electrons are free to recombine with holes, emitting light.

Whether the carriers (electrons and holes) are generated by optical or electrical pumping, excess energy is quickly dissipated, as shown in Figure 2.6. Electrons will fall toward the lowest point in the conduction band, E_C , and the holes reach the highest point in the valence band, E_V . According to this picture, when these electrons and holes recombine, the photon that is emitted will have an energy of $E_C - E_V$. This energy difference is known as the bandgap. The bandgap is generally different for each semiconductor, although alloys of different semiconductors can be made with the same bandgap.

2.6 Characterization Techniques: PL, CL, XRD.

Figure 2.6 is also useful for understanding several of the characterization techniques used for studying GaInNAs. The most widely used technique is photoluminescence (PL), in which optical pumping is used to excite free carriers, as shown in the figure, and the spectrum of the resulting emitted light is collected. Similarly, cathodoluminescence (CL) is the use of a high energy electron beam to excite free carriers. In both of these techniques, if the material quality is very poor, then there are many

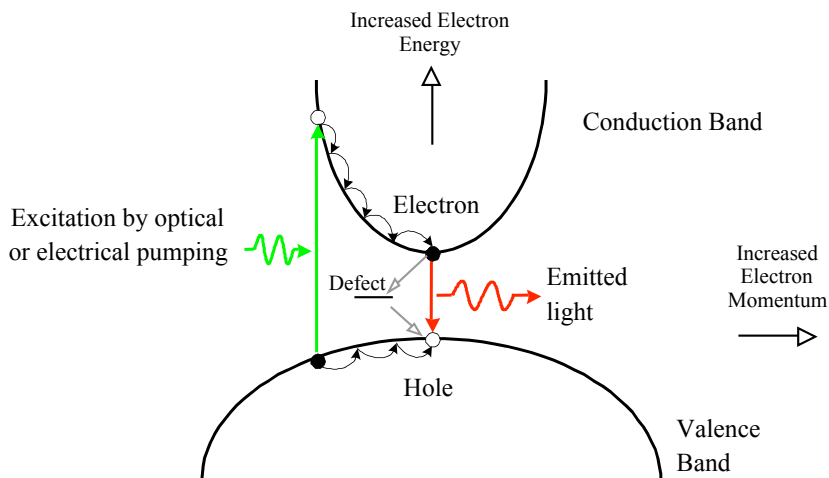


Figure 2.6: Semiconductor band diagram. Excited electrons and holes fall to minimum energy, then recombine. Recombination can be radiative, emitting light at the energy of the band gap, or nonradiative through defects (traps), emitting heat. (After Ref. [35])

carrier traps (defects) that can provide nonradiative recombination of the electron and hole. This generates heat but not light. Therefore high material quality is usually correlated with high photoluminescence intensity. If all of the nonradiative traps are removed, then the *radiative* recombination will be the dominant form of recombination, emitting the most possible light.³

The preceding picture implies that all of the light in luminescence will be emitted with an energy exactly that of the bandgap, neither more nor less. In practice, the transition energy may not be so distinct. This may be due to high doping (dopant level mini-bands), high carrier density (bandgap renormalization), high temperatures (thermal broadening), alloy fluctuations (which change the bandgap randomly depending on local composition), random variations in quantum well width, and other effects. It may also be possible for a defect level to emit light, particularly if it lies very close to either the conduction or valence bands. All of these effects lead to a broadening of the luminescence spectrum. The narrowness (linewidth, or FWHM) of the luminescence spectrum is often used as another measure of material quality,

³This assumes what is known as a direct bandgap semiconductor, such as GaAs. Silicon has an indirect bandgap, emitting almost no light.

although it is usually correlated with PL intensity.

X-ray diffraction (XRD) is another common characterization technique. In XRD, x-rays of a particular energy are focused at the wafer surface. The x-rays diffract to different angles, based on the distances between planes of atoms in the crystal. The angle of diffraction can then be used to determine the amount of strain in a thin film on the semiconductor, since a strained film will have a different lattice spacing in the wafer-normal direction. XRD can detect gross problems with a growth, such as surface roughening or phase segregation, both of which lead to disorder and wash out the diffraction peaks. But XRD is not sensitive to the point defects that lead to poor luminescence, so good XRD is a necessary but not sufficient condition for good optical quality material, such as for lasers.

Transmission electron microscopy (TEM) is another characterization technique for studying material homogeneity and growth. In TEM, a high energy beam of electrons is passed through a very thin (50–200nm) slice of semiconductor. If the beam is exactly aligned with one of the crystal directions of the semiconductor, the electrons can channel between the rows of atoms, allowing resolution of individual atomic rows. This can be used to extract the exact positions of the atomic rows, providing detailed information about strain in the semiconductor. It can also show whether the material grew uniformly or with a rough surface.

2.7 Laser Fundamentals

2.7.1 Basic Lasers

Although lasers will not be discussed in detail until Chapter 5, a basic introduction to lasers is presented here. The basics of solid state physics and laser theory have been reported in multiple papers, textbooks, and Harris Group theses, so only a simplified summary will be given below. The interested reader is referred to Refs. [36, 37, 38] for semiconductor physics, Refs. [39, 40, 41] for laser theory, and Refs. [42, 43] for VCSELs.

A laser requires two things to operate: gain and feedback. Consider the analogy of

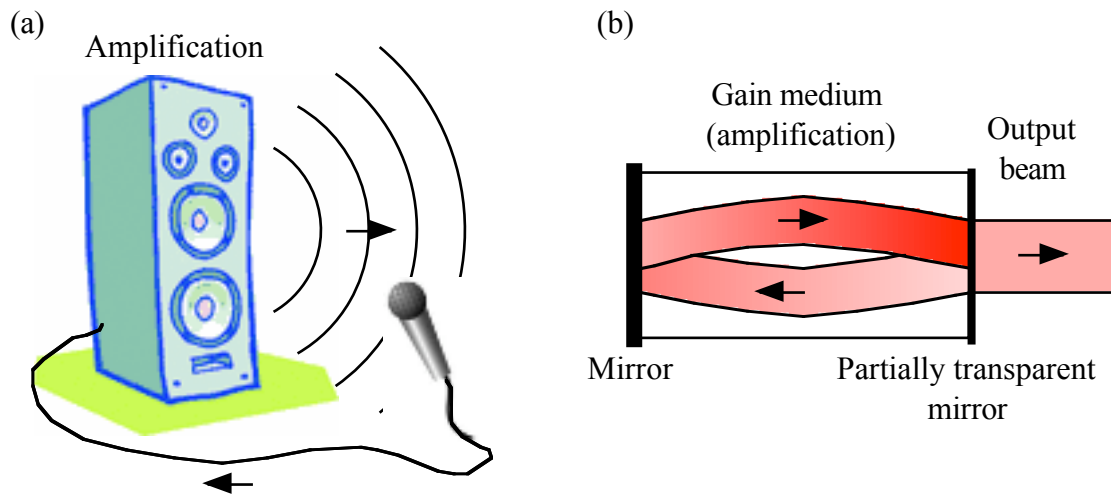


Figure 2.7: Amplified feedback. (a) Microphone near its loudspeaker produces amplified audio feedback and a loud squeal. (b) Mirrors around a gain medium produce amplified optical feedback and a beam of emitted light.

a microphone in front of an amplified loudspeaker, as shown in Figure 2.7. Any sound picked up by the microphone will be amplified by the stereo system, and the resulting sound coming out of the speaker will be louder. If some of that sound is picked up by the microphone, then it will complete a positive feedback loop. This feedback quickly amplifies the squeal to the highest volume the system can support, generally limited by the amplifier. Similarly, in a laser, if a material can be made to amplify light (a gain medium), and if some of that light is captured and circulated back through the gain medium, positive feedback will produce light at the highest intensity that the system can support. Again, this is generally limited by the amplifying material. In both cases, the feedback produces a stable oscillation: either a loud tone from the speaker, or a continuous beam of light from the laser.

2.7.2 Gain

In a semiconductor laser, gain is provided by the injection of high concentrations of electrons and holes in the semiconductor. At very low injection levels, the semiconductor absorbs nearly every photon whose energy is greater than the semiconductor

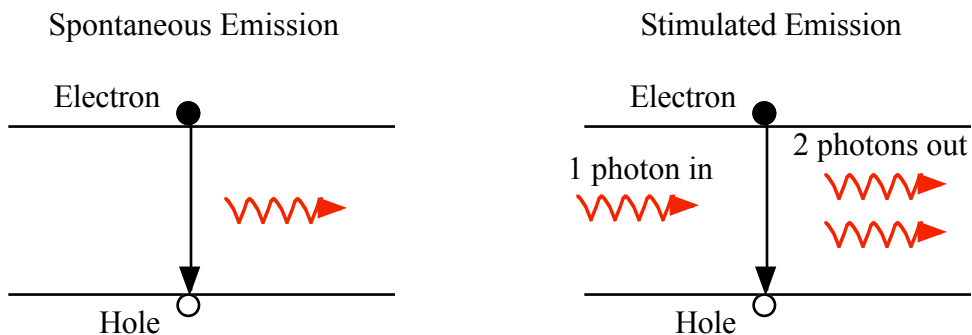


Figure 2.8: Stimulated emission: one photon in, two photons out.

bandgap. With higher carrier injection, the semiconductor emits some light through spontaneous emission but still absorbs light that strikes it. When the injection is high enough⁴, the semiconductor becomes transparent. To produce an excess of electrons at high energies, energy must be supplied in some non-thermodynamic fashion, as optical or electrical pumping discussed in Section 2.5.

At high levels of carrier injection, the material can emit light through stimulated emission. Figure 2.8 shows an electron in an excited energy state E_2 . If a photon (a small packet of light) with energy $E_2 - E_1$ happens to strike the electron, then the electron can fall to its ground state, E_1 , and two identical photons will emerge in place of the first one.⁵ Obviously, if enough time passes, an electron in E_2 will eventually fall back to E_1 of its own accord, emitting light (spontaneous emission) or heat, so it is preferable that E_2 be a relatively stable state. Spontaneous emission is by far the most common form of light emission, from light bulbs to televisions and from candles to the sun.

If there are more electrons in E_2 than in E_1 (inversion), then one incoming photon can trigger a second photon, and so on, producing an avalanche of gain: amplification of the incoming light. The higher the gain, the more light produced by the laser. Eventually, as the light gets amplified to a high intensity, it will soon deplete the

⁴i.e. if the quasi-Fermi levels of the electrons and holes are separated by an energy equal to the bandgap of the material

⁵In practice, the two photons need not be exactly identical. Thermal motion, for example, can cause small changes in energy.

excess electrons in E_2 , and the gain will drop. This is known as gain saturation, and it limits the amount of light that can be produced by a laser for a given input current or pump power. There may be other processes that limit the gain of a laser, such as heating. High gain is a good characteristic for a laser material, and GaInNAs has displayed higher gain than InP based lasers [44]. Also, if there are other pathways for electrons in E_2 to reach E_1 , such as carrier traps or defects in the crystal, then the gain will be reduced. Removal of these nonradiative recombination sites was a major push for this thesis (Chapter 4).

Gain imposes several requirements on the laser operation, mostly due to materials issues. The gain in a material is a strong function of wavelength, with peak gain occurring at the wavelength that corresponds to the bandgap of the material (plus quantum confinement). As mentioned previously, GaInNAs emits light at the desirable wavelengths in the near infrared due to its small bandgap. GaInNAs also has an unusually broad gain bandwidth (Section 5.1).

In an ideal laser, one excited input electron would correspond to one additional photon of output light. In practice, electrons and holes may be lost due to non-radiative recombination or spontaneous emission, or photons may be scattered or absorbed by impurities in the semiconductor. As a result of these losses, a certain amount of pump power needs to be supplied before the laser will reach inversion. This “overhead” is known as the laser threshold. Lasers with high losses will have high thresholds. Conversely, it is a sign of a high quality semiconductor, with very few defects, if lasers made from that semiconductor demonstrate low thresholds. Producing low threshold lasers with GaInNAs was one of the major accomplishments of this thesis, as discussed in Section 5.2.2.

Also, the output of the laser must itself be considered as a form of loss, because it removes photons that could otherwise be triggering stimulated emission. As a result, lasing will only begin when the total gain of the laser exceeds the total losses, including mirror “loss.” It is convenient to write both gain and loss in terms of unit length [40]:

$$g_{th} = \alpha_i + \alpha_{mirror} = \alpha_i + \frac{1}{L} \ln \left(\frac{1}{r_1 r_2} \right) \quad (2.1)$$

where g_{th} is the gain at threshold, α_i is the internal losses of the cavity from scattering, etc., L is the cavity length, and r_1 and r_2 are the reflectivities of the two mirrors. Γ is the confinement factor, which is a measure of the degree of overlap between the optical mode and the gain medium, from 0 to 1.

It should be noted that low thresholds are not sufficient to demonstrate a high efficiency laser. If the output mirror is highly transparent, so most of the light escapes with each pass through the cavity, then the laser threshold will also be high. Thus it is useful to also consider the differential quantum efficiency η_d , the rise in output power with input power above threshold:

$$\eta_d = \left(\frac{q}{h\nu} \right) \frac{dP_0}{dI}, \quad \text{or} \quad (2.2)$$

$$\frac{1}{\eta_d} = \frac{\langle \alpha_i \rangle}{\eta_i \ln(1/R)} L + \frac{1}{\eta_i} \quad (2.3)$$

The best lasers generally have both low thresholds and high differential efficiencies. Internal or differential quantum efficiency is not to be confused with wallplug efficiency, the overall power conversion efficiency of the device. Wallplug efficiency is generally used as a metric for very-high and very-low power laser applications, where poor overall efficiency will lead to excess heating or power drain, respectively, and was not a focus of this work.

2.7.3 Feedback and Phase

Feedback for a laser is provided by mirrors. Mirrors are used to collect the light from the output of the laser and circulate it back through the gain medium (i.e. the amplifying material). One or more of the mirrors is designed to be partly transparent, and the light that escapes through this mirror is what produces the familiar laser beam.

Feedback imposes another requirement: phase. In order to establish a standing wave (constructive interference) within the laser, the wavelength must be such that an integer number of half-wavelengths fit between the two mirrors. In other words, the light from two consecutive passes through a laser must be in phase, or no lasing will occur. This is shown schematically in Figure 2.9.

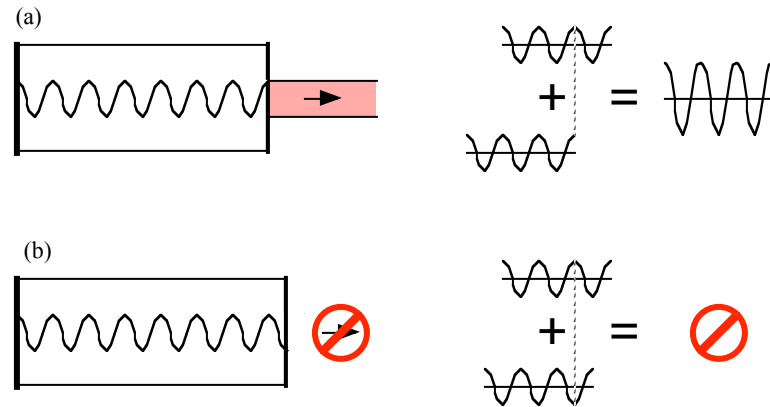


Figure 2.9: (a) Laser cavity in resonance: integer number of wavelengths add in phase.⁷ (b) Out of resonance, no light is emitted at this wavelength.

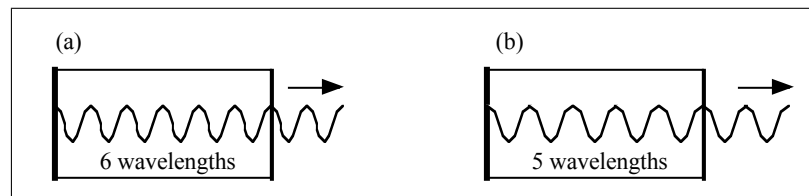


Figure 2.10: Stable oscillation is possible at several wavelengths, known as modes.

There may be several different wavelengths that satisfy this condition, as shown in Figure 2.10. The frequencies that support stable oscillation are known as modes. If the feedback loop is very short, on the order of one wavelength, only one or two modes can be supported. This is one of the most useful advantages of VCSELs over edge emitting lasers for wavelength division multiplexing (WDM), since multiple longitudinal modes tend to cause crosstalk in neighboring channels. The very short cavity in a VCSEL, i.e. the short distance between the DBR mirrors, only supports one mode.

The above discussion assumes free space operation for both the stereo and the laser, resulting in *longitudinal* modes—so named because of the restriction in length. However, if the field is also confined horizontally, such as in a waveguide or with a focusing lens or mirror, transverse modes may also be possible, as shown in Figure 2.11. Ordinary edge-emitting lasers, which use a waveguide to confine light, generally have hundreds or thousands of longitudinal modes, closely spaced in wavelength, but only

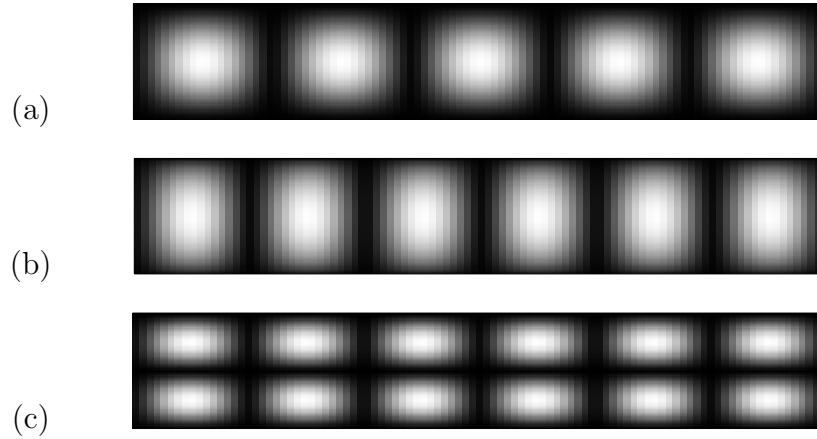


Figure 2.11: Longitudinal vs. transverse mode intensities, with mirrors on left and right ends, and metal-like boundaries. (a) 5th longitudinal mode, but the fundamental transverse mode. (b) 6th different longitudinal mode. (c) 6th longitudinal mode, but with the 2nd order transverse mode.

a few transverse modes. VCSELs, on the other hand, generally have only one longitudinal mode, but may support multiple transverse modes, particularly if the VCSEL is very wide (several tens of microns). These are generally undesirable for fiber communication, since the laser will hop chaotically between the various modes, leading to increased noise. VCSEL spectra with multiple transverse modes will be presented later (page 167).

For a symmetric waveguide, at least one transverse mode is always supported, regardless of wavelength. This is known as the fundamental mode. At shorter wavelengths or larger waveguides, additional transverse modes may be possible. For a “hard” (e.g. metal) waveguide, the longest wavelength that can be supported is one which can just fit half a wavelength within the waveguide; in microwave radio applications, this is generally referred to in terms of frequency (i.e. the cutoff frequency). For a dielectric waveguide, finding the mode profile generally requires numerical solution of a transcendental equation or, equivalently, beam propagation or tunnel resonance transfer matrix methods. The major difference between a dielectric waveguide and “hard” metal waveguides is that a significant fraction of the optical mode exists outside of the dielectric waveguide, even for true waveguide modes (i.e. lossless modes

that do not escape to propagate in space).

Multiple transverse modes can be prevented by making the laser very narrow, or by operating only at very low power. This is generally the approach both for edge emitting lasers, by making narrow ridge waveguides, and for VCSELs, by making mesas or apertures less than about $6\mu\text{m}$. Narrowing the lasers significantly reduces the amount of available power, however.

Longitudinal modes are restricted in one of two ways. Either the distance between the mirrors is made very short, or else the mirrors are made to be very selective in wavelength, so only one mode ⁸ gets reflected between the mirrors. It is extremely difficult to make edge emitting lasers short enough to restrict the longitudinal modes, so distributed Bragg reflectors (DBRs) are fabricated instead. For an edge emitting laser, this is a cumbersome process, requiring critical dimensions and e-beam lithography. On the other hand, VCSELs already have a short cavity (1λ or $\frac{1}{2}\lambda$) and DBRs. This is one of the significant advantages of VCSELs. (DBRs will be discussed in more detail in the discussion of VCSELs, Section 5.3.)

The disadvantage of VCSELs, from the perspective of mode control, is that they tend to lase easily in higher order transverse modes. Current tends to be crowded around the edge of the mesa or oxide aperture, which leads to higher gain at the periphery of the mesa than at the center. This favors the higher order transverse modes, which are stronger at the periphery. Also, top-emitting VCSELs have a ring contact on top, and this ring can provide additional mirror reflectance away from the mesa center, which also tends to support higher order transverse modes. Transverse mode control has been proposed using extended cavities [45], microlenses [46], patterned apertures [47], proton implanted apertures [48, 49], long cavities [50], and low-index-contrast DBRs [51].

To summarize basic laser operation, lasing will occur at whichever modes have gain. The higher the gain (i.e. the harder the laser is driven), the more modes will lase. As shown in Figure 2.12, many modes are supported for edge emitting lasers. There is generally only one VCSEL mode. Its wavelength may change with temperature or current, but lasing will still occur as long as the mode lies within the

⁸One mode within the gain envelope, that is.

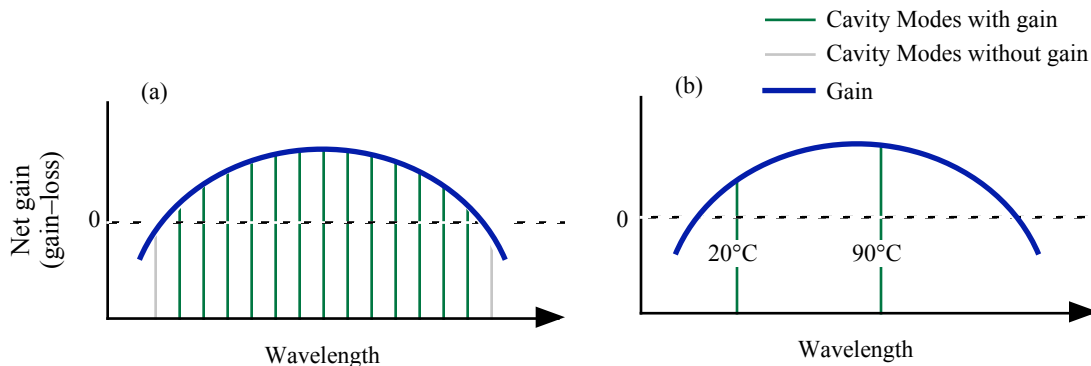


Figure 2.12: Gain vs. modes for (a) edge emitting laser, or (b) VCSEL.

gain spectrum, as shown in the figure.

2.8 Growth Technique: Molecular Beam Epitaxy (MBE)

Dilute nitrides have been grown by several techniques, including metalorganic chemical vapor deposition (MOCVD) [52], plasma-assisted MOCVD [3], metalorganic molecular beam epitaxy (MO-MBE), gas source MBE [10, 53, 54], and plasma-assisted, solid-source MBE [55]. Excellent lasers have also been reported by Tansu et al. using MOCVD [56], but there appears to be an upper limit on the wavelength achievable by MOCVD [57]. The best lasers reported to date have been grown by plasma-assisted molecular beam epitaxy (MBE), as described in this section.

Molecular beam epitaxy is a sophisticated form of evaporation and deposition. Figure 2.13 shows a simplified cross section through an MBE chamber. The wafer sits at the center of the chamber, surrounded on three sides by a cryoshroud that freezes out trace gases in the chamber. Three elemental cells are shown at right in the figure, representing (top to bottom) arsenic, nitrogen, and gallium. Each cell contains one ultrapure element, and the entire chamber is under ultra high vacuum, with a background pressure below 10^{-10} Torr. The cells are heated until the source material begins to evaporate or sublimate. There is a shutter in front of each cell

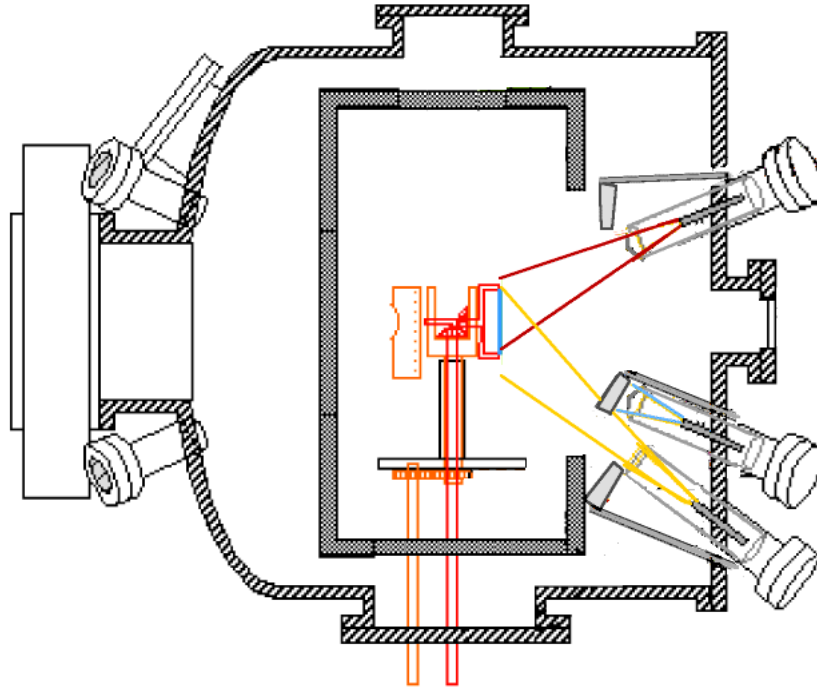


Figure 2.13: MBE chamber showing three source cells, two of which have their shutters open. The wafer is located at the intersection of the two beams.

that is used to control whether that element is allowed to reach the wafer surface. In the figure, arsenic and gallium shutters are open, allowing the growth of GaAs on the wafer. The wafer is heated to 400–650°C during growth, which gives atoms on the surface sufficient mobility to move around and find sites of relatively low energy. For a perfect crystal such as a semiconductor, the crystal structure can be maintained; for example, a cubic semiconductor can have thin films of cubic materials grown on top of it. MBE is a common technique used in the Harris Group, and interested readers are referred to, e.g., Refs. [58, 35, 43, 59]. Several of the revised MBE growth procedures are outlined below.

All of the wafers grown for this thesis are nominally (100) GaAs, either semi-insulating or n^{++} doped. The wafers were loaded onto wafer carriers in a cleanroom (class 100 to class 1000). The wafer carriers were loaded onto a trolley, which was loaded into a high-vacuum load chamber and pumped down to below 1×10^{-6} Torr.

The load chamber was pumped with a Cryo-Torr cryopump, models 7 or 100, each with a cold stage below 11K for hydrogen, as well as a larger 77K stage for most other gases. The trolley was then baked up to a temperature of 200°C by a temperature-controlled halogen lamp in the load chamber, while keeping the pressure below 1×10^{-6} Torr. The low pressures prevent thermal cracking of hydrocarbons, which would be very difficult to remove from the wafer surface. Each wafer was then individually loaded into a UHV chamber with an ion pump, where it was baked up to 350°C or 400°C for n-type or semi-insulating wafers, respectively, below the limit of arsenic desorption from GaAs. The wafer bake pressure was kept below 1×10^{-7} Torr.

The aluminum growth rates were calibrated by growing a $1\mu\text{m}$ layer of AlAs, cooling to room temperature, then measuring the normal-incidence reflectivity of the layer as a function of wavelength. This reflectivity spectrum is then compared with a model generated by the “mff” thin film simulator. The simulated film thickness is varied until it matches the measured spectrum. Then $1\mu\text{m}$ of GaAs is grown on top, and the process is repeated. The indium growth rate was calibrated using a thick film of InGaAs and measuring the thickness with X-ray diffraction. The growth rates occasionally needed to be recalibrated as the level of source material in each cell decreased. A calibration growth was made immediately before thickness-critical growths such as VCSELs, and this was frequent enough to serve the purposes for long-term calibration as well. When the indium cell on System 5 ran dry, efforts were made to build a reloading arm to refill it in-situ (Chapter B.1).

The use of chemical etching to clean wafers before MBE growth was a common technique in the past, but several authors have reported smoother surfaces and better quality growth with non-etched wafers. (See, for example, [60].) The difference appears to be whether the wafers were exposed to oxygen or water vapor for any significant period of time before being loaded into high vacuum. Modern wafer packaging appears to be cleaner than wet etching. We do see a thin layer of contaminants (C, N, O) at the $10^{19}/\text{cm}^3$ level in SIMS, but these appear to be well-behaved, and the 300nm buffer is more than sufficient to bury them.

The wafer holders themselves were cleaned 1–2 times per year using a Br:methanol etch. Unlike other etches used for this purpose, such as sulfuric acid and hydrogen

peroxide, there is no damage to the molybdenum wafer holders themselves. To prevent etching of the beaker from this caustic/solvent mixture, a 1 liter PTFE beaker was used for etching. The beaker was filled with 750mL of methanol and 25mL of bromine, agitated with a magnetic stirring rod. The wafer holders and faceplates were strung on molybdenum wires so they could be dipped into the beaker. The wafer holders should be removed before the bromine evaporates, but there are no other time constraints. This etch will aggressively remove GaAs, but does not appear to remove liquid Ga or In. However, the aggressive nature of the etch means care should be taken to prevent spills, especially since the etched material will be toxic. Also, like all GaAs etches, this generates arsine gas, which is extremely toxic.

What makes the dilute nitride growth unusual is the use of a nitrogen plasma cell within the MBE chamber. Molecular nitrogen is inert and does not incorporate in semiconductor growth to any significant extent. To create reactive nitrogen for MBE growth of nitrides and dilute nitrides, the N_2 molecules must be cracked using a plasma. Several different types of plasmas have been used for this purpose, including DC [61], ECR [62, 63], arcjet, and RF [64]. A nitrogen plasma is used to create reactive forms of nitrogen, such as atoms, radicals, and ions. However, exposure to the plasma causes damage to the semiconductor surface during growth. The properties of the dilute nitrides will be discussed in some detail in the following chapter.

2.9 Conclusion

We have seen that dilute nitrides offer tremendous promise toward the creation of cheap and high-power diode lasers covering wavelengths from 1.2-1.6 μ m. A great deal of collective work has been directed toward understanding the intrinsic material properties of GaInNAs and other dilute nitrides. A review of the state of the art in GaInNAs will be presented in the next chapter.

Chapter 3

Intrinsic Properties of GaInNAs(Sb)

3.1 Overview of the Properties of Dilute Nitrides

The previous chapter provided the background for a number of general topics. This chapter goes into significantly more detail on the topic of dilute nitrides themselves, although for fuller details, readers are encouraged to select one of the several reviews of Ga(In)NAs, which go into more depth on a number of points. (See, for example, [65, 66, 67, 68, 69] and [6].) The information presented in this chapter is, unless otherwise noted, primarily the work of others, although contributions were made to several important discoveries presented here, such as the nitride-antimonide lasers presented in Section 3.3. An ancillary purpose of this chapter is to clarify which effects in dilute nitrides are universally observed, in contrast with following chapters that identify several artifacts of growth conditions. Many, if not most, of the published dilute nitride results have been dominated by such artifacts, leading to considerable confusion about even basic properties such as electron effective mass.

Nitrogen is a small atom, much smaller than any of the other relevant Group III or Group V atoms in the semiconductor. Because it is small, nitrogen decreases the lattice constant of the alloy, resulting in tensile strain: GaNAs, for example, must be “stretched” in order for the atoms to line up with the underlying GaAs surface.

Large atoms like indium or antimony generate compressive strain, and nitrogen can be used to compensate part of this compressive strain. The effect of nitrogen on the bandgap appears to be almost completely in the conduction band. Nitrogen does not appear to affect the valence band directly, although tensile strain does change the relative energies of the different valence bands. This has consequences for the use of tensile GaNAs barriers around the (compressive) quantum wells (QWs). Section 3.2 introduces the band lineup of the various materials, including the effects of strain on the heavy hole and light hole bands. The role of indium and antimony on the band lineup are significant, and will be discussed in this section.

Indium and antimony also have significant effects on the growth kinetics. These will be discussed in Section 3.3.

This chapter will then turn to the most remarkable, and universal, property of the dilute nitrides, namely the reduction in bandgap. GaInNAs, for example, can be grown with approximately half the bandgap of GaAs. As was shown in Figure 2.4 (page 14), adding nitrogen not only decreases the lattice constant (as expected for a small atom), but the GaNAs alloy line runs diagonally in the opposite direction from all the other III–V semiconductors. The bandgap eventually reaches a minimum somewhere between 30–50% nitrogen, where some theories predict no bandgap at all. With even higher compositions of nitrogen, the alloy line rises back toward the upper left, toward GaN, obeying the normal III–V trend. Chapter 4 will present evidence that there are multiple, independent causes that contribute to the reduction in bandgap (band bowing) with small amounts of nitrogen. The primary causes of large band bowing will be discussed beginning in Section 3.4. These include band anti-crossing [70], isoelectronic co-doping, and concentrated defects.

Another universal property of dilute nitrides is that the luminescence intensity increases dramatically with anneal, and this improved luminescence is accompanied by a (generally undesirable) shift toward the visible spectrum (larger bandgap), or blueshift [71, 72]. This behavior is quite complicated and cannot be explained by any one mechanism. The strongest component of the blueshift appears to be the rearrangement of Ga and In to minimize local strain near each nitrogen atom [73, 74], discussed in Section 3.5. There are also contributions from nitrogen outdiffusion,

broadening of the QW (Ga-In interdiffusion), homogenization or quasi-ordering of the atoms, and removal of defects with anneal.

This leads to a discussion of the defects in dilute nitrides, in Section 3.6. There are many sources of defects in GaNAs and GaInNAs. Some of these are inherent to the material; many are not. There is evidence that one or more of the defect levels may occur close to the conduction band, and in fact be above the conduction band if the bandgap is small enough.

Finally, it appears that dilute nitrides are well suited for long wavelength optoelectronic applications. The width of the gain spectrum of dilute nitrides is exceptionally large, up to 50nm. The threshold current of GaInNAs(Sb) may have a higher characteristic temperature T_0 (i.e. be less sensitive to changes in temperature) than other lasers, although the improvement is less than originally hoped. The emission wavelength of GaInNAs(Sb) also be less sensitive to temperature, which is very useful for wavelength-dependent devices such as VCSELs and ARROWs. Also, the absolute gain and electroabsorption coefficients are up to two times larger than conventional III-V semiconductors, offering promise for modulators and high power lasers.

3.2 Band Alignment in GaNAs and GaInNAs(Sb)

At an interface between two semiconductors, there are three ways in which the conduction and valence bands may line up, as shown in Figure 3.1. For a Type I band alignment, the narrower bandgap material lies entirely within the bandgap of the wider bandgap material. For Type II band alignment, both the conduction band and valence band are higher in one material than the other, but there is still overlap between the bandgaps. For Type III band alignment, there is no overlap between the bands. Type III alignment is very unusual in semiconductors, although it would be useful for applications that require a tunnel junction.

Dilute nitride alloys generally form a Type I band alignment with each other and with GaAs. GaNAs with GaAs is the weakest Type I band alignment, because nitrogen does not affect the valence band [75]. In fact, GaNAs/GaAs is actually Type II for heavy holes and Type I for light holes. This is due to the tensile strain,

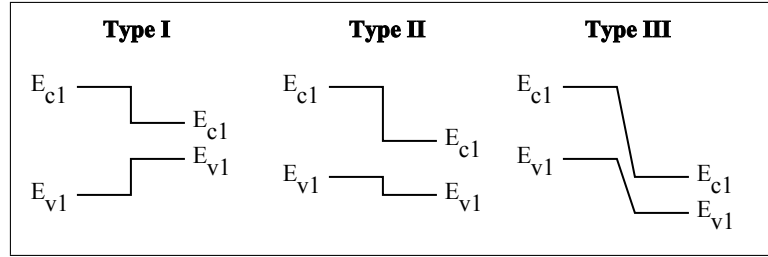


Figure 3.1: Possible band lineups at a heterostructure interface.

which raises the light hole band into the bandgap, while pushing the heavy hole band further away. This hybrid Type I/II nature has led to extensive controversy in the literature, partly because of the poor material upon which the band alignment studies were based. The evidence for a Type I band alignment is quite strong, however. Mussler reported that the luminescent lifetime of carriers is approximately 400ps, far too short for a Type II structure that would have electrons and holes separately confined [76]. The low threshold of GaInNAs(Sb) lasers is also a compelling argument for Type I band alignment [77, 56]. In the case of lasers with tensile GaNAs barriers, as reported later in this thesis, the conversion of light holes to heavy holes at the GaNAs-GaInNAs(Sb) interface is believed to be rapid due to strong alloy scattering, which breaks the semiconductor degeneracy.

L. Goddard has performed measurements of the electroluminescence transitions from GaInNAsSb/GaNAs QWs, plotted in Figure 3.2(a). A good fit with experiment can be achieved with Type I lineups for all transitions except light holes at the GaNAs/GaInNAsSb interface, which appears to have a mere 16meV barrier.

Finally, Kudrawiec has performed careful photoreflectance (PR) measurements that show a band lineup of 50–60meV to light holes in and 250meV to heavy holes in GaInNAsSb, as shown in Figure 3.2(b) [79]. Although band offsets are particularly difficult to measure to such accuracy, these show fairly good agreement with Goddard’s measurements. These measurements were performed on material with the lowest PL and low-temperature PL linewidths ever reported at $1.5\mu\text{m}$, so the measurements are believed to be representative of the actual material, with little interference from defects or other growth artifacts. The conclusion from the band lineup measurements is that GaNAs may have a slight Type II band lineup to either

GaInNAsSb or GaAs, but in either case, the offset is very small (10–15meV), and only for one type of holes, light or heavy. The other type of hole sees a Type I band lineup with no barrier to injection.

The best material to date is grown with a large amount of indium, and also, optionally, a moderately small amount of antimony. These both lead to compressive strain in the material. This is advantageous for improving the overlap of the electron and hole wavefunctions, but with high strain, the critical thickness is also very small: only thin layers can be grown before the crystal relaxes, forming many defects due to misfit dislocations. Although nitrogen can partially compensate some of the compressive strain, large amounts of nitrogen have been found to degrade the material quality.

Therefore, the longest wavelength emission to date appears to be reached using GaInNAs or GaInNAsSb quantum wells, surrounded by GaNAs barriers for strain compensation of the structure as a whole [80, 81, 21]. The GaNAs also decreases the quantum confinement in the QW, decreasing the bandgap and extending the wavelength. It also provides a source of nitrogen to prevent outdiffusion upon anneal. But compressive strain by itself tends to promote phase segregation and dislocations, leading to early device failure. GaNAs, on the other hand, is tensile strained on GaAs, so by growing GaNAs barriers below and above the QW, the total strain is reduced. Additional compressive strain from multiple quantum wells can be compensated by making the GaNAs layers either thicker or with more nitrogen. However, even with tensile GaNAs barriers for strain compensation, strain sets an upper limit of roughly 3 QWs for VCSELs at $1.5\mu\text{m}$. With more than 3 QWs, the compensating layers of GaNAs must be either very thick or contain a large fraction of nitrogen. Large nitrogen concentrations lead to defects and degraded growth, while thick layers push the QWs so far apart that they no longer overlap with the peak of the standing wave in the VCSEL cavity. It is also possible for very highly strained GaInNAsSb to reach the critical thickness within a single QW, if the strain is not already partially compensated by layers below it.

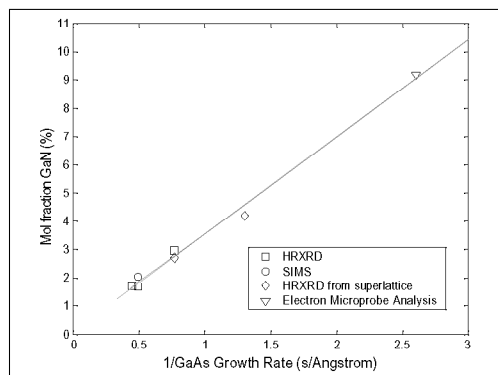


Figure 3.3: Unity (or constant) sticking coefficient leads to linear dependence on growth rate. From Spruytte [71].

3.3 Effects on Growth from N, In, and Sb

3.3.1 Nitrogen

Molecular nitrogen (N_2) is very unreactive, and does not participate in semiconductor growth, but atomic nitrogen is extremely reactive. The nitrogen coming from the plasma is so reactive that we find a “unity”—or at least constant—sticking coefficient over a wide range of temperatures, growth rates, and compositions [71]. This is apparent from the linear dependence in growth rate in Figure 3.3. It was reported by Reason [82] that nitrogen incorporates by the exchange of nitrogen for an arsenic atom on the surface, most likely with a 2×1 surface reconstruction, which has more available Group V sites than either of the other common reconstructions, 3×1 or 2×4 . (We observe 2×4 reconstruction during our growth, presumably due to high pressures of As_2 .) It should be noted that antimony actually increases the fraction of nitrogen in the crystal. Either it enables some new species of nitrogen to stick (perhaps ground-state N_2 , as opposed to excited radicals N_2^*), or else there is some temperature-independent mechanism of nitrogen escape (desorption) at the surface.

Nitrogen also increases the effective mass in the semiconductor. Early papers arguing for an effective mass of $0.5m_e$ were based on a faulty interpretation of lineshapes, particularly the omission of band anticrossing and the light hole bands [83]. There is a growing consensus that the electron effective mass is on the order of $0.08\text{--}0.10m_e$.

The composition of nitrogen is determined by x-ray diffraction (XRD), calibrated by secondary ion mass spectrometry (SIMS) and nuclear reaction analysis Rutherford backscattering spectrometry (NRA-RBS). These techniques are all easily misled by nitrogen, due to matrix effects (SIMS), surface nitrogen (SIMS and NRA-RBS), and nitrogen split interstitial defects $(N-N)_{As}$ and $(N-N)_{As}$ (XRD and NRA-RBS). Bisognin [84] discusses how to do RBS with nitrogen. Split interstitials are compressively strained, which probably explains the discrepancy between groups: Spruytte says XRD underrepresents %N for large %N [85], Li says XRD overrepresents %N [86], and Uesugi says it is just right [87]. Fan reports that XRD is fine up to 3%N then falls, being in error by 8% with $[N]=3.7\%$ [88].

The remaining properties of nitrogen will be discussed in more detail in their own sections later.

3.3.2 Indium

Indium has long been used to reduce the bandgap of GaAs. InGaAs lasers grown on GaAs are very well understood, and are effective for $0.980\mu\text{m}$ wavelengths. During growth, indium has a much higher surface mobility than gallium, so it must be grown at a correspondingly lower temperature, or else the indium will segregate and form islands (quantum dots) of InAs. Indium also tends to ride the surface (i.e. it avoids being buried by trading places with a gallium atom above it), especially at higher temperatures. The high surface mobility also allows indium atoms to find good locations on the lattice, filling vacancies and preventing arsenic antisites, even at the relatively low temperatures required for nitrogen growths, $375\text{--}450^\circ\text{C}$. This is the primary reason why Kondow's discovery of GaInNAs [8] overshadowed GaNAs [3], because indium promotes better material quality for the same growth temperature and desired wavelength. GaInNAs also benefits from the compressive strain and better electron/hole overlap mentioned earlier. Although nitrogen changes the bandgap more than indium (for the same amount of strain), GaNAs cannot be grown with the same material quality as InGaAs due to the limits imposed by phase segregation. When grown too hot, however, indium is believed to be responsible for the long-range

segregation seen in GaInNAs cathodoluminescence [59], TEM [89], and atomic force microscopy [90].

3.3.3 Antimony

Antimony was first introduced as a surfactant in GaInNAs growth by Wang et al. [91], although they reported seeing no incorporation [92]. Antimony had long been used as a surfactant in epitaxy. As a large and less reactive atom, it tends to ride the surface during growth, and reduces the mobility of Group III atoms on the surface, while maintaining a high surface mobility itself. It can thus prevent strain relaxation [93]. Several groups have reported that antimony does incorporate into the crystal, however, extending the wavelength for the same reasons as indium [16, 19].

Antimony has complex interactions with nitrogen, arsenic, and indium. As mentioned above, antimony increases the amount of nitrogen in the crystal. This is likely due to the reduction of defects in the crystal, which has been found to change the nitrogen composition (Section 4.9). It might also be due to some other growth mechanism at the surface. U. of British Columbia has reported finding an AsN dimer in the chamber when the wafer was exposed to a bismuth surfactant [94]. We were not able to replicate this finding; our AsN background pressure at the mass spectrometer did not change with antimony, although it should be noted that our mass spectrometer was not quite within line of sight of the wafer. Antimony has been used to push GaInNAsSb emission to over $2\mu\text{m}$ on InP [95] and $2.3\mu\text{m}$ on GaSb [96].

The interplay between the other Group V atoms, Sb and As, turned out to be simpler than expected. Historically, MBE and MOCVD with mixed Group V elements (other than nitrogen) suffer from non-repeatable growth, since a small change in the Group V gas or flux ratios can lead to a large change in composition. This is illustrated in Figure 3.4. However, we grow with very small amounts of antimony, and in the dilute limit, and at cold temperatures, the antimony sticking coefficient appears to be relatively constant. This is analogous to the linear regime at the extremes of Figure 3.4. We use a cracker to thermally crack dimeric Sb_2 into monomeric Sb_1 , which was thought to be more reactive, but recent growths with uncracked Sb_2 appear

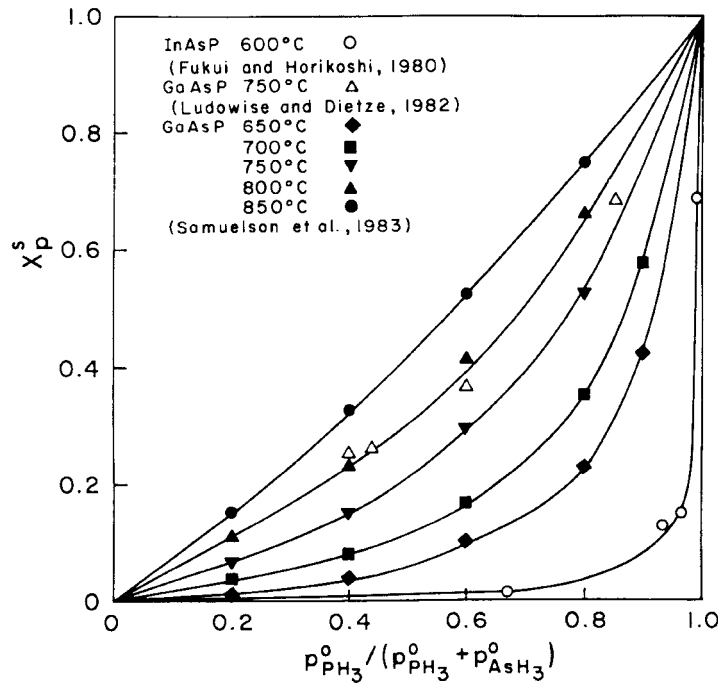


Figure 3.4: Compositions from MOCVD growth with mixed Group V elements, showing nonlinear relation between Group V precursor ratio and the ratio of incorporated species. From Stringfellow 1989. [98]

to be identical [97].

Finally, indium appears to change the concentration of antimony, but not vice versa. This is true for cracked Sb_1 [99] as well as uncracked Sb_2 [100]. The fact that there is interaction between them is probably due to the competition for surface sites, especially along step edges, which are the positions of lowest energy for excessively large atoms such as In and Sb. The fact that indium trumps antimony for incorporation is likely due to the standard kinetics of III-V growth, in which Group III atoms have a high sticking coefficient, while excess Group V atoms simply evaporate from the surface.

3.4 Reduced Bandgap in Dilute Nitrides

3.4.1 Band Anticrossing

The single most important property of the dilute nitrides is the reduction in bandgap as the mole fraction of nitrogen is increased. As mentioned in Section 2.4, the dilute nitrides surprisingly fail to obey Vegard’s Law, but instead display a large band bowing, with a decrease in bandgap as the nitrogen composition is increased. Suda et al. predict that GaNAs can be grown stably over the full range of nitrogen mole fraction from GaAs to GaN, with a wurtzite structure above 40% N, and a zincblende structure under 40%N [101]. Despite the predicted stability, most reports of GaNAs with more than 5% N are plagued by severe segregation and defects, so it is difficult to discern exactly what the band structure is doing as one leaves the dilute limit. In the absence of such measurements, considering only the dilute limit, there have been many theories proposed to explain the reduction in bandgap, including band anticrossing [70], local depressions in the bandgap, alloy fluctuations [102], impurity-like band formation [103, 6, 104], mixing of the Γ valley with the L or X conduction band minima due to symmetry breaking, isoelectronic impurity/doping levels, or multiple effects [105]. It will later be shown in Section 4.9 that the apparent impurity band is largely induced by plasma damage during growth, and may be minimized by protecting the wafer from the plasma.

Band anticrossing is the most widely accepted explanation for the reduced bandgap [70]. In the band anticrossing model, shown in Figure 3.5 nitrogen creates a defect level E^+ above the conduction band, localized in real space and extended in momentum space. The conduction band would normally cross the defect level near the center of the Brillouin zone ($k = 0$), but the two levels repel each other, or “anti-cross.” This pushes the lower band E^- further down, reducing the bandgap. This was predicted by Hjalmarson [106] and Wolford [107] but had not been experimentally observed until the dilute nitrides.

The strongest evidence for band anticrossing is the resonant tunneling into the E^+ state [108], validating the existence of a band that is not predicted by most other theories. Electroreflectance measurements have also been used to probe the E^+ and

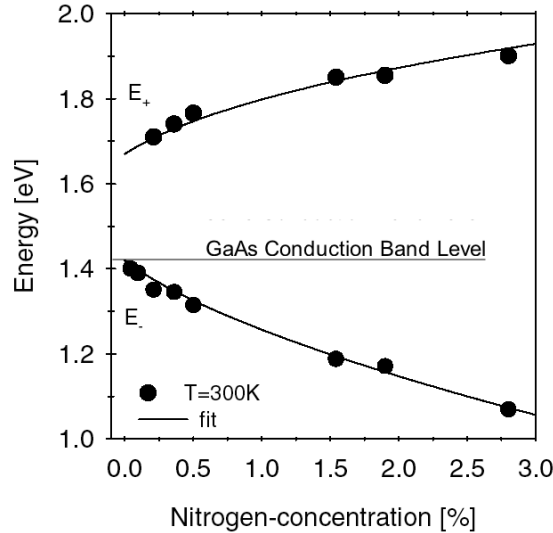


Figure 3.5: Band anticrossing. Nitrogen creates a new level, E^+ , which mixes with and repels the original conduction band level, now E^- . After Klar [105].

E^- levels [109, 110, 105], although these have been called into question due to the use of MOCVD-grown material (lower quality), as well as the lack of unambiguous identification of the ER transitions. Finally, measurements of bandgap vs. nitrogen composition were found to agree well with the predictions from band anticrossing [111], although other models could make similar predictions.

In addition, the $\Gamma - X$ band mixing in GaNAs was discredited by Weinstein using hydrostatic pressure studies [112]. The spectroscopy group at NREL suggests that E^+ can be generated by indirect transitions, which are themselves generated by alloy disorder [109, 113]. But the lack of indirect transitions even under high hydrostatic pressures all but rules out this possibility. At any rate, $\Gamma - X$ mixing is expected to be important for GaNP [6], where every nitrogen atom has a bound state.

What the band anticrossing model fails to explain are the changes with anneal, or with wafer damage, or any carrier localization effects. But these are probably due to N-N clusters, H-N clusters (especially in MOCVD & GSMBE [114]), and Ga vacancies (particularly MOCVD), and are not inherent to nitride growth. Or these effects could be caused by segregation; Zhang (at NREL) predicted that GaNAs would segregate if an N-rich plane were allowed to form [115]. However, we had a heavily nitrated

surface that did not segregate, as discussed on Page 102.

3.5 Effects from Annealing

3.5.1 Various Defects and Improved Luminescence with Anneal

From very early on, it was clear that the material quality of GaInNAs improved dramatically upon annealing, particularly with a short, high temperature anneal [116, 117, 71]. A 60 second anneal at 700–800°C could increase the photoluminescence intensity by a factor of 30 or more. This was a much stronger improvement than in most other III–V laser materials.

Many types of defects have been identified in Ga(In)NAs that could cause such an improvement with anneal. Krispin identified a number of electron traps [5, 118] and hole traps [119, 120]. The chief of these was the nitrogen split interstitial $(\text{N-N})_{\text{As}}$, two nitrogen atoms on the same Group V site. $(\text{N-N})_{\text{As}}$ is believed to break apart with anneal. Due to the inverse correlation between the concentration of $(\text{N-N})_{\text{As}}$ ¹ and luminescence intensity, it is believed that $(\text{N-N})_{\text{As}}$ is the dominant source of nonradiative recombination in high quality material. Ramsteiner identified nitrogen second-nearest neighbors (i.e. nearest Group V neighbors) as a possible source for change in PL intensity [121], but this seems a more likely cause of blueshift (below).

There are also many defects in GaInNAs that are believed to be permanent, surviving anneal, but it is possible these could also improve with anneal. Krispin also identified the arsenic-nitrogen split interstitial $(\text{As-N})_{\text{As}}$ in our material, believed to be one such stable defect. Grüning reported quasi-defects due to nitrogen clusters, although it was unclear whether these clusters referred to actual nitrogen segregation, or merely relative positions of nitrogen on nearest Group V lattice sites. For clustering to improve with anneal, the nitrogen would need to disperse to perfectly homogenous, if not ordered, lattice sites. At any rate, the material was early MOCVD growth, with extremely broad linewidth (20meV for just 0.2% nitrogen), so the results are

¹Or whatever defect was at that energy.

somewhat in question. Similarly, Buyanova reported strong potential fluctuations in low temperature PL (LT-PL), which were attributed to strong variations in the bandgap. These were found to be worse with lower growth temperatures. Again, it was unclear what the cause of the bandgap fluctuations was, and hence unclear whether these contributed to the blueshift. (Arsenic capping and ion deflection plates answered the latter question in the affirmative, as shown in Section 4.9.)

It is worth noting that PL intensity improves with anneal up to a certain temperature, above which the intensity starts to fall again. This may be due arsenic vacancies V_{As} diffusing from the surface or from elsewhere in the lattice into the vicinity of the quantum well. It may also be due to outdiffusion from the QW [122], or strain relaxation or phase segregation. Vacancies and other defects can serve as nucleation points for relaxation or segregation, so preventing defects can allow annealing at higher temperatures. This, too, will be revisited later (Section 4.9.3).

3.5.2 Blueshift with Anneal due to Ga-In Rearrangement

The other major effect of annealing dilute nitrides is the blueshift, or shift of emission to shorter wavelengths [117, 71]. The majority of the blueshift has recently been shown to be due to nearest-neighbor atomic rearrangement, when gallium and indium atoms trade places so each nitrogen is surrounded by indium, in order to reduce the local strain and the total energy of the lattice. This was suggested by Kitatani et al. based on vibration modes [73]. It was also verified by photoreflectance [123] and electroreflectance [124], although these are somewhat subjective, and Shirakata and Kondow et al. did not see it at all [125]. Further verification was found from additional Fourier transform infrared spectroscopy (FTIR) measurements [126]. It was also shown from bond lengths in NEXAFS [74], and by absorption measurements, which showed 5 distinct absorption peaks corresponding to the number of possible indium atoms around each nitrogen [44]. However, atomic rearrangement cannot explain the same blueshift with anneal observed in GaNAs, which has no indium to rearrange.

3.5.3 Other Causes of Blueshift with Anneal

Nearest-neighbor rearrangement can only explain part of the blueshift due to anneal. It is noteworthy that the blueshift of GaInNAs cannot be fitted by either a single or double exponential with temperature, which strongly suggests that three or more different physical effects of comparable magnitude are present. The source of the remaining blueshift has been the subject of controversy and heated discussion, but four principal candidates exist: nitrogen diffusion and/or removal from the QW, Ga-In interdiffusion at the QW boundary (thereby decreasing the depth of the quantum well), and localized depressions in bandgap due to either nitrogen clusters or point defects, either of which might be removable with anneal. Each of these will be examined below.

It should be noted that a strong blueshift with anneal (or, equivalently, with heating from laser operation) would be a disadvantage for dilute nitride lasers, since many laser applications require a stable wavelength. By the end of our work reported in the following chapters, however, many of the causes of blueshift had been identified and reduced. The wavelength of our lasers is significantly more stable with time or anneal.

Nitrogen outdiffusion from the QW was demonstrated by performing secondary ion mass spectroscopy (SIMS) on early samples at Stanford[127] and elsewhere[128], and even reported recently for anneals above 900°C [122]. Although these results were called into question due to the frequent run-to-run variations common with SIMS, there was a consistent decrease in nitrogen signal after annealing, as shown in Figure 3.6(a). Also, the SIMS signal from other elements such as In or Sb (not shown) did agree from run to run. Furthermore, when using GaNAs barriers around the QW, SIMS clearly showed different rates of nitrogen loss in GaInNAs QWs as compared to the GaNAs barriers, as shown in Figure 3.6(b). The GaNAs barriers also decreased the blueshift with anneal, which is consistent with maintaining nitrogen in the QW. [Picture] This nitrogen outdiffusion decreased in more recent material, and other groups reported finding no outdiffusion whatsoever [129, 117], or only with ion damage [130], leading to some controversy.

A similar controversy has centered around whether there was interdiffusion of

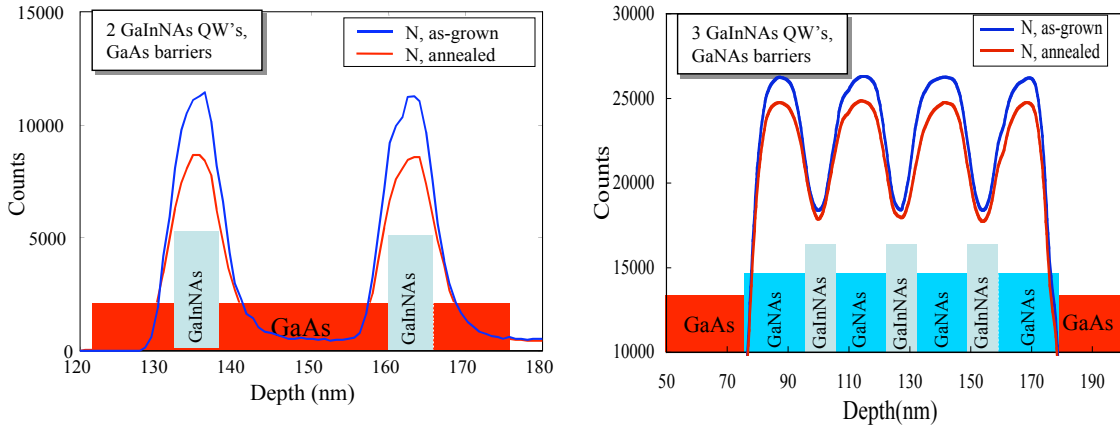


Figure 3.6: Nitrogen outdiffusion in SIMS. (a) Two GaInNAs QWs in GaAs barriers. (b) Three GaInNAs QWs in GaNAs barriers. The nitrogen in QWs is protected by higher levels in GaNAs. (From Ref. [59])

Group III elements at the QW boundary. If indium is able to diffuse into the walls of the quantum well, then the well becomes wider and shallower, leading to a strong blueshift due to the shallower quantum well. Some asserted that this was the dominant source of blueshift, without evidence, but another group established it with TEM, [129] finding 1nm of diffusion. Our material showed no such interdiffusion, to within measurable limits of TEM (approximately 1-2 monolayers) [90]. Although indium rode the surface for 3-4 monolayers during growth, and the QWs were rough to begin with, the “softness” or grading of the QW interfaces did not change with anneal according to TEM [35]. A blueshift from QW intermixing presents a long term reliability problem for VCSELs and edge emitting lasers due to the endless shift in wavelength and reduction of carrier confinement.

The discrepancy between groups appears to be due to the presence or absence of vacancies in the crystal. Sputtering SiO_2 onto the surface of GaAs creates gallium vacancies, and subsequent annealing allows those vacancies to propagate to the underlying QW and promote rearrangement. Although this mechanism has been known in industry for many years,[131] it has only recently been demonstrated and explained in GaInNAs [132]. GaInNAs growth generally starts with a layer of GaAs under normal growth conditions, but then the temperature of the substrate is reduced 100–180°C in

order to stabilize it at temperatures appropriate for GaInNAs. This results in a layer of low temperature grown GaAs before the quantum well(s). There is a similar layer of LT-GaAs after the quantum well(s), as the substrate is ramped back up to normal GaAs growth temperatures. Khreis has reported that InGaAs grown at low temperatures has a high concentration of point defects, and these defects were responsible for In-Ga interdiffusion at the QW interfaces, causing a larger blueshift with anneal [133]. For MOCVD and gas source MBE, gallium vacancies are generated by a N-H complex during growth, discussed on page 3.6.4. For solid source MBE, the defect density near the QWs is critically related to the duration and temperature of the adjacent, low temperature GaAs layers, as well as the quality of GaNAs barriers, if present. So the Ga-In interdiffusion is almost wholly dependent upon poor growth conditions in or near the QW, and even post-growth processing, and the best quality material in PL or low-threshold lasers should demonstrate the least blueshift with anneal. Indeed, as mentioned in the previous section on PL, the highest quality material from our growth, CNRS, and Infineon does not show as much shift with anneal.

Reduced fluctuations of the bandgap will be discussed in Section 4.8.

Although nitrogen dramatically decreases the band gap of the material, it also brings a host of associated defects such as arsenic antisites As_{Ga} , the split interstitials $(\text{N-N})_{\text{As}}$ and $(\text{N-As})_{\text{As}}$, vacancies, and other point defects. (See, for example, Refs. [119, 118, 6] for a list of many possible defects, with citations.) Identifying and removing the sources of these defects was crucial to the development of $1.5\mu\text{m}$ edge emitters and the VCSELs presented here. There are also random fluctuations in the bandgap due to random, statistical fluctuations in the distribution of nitrogen [104], although it is not clear that these survive anneal.

There is one additional type of defect worth mentioning: the N-H complex. Although hydrogen has been reported as improving surface morphology [134], Ptak reported that the concentrations of gallium vacancies, V_{Ga} , closely follow the concentrations of hydrogen in the structure [114]. These vacancies are theoretically unfavorable in solid-source epitaxy, but hydrogen decreases the formation energy by 2eV, making them favorable [135]. They have been observed as a dominant defect in material grown by MOCVD [136] and by gas-source MBE [54]. These vacancies are

only partially removed by anneal. The correlation between vacancies and hydrogen concentration suggests that a N-H complex is responsible for the gallium defects. The N-H complex should be a shallow acceptor, and removal of hydrogen by anneal can even cause p-type as-grown material to change to n-type material after anneal [137]. These complexes suggest that hydrogen may be responsible for the reliability problems with MOCVD-grown lasers, whereas MBE-grown lasers have been demonstrated with an extrapolated lifetime of decades [138]. It now seems likely that early studies of material parameters, such as effective mass and bandgap, were misled by the effects of these vacancies. Even today, care should be taken to distinguish the effect of widespread defects from inherent material properties of dilute nitrides, because these defects—and others that are not removed by anneal—greatly complicate the analysis.

Of the five blueshift mechanisms mentioned above (“healable” point defects, nearest neighbor rearrangement, N diffusion or removal, Ga-In interdiffusion, and nitrogen clusters), only the last three can contribute to a continuing blueshift as the wafer is progressively annealed. Nearest neighbor rearrangement and the breakup of nitrogen dimers are, in principle, processes that run to completion after a certain amount of time or temperature, so we can eliminate those as sources of “endless” blueshift with temperature.

3.6 Other Defects in Dilute Nitrides

3.6.1 Background Contamination

A number of other defects have been identified in dilute nitrides, including several due to contaminants, such as oxygen, carbon, and hydrogen. The interaction of nitrogen with aluminum is also suspected of being problematic. We do not believe any of these play a significant role in our present material, but it is good to be aware of their effects in order to be able to identify them when they appear. Another background species in the chamber, AsN, was also observed by mass spectrometry. In addition to the defects related below, a catalog of defects in GaInNAs may be found at Ref. [6].

Secondary ion mass spectrometry (SIMS) measurements on our material shows

the background level of all of these contaminants to be below the noise floor (5×10^{16} for H and O, 5×10^{15} for C), as shown in Figure 3.7. Our oxygen contamination was reduced by a factor of 5–10 when the filter on the nitrogen line was replaced. We believe there was another reduction of 5–10x when a trace leak in the nitrogen backing pump was fixed. The background levels of oxygen in the MBE chamber mass spectrometer is below the noise floor. SIMS measurements on our material shows the contaminant level to be near or below the noise floor for C, CO, CO₂, H₂O, O, and O₂, and approximately 10^{-10} Torr for H. It typically requires 1–2 months of growth after an opening to get down to these levels.

3.6.2 Oxygen

Oxygen contamination has always been a serious issue in GaAs-related growth. Oxygen contributes a deep level defect with strong nonradiative recombination. Oxygen on the surface also pins step-flow growth, leading to dislocations that can propagate as dark line defects and cause the premature death of lasers. Oxygen is one of the major contaminants in commercial grades of bottled nitrogen gas, since O₂ and N₂ condense into liquids near the same temperature. In extreme cases, oxygen contamination may be identified by its distinct spectral lines at $0.6158\mu\text{m}$, $0.7002\mu\text{m}$, and $0.7772\mu\text{m}$ in the plasma emission spectrum [139, 140]. These features have never been observed in our emission spectra, even before taking measures to reduce oxygen in the nitrogen line (Section 4.12). However, small amounts of oxygen were apparent in secondary ion mass spectrometry (SIMS). Therefore SIMS is the preferred method of measuring oxygen contamination in GaInNAs. Oxygen is still a major contaminant in many groups' material [141], and probably contributes to the “S shape” that others report in low temperature PL.

It will be noted in Section 4.6.3 that changes in nitrogen composition should only be achieved instead by changing the Group III growth rate. However, if the nitrogen gas were contaminated, this would incorrectly suggest that more nitrogen led to worse material. For example, slower growth rates would allow more time for oxygen or water to accumulate on the surface. This may have contributed to the apparent

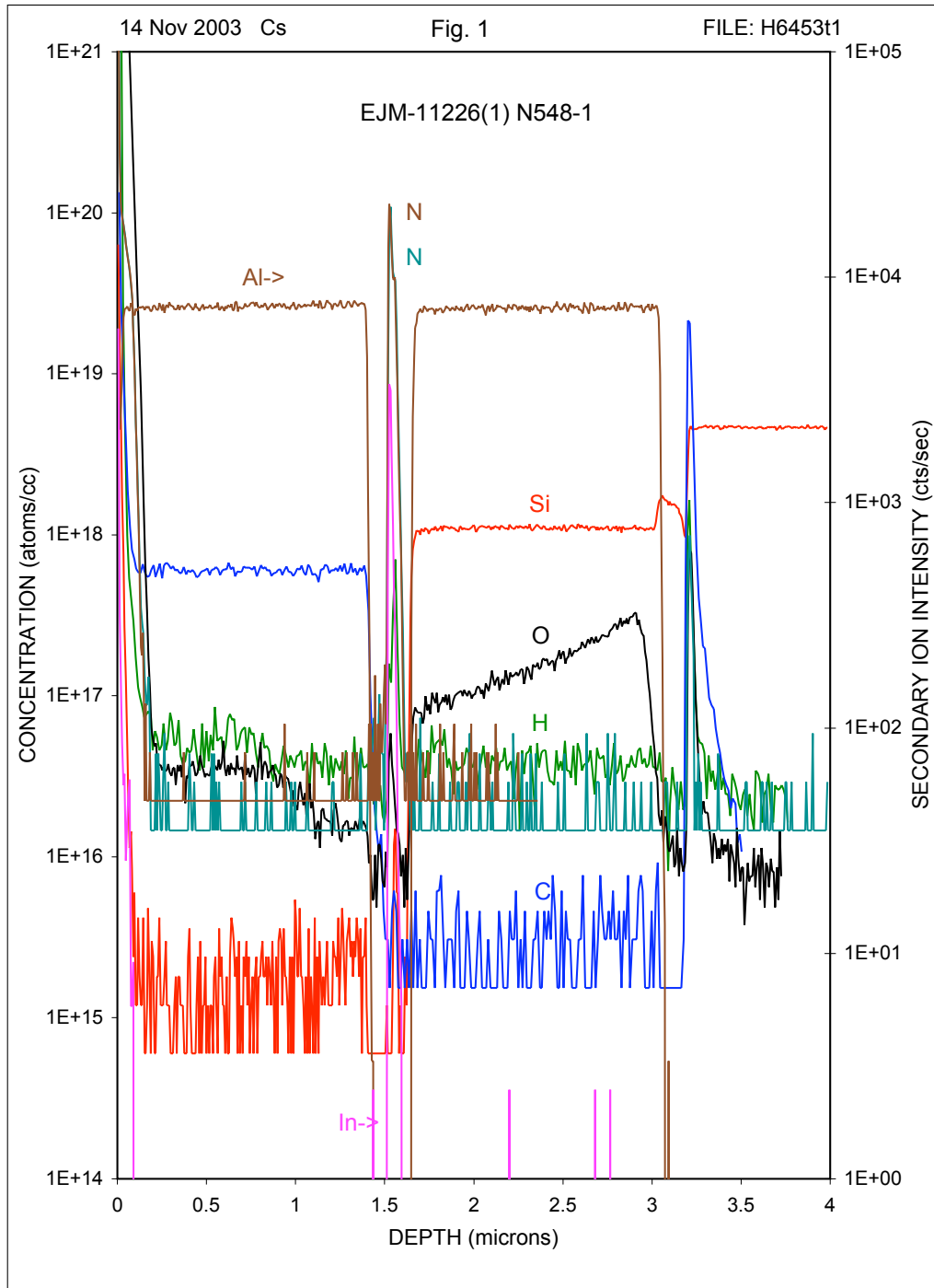


Figure 3.7: SIMS shows very low contamination unless intentionally doped (e.g. C or Si).

“nitrogen penalty” discussed in Section 4.1. Conversely, if the growth conditions were kept constant but the nitrogen RF power or flow were varied to change the nitrogen composition, this may incorrectly lead to the conclusion that more nitrogen led to better material.

3.6.3 Carbon

Even before GaInNAs was discovered, carbon was known to form a stable, deep-level defect in the presence of nitrogen [142]. During GaInNAs growth, nitrogen increases carbon incorporation, and there has been a strong correlation reported between carbon concentration and laser threshold current [57], but this may also have been due to aluminum contamination (below). Either way, carbon contamination appears to be a significant problem only for MOCVD, where the precursor gases inherently include carbon.

3.6.4 Hydrogen

Hydrogen has had a mixed reputation in the growth of GaInNAs [143]. It has been reported to dramatically increase PL intensity and reduce potential fluctuations (carrier localization) if used during growth [144] or being implanted [145]. There is also a blueshift in wavelength. These effects are reduced or eliminated by a post-anneal growth, which raises questions of long-term stability of lasers grown with hydrogen. Annealing GaInNAs under a hydrogen ambient has the same effect, and is completely reversible by reannealing with an inert gas [145, 146]. These are consistent with hydrogen eliminating one of the nitrogen levels in the conduction band [147].

But hydrogen is also responsible for defects. Hydrogen has been found theoretically to prefer an $H_2^*(N)$ complex rather than an interstitial H_2 site (which would be better behaved, having little effect on the crystal), and also H acts solely as a donor in GaNAs and GaInNAs [147]. Li used positron annihilation and found a large number of gallium vacancies in material grown gas-source MBE, which uses arsine gas (AsH_3) instead of evaporated solid arsenic [54]. Ptak reported the same result for MOCVD-grown material, and attributed it to a N-H complex [114]. It is not known

how these results would change for MBE material with either H_2 or atomic H in the chamber. Solid-source MBE does not appear to have a measurable number of gallium vacancies, but is dominated by traps associated with As sites [114, 118].

As a curious additional note, Bruno has reported that adding 3% hydrogen to the N_2 gas flow can passivate the GaAs surface at the end of growth [148]. The hydrogen appears to remove excess surface arsenic, creating a thin but exceptionally stable layer of GaN on the surface. This may have significant repercussions for transport devices, since the existence of a stable passivating layer (SiO_2) is one of the chief advantages of silicon over GaAs.

3.6.5 Aluminum

In the past year or so, there have been increasing suggestions that nitrogen may interact with the aluminum cell in MBE. Aluminum nitride is an extremely stable compound, and the deposition of AlN on the wafer would almost certainly lead to defects, as it is unlikely to be cracked on the surface. In fact, the first VCSEL at $1.2\mu m$ was made possible only after the realization that the nitrogen plasma must be ignited after the aluminum layer was finished [35]. If nitrogen interferes with aluminum layers, or vice versa, this could add a significant obstacle to the growth of GaInNAs. It would also be extremely difficult to control all of the relevant variables, since AlN apparently has a long memory effect. On the other hand, both of the other groups demonstrating GaInNAs(Sb) lasers beyond $1.5\mu m$ are using MBE machines with aluminum and nitrogen in the same machine [149, 23], so perhaps this interaction is overrated.

It may seem convenient to simply quantify the difference in AlGaAs material quality between a nitride machine such as System 4, and a nitrogen-free machine such as System 5. However, this comparison is actually not meaningful. Aluminum is an excellent gettering material: it collects oxygen and other contaminants, so aluminum cells need to be operated at high temperatures to remove these contaminants. System 4 is used for thick layers of AlGaAs, so both aluminum cells get frequent use. On System 5, the single aluminum cell only got occasional use, and only for short

periods such as a cap layer for PL structures. When we modified our standard PL structures to be aluminum-free, the cell was used even less frequently. Therefore it was likely full of contaminants that would have long been evaporated in System 4.

Although it is not a materials issue *per se*, AlN forms in the lip of the aluminum cell, or on the surface of the aluminum melt, and this may have contributed to the failure of the aluminum crucible in System 5. Nitrogen also accelerates the creep of aluminum out of its crucible [150], leading to eventual destruction of the cell. So even if there is no interaction between aluminum and nitrogen for growing high quality materials, there is still strong motivation to separate aluminum from nitrogen in the chamber.

The interactions between aluminum and nitrogen are more apparent in MOCVD. Schlenker proposed separating the strained buffer layer from the QWs, either to avoid Al-N interaction, or to bury contaminants or defects [151]. This idea goes back even further, to Kroemer and Okamoto [152]. Kawaguchi reported an improvement in lasers when GaInNAs QWs were grown in a separate MOCVD reactor from the AlGaAs cladding [153]. The most common nitrogen precursor, dimethylhydrazine (DMHz), pulls aluminum off the walls of the chamber, leading to up to 1% Al in the QW [154]. The result is that aluminum *and* its precursors need to be scrubbed from the chamber, either with another gas (an aluminum getterer) or with growth in a separate chamber. Even with QW growth in a completely clean reactor, however, Sundgren reported that an unknown aluminum-containing species rides through the GaAs buffer to the QW interface, where it apparently bonds with nitrogen [155]. These are some of the obstacles in the way of growing longer-wavelength GaInNAs by MOCVD.

3.6.6 AsN

One unusual species that has been observed in our chamber is the AsN dimer. A group at the University of British Columbia has observed AsN being produced when they grow GaInNAs with bismuth as a surfactant [94]. AsN was visible in our mass spectrometer (89 amu) when the RF was turned up and the cell was hot, whether or

not the plasma was running. The flux increased sharply when the nitrogen shutter was opened, indicating that the dimer was coming from inside the cell. Like arsenic, AsN eventually goes away with time, so it is believed to be evaporating from the plasma cell. It is unknown what effect AsN has upon GaInNAs growth. Conventional wisdom in elemental chemistry is that double bonds generally form only among elements on the first row of the periodic table, so it may be unlikely that AsN is stable, and it probably cracks on the hot wafer surface. If it did not crack, it would incorporate as the dreaded $(\text{As-N})_{\text{As}}$ split interstitial defect [85, 54].

3.7 Conclusions for GaInNAs for Optoelectronics

We have seen that the dilute nitrides are a favorable material for creating lasers and other optoelectronic devices in the 1.3–1.5 μm range of wavelengths. It emits further into the infrared than GaAs, while still allowing growth on GaAs substrates, with AlAs/GaAs DBRs available for VCSELs. The inherent and intrinsic properties of the material include a small bandgap, an improvement in luminescence with anneal, and a shift of the emission to shorter wavelengths with anneal. GaInNAs has a Type I band alignment with GaNAs or GaAs, and a larger electron effective mass provides a better overlap between the electron and hole wavefunctions, leading to higher gain.

GaInNAs may have several additional properties that are particularly favorable for optoelectronic devices. It appears to have less of a shift in wavelength with temperature [124], so VCSELs and anti-resonant ridge optical waveguides (ARROWs) can operate over a wider temperature range. (Antimony appears to reduce this advantage somewhat.) Also, the gain appears to be stronger than competing materials, with an oscillator strength twice that of InP [44]. GaInNAs also has an unusually large gain bandwidth; Hashimoto reported 49nm of 3dB gain in a GaInNAs semiconductor optical amplifier based at 1.3 μm [156], and Choulis reported an optically-pumped VCSEL operating from 30–360K [124]. This suggests the possibility of widely tunable VCSELs [157], modelocked VCSELs at 1.5 μm , as well as an optical amplifier that could cover the entire WDM band from 1.53–1.56 μm . The wide gain bandwidth also reduces the sensitivity of VCSELs and ARROWs to errors in cavity thickness.

This chapter has focused on the properties of Ga(In)NAs that are universally observed by all groups growing reasonably good material. The following chapter will present the means by which good material can be grown.

Chapter 4

Advances in Growth of Dilute Nitrides by Molecular Beam Epitaxy

“The most important thing is to get the material — then you can develop the device. Without the material, you can’t make any progress! You get nowhere.” — Nick Holonyak

4.1 Motivation for Growth Improvement

The preceding chapter discussed some of the intrinsic properties of dilute nitrides, i.e. properties that are unavoidable and even desirable in the material. For several years, it was thought that the poor electronic and optical quality of dilute nitrides was also an inherent result of incorporating nitrogen into the semiconductor.¹ Although plasmas have been used in MBE for just over a decade, starting with nitrogen doping of II-VI materials for blue-green ZnSe lasers [64] (and references therein), the use of a plasma cell in MBE is still a fairly new technique, and improvements are still being made to the plasma cells themselves, as well as to plasma growth methods. Significant

¹Hence the running joke that there is no material so bad that adding nitrogen can’t make it worse.

strides have been made in the ability to grow dilute nitrides, particularly over the last four years, with the resolution of such problems as oxygen contamination, ion damage, growth temperature variation, and ignition of the plasma. Earlier empirical results showing better material quality with high flow rates, low RF power, and small apertures have been explained with a better understanding of the properties of the plasma. Dilute nitrides may soon be grown with material quality rivaling that of GaAs or InGaAs.

A great deal of collective literature, as well as our own early experiments, suggested that nitrogen disrupts the growth of otherwise excellent GaAs or InGaAs. When our early growths were monitored by RHEED, the 2×4 surface reconstruction pattern immediately disappeared upon opening of the nitrogen shutter, and the RHEED pattern showed spots indicating 3D growth. Similarly, in an attempt to grow an ultra-thin, protective layer of SiN on an oxide-free silicon wafer, RHEED showed that the 7×7 silicon surface reconstruction disappeared when the nitrogen plasma was ignited, and the RHEED pattern again developed spots.

The optical quality of early dilute nitrides was also suggestive of a supposed “nitrogen penalty,” i.e. the increase in nonradiative defects with nitrogen [66]. For example, photoluminescence (PL) from GaInNAs was several orders of magnitude weaker than from InGaAs with the same fraction of indium. The apparent nitrogen penalty was most clearly observed by plotting the early reports of laser threshold vs. wavelength near $1.3\mu\text{m}$, as shown in Figure 4.1(a). With very small amounts of nitrogen, laser thresholds were reasonably low, as shown by the nearly-horizontal fit line at the bottom of Figure 4.1(a). But larger amounts of nitrogen were necessary to reach longer wavelengths, and the laser thresholds increased sharply. The same was true for photoluminescence: a small increase in indium and nitrogen caused the luminescence intensity to drop, as shown in Figure 4.1(b). Historically, the dominant source of laser threshold current was nonradiative recombination due to defects [158]. This was apparent from the high characteristic temperature T_0 reported for early lasers: nonradiative recombination through defects is independent of temperature, so laser thresholds did not change with temperature. (This was originally taken to be a good thing, but the optimism was somewhat premature, as we shall see later.) Similarly,

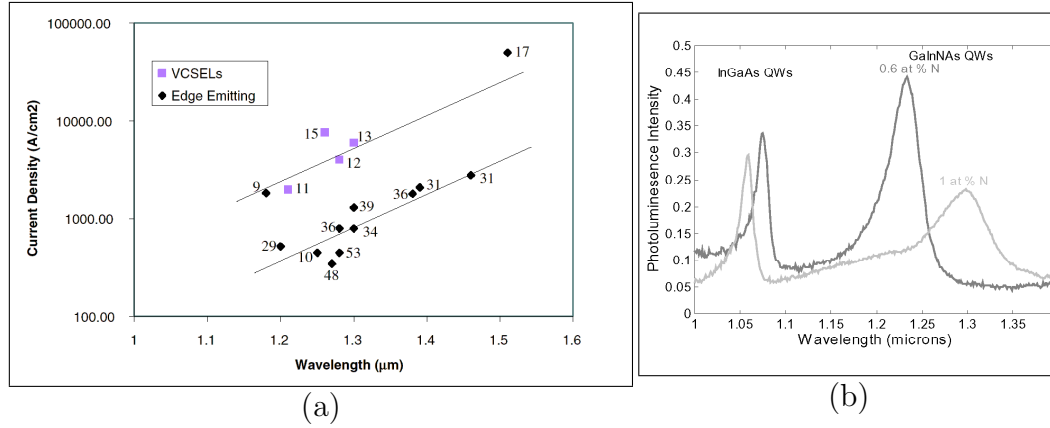


Figure 4.1: Adding nitrogen to reach longer wavelengths causes: (a) an increase in laser thresholds (Ref. [66], with numbering from references therein), and (b) a decrease in photoluminescence [35].

the fact that PL improved by 20–50 times with anneal suggested the formation of some kind of temporary defect in the material that needed to be removed with anneal [117, 159].

Further evidence for damage was suggested by the large number of defects present in GaInNAs and GaNAs films, as measured by deep level transient spectroscopy (DLTS) [5, 160, 119, 118]. Low temperature photoluminescence (LT-PL) also showed a significant deviation from the classical Varshni fit of bandgap vs. temperature, suggesting carriers were being locally trapped at low temperatures [161]. Other groups reported not only a deviation from the Varshni fit, but an actual “S” shape in the LT-PL curve (see, for example, Ref. [102]). Also, transmission electron microscopy (TEM) showed rougher quantum wells in early material grown with nitrogen. X-ray diffraction (XRD) showed broad features rather than distinct diffraction fringes, and reciprocal space maps showed smearing of the film peaks along the in-plane direction, a sign of phase segregation and relaxation. Cathodoluminescence (CL) showed strong inhomogeneity [59]. And growing the wafer even 10°C too hot would cause such severe phase segregation that the wafer turned white [59], suggesting that phase segregation might already be occurring on the mesoscopic scale. Finally, there were reports that ions from the plasma would cause significant wafer damage, and that removing the ions improved both GaN and GaInNAs [162, 163]. Identifying and removing the

sources of wafer damage was a major focus of the present work.

This chapter will offer new and revised techniques that were developed in order to grow high quality dilute nitrides. Several characterization techniques were used to study the condition of the plasma itself, such as optical emission spectra and the reflected RF power, but these were found to be incomplete as indicators of plasma condition. A remote Langmuir probe was used to measure the actual ion density reaching the wafer position from the plasma, and this was found to be the cause of a significant amount of wafer damage. Ion deflection plates were used to remove ions from the plasma beam, and low voltages were found to be surprisingly more effective at producing good material than high voltages. A significant amount of wafer damage was observed in the wafer at the interface where the plasma was first ignited, and an arsenic capping technique was developed to protect the wafer surface during plasma ignition and stabilization. The ability to controllably damage or protect the wafer with either an arsenic cap or with ion deflection plates led to the discovery that a non-negligible fraction of the change in bandgap was due to damage during growth, and is not an inherent property of GaInNAs itself. The bandgap of the wafer was used to calibrate the wafer temperature, allowing standardization and control of the wafer temperature from run to run. Low temperature growth was found to be responsible for some of the defects, and by reducing the arsenic overpressure during low temperature GaAs or GaNAs layers, the material quality improved. The final section in this chapter concludes with a number of additional lessons that have been learned.

4.2 Basic Plasma Physics

A plasma is an ionized gas. Electrons are stripped from the atoms in a gas using an electric discharge (DC plasma), a large electric field (capacitively-coupled plasma), a magnetic field (inductively-coupled plasma), or the resonance of electrons at microwave frequencies (electron cyclotron resonance, ECR plasma). The plasma source used in this work was a radio frequency (RF) plasma, which was inductively coupled during normal operation but capacitively coupled when first ignited. Plasmas are generated when a free electron is accelerated to high energies and collides with a

neutral atom, ionizing it by knocking off another electron. Both electrons are accelerated again, knocking more electrons free in an avalanching process. This ionization reaches a plateau when the free electron concentration (and to a lesser extent the ion concentration) is so large that the free charges screen, or shield, the remaining gas from any applied electric field. Whatever mechanism is used for stripping electrons, a cloud of both positive particles (ions) and negative particles (electrons and negative ions) is generated. The motions of these particles are extremely complex, due to the dynamics of not only collisions, as in a conventional gas, but also the electromagnetic interactions between the particles and the fields they generate. Within the plasma, the various charged particles tend to move and act collectively [164].

High density plasmas, with pressures of 0.1–100 mTorr, are used in semiconductor processing and epitaxial growth, such as in this work. Although these pressures are much lower than atmosphere, they are high enough that the particles frequently collide with each other. These collisions reduce the energies of the particles, and tends to allow electrons to recombine with ions, quenching the plasma. High pressures tend to produce low-energy ions, but might not be energetic enough to dissociate strongly-bonded gases like N_2 . In other words, accelerated electrons may collide too many times before acquiring enough energy to actually cause impact ionization. Lower pressures produce higher-energy ions, with a greater efficiency in dissociation. If the pressure is too low, accelerated electrons will run into the walls of the chamber rather than ionizing another molecule, so the avalanche of ionization will cease. These points will be revisited later.

Because of the difference in mass, electrons can respond to a change in fields much more rapidly than ions can, and reach higher velocities. When a plasma is near a solid surface, the electrons are therefore much more likely to reach that surface than ions are, so the electrons will be equilibrated to the potential of the nearby surface. The ions that are left behind in the bulk of the plasma are at a higher potential, known as the plasma potential. Within the bulk of the plasma, the potential is constant, as carriers are well-screened, and both electrons and ions tend to have a Maxwell distribution of energies, although electrons have a higher temperature than ions. Between the bulk and the nearby surface, however, the plasma forms a sheath,

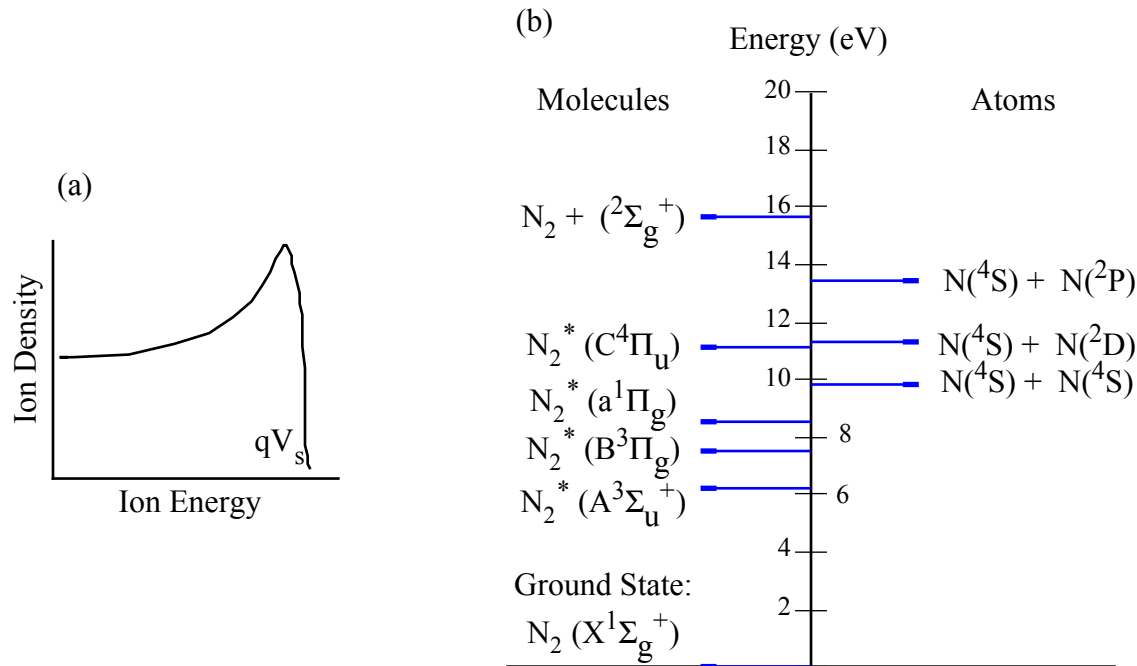


Figure 4.2: (a) Ion energy distribution coming from a plasma. (b) Excited energy levels of atomic and molecular nitrogen. (After Newman. [167])

or skin. There can be a significant potential gradient across the sheath. If an ion drifts out of the bulk plasma into the sheath, it will be accelerated out of the plasma by the potential gradient across the plasma sheath. This produces ions with higher kinetic energies than in the bulk of the plasma, and also higher energies than the electrons. In fact, the ion kinetic energy will be very non-Maxwellian, with a sharp distribution near that of the sheath potential V_s , as shown in Figure 4.2(a), and a low-energy tail due to collisions. In an RF plasma, as the sheath collapses with each RF cycle, the ions are free to escape [165]. The plasma tends to approach the potential of the most positive probe nearby, plus the drop across the sheath. This is significant because even 20eV ions (such as Ar^+) are sufficient to etch GaAs [166], and even lower energies are presumably sufficient to damage the wafer surface during growth.

A nitrogen plasma will produce a number of species, shown in Figure 4.2(b). In decreasing order of occurrence, these are neutral molecules in the ground state (N_2),

excited radicals (N_2^*), neutral atoms (N), molecular ions (N_2^+), and atomic ions (N^+) [168, 167]. It requires 15.8eV of energy to ionize N_2 , or 14.53 eV to ionize a nitrogen atom, but N_2 dissociates into atomic N with just 9.7eV. Therefore dissociation of nitrogen is favorable over ionization if the plasma is in thermal equilibrium. RF plasmas do tend to produce mostly neutral atoms and 1st-positive excited radicals, whose energy of formation is 6eV. ECR plasmas, on the other hand, produce mostly ions and 2nd-positive excited radicals, both with much higher energy. ECR plasmas are thus useful for ion etching in semiconductor processing, but are poor for semiconductor growth [62]. It is also possible to use a mixture of gases to change the dissociation or ionization of nitrogen. Argon has a similar ionization potential (15.57eV), so it can be used to ignite the plasma before switching to all nitrogen [169, 149]. Neon can be used to increase the atomic dissociation, due to Penning ionization from metastable Ne [169]. Several excited, metastable states are possible in N_2 , but the $A^3\Sigma_u^+$ state (~ 6 eV) has a particularly long lifetime of 1.3 ± 0.3 seconds, long enough to reach the wafer [168].

4.3 Implementation of Plasma-Assisted MBE

This section presents the techniques by which the nitrogen plasma cell is operated. All of the studies presented in this thesis were grown using a Varian Mod-Gen II molecular beam epitaxy (MBE) machine, as introduced in Section 2.8. An SVT Associates model 4.5 RF plasma source was used to crack neutral N_2 into reactive species. A schematic diagram of the plasma cell and gas handling system is shown in Figure 4.3. RF power was supplied by an Advanced Energy Industries RFX 600 RF generator operating at 13.56MHz. Unless otherwise specified, an RF power of 300W was used, corresponding to approximately 2.45A at 122V. The RF coil in the plasma cell was water cooled. The inductance of the plasma and coil are compensated by a shunt-series capacitance matching network, with a fixed capacitance from the RF port to ground, and a manually variable capacitance between the RF port and the feedthrough into the cell. The matching capacitance is used to ensure full conversion of input RF power to plasma power, by matching the inductive impedance of the

plasma to the resistive impedance of the RF power supply and cable. The relevant distances are much shorter than a wavelength (22 meters at 13.56MHz). The return line from the coil is welded to the wall of the cell, which serves as the RF current return path to the RF supply. The plasma is generated within a pyrolytic boron nitride (PBN) crucible with a small aperture to maintain a high gas pressure within the cell. Because PBN is an insulator, and the plasma is in proximity to a metal contact (the gas line) in the back, the plasma cannot be biased positively or negatively with respect to the wafer. This makes it impossible to remove ions by biasing the plasma potential itself.

A standard 1" pyrex viewport allows a view into the plasma from outside, for monitoring the plasma emission intensity and spectrum. Nitrogen is supplied from a tank through stainless steel tubing. The tubing is kept above atmospheric pressure to prevent any contamination from possible leaks, and baked after any exposure to air. A Pall brand, resin-based gas filter purifies the nitrogen to better than parts-per-billion. A 5sccm mass flow controller (MFC) from Unit Instruments controls the nitrogen flow rate over a wide range of pressures. Isolation valves are installed on either side of the filter, and after the mass flow controller. A gas bypass (not shown) allows purging of the line without contaminating the filter. The MFC supplies gas to the nitrogen foreline, which runs to the plasma cell and also to a Varian V70 turbomolecular pump with a dry backing pump (Tribodyn). With the MFC set to 10% flow (0.5sccm), the pressure before the Tribodyn is below 10^{-5} Torr. A Pirani gauge (not shown) measures pressures in the foreline from 10^{-4} Torr to atmosphere.

The plasma ignition procedure is as follows. With all valves closed, the Tribodyn is started. When the backing pressure falls below 1 mTorr, the valve after the turbopump is slowly opened, and then the turbopump is started. When it reaches full speed (75kRPM), the valve between the foreline and the turbopump is opened, as is the valve after the MFC, and the valves before and after the filter (which are generally left open anyway). The MFC is set to 10% flow in Flow mode. The RF power is ramped to 150–165W over 15 minutes by computer, and the matching capacitor is tuned for minimum reflected power. Then the wafer is loaded into the growth chamber. The gate valve to the ion pump is closed, as is the gate valve to the UHV

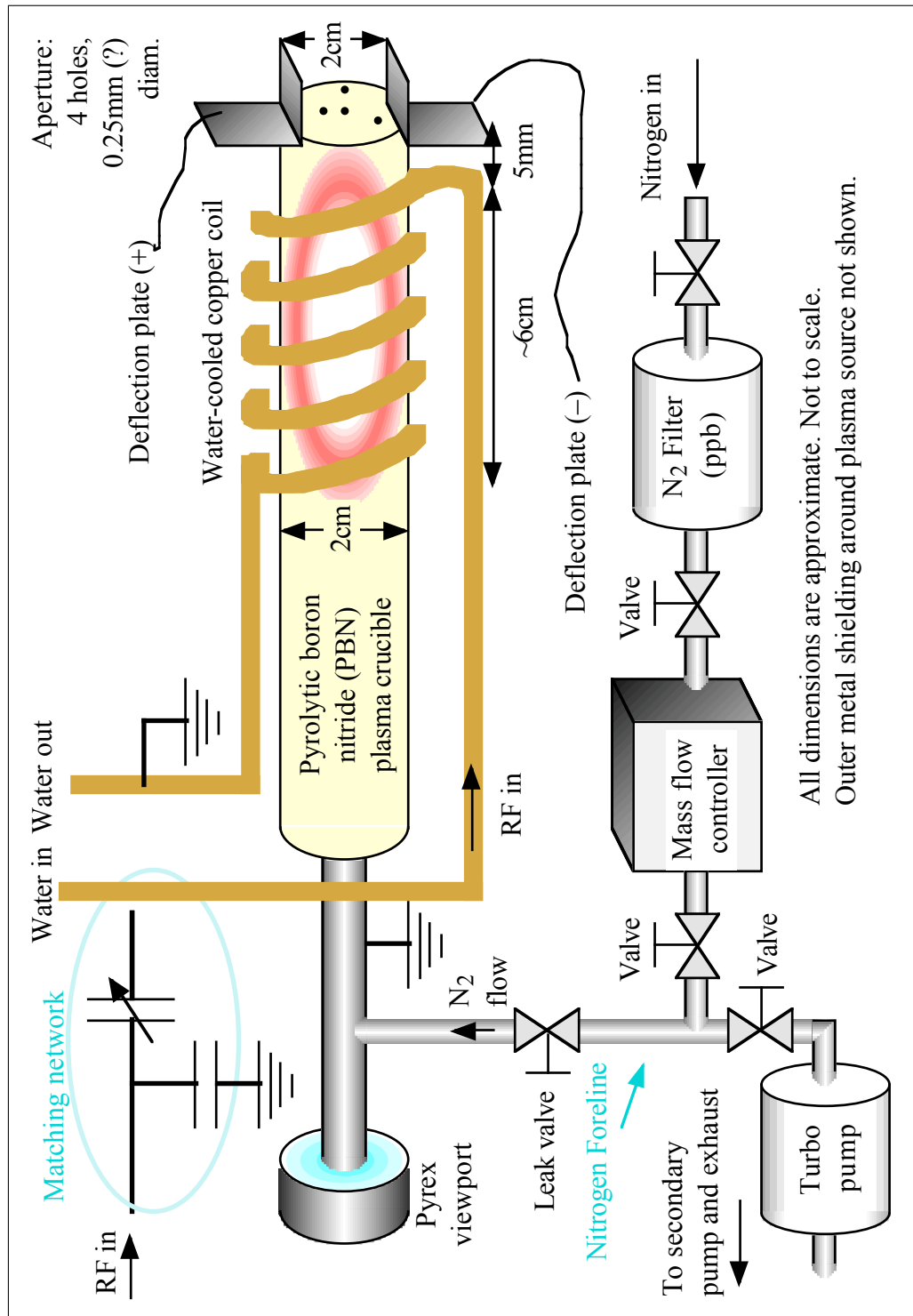


Figure 4.3: Nitrogen plasma cell with matching network and gas handling system.

transfer tube (TT). The leak valve is opened from 99977 to 00100 (through zero), and the valve to the turbo is partially closed. The valve to the turbo is then rapidly closed and the RF turned up to 300W nearly simultaneously, but with the turbo valve first to avoid a high-RF, low-flow condition that generates energetic ions. If the plasma does not ignite by itself, the flow is turned up briefly. The plasma ignites in a capacitively-coupled (E-coupled, or low intensity) mode. The matching knob is tuned to minimize the reflected power again. The flow is turned down, as low as 2.0%, until the plasma switches to the inductively-coupled (H-coupled, or high intensity) mode. The matching knob is tuned a third time, and the flow rate is turned up to 10% over several minutes. The plasma will often drift for several minutes, requiring the matching knob to be turned counter-clockwise (toward 0 on the dial) to compensate. The relevance and importance of each of these steps will be discussed in the rest of this chapter.

The major “knobs” controlling the plasma are the flow rate, the RF power, matching capacitance, deflection plate voltage, leak valve, aperture, and shutter. The flow rate can be set from 1.0% (roughly closed) to 100% (5sccm) on the MFC, with a “purge” mode also available. Purge opens the internal MFC valve much more than the 100% setting does. The plasma can operate at any gas flow from 2% to 100%, although plasma properties vary widely over this range. The plasma is easier to ignite at higher flow rates, and easier to get into high intensity mode at low flow rates. The RF power is adjustable from 0 to 600W, but it is usually operated at 300W for normal growth. The plasma cell cannot withstand more than 400W for extended periods, or the copper coils deform and short to the metal shielding. The use of high RF powers in the past may have also contributed to atmospheric leaks and the breakdown of the fixed matching capacitors. High RF powers generate a more intense plasma, and may be necessary at higher flow rates. The effect of the matching capacitor is complex, and will be described in more detail in Sections 4.4 and 4.5. The deflection plate voltage does not appear to affect the plasma directly, but does affect the ions coming out of the plasma, as will be discussed in Section 4.7.1. The leak valve is used to provide some backpressure to the MFC for stability. It also serves to tightly seal the MBE chamber in case maintenance to the nitrogen system is necessary.

The cell aperture is not changeable without opening the MBE machine. Small apertures produce higher pressure within the cell for the same flow rate, increasing plasma stability and decreasing ion energy. This results in better quality growth for GaN [62, 170] as well as GaInNAs [163, 59]. Plasmas for GaN growth operate at much higher flow rates, so they often do not require any restrictive aperture at all, or have an aperture with large and/or many holes. The aperture also ensures that the wafer is in the “remote plasma” regime, where it is unable to perturb the plasma [171]. Another possibility is to add argon to the gas mixture, since the additional gas collisions would reduce the ion energies and ion flux [169]. When growing dilute nitrides, a plasma cell is generally operated with low flow and moderate power. It is well known that lower cell pressures lead to greater ion density, which is undesirable [172]. This condition is distinct from the high flow and high power generally used for GaN growth, for which most plasma cells were designed. It is therefore important to characterize the actual output of a particular cell rather than relying on claims from competing manufacturers.

The shutter in its present form (i.e. ceramic) has no effect on the nitrogen plasma, but does serve to block direct exposure of the wafer by the plasma. Even this is only partly successful, since the nitrogen incorporation only drops by a factor of 20 or so with the shutter closed. Fischer has reported the use of a gate valve instead of a shutter [81], but this presents problems with RF parasitics and sudden changes in pressure, both of which can cause plasma instability. (See shutter instability on Page 125.) The gate valve also cannot be used to seal off the nitrogen cell from the chamber for venting to atmosphere, due to thick, rough arsenic deposits on the sealing surfaces [173]. A better solution, which requires no changes to the MBE chamber, is offered in Section 4.8.

The comparison of nitrogen plasma cell operation between different groups is difficult, due to the many significant variables involved: gas pressure, parasitic RF losses, thermal profile near the plasma cell, purity of the supplied nitrogen gas, aperture size, and many others. But the gas pressure is particularly important for understanding plasma condition [171, 163], so it merits investigation. There are several methods for determining the gas pressure inside the plasma cell. It can be calculated based

on the gas flow rate and the conductance of the aperture [170], or the volume of the cell and its $1/e$ pumpdown time can be used to estimate both the cell pressure and the aperture conductance. Unfortunately, the nitrogen cell in System 5 was not fully characterized before it was installed, so the dimensions of the aperture are unknown, as is the conductance of the leak valve immediately before the cell. The aperture consists of four holes drilled through a PBN plate approximately 1mm in thickness, but the diameter of the holes is unknown. The cell manufacturer could not recall the diameter either, since this particular aperture was specially created for our cell. The aperture holes will be measured at the next opening of System 5. Estimates of cell pressure based on 0.25mm holes, as previously reported [59], produce pressures that are higher than the measured foreline pressure, which is physically impossible. The best estimate of cell pressure appears to be taking the asymptote of an exponential fit to the foreline pressure as a function of leak valve position, as shown in Figure 4.4. It is estimated that the cell and foreline would both be at 0.6 Torr if the leak valve were infinitely open. The pressure is 1–2 orders of magnitude higher than reported for other cells, so these estimates may be in error. In particular, the preceding analysis ignores the finite conductance of the foreline and assumes a linear and continuous change in leak valve conductance with valve position, with no upper limit to conductance.

4.4 Plasma Optical Emission Spectra

As mentioned above, the best devices reported to date have all been grown using RF plasmas, presumably due to cracking efficiencies as high as 40% [140], as well as a minimal ion flux, and decreased energy of excited species. [168]. It is desirable to operate the RF plasma cell under conditions that produce a large amount of atomic nitrogen, but it is particularly valuable to maximize the ratio of atomic nitrogen to molecular nitrogen. Each of these species produce characteristic features in the visible and near-IR spectrum [64, 174], as shown in Figure 4.5, and many RF plasma cells provide a clear viewport through which the emission spectrum can be recorded. The use of optical spectra to characterize the plasma cell has the benefit of simplicity, but

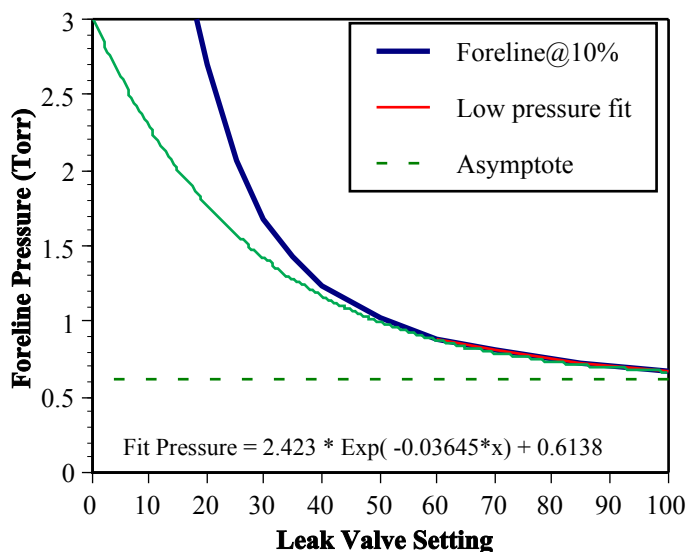


Figure 4.4: Nitrogen foreline pressure vs. leak valve setting. Extrapolated final pressure is 614 mTorr.

also several shortcomings which this work revealed.

The optical spectrum is useful as a rough guide to finding the best combination of gas flow, RF power, and impedance matching conditions. Every plasma cell has a certain amount of inductance or capacitance that must be compensated by an equal and opposite reactance. In an RF plasma cell, a large, variable capacitor is used to match the real impedance of the cell to that of the power supply, to avoid reflections from an impedance mismatch. A second capacitor, which may or may not be variable, is shunted to ground to compensate the total reactance of the cell and the first capacitor, thereby enabling unity power factor and minimal reflected power. Figure 4.6 shows the results of detuning the capacitor on the impedance matching network. The lower spectrum was taken with an impedance mismatch sufficient to cause 10W of reflected RF power, due to excess capacitance in the matching network. Although this amount of reflected power is modest, just 3% of the total power, the atomic emission lines have been reduced by nearly 20%, and the molecular bands reduced by nearly 5%. This demonstrates the need to maintain constant *net* power applied to the cell to provide stable output. For example, if the minimum reflected power were to drift upward from 0W to 5W, then the forward power would need to

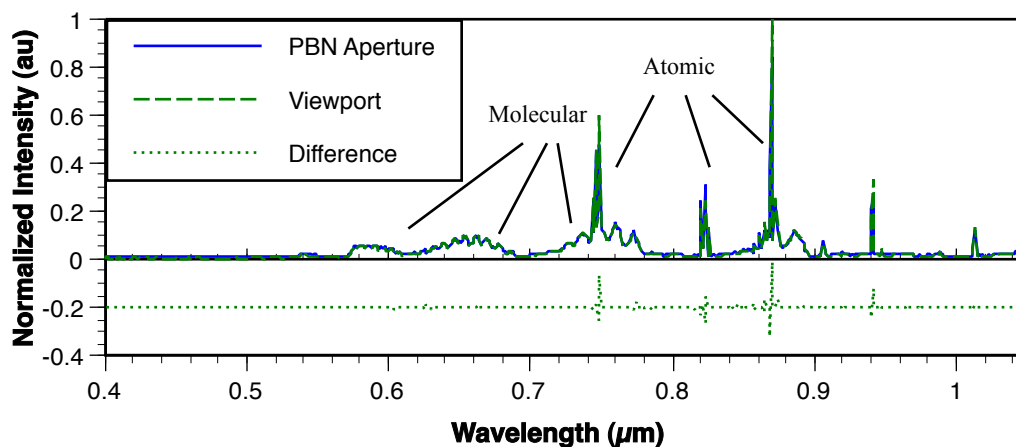


Figure 4.5: Relative emission from several nitrogen spectral lines, taken from the front PBN aperture and from the rear viewport. The difference has been plotted with an offset for clarity. Crosses represent well-known emission peaks from nitrogen.

be increased from 300W to 305W. Upon increasing the forward power, the spectrum returns to its original form (not shown).

However, optical spectra can also be misleading. The upper spectrum in Figure 4.6 is nearly unchanged even though the cell is operating in a very different regime, as evidenced by the increase in high energy emission at $0.316\mu\text{m}$ (aliased by the spectrometer to $0.946\mu\text{m}$). The deficiency in capacitive compensation led the plasma to be extinguished soon after this measurement. In other words, if the cell drifts toward this condition, monitoring the optical emission spectrum will not provide sufficient warning of cell instability. We will return to the topic of cell stability in the next section.

The total intensity of emission can likewise be misleading. It was noted earlier that there is a comfortable growth window when the atomic emission lines are much greater than the molecular emission lines. The overall intensity of the plasma is dominated by very strong atomic lines, particularly near $0.869\mu\text{m}$. However, excited molecular nitrogen in the form of radicals can also contribute significantly to nitride and dilute nitride growth. [175, 163] Under certain conditions, the excited molecular species can increase while the atomic species remain constant or even decrease. It is not necessarily sufficient to monitor the total intensity of emission, nor a single set of

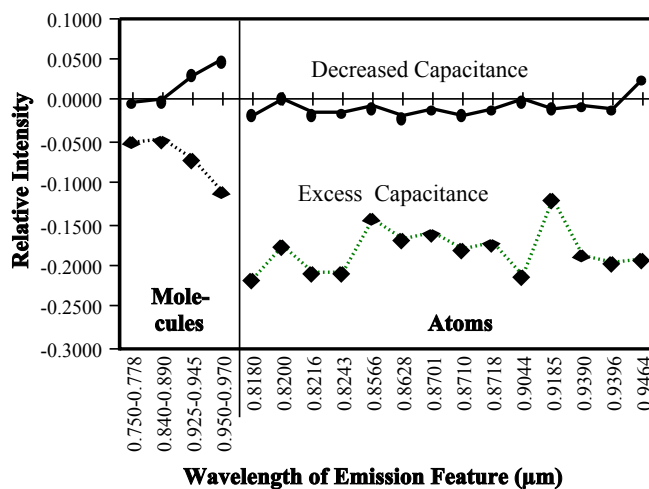


Figure 4.6: Emission intensities for several settings of the matching capacitor, relative to the matched condition. Above: decreased capacitance led to 10W of reflected power, but the spectrum was essentially unchanged from matched condition. Below: increased capacitance again led to 10W of reflected power, with a 15-20% decrease in atomic peaks and 5% decrease in molecular bands.

atomic lines. [175]

This raises another issue. In order to make a valid comparison between any two wafers with different nitrogen compositions, the plasma conditions must be kept identical, and only the growth rate may be varied. Since excited radicals can participate in growth [176], any technique that affects either their energy or their relative abundance must take this into account. This is even more true for a change in ion density or ion energies, as will be discussed in later sections of this chapter. Changing the RF power or gas flow merely to change the rate of nitrogen incorporation raises a number of additional questions that are not easily answered. Higher RF powers do increase the amount of atomic nitrogen [177], and hence the fraction of nitrogen in the semiconductor, but the higher RF powers also change the *fraction* of ions in the beam [163]. There have been many reports in the literature of better or worse growth with a change in nitrogen concentration, but many of these groups have varied their plasma conditions for different growths, invalidating those studies.

It may be objected that changing the growth rate can also affect the quality of

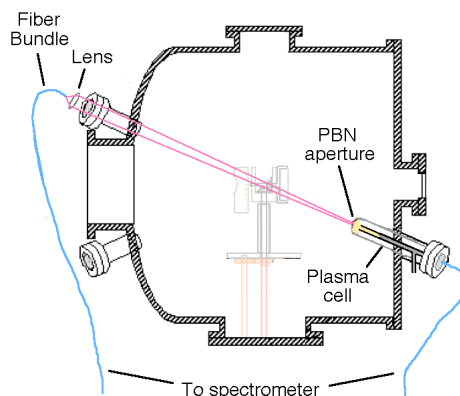


Figure 4.7: Optical emission spectra collected from both front and rear of plasma source.

the material [178]. However, this seems to be merely a straightforward extension of conventional wisdom in epitaxy, namely that higher temperature increases surface mobility, allowing adatoms to reach low energy states before being buried by subsequent layers. An increase in growth rate should be accompanied by a slight increase in wafer temperature to compensate for the change in surface time. Of course, this presumes that there are no other significant sources of wafer degradation, such as phase segregation, which would be initiated by a change in temperature.

Another difficulty in using optical spectra to characterize the plasma is that some cells do not have optical viewports. This is not a problem for the visible and near-IR wavelengths. Figure 4.5 shows the spectra collected through the clear viewport at the rear of the cell, and also through the PBN aperture plate at the front of the cell, facing the wafer. To cover a wider range of wavelengths, these spectra were taken using an Oriel 77200 spectrometer with 0.20mm slits and a grating with 600lines/mm blazed at $0.500\mu\text{m}$. The rear viewport spectrum was recorded by butt-coupling a fiber bundle to the viewport. In order to improve light collection for the front aperture spectrum measurement, the fiber bundle was imaged onto the plasma aperture plate using a 2" diameter lens with a 0.5m focal length. Both fiber bundle positions are shown in Figure 4.7. The spectra in Figure 4.5 are mostly identical when normalized in intensity, with some variation in the atomic emission lines near $0.869\mu\text{m}$.

It should be noted that the emission from the front of the cell is not necessarily

restricted to transmission through the solid portion of the PBN aperture plate; by far the brightest optical emission is what comes through the pinholes in the aperture. But the lack of a clear viewport in some cells may present difficulties for studying the ion content of the plasma, because PBN can absorb some of the ion-related emission lines in the UV. Also, our fiber bundles were only weakly transparent to UV, so the UV emission spectra are not shown here.

4.5 Radio Frequency Impedance Matching & Cell Stability

4.5.1 RF Circuit Model of Plasma and Matching Network

The stability of the plasma is paramount in performing careful materials studies and in growing lasers. There are many factors that can contribute to plasma instability, and we shall discuss several of them in turn.

The above optical measurements showed an asymmetry in the operation of the cell with respect to the variable capacitor(s) on the matching network. Let C_{v0} be the series capacitance in the matching network that produces the minimum reflected power from the system back to the radio frequency (RF) power supply. If the capacitance is increased above C_{v0} , the plasma may grow somewhat dimmer, but it will continue to operate in H-coupled mode (high intensity), even with reflected powers as high as 65W out of 300W. But if the capacitance is decreased slightly below C_{v0} , the plasma rapidly becomes unstable and either drops into E-coupled mode (low intensity) or extinguishes completely, usually before the reflected power even gets as high as 30W. The existence of the asymmetry is corroborated from current measurements at the deflection plates mounted across the output of the cell. Figure 4.8 shows the current collected through one of the deflection plates as a function of the matching capacitor position. Note that increased capacitance (turning the knob clockwise to higher numbers on the dial) produces a sharp rise in current.

To study the effect of changes in the matching capacitor, we consider a simplified, lumped circuit model of the plasma cell. An inductive plasma may be modeled roughly

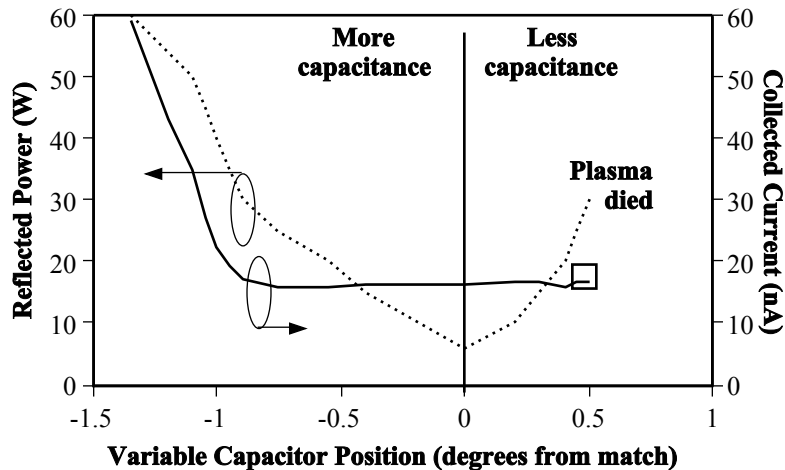


Figure 4.8: Current captured through grounded deflection plates vs. matching capacitor position. Dotted line shows reflected power. Note that the plasma died very close to the matched impedance point, but only with insufficient capacitance. The collected current was also rising (square box) when the plasma died.

as shown in Figure 4.9. It be noted that the plasma is modeled as a linear element here, i.e. unchanged by power factor or forward power. More sophisticated modeling would be necessary to fully capture the complete behavior of the plasma cell, including the change in coupling to the plasma with RF power or capacitive loading, but the circuit model is a reasonable approximation for the qualitative argument made here [179].

The values of C_{ser} and C_{shunt} can be determined by impedance matching if R_{equiv} and L_{equiv} are known. The shunt capacitance is purely reactive, so it cannot be used to generate a resistance (50Ω) for impedance matching. Instead, the series capacitor C_{ser} performs the impedance matching as follows. The real part of the impedance looking into A-A' in Figure 4.9 must equal the output impedance of the RF source, 50Ω . It is convenient to use a series-parallel transform will convert the C-R-L series circuit to its parallel equivalent:

$$R_{\parallel} = \frac{R_s^2 + X_s^2}{R_s}, \quad (4.1)$$

$$X_{\parallel} = \frac{R_s^2 + X_s^2}{X_s}, \quad (4.2)$$

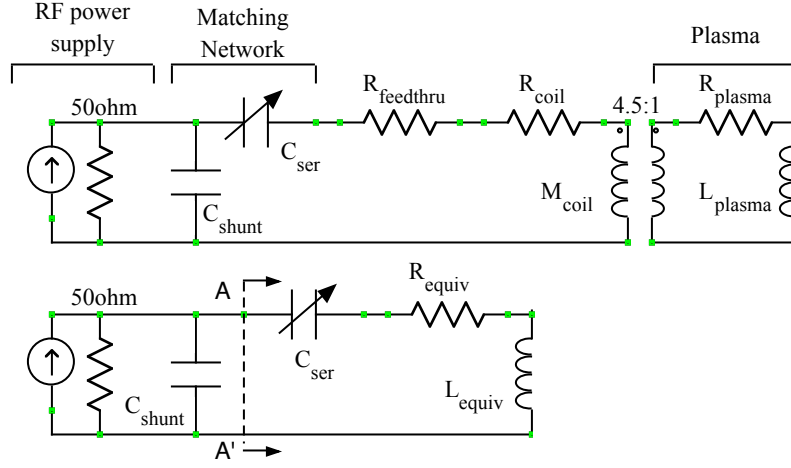


Figure 4.9: Lumped circuit model of inductive RF plasma cell (top). By treating the coil and plasma inductance as a current transformer, the plasma inductance can be approximately modeled as a simple linear circuit (bottom).

Now $X_s = X_{C_{ser}} + X_{L_{equiv}} = -1/(\omega C_{ser}) + X_{L_{equiv}}$ and $R_s = R_{equiv}$. The parallel impedance looking into A-A', from Equation 4.1, is set to 50Ω , as mentioned above. Then

$$50\Omega \times R_{equiv} = R_{equiv}^2 + \left(\frac{-1}{\omega C_{ser}} + X_{L_{equiv}}\right)^2 \quad (4.3)$$

$$\sqrt{50\Omega \times R_{equiv} - R_{equiv}^2} = \frac{-1}{\omega C_{ser}} + X_{L_{equiv}} \quad (4.4)$$

$$C_{ser} = \frac{1}{\omega} \left(X_{L_{equiv}} - \sqrt{50\Omega \times R_{equiv} - R_{equiv}^2} \right)^{-1} \quad (4.5)$$

For illustrative purposes, choose $X_{L_{equiv}} = 80\Omega$ and $R_{equiv} = 2\Omega$, which are reasonable values for a similar ICP impedance, referred to the input side of the coil [179]. Using these values and $\omega = 2\pi \times 13.56\text{MHz}$, it follows that $C_{ser} = 167\text{nF}$. Plugging these into Equation 4.2 produces the necessary reactance needed from C_{shunt} to cancel $X_{||}$.

$$\frac{1}{\omega C_{shunt}} = X_{||} = \frac{R_{equiv}^2 + (X_{equiv} + X_{C_{ser}})^2}{X_{C_{ser}}} \quad (4.6)$$

$$C_{shunt} = \frac{1}{\omega} \frac{X_{C_{ser}}}{R_{equiv}^2 + (X_{equiv} + X_{C_{ser}})^2} \quad (4.7)$$

Substituting the above values results in $C_{shunt} = 1.15\text{nF}$. At the matched condition, the matching network converts in-phase RF at 2.45A and 122V to mostly inductive

RF at 12.2A and 976V. Preventing arcs from these high voltages will be described on page 127. Note that these high voltages arise because the bulk of the energy oscillates between C_{shunt} and L_{equiv} with each RF cycle. For this reason, C_{shunt} is known as the amplitude capacitor. C_{ser} serves only to shift the phase of the oscillation, and is known as the phase capacitor. Another way to look at this is that the variable series capacitance cancels the inductive component of the plasma, while the shunt (parallel) capacitor supplies power to the resistance component of the plasma.

4.5.2 Effects of Cell Drift and Impedance Mismatch

We are now in a position to investigate the plasma changes predicted for a change in matching capacitance. Figure 4.10 shows the results of a simulation in which the series capacitor was varied from 80% to 125% of its nominally impedance-matched value. Note the lack of asymmetry in any of the plots. The top plot (a) shows the current through the feedthrough. It is apparent that the majority of the current at the matching condition is reactive, out of phase with the input RF. The next plot (b) shows the voltage drop across the equivalent plasma resistance, as referred to the supply side of the coil. The third plot (c) shows the real power delivered to the plasma, the product of (a) and (b). This was where any asymmetry in the forward power vs. capacitor position would be apparent. To show the lack of asymmetry, the mirror image of the plot has been overlaid.² Finally, (d) shows the voltage reflection coefficient, in both its magnitude and phase angle. The angle does show asymmetry, but there is no change in magnitude, so there would be no change in power delivered to the cell. In the absence of parasitic effects, it is not possible to explain the recorded asymmetry in cell operation that was shown in Figure 4.8.

Further investigation showed that parasitic resistance at the shunt capacitor is a likely cause of the asymmetry. The shunt capacitor in the matching network consists of several fixed, air capacitors in parallel, with a cooling water panel attached to the hot RF terminal. These capacitors get very hot during plasma operation, even with the cooling water. With the heat from the shunt capacitor and feedthrough, multiple

²Actually the mirror with respect to impedance, not capacitance: $Z \propto 1/C$.

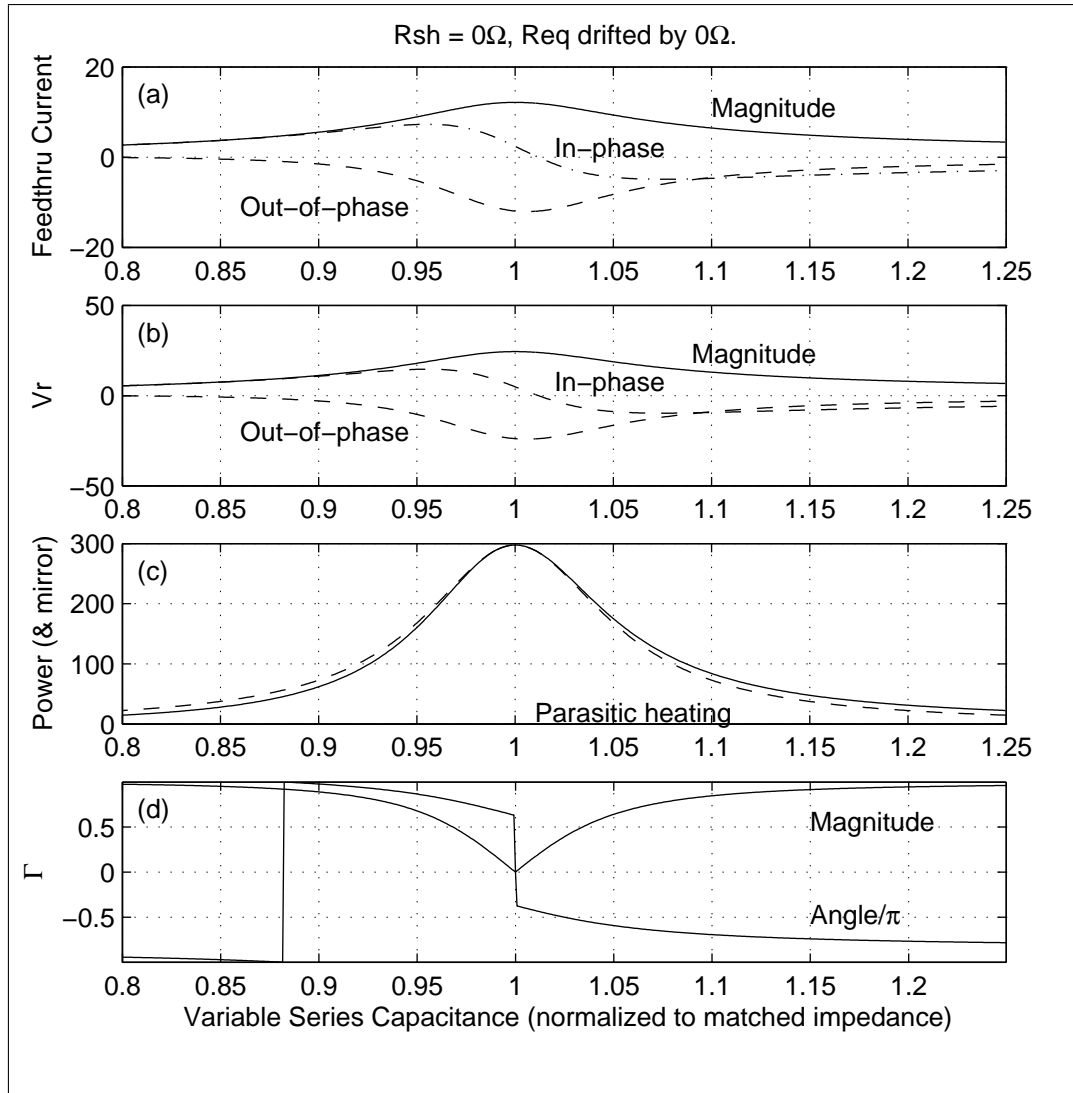


Figure 4.10: Circuit simulation of plasma cell with no parasitic losses. Note symmetry throughout. (a) Current into coil. (b) Voltage across the plasma-equivalent resistance. (c) Power delivered to plasma. (d) Voltage reflection coefficient as seen from RF power source.

fans are required to keep the matching network at a reasonable temperature. In order for the shunt capacitor to generate so much heat, the parasitic resistance must be considerable. The previous simulations were repeated, but with a 0.5Ω resistance added in series with the shunt capacitor C_{shunt} . A clear asymmetry emerged, as shown in Figure 4.11. The voltage across the shunt (a) followed the RF supply closely (i.e. mostly in-phase near matched impedance), but the power delivered to the lossy shunt capacitor (b) was strongly asymmetric. This is most clearly apparent in (c), where the power delivered to the plasma is shown plotted with the power delivered to the lossy shunt capacitor.

It is believed that the reason the shunt capacitor contributes so much to the instability of the cell is because the heating is a runaway process: when the capacitor is cool, losses are low, and the ideal model follows. As the capacitor begins to heat, the increase in loss causes a change in impedance that drives the cell toward the condition in Figure 4.11(c). Even more RF power is therefore absorbed, completing a vicious cycle. The solution to this appears to be to start the cell in the relatively flat range of parasitic heating shown in Figure 4.11(c), which rapidly heats the capacitor to its final, steady state temperature. Contrary to previous reports [59], reflected power (as reported by the RF power supply) is not dissipated in the matching network, but in the RF power supply itself. Because the matching network is integral to the plasma cell, there is no easy way to insert a power or phase meter to see how much power is actually reaching the cell. A rough approximation might be to measure the temperature of the RF feedthrough (i.e. power delivered to the plasma) relative to the shunt capacitor (power lost in the matching network).

Using an automatching network or continually monitoring the cell to make sure it remains impedance matched, the plasma can be kept in a stable operating range. However, an extra cushion of stability might be provided by forcing a slight amount of excess capacitance at the matching network [180]. This is currently used to improve cell stability when the cell is first ignited.

The excess capacitance is particularly useful as the cell warms up. After igniting the plasma or making a major change to its operating point, such as turning up the RF power, there is a period of 10–15 minutes during which the condition of the plasma

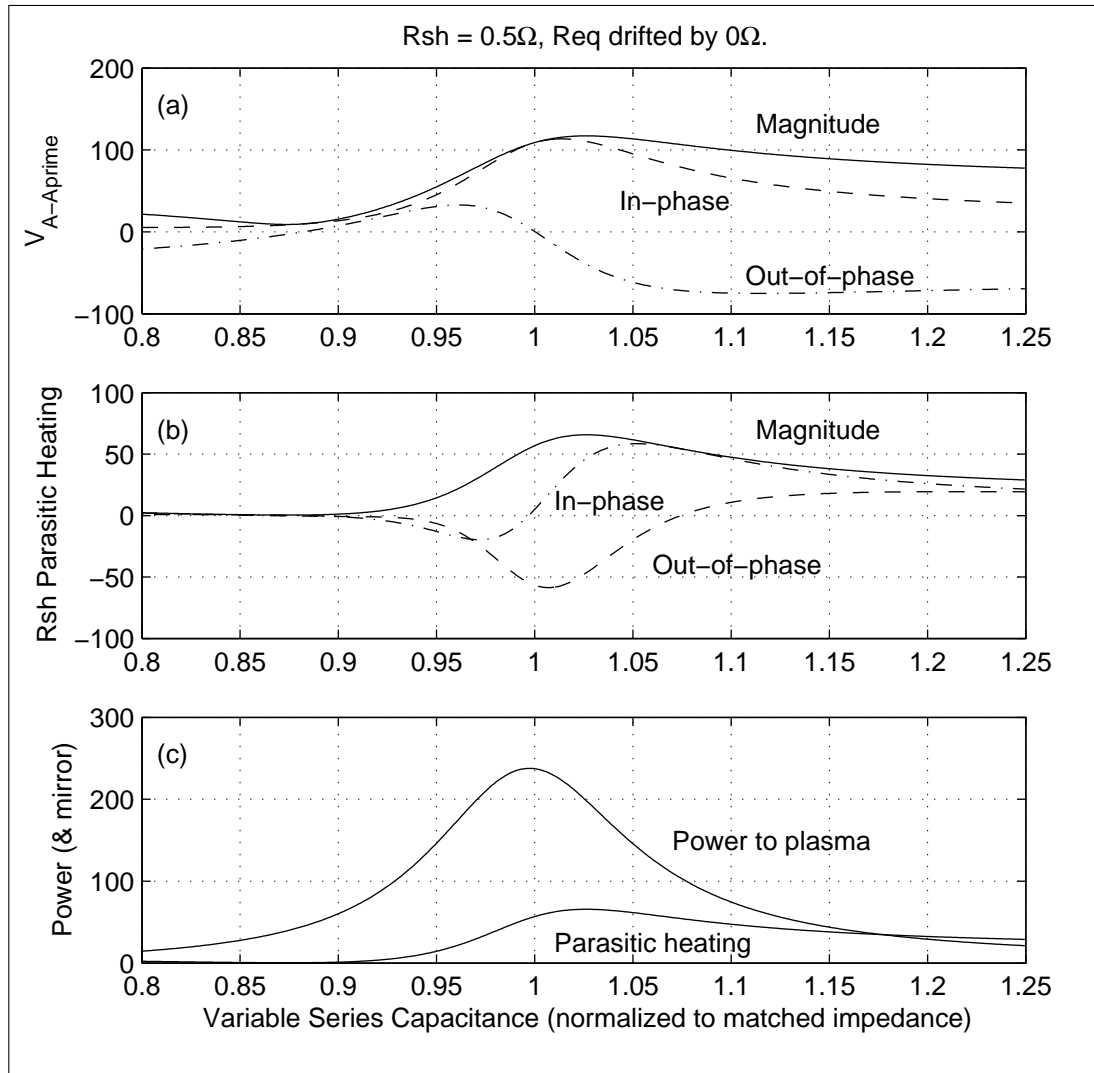


Figure 4.11: Circuit simulation of plasma cell model with a lossy shunt capacitor. (a) Voltage across shunt (at A-A' in Figure 4.9). (b) Heating in the lossy shunt capacitor. (c) Power delivered to the plasma and to the parasitic loss in shunt capacitor.

changes as it reaches steady state. This is probably due to heating in the matching network, which uses air capacitors. Contrary to previous reports [59], cells from a different major manufacturer have been privately reported to display the same drift while they warm up. [181, 165] Regardless of the cause, during this warmup period, the ideal matching capacitance C_{v0} changes with time, so the matching network will require periodic adjustment. If the cell is not kept matched during this transition, when the matching capacitor is finally tuned, yet another delay will be required before the cell is fully stable. It should be noted that the preceding model with a lossy shunt capacitor does not explain the change in the location of the minimum reflected power point. There may be other parasitic effects, such as heating in the feedthrough or coil, which change the optimum series capacitance.

A thermocouple mounted on the RF feedthrough to the plasma cell provides another noninvasive means to monitor the condition of the plasma. We have found that the feedthrough will reach 130–140°C when the plasma is first lit, but after 10–15 minutes, the feedthrough will cool to 90°C and remain there indefinitely. Fischer reported the use of a gate valve to separate the plasma from the chamber while the cell was warming up [81]. But a metallic gate valve, like a metallic shutter, can itself lead to instability, as mentioned in Section 4.12. In short, some sort of provision must be made to allow the plasma to stabilize before starting each growth. [182]

In addition to the anomaly due to the warmup time, the plasma often behaves subtly different during first run of the day. There appears to be a significant benefit in cell stability and performance if the plasma is pre-lit or “seasoned” for some time before performing any growths in a day. Reflected power will often reveal whether the cell has been seasoned or not, particularly for a cell reaching the end of a long growth campaign. The plasma will often start with a high reflected power, 7–9W, then gradually reach a constant 2–3W of reflected power. Subsequent growths would be easier to light and would sustain 2–3W of reflected power. Based on prior experience, we believe that the major effect of seasoning is to remove arsenic that has condensed on the crucible, partially shielding it from the RF fields. Running the plasma for 30–60 minutes will re-evaporate much of this arsenic.

4.6 Using Beam Flux Gauge as Langmuir Probe

4.6.1 Measuring Ion Flux from Plasma

Ion damage from the nitrogen plasma had been reported by several groups, for GaN as well as GaInNAs. These ions could be reduced several ways. RF plasmas generate fewer ions than ECR or arcjet plasmas, while still demonstrating a high cracking efficiency [62, 162, 169, 63]. Kageyama also reported that the ion density saturates with increasing RF power [163]. However, at high RF power or low flow rates, the energy per atom climbs, and the ion density rises again. But high power and low flow rates also produce desirable atomic nitrogen. To minimize ion generation, a small cell aperture is used to raise cell pressures: increased collisions in the gas neutralize ions and strip energy from the higher energy radicals [163, 62, 170]. In addition, Blant reported that hot walls of the plasma chamber would lead to negligibly small fluxes of ions, less than 1nA [175]. Our RF cell was built to take these considerations into account.

There are also several techniques for removing ions from the plasma beam, such as magnets[183, 130], ion deflection plates [163], ion collection within the cell [184], or biasing the substrate to repel ions [162, 185, 186]. Because the nitrogen gas feedthrough in our cell is grounded, the plasma potential cannot be directly biased with respect to either the wafer or the beam flux gauge. Also, our MBE chamber does not have the capability of biasing the substrate to repel ions. Another technique is to use a set of dense metal meshes with different voltages, to repel charged species. This is useful for studying plasma conditions,[171] but has not been reported as a useful growth technique due to the restriction in the beam path and, presumably, the risk of sputtering undesirable materials from the mesh onto the wafer.

The cell RF power and flow rate were chosen based on the optical spectrum, and optimized after a series of test growths, which seemed to produce reasonably good material [35]. Empirical results showed the best material quality corresponded with high gas flow, low RF power, and a restricted aperture between the plasma and the chamber [59].

Although optical methods are convenient for rough tweaking of a cell, conventional

Figure 4.12: Ion current as captured by ion deflection plates. From Reifsnider [1].

optical spectra are insensitive to ions coming from the plasma cell, so there was no way to measure ion production. Nevertheless, deflection plates were installed on our plasma cell to remove any remaining ions. These are simply two parallel, metal plates that straddle the output beam of the plasma. (See Figure 4.3, page 63, or Figure 4.20, page 90.) If a bias is applied across the two plates, the resulting electric field drives electrons and ions away from the beam center. Young and Kageyama both reported needing high voltages to deflect ions [187, 163]. The use of high voltages appears to be motivated by the difficulty in capturing ions at the deflection plates, as shown in Figure 4.12 For this measurement, one of the deflection plates is biased, while the other is grounded. The figure shows the current through the biased deflection plate as a function of applied bias. As the bias increases, more electrons and ions are captured by the plates. The I-V curve approaches a constant when all the available ions and electrons have been captured. Negative ions are assumed to be negligible. [168]

To test the use of high voltage deflection plates, GaInNAs quantum wells were grown with either GaAs or GaNAs barriers. A bias of $\pm 800\text{V}$ was applied across two parallel plates approximately 1cm long and 2cm apart, mounted at the output of an SVT RF plasma source. The samples were grown using 300W of RF power and 0.5sccm of ultra-pure nitrogen. There was no consistent improvement in photoluminescence, as shown in Figure 4.13. It appeared that ions were indeed negligible.

Despite this result, laser thresholds remained extraordinarily high. It is well known that lower cell pressures lead to greater ion density This condition is distinct from the high flow and high power generally used for GaN growth, for which most plasma cells were originally designed. It is therefore important to characterize the actual output of a particular cell.

One method of measuring the density of ions in a plasma is to use a Langmuir probe, a bare wire within or near the plasma, with a second electrode nearby that provides a reference potential. A voltage is applied to the probe, and the resulting I-V curve can provide ion density and electron and ion temperatures (kinetic

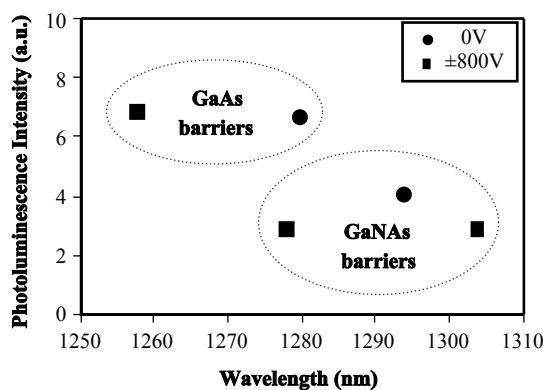


Figure 4.13: Photoluminescence intensity vs. wavelength for various samples grown with (circles) and without (squares) deflection plates. Each sample was annealed to peak intensity.

energies). Langmuir probes have been used for studying ECR plasmas with higher ion currents,[188] planar, inductively coupled plasmas,[189], and in studies of GaN growth,[172] where it is believed that a small difference in particle energy makes the difference between growth and etching.[63] Unfortunately, for the RF plasma cells used for MBE, it is extremely difficult to probe the bulk plasma inside the crucible, due to the solid ceramic crucible and the aperture plate at the end of the plasma cell. Even if one could probe the plasma directly, the small sizes of these cells make it all but certain that the probe would perturb the plasma.

An alternative approach was developed. Most MBE chambers use a Bayard-Alpert ionization gauge to measure the beam equivalent pressures from the effusion cells. We disconnected the beam flux gauge (BF) from its controller and connected one or more of the pins to a Keithley 485 picoammeter, making a remote Langmuir probe. The input gas line to the plasma cell was grounded by design, providing the reference electrode. No changes were necessary inside the MBE chamber. This has the advantage of directly sampling the ions coming from the plasma, with no need to infer ion density from plasma conditions, optical spectra, or plasma cells mounted in dissimilar test chambers. Furthermore, the measurement can be made at the actual wafer position, unlike mass spectrometer based measurements. An ion gauge controller might be programmed or modified to perform this measurement

directly, by turning off the filament and grid biases and measuring the current on the collector wire, but as we show later, the filament wire provides more signal than the collector wire does. We will show that the beam flux gauge-Langmuir probe presents a convenient and powerful tool for the measurement of ion flux, and we will show the changes in ion current produced by changes in RF power, warmup time, and other variables.

A careful reading of prior literature suggests the possible use of the beam flux gauge as a Langmuir probe, but this was not made explicit if it was indeed the case [172, 63, 175]. Molnar et al. used the beam flux gauge to study an ECR plasma,[170] but other applications have not been reported until recently, presumably due to several shortcomings that will be discussed below. There have been reports that this method has been independently applied, but these results were inconclusive and unpublished [181]. We have recently become aware of another group that has reported a similar measurement,[190] which appears to be an independent rediscovery of our previous reports [191].

To make this measurement, as previously mentioned, a picoammeter was connected between the beam flux gauge and ground. A voltage source, shown in Figure 4.14, allowed separation of ion current from electron current. The beam flux gauge was mounted within a cylindrical metal shield, with an opening on the side facing the effusion cells. The bracket was grounded and served as a Faraday cage for the beam flux gauge in normal operation. Unless otherwise specified, only one wire on the beam flux gauge was used at a time, and the other wires remained unconnected, to minimize collection of secondary electrons [171]. RF chokes and high-frequency capacitors prevented coupling of electromagnetic interference into the picoammeter. It should be noted that all ion flux measurements in this paper are relative, as it is difficult to determine absolute ion densities in this geometry.

4.6.2 Langmuir Probe Results

A typical Langmuir probe measurement from our cell is shown in Figure 4.15. The highest energy ions ranged in energy up to approximately 35eV. Electron energies

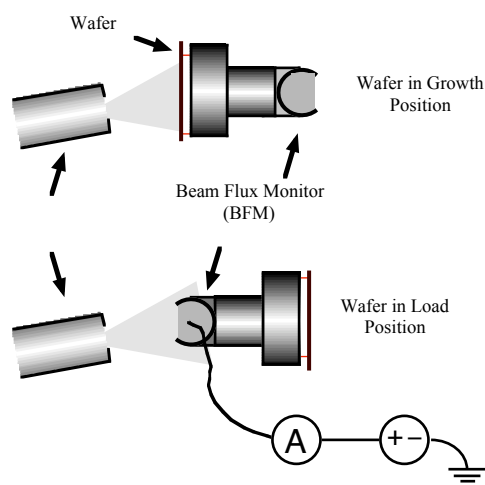


Figure 4.14: Beam flux gauge as Langmuir probe.

were under 8eV, consistent with reported values for RF plasmas [189]. The extra inflection points at 9 and 12V, shown as the valley and second peak in the inset derivative plot, may indicate a bimodal distribution of electron or ion energies, but it is difficult to deconvolve the effects of ions, electrons, and secondary electrons in this range and geometry, and no attempt was made to compensate RF modulation of the plasma potential [192, 193, 194]. The large slope of the saturation current is due to secondary electrons, and remains linear at higher voltages.

The beam flux gauge has three parts: the collector wire, grid, and filaments. Any of these can be used for the Langmuir probe, and each has a different response, as shown in Figure 4.16. The small size of the collector produced a weak signal, although it may be useful for spatially-resolved measurements. Because the collector is well shielded by the metal bracket, bias on the collector did not efficiently attract (focus) charges exiting the plasma at large angles. The filaments, on the other hand, are not shielded, so they can detect the nonzero plasma potential due to the plasma. The filaments also have a larger cross section, and are not shadowed by other parts of the ion gauge, so they collect more current: $\sim 1\text{nA}$, compared to $\sim 10\text{pA}$ for the collector. This stronger current was easily measurable with an HP 34401A voltmeter with a $10\text{M}\Omega$ input impedance, and agreed with the picoammeter. Figure 4.16 also shows a

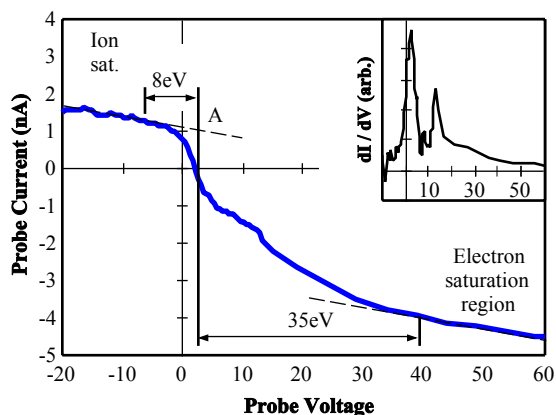


Figure 4.15: Langmuir probe measurement at beam flux gauge filaments. Saturated ion current, at A, is approximately 1nA. The most energetic electrons and ions are 8 and 35eV, respectively. Inset: derivative of measurement.

decrease in ion density after the cell reached steady state, after the warmup period described in Section 4.5.2.

We also applied a DC bias to the grid of the beam flux gauge during the measurement to try to identify particular species in the plasma output [188]. Figure 4.17 shows the collected current as a function of grid bias, with the collector wire grounded. Contrary to the expected results, in which a positively-biased grid would repel positive charges and vice versa, the polarity of the grid bias matched the polarity of the collected current. This indicates that secondary electrons were being generated at the grid and/or collector, at a rate greater than the collection of charges from the plasma. The current dropped below the noise floor ($\sim 1\text{pA}$) when the plasma was extinguished, so this current was not merely leakage from the grid to the collector over some other conductive path. Since the grid is a very sparse mesh, the high biases may have also amplified the measured current through the Bayard-Alpert process.

4.6.3 Do Not Vary Nitrogen

Also, there have been numerous reports of comparison of PL from samples grown with different plasma RF power or flow rate, apparently assuming that the quality of XRD represented the optical quality of the material. However, the Langmuir probe

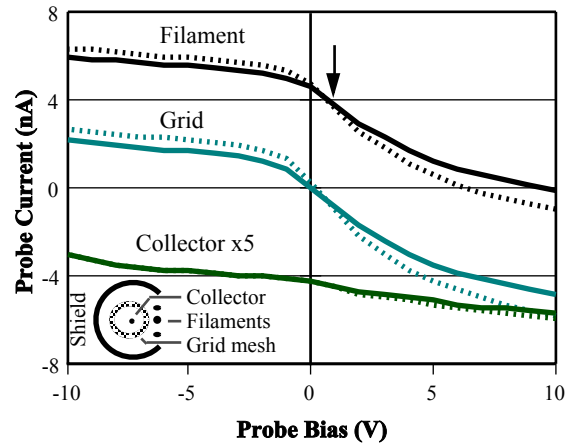


Figure 4.16: Langmuir probe current using various wires on beam flux gauge. Offset for clarity. Arrow shows nonzero floating potential at wafer position. Dashed lines measured immediately after plasma ignition; solid lines measured 15 minutes later. Inset: cross section of beam flux gauge.

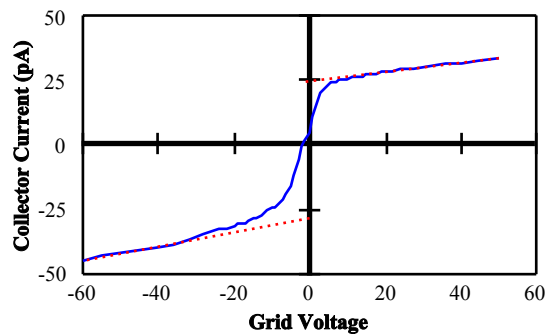


Figure 4.17: Current through grounded collector wire vs. voltage applied to grid

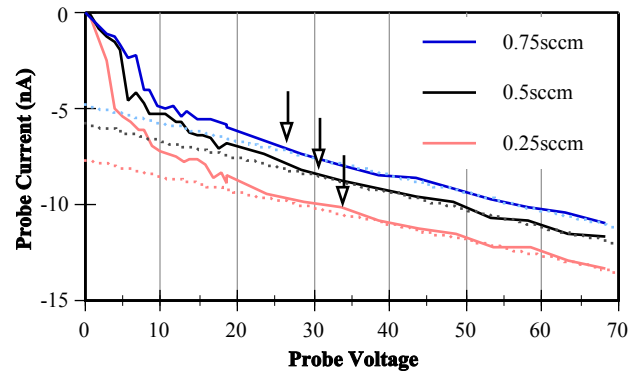


Figure 4.18: Langmuir probe measurement at several flow rates. Arrows mark the energy (eV) where current deviates from linear range, due to the highest-energy ions; error bars are approximately ± 5 V. Note the nonlinear relation between ion current and fraction of atomic nitrogen, as measured from the plasma optical emission spectra.

shows that varying the flow rate can change the energy of incident ions, as shown in Figure 4.18. The resulting change in ion damage and nonradiative recombination centers would not be easily detected by XRD, and the ion flux is more complicated than simple optical emission spectra would predict [163]. Therefore, in order to make valid comparisons from wafer to wafer, one should not vary the gas flow, RF power, or any other plasma condition. Only the Group III growth rate should be changed in order to change the nitrogen composition. This may also require a slight change in substrate temperature: lower growth rates increase the surface lifetime of Group III adatoms before they are buried, increasing the probability of strain relaxation and the formation of InGaAs QDs.

4.6.4 Discussion

It should be noted that this method fails to provide the detail of a conventional Langmuir probe, and care should be exercised before drawing conclusions about the plasma density or temperatures. The beam flux gauge is far from the interior of the cell, so it does not sample the ions within the plasma itself, nor a large fraction of the emitted ions. The aperture plate at the exit of the plasma cell further separates the beam flux gauge from the interior of the plasma. Also, the reference electrode

consists of the gas supply line at the rear of the cell, which is some 6-8cm from the plasma itself, so there may be a significant potential drop between the plasma and the reference electrode, leading to errors [195]. Also, it is impossible to perform a longitudinal profile of the plasma by this method to extrapolate back to the plasma [171]. Because of these restrictions and the probe geometry, estimates of electron and ion temperatures using the Laframboise method, for example, are generally not valid [196, 197].

Secondary electrons may also be generated from nearby surfaces by impact ionization[171] or by photoemission, but in either case, the generation of secondary electrons even at low bias suggests that the plasma is energetic enough to cause ionization and ion damage to the wafer. Photoemission is especially likely if the aperture holes are large enough to illuminate nearby metal surfaces with direct radiation from the plasma. Photons from N_2^+ , recombining N_2 , and the metastable $A^3\Sigma_u^+$ state all have more energy than the workfunction of nearby metals [168]. Whatever the origin, secondary electrons complicate the analysis of the I-V curve in several ways. First, the intermediate region, $|V| < 30V$, may be dominated by these lower energy electrons. This makes it very difficult to extract the ion or electron energy distributions. If the effect of secondary electrons could be eliminated, perhaps by applying a positive bias to the grid, it might be possible to extract the distribution of ion energies. The recent report by Miguel-Sánchez indicates this may be a possibility [190]. However, even with a biased grid, it is still possible for secondary electrons to interfere with the measurement, since they may be optically generated near the grid, as is believed to have happened in Figure 4.17. The other effect of secondary electrons is to add a nonzero, linear slope to the I-V curve. This is taken into account by extrapolating from the linear region back to the floating-potential point (zero current). This slope appears to be qualitatively correlated with the optical brightness of the plasma.

Nevertheless, using the beam flux gauge as a Langmuir probe provides an extremely useful measure of the actual ion flux at the wafer, which would seem to be the most pertinent information for plasma-assisted growth. In particular, the saturated ion current (point A in Figure 4.15) and the energies of the most energetic ions and electrons (arrows in Figure 4.18) can be unambiguously determined. Although

the ion current varies with geometry and is only a relative measure, it is repeatable from run to run. It can be monitored in real time while adjusting the plasma parameters, such as RF power or flow rate, to produce a beam with the fewest ions. If an ion trap is available for the cell, the Langmuir probe can measure its effectiveness.

We had previously required dozens of GaInNAs samples under varying conditions of growth rate, gas flow, and RF power to characterize the cell. Using the Langmuir probe, we were able to verify that our optimal conditions in fact led to the smallest ion flux while maintaining the efficient generation of atomic nitrogen based on optical emission spectra. The remaining ions needed to be removed by deflection plates as noted above. The ability to characterize the plasma cell ion flux in real time allows optimizing the cell operation in a few hours, rather than dozens of growths.

As previously mentioned in Section 4.5.2, plasma cells from several vendors have shown 15-20 minutes of instability before the plasmas reach a fully stable state, believed to be due to thermal processes in the cells. The Langmuir probe usefully shows that the ion current varies with time, particularly in the first few minutes, then is stable after that, as shown in Figure 4.19. This has implications for comparison between groups, or wafer to wafer, as the plasma variation may lead to differences in ion damage, nitrogen incorporation, etc. If the plasma has not reached its stable operating point before the growth of multiple quantum wells, there may be significant differences between the quantum wells. Our method of overcoming this instability will be reported in Section 4.8.

The ion energy distribution had the appearance of a bimodal distribution of energies, with two distinct energy peaks. There appears to be a kink in the I-V curve near 10V, followed by another asymptotic approach at the electron saturation region. Each kink and asymptote represents the range of one particular distribution. Two sets of features were apparent, one centered at +2eV, and the other covering the range from 10–35eV, as shown in the inset of Figure 4.15. This would make sense from Figure 4.2 if there were sources of ions at lower energies, such as ions escaping from the plasma during the “off” portion of the RF cycle when the sheath collapses. However, at low energies, the Langmuir ion measurement is convoluted with the attraction (focusing) of electrons, as well as the onset of secondary electron collection,

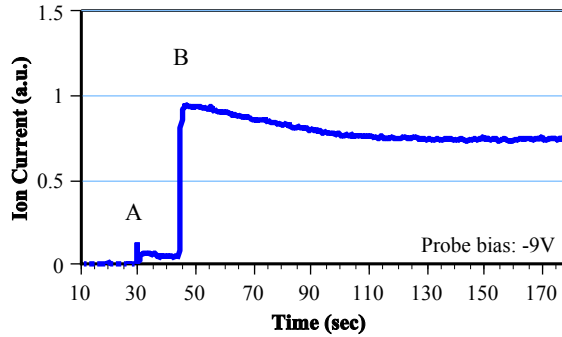


Figure 4.19: Ion flux at wafer position, showing a brief transient when the plasma is first ignited in capacitively-coupled mode (A) followed by transition to the inductively-coupled mode (B), with a long adjustment period after that.

so care should be taken before attributing low-energy features to any one effect. The higher energy peak, on the other hand, can only be attributed to high energy ions, and these are of particular concern for wafer damage.

4.7 Low-voltage Ion Deflection Plates

4.7.1 Improved Material with Deflection Plates

Having determined that there was a considerable flux of ions from the plasma, steps were taken to remove the ions from the plasma beam. Ion deflection plates had been installed on the cell, with the intention that high voltages would deflect any charged ions (and electrons) away from the wafer, as shown in Figure 4.20. However, as previously mentioned, when $\pm 800\text{V}$ was applied to the deflection plates, there was no significant improvement in photoluminescence (Figure 4.13). Based on the results of the Langmuir probe, it was believed that lower voltages deflected ions. This section will show from theory and experiment that ion deflection voltages under 100V are more than sufficient to remove even energetic ions from the plasma beam.

Three $\text{Ga}_{0.62}\text{In}_{0.38}\text{N}_{0.025}\text{As}_{0.948}\text{Sb}_{0.026}$ photoluminescence samples were grown, each with one 7nm quantum well, nominally emitting at $1.450\mu\text{m}$. A bias of $+18\text{V}$, 0V , and -40V was applied to one deflection plate for the respective samples, and the other plate

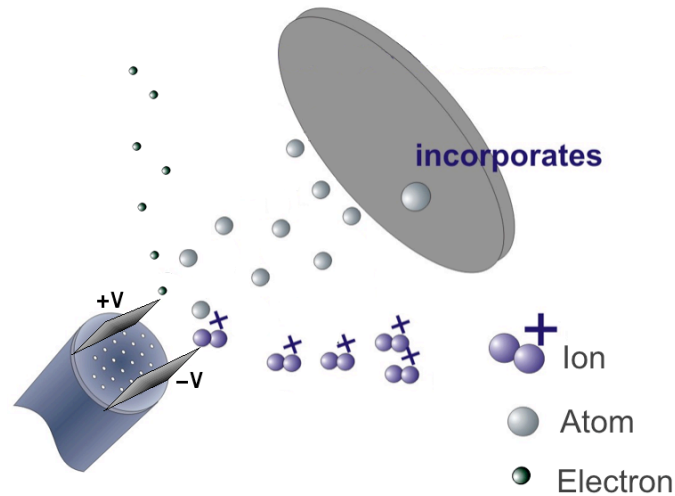


Figure 4.20: Ion deflection plates prevent wafer damage. After Kovsh [2].

was grounded. Figure 4.21 shows a clear improvement in photoluminescence (PL) with deflection. PL intensity at room temperature was increased by 3–5 times over all annealing conditions, and PL intensity at 15K was also dramatically enhanced, and the linewidth was somewhat decreased as well. Higher anneal temperatures were reached before the PL was quenched. RHEED also showed better surface morphology. It should be noted that the 0V sample was comparable to the best photoluminescence at $1.5\mu\text{m}$ that had been demonstrated at the time, so this was not merely a question of a single bad growth.

We determined that -40V applied to one deflection plate was sufficient to remove the majority of ions from the plasma [182]. Photoluminescence (PL) from GaInNAsSb quantum wells improved by a factor of 3–5x, as shown in Figure 4.21.

Low power PL showed that deflection plates reduced the PL linewidth [182]. For samples annealed at 720°C , the linewidth was reduced from 39meV to 37meV or 35meV , for positive, zero, or negative deflection, respectively. A PL linewidth of 32meV was observed after 800°C anneal. The reason for the larger linewidth at net positive deflection biases is still unclear. It may be that $+18\text{V}$ was not quite sufficient to deflect all ions, while the PL intensity of the -40V sample was reduced due to some

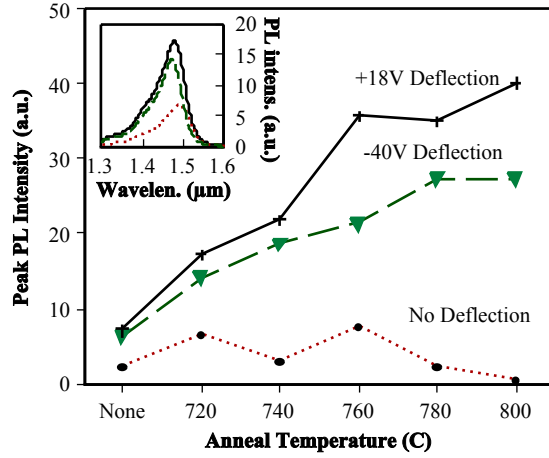


Figure 4.21: Peak PL intensity increases 3–5x with moderate deflection plate bias.

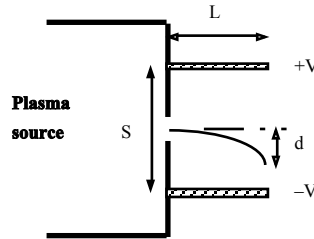


Figure 4.22: Simplified model of ion trajectory calculation.

other cause.

4.7.2 Deflection Model and Verification

The use of low voltages for the deflection plates is consistent with a first-order model of a charged particle in a uniform electric field. The partial pressure of charged species outside the plasma source is below 10^{-5} Torr, so we can neglect shielding by other charges in the first approximation. If we further neglect fringing fields, then we can treat the deflection plates as an infinite, parallel plate capacitor with a fixed voltage. We assume a particle with charge q , mass m , and velocity v , moving horizontally between two parallel, biased plates as shown in Figure 4.22. The two plates are biased at $+V$ and $-V$, respectively, with a separation S and length L . The particle will therefore spend a time $t = L/v$ between the plates, and we are interested in the

vertical deflection $d = at^2/2$ that it will experience in that time. Using $F = ma$, $F = qE$, and $E = 2V/S$, by straightforward substitution,

$$d = \frac{qVL^2}{Smv^2} \quad (4.8)$$

Particles that start midway between the deflection plates with horizontal kinetic energy $K = mv^2/2$ will be captured when $d = S/2$, or when

$$V \geq \frac{2d^2K}{qL^2}, \quad (4.9)$$

Note that mass plays no role in this equation.

For typical values of $L = 1\text{cm}$, $d = 2\text{cm}$, and $K = 25\text{eV}$, the ions will collide with the deflection plate with a bias of just 200V. Although this model overestimates the effectiveness of ion capture (collision) for a given voltage, ions do not actually need to collide with the plates, but can merely be deflected away from the wafer surface.

To try to study the minimum deflection voltage that would adequately remove ions from the plasma, a basic simulation of particle trajectories and the electric field profile in the vicinity of the deflection plates was performed. An iterative, finite element method was used to solve Poisson's equation in the region near the deflection plates and plasma. The wafer was modeled as a grounded conductor at a distance of 5cm from the tip of the deflection plates. The deflection plates were modeled as fixed potentials, 2cm apart and 1cm long. The open boundary conditions were modeled as an exponential decay ($dV/dx \sim x$, $dV/dy \sim y$), which provided a more rapid convergence to the final values for the same size grid, and compared favorably with zero-potential boundaries on a grid 4x larger in each dimension. For one simulation, shown in Figure 4.23(a), the plasma itself was neglected. Because the pressure in the plasma cell is tens or hundreds of mTorr, with a high density of free electrons, the simulation was then repeated to include the plasma as a conductor. In either case, after the Poisson solution had converged, it was used to calculate the trajectories of particles starting at the plasma side of the deflection plates, as shown in Figure 4.23.

The figure shows the importance of including plasma conductance in the model. Treating the plasma as free space overestimates the effectiveness of the ion deflection plates at both deflecting ions, up to 221eV, and collecting them, up to 16eV. But

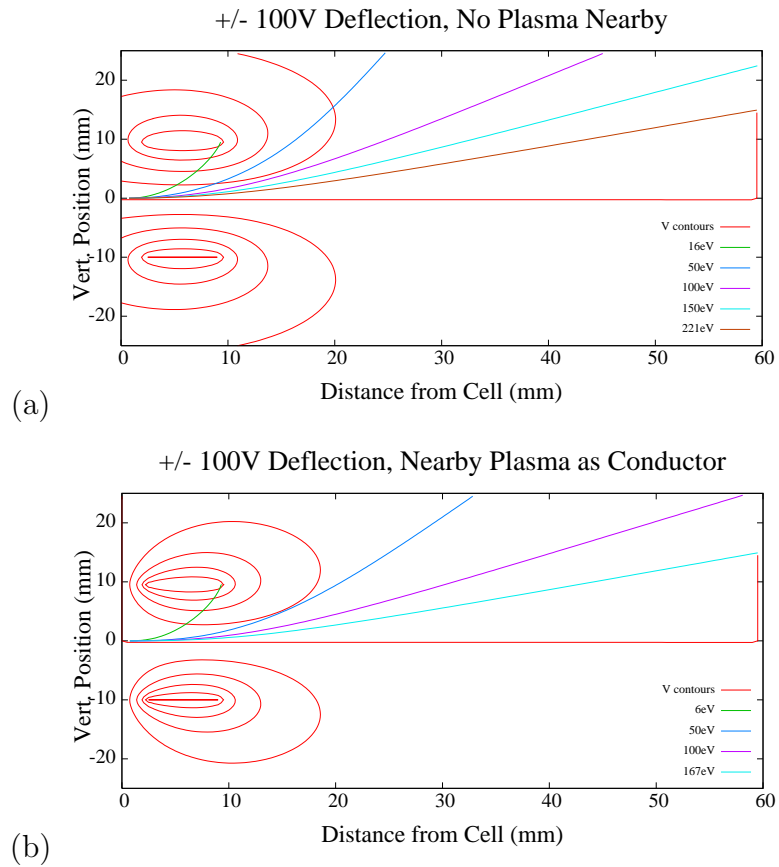


Figure 4.23: Simulated particle trajectories due to ion deflection plates and either (a) no plasma (open space), or (b) plasma treated as a conductor. The top and bottom plates are negatively and positively biased, respectively. Circular lines represent equipotentials around each deflection plate, 20V apart. The energies of the slowest deflected ion and the fastest captured ion are shown, along with several intermediate ion energies.

the electrostatic fields are much closer to the picture presented in Figure 4.23(b), in which the conductive nature of the plasma just inside the crucible, 2mm from the deflection plates, has repelled the equipotential lines. Fringing effects clearly cannot be neglected in the presence of the conductive plasma, and even closed-form solutions to fringing fields [198] are inadequate to describe this situation. However, even taking into account the fringing fields, the simulation shows that $\pm 100\text{V}$ deflection plates are capable of deflecting ions up to 167eV from the wafer, which is 5 times higher than the highest energy ions measured by the Langmuir probe. Ions with less than 6eV of initial kinetic energy are fully collected.

Another experiment was performed which verified that low voltages were indeed sufficient to deflect ions. In a Varian Gen II MBE system, the beam flux gauge and the wafer carrier are mounted on opposite sides of a rotatable stage, or car, such that either the ion gauge or the wafer may be pointed toward the source furnaces. The ion gauge is parallel to and approximately 7cm from the axis of rotation, so the gauge moves up or down as the car rotates to different angles. This allows spatial profiling of the beam, as shown at the bottom of Figure 4.24. The upper portion of Figure 4.24 shows a very approximate relation between the voltage applied to deflection plates, and the resulting angle of deflection. Only a few volts were sufficient to move the peak ion location by several centimeters. For maximum spatial resolution in this measurement, the beam flux gauge collector wire was used for the probe, rather than the filament wires. The outlying data point at -28 degrees is believed to have been caused when the probe wire fell behind one of the ion gauge filaments. Such shadowing could be prevented by using the filament itself as the probe, but with some loss of spatial resolution. The nonzero voltage offset is a result of the beam flux gauge collector being not quite centered in front of the plasma cell, and also the convolution of electron and ion currents. The deviation above +18 degrees was due to blocking of the plasma beam by the beam flux gauge's protective bracket, when the gauge was turned too far away from the plasma source. Also, the Langmuir probe was restricted to vertical motion, but the deflection plates were mounted at an angle of $55 \pm 5^\circ$ on the cell, so deflected ions tended to miss the probe at higher deflection angles. These geometric complications prevented quantitative analysis of the ion energy with

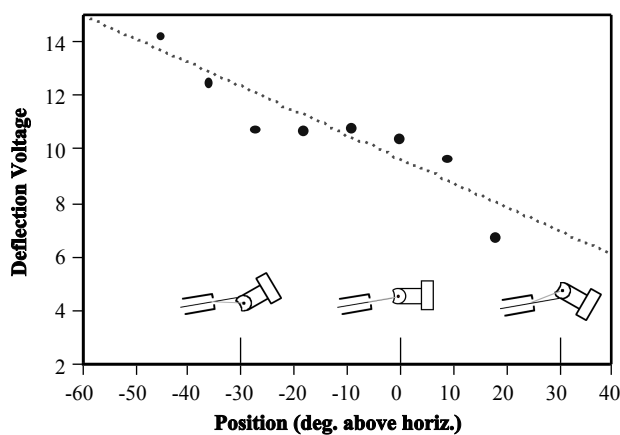


Figure 4.24: Deflection of peak ion current to different angles as deflection voltage changes. Probe is swept across beam by rotating the car, as shown at bottom.

respect to the angle of deflection. Nevertheless, small voltages were sufficient to have a significant effect on ion distribution.

It is still unclear why high deflection voltages did not improve the material. We believe that the high voltage bias may have sputtered neutral, adsorbed contaminants from the deflection plates or cryoshroud onto the wafer, or generated energetic but neutral nitrogen species. There does not appear to be a DC-enhanced plasma or field ionization of N_2^* , as there is no sign of breakdown in the current through the deflection plates themselves (not shown). It is also possible that the high deflection voltages generated energetic ions at the tips of the deflection plates, particularly the positive plate. The net electric field has a large component in the direction of the wafer, which would accelerate ions toward the wafer. Although we did not find evidence in the Langmuir probe measurement of any sharp increase in current at high voltages, even a small number of ions could cause significant damage to the wafer surface, since the net potential is 800V from the positive plate to the (grounded) wafer. Finally, it is possible that the high voltage may have caused an arc from the feedthrough to the walls of the cell, shorting out the high voltage supply and causing it to revert to a safe, “standby” mode with no voltage applied. A similar arc outside the cell has been reported by others [165].

There was some early concern that the deflection plates were close enough to the

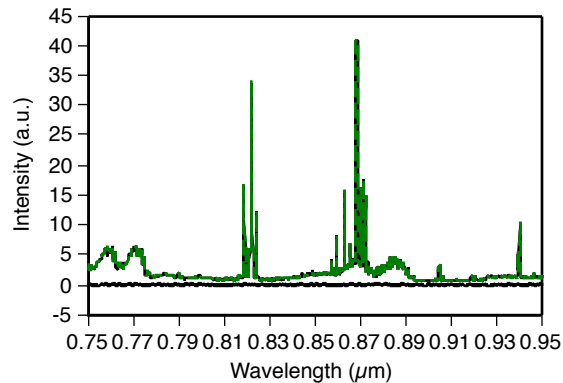


Figure 4.25: Optical emission spectra with -1000V (solid line) and 0V (dashed line) deflection bias. The bottom line, near 0 intensity, is the difference between the two spectra.

plasma that very large electric fields could perturb the plasma itself. However, as Figure 4.25 shows, there was no change in reflected power or thermocouple temperature with deflection bias, and less than 1% variation throughout the spectrum, even with deflection voltages as large as 1000V . It is believed that the plasma is well screened by the high carrier density.

It is worth noting that the deflection plates need not be equally or even oppositely biased. If the average bias of the two deflection plates is nonzero, then they can be used to provide a potential barrier to either electrons or positive ions. For example, if one deflection plate were biased to $+30\text{V}$ and the other to -10V , there would be a net $+20\text{V}$ potential that would tend to repel positive ions and extract more electrons from the plasma, assuming the plasma is in good electrical contact with the grounded pipe at the rear of the source [195]. Electrons are believed to be less damaging than ions, so a net positive bias should prevent the most damage to the wafer. It should be noted that a $+10\text{V}$ net potential would not necessarily repel 10eV ions, due to screening by electrons and the finite size of the deflection plates.

4.8 Protecting Wafer using an Arsenic Cap

4.8.1 Damage Below the Quantum Well

The preceding reports have focused on plasma-induced damage during the quantum well (QW) and/or GaNAs barriers, when the wafer is directly exposed to the plasma. However, defects before and after the QW are often overlooked as significant sources of nonradiative recombination and wafer damage. Point defects such as vacancies, even when they originate far from the QW boundary, can promote intermixing of either Group III or Group V elements, depending on whether the dominant vacancy is V_{Ga} or V_{As} [199, 131]. Defects also reduce the lifetime of semiconductor lasers. They can lead to a quenching of luminescence during anneal, despite some distance from the quantum well. Finally, defects which nucleate before the QW is grown can propagate an extended defect through the QW, leading to nonradiative recombination and increased laser thresholds.

Indeed, we find that plasma-related damage of the wafer is not limited to the QWs. Deep level transient spectroscopy (DLTS) measurements show a transient increase in traps in the layer at which the plasma was ignited, even though the nitrogen shutter was closed [35]. A Langmuir probe measurement similarly shows a strong, temporary increase in ion flux when the plasma reaches H-coupled mode, as shown in Figure 4.19. SIMS shows a sharp but short-lived spike in the nitrogen composition of the wafer when the plasma is ignited, as shown in two samples in Figure 4.26, grown two years apart. Preventing this damage is vital to high quality GaInNAs growth.

One possible explanation for the additional defects at plasma ignition may be the operating point of the cell: low gas flow and high RF power may be necessary to ignite a high intensity (H-coupled) plasma, but these maximize ion production from the plasma. Ions are known to cause significant wafer damage.[163, 200] Several techniques have been used to minimize damage due to plasma ignition. It was buried under a thick GaAs buffer layer [35]. Wang et al. reported improved photoluminescence (PL) from increased arsenic overpressure attributed wafer damage to premature nitridation of the surface, leading to phase segregation [201]. In that paper, it was suggested that excess arsenic prevented nitrogen incorporation. This does not agree

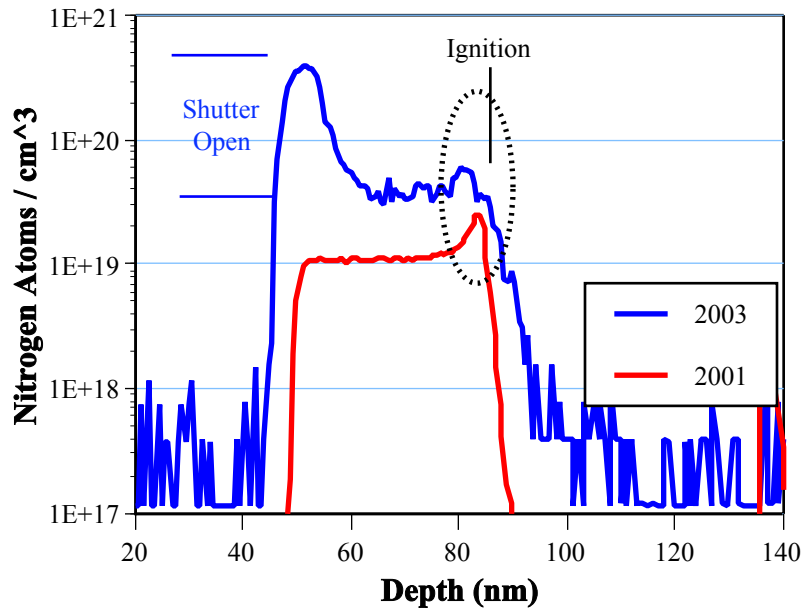


Figure 4.26: SIMS depth profile shows excess nitrogen incorporated when the plasma is ignited.

with several published results showing independence of nitrogen incorporation above a certain ratio of arsenic to nitrogen fluxes, and the technique suffers from a long growth pause.

Another problem with plasma sources, in addition to the generation of defects, is repeatability. Careful observation of plasma cells from several vendors has shown 5-20 minutes of instability before the plasma cell reaches a fully stable state [181, 165]. This is believed to be due to thermal processes within the cells, at least when operating in the low-flow regime for dilute nitrides. The instability necessitates running the plasma for several minutes before the first nitride layer, to assure repeatable operation from run to run. Also, the DLTS and SIMS features are not always present, suggesting they may be the result of some unknown variation in the way the plasma is ignited, despite efforts to standardize the plasma ignition process. If the plasma has not reached its stable operating point before the growth of quantum wells, there may be significant differences among the quantum wells, even emission at different wavelengths. It would be of some benefit to be able to ignite the plasma cell and adjust it to a desired state

before exposing the wafer to the plasma.

Fischer has proposed the use of a gate valve between the plasma cell and the chamber, which allows the plasma to be ignited and tweaked to a desired steady state without affecting the wafer [81]. But the operation of a gate valve in close proximity to the nitrogen plasma can cause the plasma to become unstable again or even go out [181, 165]. This may be a sign of an inductively coupled parasitic load on the RF coil, as we had previously seen with a standard, tantalum MBE shutter in front of the cell. It might also be due to a change in background pressure at the exit of the plasma cell when the valve opens.

We propose the use of an arsenic cap[202] to protect the wafer during the ignition and stabilization of the plasma. This technique requires no changes to the MBE chamber, and has no effect on the plasma stability.

4.8.2 Arsenic Capping Procedure

For this study, a 7 nm GaInNAsSb quantum well in 20 nm GaNAs barriers was grown using a Varian Mod-Gen II solid source MBE machine, with an SVT Associates model 4.5 RF plasma source to supply reactive nitrogen. After the native oxide was thermally evaporated, a 300 nm GaAs buffer layer was grown, with an As₂ flux provided by a valved cracker at 15 times the gallium flux. The wafer was then cooled to 10°C for one hour with an As₂ flux of $0.5 - 1.0 \times 10^{-5}$ Torr, in order to deposit a thick arsenic cap, while being rotated slowly to ensure uniform deposition. (150°C was sufficiently low to deposit thick arsenic, although this is much higher than temperatures in the literature. The difference appears to be due to the use of As₂ vs. As₄.) To best simulate our laser growth process, the buffer growth and nitrogen growth took place in separate MBE chambers, and the wafer was transferred under UHV while still capped. Once in the second chamber, the wafer was heated slowly to 160°C (thermocouple), then the plasma was ignited and operated for 20 minutes. A large arsenic flux of 6×10^{-7} Torr was used to prevent early desorption of the cap. A purely diffuse pattern in reflection high energy electron diffraction (RHEED) was used to verify that the cap remained thick and amorphous. The wafer was then

rapidly heated to oxide blowoff temperatures (720°C), which desorbed the cap. The RHEED pattern showed metallic rings between 350–450°C, which in turn gave way to a clear (2x4) reconstruction pattern as the final layers of the cap were desorbed.

For comparison, another sample was grown and capped using an identical process, except that the arsenic cap was removed before the plasma was ignited. The wafer was heated to oxide blowoff temperature (720°C) to evaporate the arsenic cap, and 50nm of GaAs was grown while progressively cooling the wafer to 525°C for GaInNAs growth. The plasma was ignited as soon as this GaAs layer began, after the cap was completely removed. The thick GaAs had previously been believed to bury plasma-related damage, as previously mentioned [35].

4.8.3 Arsenic Capping Results

The wafers were cleaved, and each piece was annealed for 60 seconds in a rapid thermal anneal. The photoluminescence (PL) intensities for each sample are shown in Figure 4.27. The intensity was increased by 2-3x over all annealing conditions, indicating the removal of nonradiative recombination sites. This is in comparison with our best 1.5 μ m material at the time, and shows a significant improvement in luminescence using the arsenic cap. Curiously, unlike the use of deflection plates,[203] arsenic capping does not change the annealing characteristics of the material: the luminescence begins to fall at annealing temperatures above 760°C. This suggests that the arsenic capping prevents a different type of damage than ion deflection plates do.

Transmission electron microscopy (TEM) shows a decrease in damage with capping, and the effect on the wafer is highly localized at the cap interface. Several typical TEM (002) dark field samples are shown in Figure 4.28. These are different samples from the previously mentioned PL samples, but are typical for arsenic capped and uncapped interfaces. The change in contrast from white to dark, similar to the GaNAs barriers adjacent to the QWs, is evidence of excess nitrogen at the capped surface. This shows that there was too much of a delay between the removal of the arsenic cap and the onset of GaAs growth, allowing accumulation of nitrogen at the

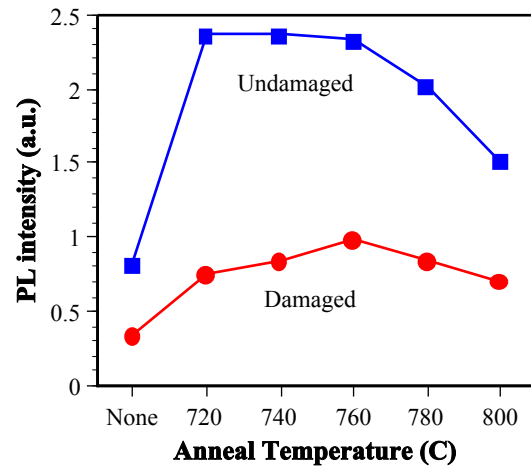


Figure 4.27: PL intensity at several anneal temperatures, for samples grown with (circles) or without (squares) extended damage before the QW.

surface. The change in brightness in the QW is due to the different compositions used, and is not significant for this study. There does appear to be somewhat better uniformity in and between the QWs, however. We suspect that the ignition damage promotes extended defects or prevents their burial under subsequent growth, and contributes to surface roughening.

It was initially unclear whether arsenic capping was redundant with ion deflection plates. Deflection plates had not been used in the first arsenic capping samples, and it was possible that the arsenic cap merely prevented ion damage before the QW just as deflection plates would. (Recall that removing ions from the plasma beam caused a 5x increase in PL, as reported in Section 4.7.1 [203].) To study whether ion deflection plates could fill the same purpose as arsenic capping, lasers were grown with both arsenic capping and ion deflection, with arsenic capping alone, and with neither technique. Figure 4.29 shows the distribution of measurements of laser threshold current densities with each technique(s). Clearly each technique has a clear and distinct effect, so arsenic capping is desirable even when ion deflection plates are in use.

Finally, the improvement from arsenic capping has been a significant boon to the development of GaInNAs modulators at $1.5\mu\text{m}$. Arsenic capping, along with several

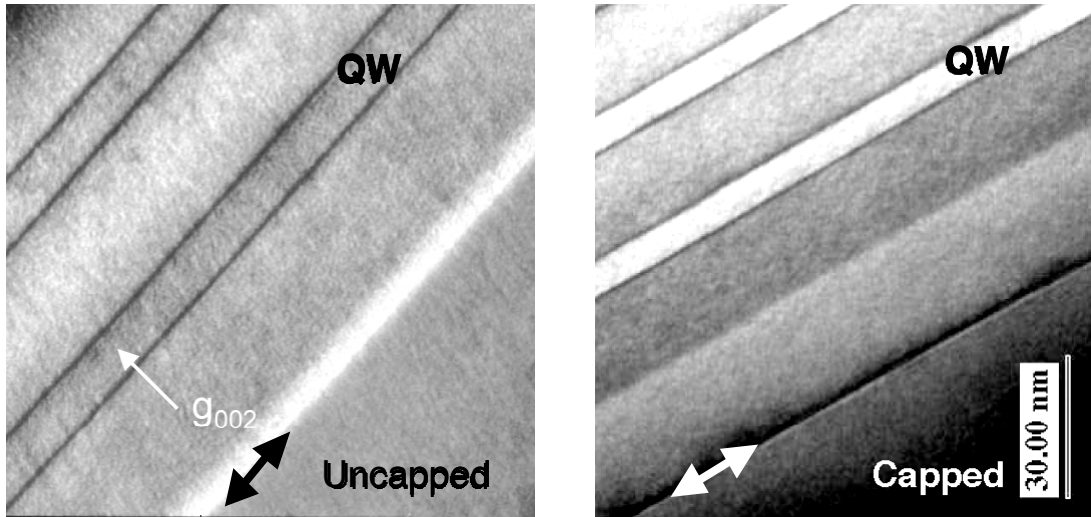


Figure 4.28: TEM of GaInNAsSb/GaNAs QW without (left) or with (right) arsenic cap. The point of plasma ignition is marked with a heavy double arrow. Growth direction is toward the upper left. The right picture also shows GaNAs barriers before QW.

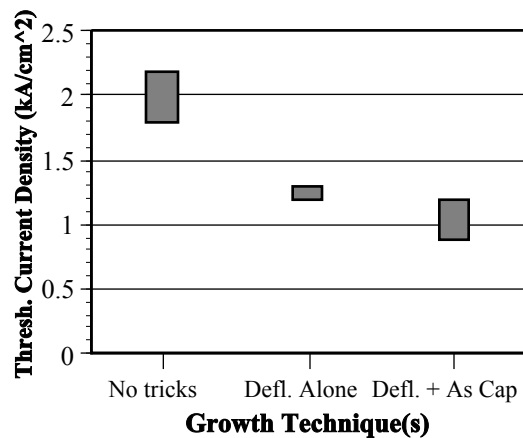


Figure 4.29: Threshold current densities for edge emitting lasers grown with ion deflection plates (middle), deflection plates and arsenic capping (right), or neither (left).

improvements outlined in Section 4.12, led directly to the first demonstration of a room temperature exciton peak and absorption Stark shift in any dilute nitride beyond $1.25\mu\text{m}$ [44]. Sharp exciton absorption peaks, with linewidths less than 25meV , were demonstrated at both 1.3 and $1.5\mu\text{m}$, with absorption coefficients as high as $20000/\text{cm}$. These results offer excellent promise for modulators at these wavelengths. We have also demonstrated the smallest reported room temperature photoluminescence linewidth at $1.5\mu\text{m}$, just 28meV [204]. We believe the narrow linewidths in the absorption (exciton) and PL measurements result both from removal of variations in the bandgap (carrier localization) and from removing both nonradiative recombination centers (traps).

In summary, defects that originate outside of the QW are commonly overlooked as sources of nonradiative recombination in GaInNAs-based lasers. The existence of such damage has been verified by SIMS, TEM, and DLTS at the layer at which the plasma was ignited in the high intensity (inductively-coupled) mode. Plasma seasoning and stability would both suggest the need to allow the plasma to run for some period of time before exposing the wafer, but such exposure leads to surface damage.

This surface damage can be prevented by depositing a thick, temporary cap of solid arsenic onto the wafer surface. With the surface protected, the plasma can be ignited and tuned as desired, and then the wafer is quickly heated to growth temperatures, rapidly evaporating the excess arsenic. This technique requires no changes to the vacuum system. Unlike a gate valve, there can be no effect on the plasma condition when growth begins. The contaminants usually associated with an extended growth interruption are avoided, since the cap comes off within about one minute of the wafer reaching Ga(In)NAs growth temperature. There are also fewer defects associated with low-temperature GaAs, since the wafer is quickly ramped up to Ga(In)NAs growth temperatures, with minimal or no low temperature GaAs growth. Using the arsenic capping technique, PL was enhanced by 2–3x, and laser thresholds were reduced by 30%. This was shown to be independent from the use of ion deflection plates, and was another significant advancement in the development of laser-quality GaInNAs(Sb) devices, including lasers and modulators.

4.9 Redshift Induced by Plasma Damage

4.9.1 Defects Induced by Ion Damage

The preceding sections have offered methods of removing two distinct types of defects: arsenic capping to prevent plasma damage upon plasma ignition, and ion deflection plates to prevent ion damage during the growth of the quantum well itself. With these two types of wafer damage now under human control, it is worth investigating the broader subject of nitrogen-related defects in general. Wafers with and without each type of damage were grown, and the results show several striking similarities. This section offers evidence that the reduction in bandgap in dilute nitrides is actually not entirely due to intrinsic properties of the material, but is partially due to wafer damage during growth. Surprisingly, damage to the wafer well before the quantum wells can produce a significant change in not only the material quality, but the nitrogen composition as well. This suggests that even very small quantities of nitrogen (0.1%) can either nucleate extended defects, which grow through the quantum well, or else the nitrogen prevents existing defects from being buried by subsequent growth. Finally, the annealing behavior of the different types of defects may help other groups identify defects that may be present in their material.

Dilute nitrides such as GaInNAs have a significantly smaller bandgap than the GaAs on which they are grown, making them attractive candidates for near-infrared lasers and multijunction solar cells. Despite extensive study, the cause of the small bandgap remains controversial. Experimental results have supported multiple models, such as a resonant level above the conduction band that repels it due to band anticrossing,[70] or distributed levels from local depressions in the bandgap, whether due to defects, alloy fluctuations,[102] an impurity band,[104] or multiple effects [105]. The band anticrossing model is the best established, with validation of the existence of the unique E_+ nitrogen band,[109, 108] but the origin of localized potential variations or disorder bands has not been adequately explained. We propose that the apparent impurity band[103, 6] is primarily due to defects accrued during growth, even if the material does not relax [205], and that the band is not an inherent property of nitrogen in GaAs. Several defects near the conduction band edge that may be

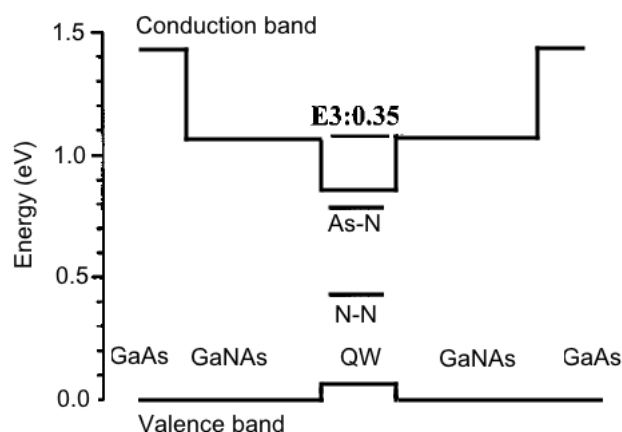


Figure 4.30: GaInNAsSb/GaNAs quantum well band structure, plus defect levels from *DLTS[118] and †predicted by theory [7].

responsible for this behavior have been suggested from GaNAs DLTS[118] and theory [7]. These are shown in Figure 4.9.1.

Several quantum well (QW) samples were grown by solid source molecular beam epitaxy (MBE) with an RF nitrogen plasma source. Each QW consisted of 7nm of $\text{Ga}_{0.62}\text{In}_{0.38}\text{N}_{0.025}\text{As}_{0.948}\text{Sb}_{0.026}$ surrounded by 20nm $\text{GaN}_{0.03}\text{As}_{0.97}$ barriers. Growth details are provided elsewhere [77]. The wafers were cleaved and annealed for 1 minute at various temperatures under a GaAs proximity cap. For one of the samples, a DC bias voltage was applied to ion deflection plates in front of the plasma source during growth [163, 187]. Using moderate bias voltages resulted in a substantial increase in photoluminescence (PL) intensity at all annealing temperatures,[203] but more significantly, the peak wavelength was blueshifted by 10meV, as shown in Figure 4.31. In other words, deflection of nitrogen ions away from the wafer during growth increased the bandgap. This would be expected from a decrease in the nitrogen composition of the film.

However, high resolution X-ray diffraction (HRXRD, Figure 4.31) indicated a slight shift toward *tensile* strain in both the QW and barriers when using deflection plates. It appears that *more* nitrogen was incorporated in the wafer, even though less nitrogen was reaching it. This counterintuitive result prompted us to regrow these

samples, with an identical outcome. Combined with the PL, these results ruled out changes in strain, relaxation, Sb drift, and a decrease in nitrogen as sources of the redshift. Furthermore, the linewidth was slightly increased with ion damage, also shown in Figure 4.31, which suggests that the damage contributed random states below the band edge.

To firmly establish whether the nitrogen fraction was changed by using deflection plates, Rutherford backscattering spectrometry with nuclear reaction analysis (NRA-RBS) was performed. 150nm thick layers of GaInNAs (8% In) in GaAs barriers were grown with and without deflection plate bias, as above. These samples were grown without antimony, as antimony is known to affect nitrogen composition [99]. The nitrogen concentration was measured to be $2.2 \pm 0.1\%$ and $2.1 \pm 0.1\%$ with and without deflection plates, respectively, and these numbers were unchanged after anneal. Clearly, the deflection of ions did not reduce the amount of nitrogen in the crystal and, within the error bars, may have increased it, consistent with the XRD results.

The NRA-RBS also showed that without deflection plates, 5.3% of the nitrogen was in the form of interstitials before anneal, increasing to 7.0% upon anneal. With deflection plates, however, the interstitial nitrogen was initially higher at 11.4%, but dramatically decreased to just 3.7% after annealing. This suggests that ion-damaged material formed extended defects such as phase segregation, or stable defects such as the split interstitial $(\text{As-N})_{\text{As}}$ (two atoms on the same Group V lattice site) [85, 54, 118, 7]. In the presence of damage, annealing apparently caused some of the desirable substitutional nitrogen to move to clusters or complexes. In undamaged material, the large fraction of interstitials (11.4% of all nitrogen) was probably due to nitrogen dimer $(\text{N-N})_{\text{As}}$, which is energetically favorable over other defects at typical GaInNAs growth temperatures [7]. The remaining 3.7% interstitials suggests that there is still room for improvement in material growth.

The $(\text{N-N})_{\text{As}}$ mostly decomposes upon anneal.[118, 121] Although the error bars on the interstitial measurement were large (roughly 5%), it is unlikely that all of these last four measurements were coincidentally in error in such a way as to reverse these conclusions. The excess nitrogen from $(\text{N-N})_{\text{As}}$ is expected to recombine as N_2

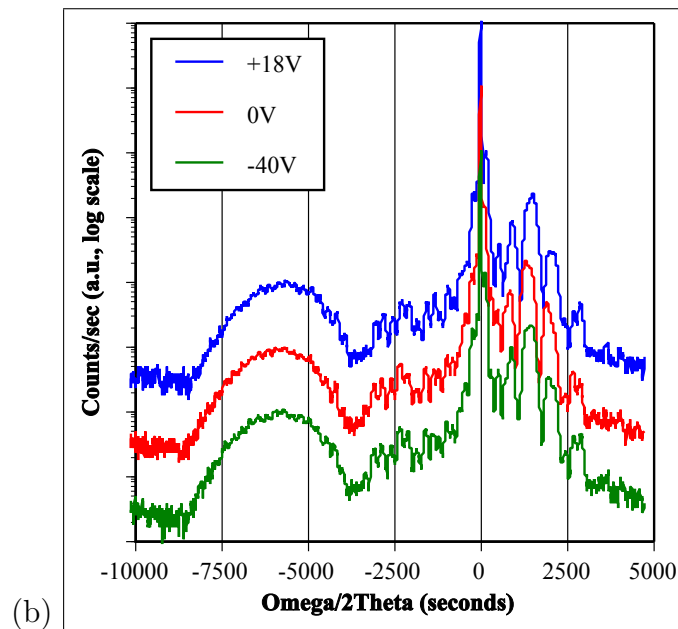
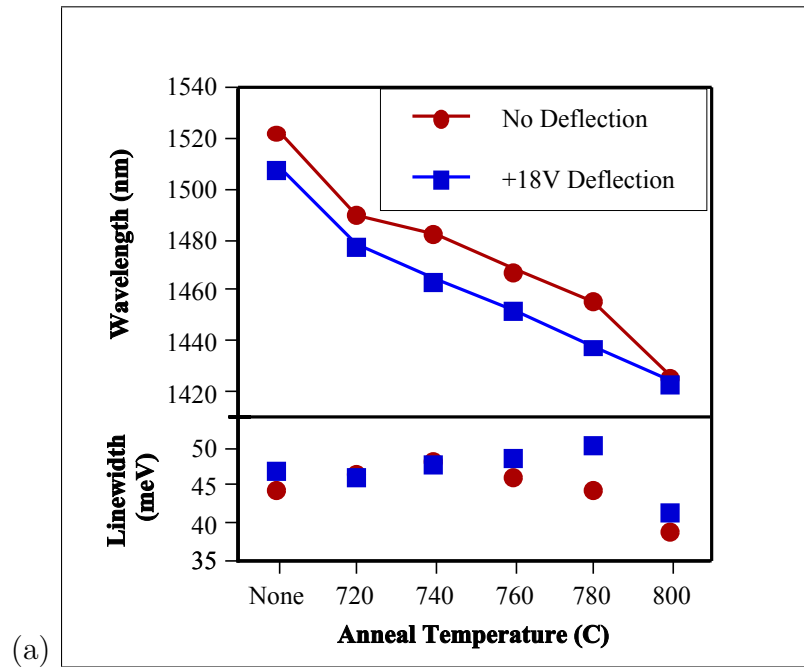


Figure 4.31: Effects of ion deflection plates. Photoluminescence (top) shows decreased wavelength and comparable linewidth. Peak PL intensity was at an anneal temperature of 780°C. XRD (bottom) shows more tensile strain in QWs and barriers alike (a shift to the right).

and diffuse out of the lattice, or else fill any arsenic vacancies with nitrogen. Arsenic vacancies diffuse from the surface during anneal, and the filling of these vacancies might explain why higher anneal temperatures are possible before PL rollover.

The microscopic cause of the damage-induced band shift is still uncertain. The defect level associated with the $(\text{N-N})_{\text{As}}$ split interstitial is well below the conduction band, so it probably does not affect the bandgap significantly. The $(\text{As-N})_{\text{As}}$ split interstitial apparently survives anneal, and is probably either just below[7] or just above[118, 6] the conduction band of GaInNAsSb. With the interstitial concentration well above $10^{19}/\text{cm}^3$, this defect level would broaden into an impurity band, and a dopant-like miniband could reduce the bandgap. If the conduction band approaches or crosses this level, it may also add to the PL broadening [104]. However, extended defects are a more likely cause, as we shall demonstrate.

A decrease in the bandgap of GaInNAs or GaInNAsSb is usually caused by an increase in N, Sb, or In. But in these samples, the nitrogen composition and the bandgap both decreased. The mechanism for the reduction in nitrogen is not yet known, but may be due to extended defects providing an escape path for N_2 to reach the surface during growth, or the escape of AsN dimers [94]. The peak PL wavelength from all the various samples shifted similarly with anneal, suggesting that the shift was not simply premature rearrangement of Ga-In atoms [124, 74, 206]. Furthermore, the wavelength shift survived anneal, as did the decrease in luminescence, consistent with ion damage [131]. This may also explain part of the redshift associated with using GaNAs barriers around the QWs, since GaNAs tends to increase the number of defects at these growth temperatures [81]. The defects may also increase the redshift (decrease the bandgap) in the GaNAs barriers, and also in the GaInNAs(Sb) if they propagate into the QW.

4.9.2 Damage Preceding the Quantum Well

To understand the nature of defects in this material, we grew two additional GaInNAsSb/GaNAs QW structures with identical plasma conditions and no deflection. Both wafers were covered with an arsenic cap, with details provided elsewhere,[182]

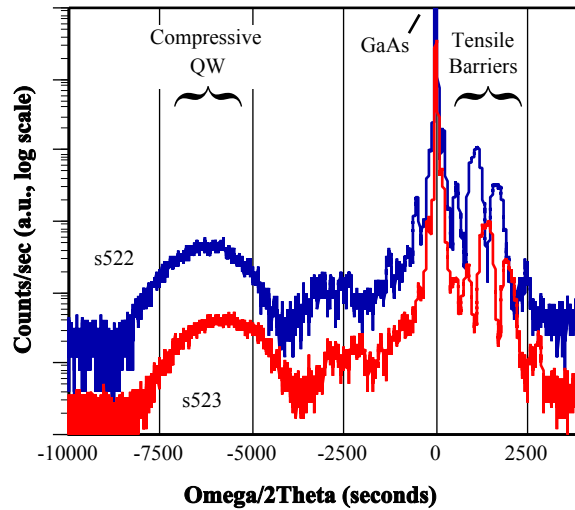


Figure 4.32: XRD of GaInNAsSb/GaNAs QWs that were exposed to long (s522) or short (s523) plasma exposure before the QW. (Offset for clarity.)

and the nitrogen shutter remained closed until the GaNAs layer. Growing with the shutter closed incorporates very little nitrogen (0.01–0.02%), but it has been found to introduce defects [207]. The arsenic cap on one sample (s522) was intentionally removed before the plasma was ignited, exposing it to damage from ignition, but GaAs growth began almost immediately. The arsenic cap on the other sample (s523) was left in place until the plasma was ignited, but then the wafer had an unintentionally long exposure to the plasma while being heated slowly to growth temperatures, and is presumed to have been damaged by heavy nitridation of the surface.

XRD of these two samples shows a significant difference in nitrogen incorporation in both QWs and barriers, as shown in Figure 4.32. The peak PL from these samples showed a striking redshift of 17meV in s523, as shown in Figure 4.33, which is similar to the redshift from ion damage presented above. The PL linewidth also increased 6meV with the extended exposure. It is unclear whether the change in nitrogen in the QW is due to plasma ignition or extended exposure, but what is notable is that there is any change at all.

The GaNAs and GaInNAsSb growth conditions were identical, and the samples were grown within two hours of each other. Yet surprisingly, damage to the wafer

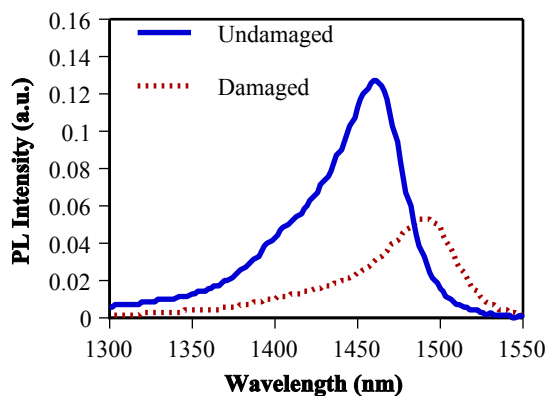


Figure 4.33: PL spectra from GaInNAsSb QWs annealed at 760°C, with and without plasma damage before the QW.

before the QW made a significant difference in the composition of the QW itself.

Kudrawiec reported a blueshift in photoreflectance (PR) with anneal, and stated that this ruled out defects as the origin of the blueshift with anneal, because PR is insensitive to absorption at point defects [206]. But this argument only shows that there must be another effect in addition to the defect redshift, not that there is no defect redshift. In fact, the reported bandgaps decrease below 50K, which is the sign of a defect band or bandgap fluctuations of some kind. Kudrawiec attributed 40meV of the blueshift to band anticrossing, and 40meV to some unknown factor.

4.9.3 Comparison of Wafer Damage

Both types of wafer damage were found to produce a strong redshift in the photoluminescence. The change in PL and XRD can only be explained by extended defects initiated before the QW and propagating upward through the QW. This suggests that nitrogen either nucleates extended defects or prevents existing defects from being buried during subsequent growth. This demonstrates the importance of minimizing defects during growth of all layers preceding or including dilute nitrides.

On the other hand, the difference in annealing behavior at high temperatures may be useful for identifying the source of defects in other material. Removing ion

damage allows annealing up to 800°C before the PL intensity falls, whereas pre-QW damage has PL quenching around 760°C. Also, the luminescence linewidth was strongly degraded by damage before the quantum wells, but was less affected by ion damage. This suggests that high linewidth may be indicative of problems early in the growth. It also affirms that two different mechanisms are at work, although they both lead to a redshift in luminescence and a decrease in both photoluminescence and laser emission (as was seen in Figure 4.29 on page 102).

In summary, wafer damage from two different origins has been found to cause similar effects in GaInNAs(Sb). First, it decreases the bandgap, causing a redshift in the emission wavelength. We believe this is due to impurity-like levels, induced by the damage, near the conduction band of GaInNAs. Extended defects propagate through the QW, though other defects might be responsible for the bandgap shift. The interstitial nitrogen concentration increases upon anneal, suggesting the formation of undesirable split interstitials or extended defects. The second effect of wafer damage is that the nitrogen composition is reduced. Antimony reduces defects in dilute nitride growth, and also increases nitrogen, which we now believe to be the same effect.

Finally, it should be noted that because the defect density can vary significantly depending on plasma, wafer preparation, growth technique, and other factors,[208] it becomes notably difficult to compare results between different groups, or even different growers within the same group, so past attempts at extracting material parameters have likely been misled by ion damage and/or other defects. Only low-defect material should be considered for characterization of fundamental physical parameters.

4.10 Substrate Temperature & Bandgap Thermometry

4.10.1 Importance and Difficulties of Temperature Calibration in MBE

Due to the very different nature of nitrogen bonds compared with GaAs bonds, Ga(In)NAs is prone to phase segregation. Phase segregation occurs when a homogeneous alloy of normally-immiscible materials separates into clusters, each of which is rich in its own type of material, like oil separating from water on a microscopic scale. This may occur through spinodal decomposition, which is a well known process in metal alloys, and predicted to occur in semiconductors, although the actual mechanism in Ga(In)NAs is unclear. Spinodal decomposition is a bulk process, rather than a surface or growth-related process, occurring in the bulk of the material after time or thermal cycling. Phase segregation can also occur on the surface of the semiconductor during growth. In epitaxial growth, this leads to roughening of the surface. Well-behaved segregation on the surface can result in self-assembly of quantum dots. InGaAs quantum dots have been used to create lasers and other devices, in large part because the segregation of InGaAs into islands retains the lattice spacing of the underlying GaAs wafer. But gallium and nitrogen tend to form GaN, and the hexagonal crystal structure of GaN is incompatible with the zincblende structure of GaAs, so segregation of GaN inevitably forms voids and defects in Ga(In)NAs. Phase segregation in GaNAs can be severe enough to turn a wafer white [59].

Phase segregation is a thermodynamic process, so low temperatures can be used to prevent the material from making the transition toward its preferred equilibrium, i.e. segregated. This is a well-understood technique in growth of heterostructures by MBE, relying on kinetically limited growth, rather than thermodynamically-limited. But there are equally severe problems with growth at low temperatures. Both Group III and Group V atoms can be buried on the wrong lattice site, leading to antisite defects; As_{Ga} arsenic antisite defects are the most common. Also, since the mobility of Group III atoms is the limiting factor in growth, if the temperature is

too low, the Group III atoms may not be able to diffuse to fill empty holes, leading to vacancies in the crystal. These problems can be minimized by adding an element with high surface mobility. This is why GaAs can be grown 50–75°C cooler than AlAs, and InGaAs can be grown 75–100°C cooler than GaAs. But dilute nitrides need to be grown even cooler than InGaAs, making temperature control an issue. Also, although nitrogen incorporation is independent of growth temperature up to $\sim 500^\circ\text{C}$, the temperature does strongly affect the ratio of As and Sb for large fluxes of Sb ($\sim 8\%$ mole fraction). Therefore it is of great importance to be able to grow dilute nitrides at a well-controlled, repeatable temperature.

It is worth noting that over the course of this research, the available temperature range for growth of GaNAs and GaInNAs(Sb) has increased dramatically. GaNAs can now be grown routinely up to 500°C or hotter, and GaInNAsSb up to 465°C . It appears that phase segregation can be strongly suppressed by avoiding surface defects from ion damage or oxygen contamination. However, the photoluminescence intensity of the film is still a strong function of growth temperature, so temperature control is necessary.

Unfortunately, reading absolute temperatures in MBE is very difficult. The approximate wafer temperature is roughly measured by a thermocouple in the heater assembly, which may or may not be touching the back of the wafer holder. Due to the vacuum system, it is generally not possible to place a thermocouple directly onto the front of the wafer to measure its temperature. The wafer holder typically includes a sapphire or graphite diffuser plate for even heat distribution across the wafer, so the thermocouple behind the wafer is further removed from the actual wafer temperature. For n-type wafers, the thermocouple temperature therefore reads 80–100°C hotter than the actual wafer temperature for a bare wafer, or 130–150°C hotter with a sapphire backing plate. There is another 50°C difference between Systems 4 and 5, presumably due to thermocouple placement.

Conventional pyrometry, which uses a single wavelength, is generally unreliable in semiconductors: the bandgap of a semiconductor dramatically changes the emission spectrum, making it very unlike the black body radiation that pyrometers normally use. Pyrometers can also be misled by a change in the reflectivity (emissivity) of the

growth surface, by misalignment, by deposition of arsenic on the viewport, and by heat from a heated viewport or a hot source such as gallium. The signal available for pyrometry is also quite low at GaInNAs growth temperatures (near 400°C). Two-color pyrometry can correct for the bandgap problem as long both wavelengths are well below the bandgap, but still suffers from the other problems mentioned above. Because of these difficulties, all pyrometers need to be calibrated to a known reference temperature, which negates the whole purpose of using the pyrometer as a temperature reference.

A number of attempts have been made, in our group as well as others, to calibrate pyrometry using the oxide blow-off temperature, which is the temperature at which the native oxide on a GaAs wafer evaporates. This is nominally at 580–585°C, and Sun et al. at U. Texas at Austin [209] reported seeing less than 2% variation in the oxide desorption temperature in over 50 growths. But we have found up to 40°C variation from vendor to vendor, and a large variation even from one wafer batch to the next. Preliminary data are plotted in Figure 4.34. It appears that the oxide blowoff is not useful as a reference temperature, but varies with wafer preparation and the type of oxide on the surface. It may also vary significantly depending on the wafer holder [210], although we have not seen such a correlation with our wafer holders.

Other methods for calibrating wafer temperature have been tried in the course of this research as well. The silicon-aluminum eutectic is often used in silicon MBE, but the temperature of a silicon wafer is different from GaAs, due to the smaller bandgap (absorbing a larger fraction of infrared from the heater), and the aluminum changes the emissivity of the silicon, and reflects infrared back through the wafer for a second pass. For calibrating the thermocouple for low temperature growths for K. Ma, small droplets of indium were melted onto a clean GaAs wafer using an ultra-clean soldering iron tip. Each droplet was stretched as it cooled, so it stood with a 3:1 or even 6:1 aspect ratio. This made it easy to see when the droplet melted and coalesced. However, the long “post” was probably an efficient radiator of heat, standing relatively tall from the wafer surface, so it served as a sort of heat sink for the surrounding wafer. Using indium to solder small pieces of wafer edge-on onto the GaAs wafer suffered

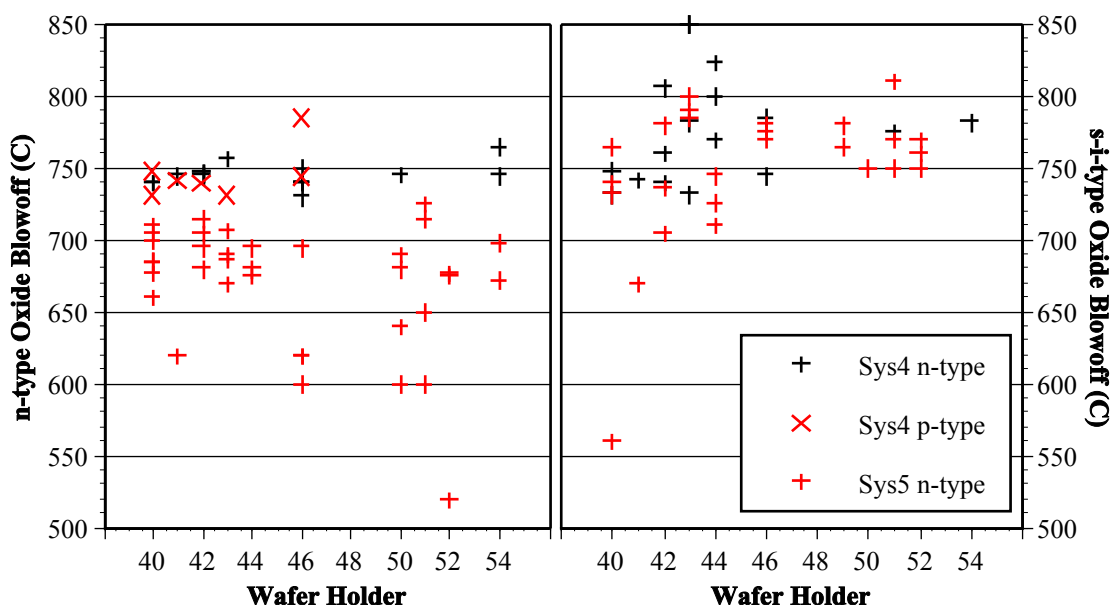


Figure 4.34: Oxide blowoff temperatures, measured by thermocouple.

from the same cooling problem, and is probably even less representative of the actual GaAs wafer temperature. Using smaller droplets of indium, monitoring their melting with the RHEED gun [211], would probably give more accurate results, as long as the RHEED beam did not heat the droplets excessively. As is often the case with MBE, it was eventually decided that the absolute wafer temperature was not important as long as the temperature could be repeated.

4.10.2 Bandgap Thermometry using Direct Reflection

The bandgap of a semiconductor decreases with temperature, so by measuring the bandgap, in principle, one can determine the temperature of the wafer with great accuracy and precision, as described by Hellman [212]. The GaAs bandgap is about 970nm at GaAs growth temperatures. At these temperatures, the substrate heater emits enough infrared near 970nm to make a transmission measurement through the wafer. Unfortunately, at GaInNAs growth temperatures, the substrate heater does not emit enough infrared light for this technique to work, so another source of light must be used. The original solution, a small, heated filament, produced

too much temperature nonuniformity at the center of the wafer. It is also possible to use an optical fiber to supply light behind the wafer for the same transmission measurement, although this is difficult for MBE chambers used for GaAs growth, both because the high temperature damages the wafer, and because opaque arsenic deposits on the fiber tip. Johnson has reported a diffuse reflectivity measurement, in which light is transmitted through the front of the wafer, scattered off the heater face, and transmitted back through the wafer [213]. It has been asserted that specular (mirror-like) reflection from the wafer would overwhelm the detector.

However, as Figure 4.35 shows, specular reflection is more than adequate to provide the bandgap of GaAs at all temperatures of interest. For this measurement, a 20W halogen lamp was placed at one of the ellipsometry ports on the MBE machine, focused onto the GaAs wafer using one or more lenses, and the reflection was focused onto a fiber bundle that went to an Oriel 77200 spectrometer. The bandgap is clearly detectable as a change in reflectivity over a wavelength range of $\sim 20\text{nm}$. The input optics were designed to produce the smallest possible image of the lamp filament onto the wafer, in order to sample the smallest possible area and avoid temperature gradients across the wafer. The ellipsometry ports allow a large opening for high light collection efficiency. An InGaAs detector was used at the output of the spectrometer, with strong responsivity up to $1.6\mu\text{m}$. To remove the system response, a special wafer was loaded, with 100nm of aluminum deposited on a 3" silicon wafer to act as a mirror. This mirror wafer is also used for the white-light reflectivity growth calibration (page 28, [43]). The lamp spectrum as measured off the mirror is divided from all other spectra. Also, to minimize noise in the measurement, the spectra are convoluted with a Gaussian lineshape with $1/e$ width 10nm. No lockin was necessary. The Matlab code used for extracting the bandgap has been made available to the group.

This technique is immune to changes in alignment or coating of the viewports, since these affect all wavelengths more or less equally. Because it uses the ellipsometry ports, the main center viewport is still available for conventional pyrometry or wafer curvature measurements. This technique also does not displace precious sources from the MBE machine, unlike commercial solutions based on diffuse reflectivity. Because

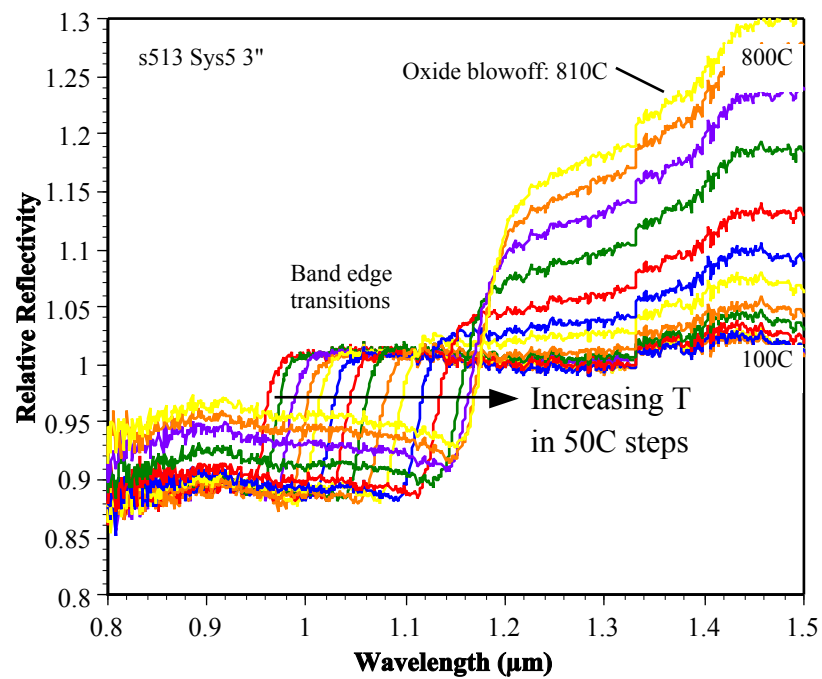


Figure 4.35: Specular reflection from semi-insulating GaAs vs. temperature. No filtering was necessary to see the band edge transition.

of the time required to scan the spectrometer, this measurement cannot be performed with wafer rotation enabled. Using an infrared CCD array in place of the InGaAs detector would allow measurement during rotation and growth.

The most significant limitation to bandgap thermometry is that it only works on semi-insulating wafers. Doped wafers, which are necessary for lasers, lack the distinct band edge of undoped wafers, due to bandgap renormalization and free carrier absorption over the range of wavelengths near the bandgap. It is still possible to extract the bandgap from n-type wafers, but the measured bandgap changes with dopant type and density, rendering the technique useless for establishing an absolute temperature reference. Efforts to combine bandgap thermometry, conventional pyrometry, oxide blowoff, and other techniques to produce accurate substrate temperatures are ongoing, and will be continued by future students.

The results of bandgap thermometry for a number of wafers are shown in Table 4.10.2 and plotted in several ways in Figure 4.36. Because we occasionally use old wafer holders for non-temperature-critical growths, sample s498 was mounted on a Varian wafer holder, with light spring pins and no sapphire backing plate, and is essentially a bare wafer in the chamber. The remaining samples were mounted on Veeco/Applied Epi Uniblock wafer holders with sapphire backing plates. The 2" wafers and the quarter-3" wafer were held in place with a molybdenum faceplate. The highest temperature in each plot represents the temperature at which the native oxide desorbed.

These are only preliminary measurements; a longer series of measurements, with pyrometry, will be taken by H. Bae. But from the preliminary results, it appears that, for the same real wafer temperature (i.e. same bandgap):

- For 3" wafers, System 4 reads 30–36°C hotter than System 5 at oxide blowoff temperatures, or 54–68°C at GaInNAs temperatures. In other words, if oxide blowoff occurs at 750°C in System 5, it will be approximately 780–786°C in System 4.
- For 2" wafers, System 4 reads 35–45°C hotter than System 5. (53–115°C for GaInNAs temperatures.)

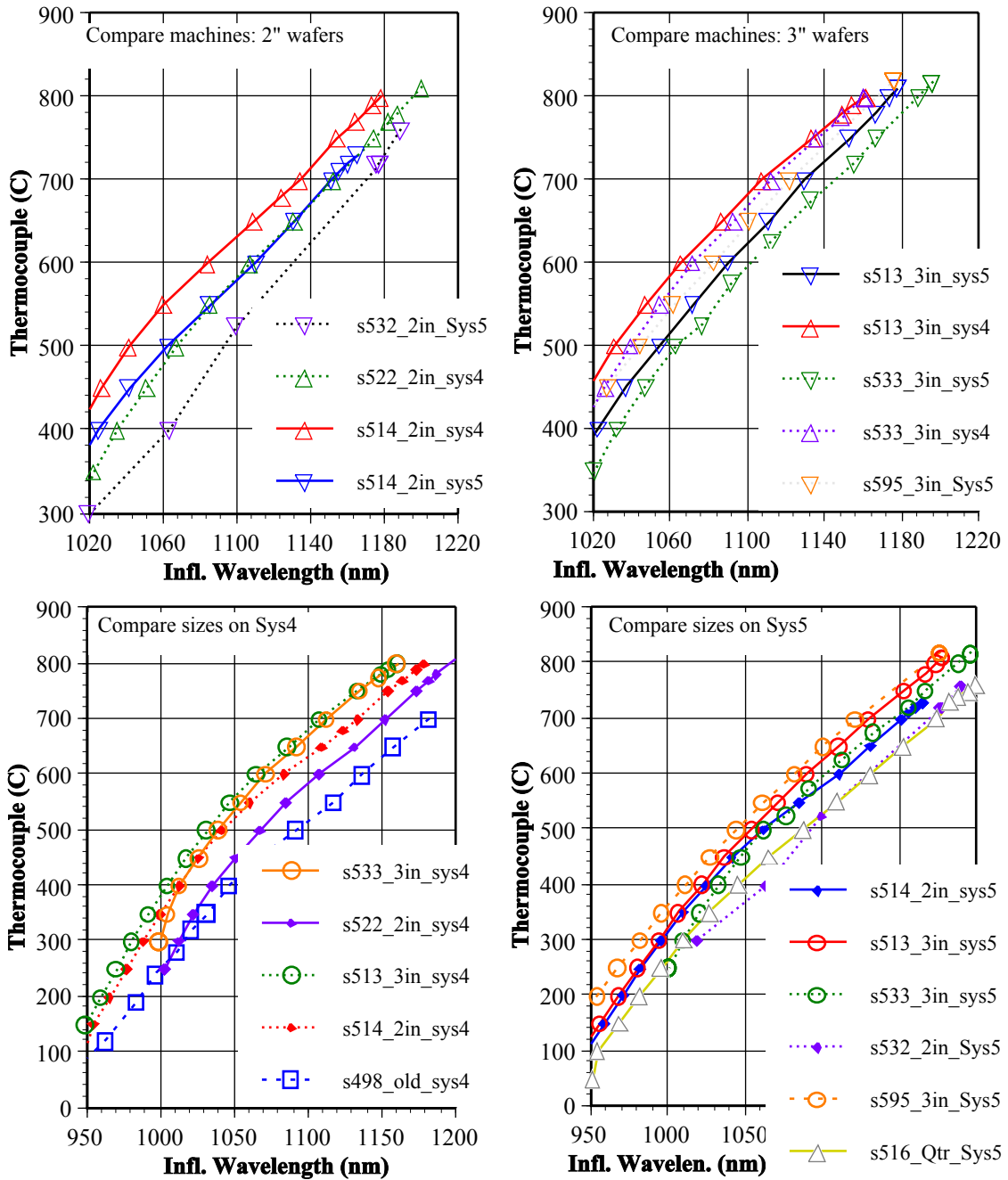


Figure 4.36: Bandgap thermometry (reflective pyrometry) results for semi-insulating GaAs. The System 4 thermocouple reads about 50C hotter than System 5 for the same actual bandgap or wafer temperature (top).

Table 4.1: Comparison of bandgap thermometry from various wafers and MBE chambers

(a) System 4

s498-Old		s514-2"		s522-2"		s513-3"		s533-3"	
TC (°C)	μ m	TC	μ m						
40	0.934	100	0.948	250	1.004	100	0.941	300	1.000
80	0.946	150	0.955	300	1.013	150	0.950	350	1.005
120	0.964	200	0.966	350	1.023	200	0.960	400	1.013
190	0.984	250	0.978	400	1.036	250	0.971	450	1.027
240	0.998	300	0.989	450	1.052	300	0.981	500	1.040
280	1.012	350	1.001	500	1.068	350	0.992	550	1.055
320	1.022	400	1.014	550	1.086	400	1.005	600	1.072
350	1.032	450	1.027	600	1.108	450	1.018	650	1.093
350	1.032	500	1.042	650	1.132	500	1.032	700	1.113
400	1.048	550	1.061	700	1.153	550	1.048	750	1.136
450	1.068	600	1.085	750	1.175	600	1.066	775	1.149
500	1.092	650	1.110	770	1.183	650	1.087	800	1.161
550	1.118	680	1.125	780	1.188	700	1.108		
600	1.138	700	1.135	811	1.201	750	1.134		
650	1.158	750	1.155			780	1.150		
700	1.182	770	1.165			790	1.155		
		790	1.174			800	1.162		

(b) System 5

s514-2"		s532-2"		s513-3"		s533-3"		s595-3"		s516-Qtr	
TC (°C)	μ m	TC	μ m								
50	0.938	300	1.020	100	0.944	250	1.001	150	0.941	100	0.955
100	0.947	400	1.064	150	0.957	300	1.010	200	0.955	150	0.969
150	0.960	525	1.100	200	0.969	350	1.021	250	0.968	200	0.982
200	0.972	719	1.178	250	0.981	400	1.033	300	0.983	250	0.996
250	0.983	720	1.176	300	0.995	450	1.048	350	0.997	300	1.011
300	0.997	720	1.178	350	1.007	525	1.077	400	1.012	350	1.028
350	1.011	760	1.190	400	1.023	575	1.092	450	1.028	400	1.046
400	1.026			450	1.037	625	1.113	500	1.045	450	1.066
450	1.042			500	1.055	675	1.133	550	1.062	500	1.088
500	1.063			550	1.072	720	1.156	600	1.083	550	1.110
550	1.086			600	1.090	750	1.167	650	1.101	600	1.131
600	1.111			650	1.111	800	1.189	700	1.122	650	1.153
650	1.132			700	1.130	817	1.196	820	1.176	700	1.174
700	1.152			750	1.153					730	1.183
710	1.156			780	1.167					740	1.188
720	1.161			800	1.174					750	1.195
730	1.166			810	1.178					762	1.200

- On System 4, 2" wafers read 36°C hotter than 3" wafers. (33°C for GaInNAs.)
- On System 5, 2" wafers read 48°C hotter than 3" wafers. (23°C for GaInNAs.)
- A quarter-3" wafer reads 92°C cooler than a full 3" wafer. (97°C for GaInNAs.)
- A 2" wafer reads 84°C cooler in an old wafer holder than in a Uniblock holder. (97°C for GaInNAs.)

The margin of error for these measurements may be as large as the variation in oxide blowoff temperatures (tens of degrees, Figure 4.34). These are intended only as a rough guideline.

One of the interesting possibilities with thermometry is the possibility of measuring the wafer temperature as the growth progresses. Bandgap thermometry is not well suited to measure wafer temperature for wafers that include a long-wavelength quantum well, because the quantum well absorbs infrared light. However, it is possible to show that the wafer temperature increases when the source shutters open. For example, the wafer temperature increased approximately 5°C when the Ga shutter opened (not shown).

The absorption of infrared light by GaInNAs quantum wells suggests that the wafer may be increasing in temperature as growth progresses. There is significant energy in the infrared that is below the bandgap of GaAs, but well within the absorption range of GaInNAs(Sb) QWs. (Note the bulge in optical emission from 1.2–1.5 μm , due to the wafer heater, at the higher temperatures in Figure 4.35, page 117.) To study whether bandgap thermometry could be used to investigate the change in wafer temperature as the growth progressed, a series of growths were made on the same wafer. The reflectivity spectrum of the wafer was taken after the GaAs buffer growth, and again after each quantum well. Unfortunately, as Figure 4.37 shows, there was no measurable difference change in the average wafer temperature with successive quantum wells, at least not within the noise of the measurement. Nevertheless, transmission electron microscopy (TEM) shows better quality material when the substrate is cooled by 5–8°C per QW.

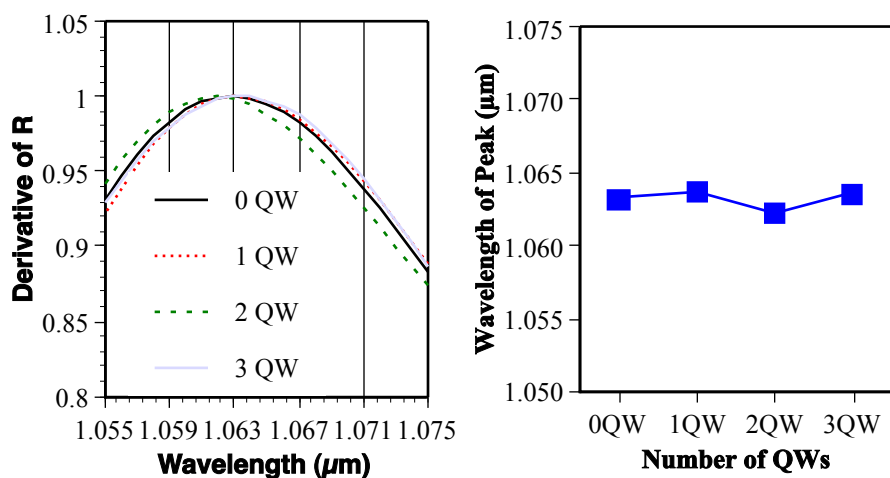


Figure 4.37: Bandgap thermometry vs. number of QWs.

The problems with measuring wafer temperature of doped (n-type) wafers, and of measuring the surface temperature during growth, both suggest that a surface-sensitive technique may be more successful. Spectroscopic ellipsometry has been used for measuring properties of thin films, but we have had no end of difficulty using the Hitachi ellipsometer in the Ginzton Labs for long wavelength measurements: the results of the layer simulation are controlled more by guesses at fitting parameters than by actual material properties. A related technique may be useful, however. Polarized light could be used to measure only reflected light near the Brewster condition, which would not be transmitted into the wafer, and the reflection would be almost entirely determined by the refractive index at the surface. However, refractive index changes very slowly with temperature, and measuring such small changes in refractive index is a challenging task.

4.11 High Quality Material at Low Temperatures

As mentioned in the previous section, dilute nitrides are grown at temperatures significantly lower than other GaAs-based materials. For example, AlAs is typically grown above 700°C, GaAs is grown at 550–600°C, and InGaAs is grown at 475–550°C.

GaNAs can be grown up to 450°C, although higher temperatures lead to phase segregation and loss of nitrogen. GaInNAs is usually grown at 380–425°C. The growth of GaInNAs at higher temperatures is believed to produce better material, if techniques can be developed to prevent phase segregation [2]. With the addition of antimony and the removal of plasma damage and oxygen contamination, we were able to grow at temperatures up to 460°C, but this is still fairly low. The primary consequence of low temperature growth is the inclusion of arsenic antisite defects (where arsenic sits on a gallium site in the crystal lattice). Arsenic can also be incorporated in interstitial sites. If excess arsenic is incorporated as antisites or interstitials, when the wafer is annealed, the arsenic precipitates out, forming clusters that lead to rapid nonradiative recombination, i.e. poor optical material.

To prevent the segregation of arsenic during or after growth, the arsenic overpressure should be reduced. Based on recent discussions with Kai Ma[214], a GaAs wafer was heated to the desired GaNAs growth temperature, and the arsenic and gallium shutters were opened to start growing plain GaAs. Surface roughness and reconstruction were monitored by RHEED as the arsenic flux was slowly decreased. The RHEED began to degrade with a V/III ratio of 3 to 4. GaInNAsSb photoluminescence samples were then grown with this lower arsenic flux during the low-temperature GaAs layers and GaNAs layers showed a 2x improvement in photoluminescence intensity. Lasers based on this technique are eagerly awaited. It should be noted that this reduction in arsenic overpressure was a recent modification to our growth technique, and had not been developed in time for the VCSELs or edge emitting lasers that follow.

It should be noted that Infineon has reported high quality GaInNAs grown near the stoichiometric limit, with the V/III ratio just over 1.0 [23]. However, growing near the stoichiometric limit leads to a number of instabilities in the growth, such as a strong dependence on temperature and Group V flux, and the necessity of growing at even lower temperatures. We have found better results with higher temperatures and higher arsenic fluxes during the GaInNAs(Sb) layers. Because indium has a high surface mobility at low temperatures, GaInNAs is more similar to InGaAs than to GaNAs, and does not need lower arsenic fluxes.

4.12 Care and Feeding of an MBE Plasma Source

(The subtle difficulties of growing with an RF source)

The introduction of a high-density plasma source into a UHV system such as MBE is not without its risks and difficulties. Many of the major issues have been covered previously in this chapter and in Chapter 3, such as ion damage, plasma aperture, etc. There are also a number of subtle factors which are often overlooked, but which have proven to be just as important for making a stable plasma and for growing high-quality dilute nitrides. These factors will be discussed in more detail in this section. They include plasma instability, noise in the mass flow controller, RF leaks that affect other instruments, sparks and shocks, oxygen contamination, leaky feedthroughs, arsenic contamination of the PBN crucible, background hydrogen in the chamber, and the effect of the plasma on ion pumps, Knudsen cells (particularly aluminum), and all hot filaments in the chamber. These problems can lead to machine contamination, plasma instability, poor growth, atmospheric leaks, and destruction of MBE components.

At the beginning of this project, the plasma source was notoriously unstable. In fact, the plasma could be extinguished by the mere act of a person walking past the MBE machine, which would ruin the growth. This also had the unfortunate effect of preventing new students (including the author) from learning MBE from the prior generation, since they were not permitted in the same room while the plasma was running. This plasma instability was considered by the prior generation of students to be normal and unavoidable, and they graduated without solving it,³ although they had tried wrapping several cables with loose copper mesh. The curious nature of the interaction—coupling to a human body—led this author to suspect that stray RF from the plasma was being coupled as noise into the mass flow controller (MFC). By monitoring the electrical output from the MFC valve controller with an oscilloscope, it was possible to see that the valve position was swinging wildly, and that in fact there was a large RF component being picked up by the pressure sensor. This coupling indeed changed when one walked anywhere near the source. The manufacturer of the

³And, for that matter, without teaching the new students how the plasma worked.

MFC (Unit Instruments) was contacted, and they reported that the control circuit had been poorly designed, with a shared ground between the digital components and the analog components.⁴ The MFC was rebuilt properly, which reduced the RF coupling, and the ribbon cable from the MFC controller was replaced with a shielded cable. The source of all of the RF noise was discovered to be poor shielding in the RF matching network. The stray RF was clearly apparent with an unconnected oscilloscope probe, and it also caused noise in other nearby instruments. Conductive tape was used to cover all of the seams in the matching network shielding, and all openings were either plugged or covered with mesh or perforated aluminum. The level of RF in the room dropped dramatically. An oscilloscope probe still shows “hot” spots near the matching network, particularly near the corners and especially the main feedthrough opening.

Mass flow controllers are not well suited for the low flow rates (0.25–1scm) used for dilute nitrogen plasmas. We are operating near the lower end of the permissible range for this MFC, even though it is the lowest-flow model known to be on the market. Other groups use a Baratron gauge to control a leak valve in a pressure-regulated feedback loop. This may be a consideration for future designs.

Another source of instability was the opening and closing of the shutter in front of the nitrogen cell. Since the shutter is about 1cm from the end of the cell, it seemed unlikely that it could be causing a change in pressure in the cell. However, the shutter was made from a solid sheet of metal (tantalum), and was close enough that it could be inductively coupled to the RF coils. The reflected RF power would change by 1–2W when the shutter was operated, which further suggested parasitic RF coupling. It should be noted that the use of a gate valve in front of the plasma cell can have the same effect, and at least one group has reported plasma instability from use of the gate valve [165]. The troublesome tantalum shutter was replaced with a ceramic PBN shutter (pyrolytic boron nitride), and the shutter instability was never seen again.

Several problems with the physical design of the matching network also became apparent. The “hot” RF feedthrough is connected to the matching capacitors using

⁴A common undergraduate mistake. This author highly recommends Henry Ott’s very readable book on noise reduction [215], in order to prevent such rudimentary errors in the lab. It is also helpful for understanding the RF leakage problem, which has not been completely solved.

a copper clamp, which oxidizes periodically. This leads to a high level of reflected power back to the RF power supply, and makes the plasma more difficult to light and less stable when lit. Twinkle brand copper cleaner was found to be excellent for cleaning this copper connection, but this did not prevent the problem from recurring. It is strongly recommended that the junction be protected by some sort of high temperature, conductive paste that would prevent this oxidation. Also, it had previously been reported that the tunable air capacitor used in the matching network was a problem due to exposure to dust or humidity [59], but this has not seemed to be the case; cleaning the capacitor had no effect on plasma stability or RF matching. On the other hand, the fixed shunt capacitors may be subject to breakdown. They get very hot despite partial water cooling. This could also explain part of the persistent change in plasma condition with time.

The same long-term change in plasma operating condition might also be caused in part by the plasma etching larger holes in the cell aperture. We do not believe the plasma significantly etches PBN, since we do not see boron in SIMS measurements of our films, but a slow etch might still be possible, and even a slight widening of the aperture holes would significantly reduce the pressure in the cell, as discussed on page 64.

In addition to the copper oxidation mentioned previously, the feedthrough itself gets very hot during operation of the plasma. When RF power is applied, but before the plasma is lit, the feedthrough can reach temperatures approaching 200°C. Rapid thermal cycling has periodically cracked the ceramic-metal junction in the feedthrough, causing a small leak into the MBE chamber. This leak is generally only noticeable at first because the beam flux gauge reads a slightly higher pressure, but only when facing the source flange. In other words, it creates a highly directional gas source, similar to a leak on the heated viewport (which we have also had). At the moment, both the heated viewport and the RF feedthrough have been patched with Vacseal, applied in liquid form with a brush. The Vacseal is naturally baked due to the high temperatures of the feedthrough and the viewport, but outgassing is still suspected. These parts should be replaced the next time the MBE machine is opened. To prevent leaks due to rapid thermal cycling of the feedthrough, the

RF power supply was connected to computer control, and a ramping procedure was established as follows. Before a growth, the RF is ramped in 5 Watt steps every 30 seconds up to 150–165W. This heats the feedthrough up to its final temperature of 90–95°C. When it is time to light the plasma, the gas flow is rapidly turned on (valve to the turbo pump closed), and the RF is rapidly switched to 300W. Although this is twice as much RF power, more of it is dissipated in the cell when the plasma is lit, so the feedthrough stays at roughly the same temperature. The cooldown procedure is the reverse: the RF is turned to 150W and the gas flow is turned off (the turbo valve is opened), rapidly extinguishing the plasma while maintaining the feedthrough at 90–100°C. If no more growths are to be performed, the RF is ramped down at 5W/minute.

Another problem with the feedthrough is its proximity to neighboring metal. Recall from Section 4.5 that the voltage at the feedthrough can be on the order of 1000V or more. It is possible for the electric fields to be so high that they cause an arc from the feedthrough to the walls of the matching network or the plasma cell. This has been minimized by removing all sharp metal points nearby, and by reshaping the perforated aluminum cover that we used to shield the hole in the matching network. We also had to remove the cooling water line that we had wrapped around the feedthrough to avoid the heat problems above. Users are cautioned to avoid reaching near the feedthrough while the RF is on—especially with any metal object—in order to avoid a nasty burn, or worse. The same caution applies if the cover is removed from the matching network.

One of the difficulties in growing dilute nitrides is that the operating parameters published in the literature are virtually useless, because every plasma cell appears to operate differently. This has led to some controversy between groups over the proper way to grow material, with the eventual conclusion that each group needs to separately optimize their own process. Although this ad-hoc approach has been necessary in the past, newer methods of characterizing the cell such as a simulation of magnetic field intensity within the coil and measurement of gas pressure within the crucible [170] suggest that comparisons may soon be possible between groups. This would be especially useful for people setting up a new MBE machine. As mentioned

in Section 4.3, the gas pressure in our plasma cell is still unknown, because of the uncertainty in the conductances of the aperture and the leak valve, but appears to be under 0.3 Torr.

The plasma generates many excited species that may react with various components inside the MBE chamber. Energetic ions have been mentioned in previous chapters, and atomic nitrogen is extremely reactive. These can and do react with hot metal, whether molybdenum faceplates, tantalum heaters in the various Group III cells, or the aluminum itself in the aluminum cell. The latter reaction may have contributed to the failure of our aluminum cell after a power failure, since the aluminum looked quite strange, and AlN may have prevented flexing of the aluminum as it cooled, causing stress to the crucible. It is known that nitrogen can promote the growth of AlN at the lip of the aluminum cell, promoting the creep of source material, and probably accelerating crucible failure [150]. Others have reported privately that their substrate heater crumbled upon opening the chamber, after repeated exposure to the plasma, requiring repairs.

Also, although ion pumps should last decades at UHV pressures, the ion pump in System 5 ceased to be functional after it had been mistakenly left open to the chamber for several growths. Ion pumps work by ionizing any gases and accelerating the ions deep into a thick plate of titanium, where they are trapped. The pump controller works correctly, but we believe the surface of the Ti plates has been coated with TiN. TiN is used in semiconductor processing as a robust mask against ion implantation, so its creation inside the ion pump would prevent ions from being buried.

In addition, when nitrogen atoms recombine to form N_2 at the chamber walls, 15.8eV of energy is released as heat. This can desorb contaminants from the cryoshroud, contaminating the growth. This is probably the leading cause for the improvement of material early during a growth campaign, as the contaminants such as CO_2 , O_2 , and H_2O get progressively evaporated from the front surface of the cryoshroud and deposited either in the cryopump or onto other parts of the cryoshroud farther from the plasma. However, the energy of formation of N_2 is sufficient to desorb not only the N_2 but neighboring molecules as well, even from the first stage of the cryopump. These molecules can then recontaminate the chamber. Furthermore,

if the nitrogen bypasses the first stage (77K) of the cryopump this way, it can evaporate hydrogen from the cold stage (8K). Similarly, if the high gas load overwhelms the first stage of the cryopump, the nitrogen gas can then reach the cold stage, where it displaces adsorbed hydrogen gas. Hydrogen is known to have strong effects on dilute nitride growth, and the uncontrolled dumping of hydrogen from the cryopump can lead to unpredictable effects in the growth. This background hydrogen is only detectable with a mass spectrometer (or residual gas analyzer, RGA), but the RGA is rarely operated when the plasma is running, because the high chamber pressure ($\sim 10^{-4}$ Torr) is destructive to the hot filament in the RGA. The excess hydrogen can also contribute to hydrogen embrittlement of hot filaments in the machine. There does not seem to be a good solution to this problem other than to regenerate the cryopump and occasionally monitor the H_2 pressure when the plasma is ignited, even though this shortens the life of the RGA.

One problem with using an older style of nitrogen plasma cell, which was designed for GaN growth, in a GaAs-based MBE chamber is that arsenic gets everywhere. The original SVT Associates plasma cell had several large holes in the shielding through which arsenic could enter and deposit on the outside of the PBN crucible. This led to progressive impairment of the plasma over the course of a growth campaign: the arsenic deposits were so thick that they formed a metallic layer around the crucible, shielding the gas inside from the RF coils. (The conductance of the deposit was high enough to read with an ohmmeter: just a few $k\Omega$ across several cm.) The plasma cell had to be disassembled and cleaned to remove this arsenic. The cell was hand-carried to SVT for discussion about this and other forms of cell instability. The cell was modified by SVT to reduce the arsenic exposure, and also had a new matching network and 4-hole aperture installed at this point.

Finally, sometimes the plasma simply does not light even with high flow and high power. This occurs most frequently after the cell has been rebuilt, although the exact reason remains unknown. To start a reluctant plasma, a number of options are available. They are listed here in increasing order of extremity.

- Verify valve to turbo pump is closed.

- Increase flow rate, up to 100%.
- Turn mass flow controller to Purge mode very briefly.
- Increase power, up to 350W, or as high as 500W for very brief periods (a few seconds). Bad for coil; tends to soften and deform the copper windings.
- Turn on the beam flux gauge and point it toward the plasma cell, in order to provide a source of electrons/ions to seed the plasma. Bad for the ion gauge filament. A large positive bias applied to both deflection plates may help accelerate electrons toward the plasma cell, but this has not been tried.
- Turn off the pumps and let the pressure rise in the growth chamber. Bad for cells: cool cells to 100–200°C beforehand; hopefully you have not melted the aluminum at this point.
- Apply a Tesla coil to one of the feedthroughs. Bad for all the instruments in the lab.⁵

Although these all sound like serious problems for MBE, it should be noted that the situation for MOCVD is worse. To date, no lasers have been reported from MOCVD growth beyond 1.4 μ m. The growth of nitrogen-containing material requires high temperatures to crack the appropriate precursors (e.g. ammonia or hydrogen azide) on the surface, but high temperature leads to phase segregation and poor growth. Also, hydrogen from precursor gases leads to problems with material quality. Finally, carbon from precursor gases leads to a number of defects [57]. The carbon and hydrogen contamination do not affect MBE growth (except as mentioned above), and SIMS measurements show C and H to be below the noise floor, approximately $2 \times 10^{16}/\text{cm}^3$.

A number of other difficulties that were solved jointly with Vincent Gambin have been addressed in his thesis [59], and will not be repeated here. Some of the major contributions of coworkers (Seth Bank and Homan Yuen) include the removal of trace oxygen from the nitrogen line and backing pump, and the discovery that running the

⁵It also ignited the plasma outside the crucible, but that is another story.

cell at the edge of stability produces strong variations in material quality. The oxygen was a particularly difficult problem to track down. Replacing the parts-per-billion filter on the nitrogen line only marginally reduced the oxygen content in our films, as measured by SIMS. Eventually a small leak on the backing pump was discovered. The pressure at the backing pump dropped from 5 mTorr to below 10^{-5} Torr. Assuming a compression ratio of 10^4 in the turbo pump, the 5 mTorr at the backing pump would translate to a partial pressure of oxygen in the nitrogen line on the order of 10^{-7} Torr, which is many orders of magnitude higher than UHV background contamination. Oxygen contamination (Section 3.6) is believed to be a strong component of many groups' GaInNAs growths [141].

Finally, future growers should be warned that the use of antimony is not a panacea for bad material. Antimony does improve bad material, but by doing so, it also obscures a number of variables that must be investigated together, as a whole. For example, raising the wafer temperature may cause worse photoluminescence, but is that because the antimony has evaporated from the surface, or the antimony still incorporates and contributes to strain relaxation, or because strain relaxation was inevitable? It is important to fully optimize the growth of GaInNAs without antimony, solving problems with contamination, plasma conditions, growth kinetics, etc., before adding antimony to the confusion.

4.13 Summary

4.13.1 Major Contributions

This chapter discussed the best operating conditions for a nitrogen plasma cell in an MBE growth chamber. The major thrust of this work was the identification and removal of various causes of damage to the semiconductor during growth of dilute nitrides. This was accomplished by three major techniques. First, the actual ion output from the plasma cell was measured using a novel Langmuir probe, allowing the cell operating parameters to be adjusted in real time for minimal ion output. Low

voltages on ion deflection plates were found to be adequate and preferable for removing remaining ions from the plasma beam. Second, an arsenic capping technique was developed to minimize the exposure of the wafer to the plasma during the initial ignition of the plasma. The arsenic cap also protects the wafer during transfers between machines, and allows unlimited time for the plasma to be stabilized before growth. Finally, reflective bandgap thermometry was shown to be adequate for measuring the relative temperature of semi-insulating GaAs wafers. Temperature measurements are ongoing, and solid calibrations for even n-doped wafers are expected in the future.

The major results of this work were the identification of ion damage, plasma ignition damage, and nitridation before the QW as the major sources of nonradiative recombination in our material. By comparing the effects of each of these types of damage, it was found that damage contributes to the redshift of light emitted from GaInNAs(Sb), shifting the wavelength by as much as 20nm. This calls into question many of the materials studies in prior published reports, including band offsets and effective masses. These studies are being repeated, and will be reported by others in the group [78, 79, 216, 217, 218].

The significant reduction in plasma damage also led directly to record long wavelength, low threshold lasers. These will be reported in the following chapter.

4.13.2 Minor contributions

Strong contributions were also made to the following categories (with coworkers noted in parentheses): Replaced cell aperture with fewer/smaller holes (with V. Gambin). Replaced the MFC with an RF-shielded version (with V. Gambin). Improved the shielding of the matching network to avoid RF interference with other devices (with V. Gambin). Developed new growth techniques: before loading a wafer for the first growth of the day, pre-light the plasma and operate it for at least 20 minutes, then extinguish it and load the wafer. Keep the RF at half power to maintain constant cell temperature between growths (ramping: V. Gambin). Keep the net power to the cell (forward power minus reflected power) constant, either manually adjusting forward power or configuring an RF supply to keep constant load power. Demonstrated

why one should not change flow or RF power to change the nitrogen concentration. Minimized the number of non-plasma growths (H. Yuen) and had the cell modified to limit arsenic contamination. If the cell operating condition changes, operate the plasma for several hours to burn off arsenic deposits. Standardized the plasma ignition sequence. Demonstrated that source flux measurements taken with the RF on were inaccurate. Replaced the metal shutter on the cell with an insulator to avoid cell instability when shutter opened. Demonstrated that if the plasma dies during a growth, the growth is not recoverable: plasma ignition (and re-ignition) causes significant and unpredictable damage. However, after making the improvements mentioned here, although the plasma may still be difficult to ignite at times, it has yet to die during a growth.

Chapter 5

Long Wavelength VCSEL Design & Fabrication

5.1 GaInNAs Laser Properties

Previous chapters have discussed the inherent properties of GaInNAs(Sb), and how to grow material with very high optical quality. This chapter will describe the actual implementation of GaInNAs(Sb) in several types of lasers. The properties of GaInNAs(Sb) that are useful for lasers will be discussed first. This will be followed by a summary of edge emitting lasers, which were used as a proof of principle and to characterize the material in preparation for growing VCSELs. Finally, the growth and processing of VCSELs will be presented, including the first demonstration of VCSELs on GaAs at a wavelength of $1.46\mu\text{m}$. The chapter concludes with measurements from these VCSELs, and discusses the prospects for future GaInNAs(Sb) VCSELs.

As discussed in Section 2.7, a laser requires gain and feedback. The gain in a material is a strong function of wavelength, with peak gain occurring at the wavelength corresponding to roughly the bandgap of the material (plus quantum confinement). There is usually an additional redshift of 10–15nm due to heating (lattice expansion), bandgap renormalization from the large density of carriers, and dopant minibands, although these are partially offset by thermal broadening of the carrier distributions,

band filling, and in bulk material, the small density of states at the band edge. GaInNAs has a large gain bandwidth, with semiconductor optical amplifiers demonstrated with over 50nm of 3dB bandwidth [156] and optically-pumped VCSELs operating over a 360°K range of temperatures [124]. This large bandwidth may be due in part to material inhomogeneity, analogous to the broad gain spectrum from random distribution of quantum dots.

5.2 Edge Emitting lasers

5.2.1 Growth of Edge Emitting Lasers

Edge emitting lasers are very useful for research devices, particularly when developing a new material system such as GaInNAs. This is because the epitaxial growth of an edge emitting laser is simple, with no critical dimensions and only 3–5 layers. Also, light travels a relatively long distance (hundreds of μm) through the wafer before reaching the end mirrors, which gives significant gain. This is in contrast to VCSELs, for which the light travels through less than $0.025\mu\text{m}$ of gain medium per pass through the cavity. Detailed measurements and results from the edge emitting lasers will be provided by S. Bank and L. Goddard, who performed the design and characterization, respectively [77, 78]. The detailed results will not be repeated here, but the growth and characterization of the VCSELs and edge emitting lasers were similar, and these will be reviewed below. Also, edge emitting lasers are important for extracting several critical parameters for VCSEL design, such as the gain coefficient and wavelength.

The edge emitting lasers were grown by plasma-assisted, solid-source MBE, as described in Sections 2.8. n-type, (100)-orientation GaAs wafers were baked under UHV to remove surface water and hydrocarbons. The bottom AlGaAs cladding was grown in System 4, which is optimized for AlGaAs growth. The bottom, n-doped cladding consisted of a 300nm GaAs buffer and 900nm $\text{Al}_{0.33}\text{Ga}_{0.67}\text{As}$, both doped with silicon at nominally $3 \times 10^{18}/\text{cm}^3$, followed by another 900nm of AlGaAs doped at only $7 \times 10^{17}/\text{cm}^3$ to reduce free carrier losses. The GaAs waveguide core was then

grown, stopping 20nm before the QW. An arsenic pressure of 15 times the Group III growth rate was used throughout these layers. The AlGaAs was grown 20°C above the oxide desorption temperature, or about 600°C. The wafer was then cooled to 10°C under an arsenic overpressure in order to deposit a thick arsenic cap, as discussed in Section 4.8.

Because the nitride MBE system did not have enough ports for multiple AlGaAs compositions, the AlGaAs layers were grown in a separate MBE machine from the nitride layers. After capping, the wafer was then transferred under UHV to System 5, our dilute nitride/antimonide machine. Reactive nitrogen was supplied by an inductively coupled, RF nitrogen plasma cell, with 300W of forward power and 0.5scm of ultra-filtered N₂. Gallium and indium sources were both Veeco SUMO cells with dual zone heating, as discussed in Section 5.5. Antimony was provided by an unvalved cracker, with the cracker temperature at 850°C, sufficient to crack all of the antimony into monomeric Sb₁. The beam equivalent pressure of antimony was $1 \times 10^{-7} \pm 5\%$ Torr, producing 2.7% Sb in the quantum well. Arsenic was provided by a valved cracker at 850°C, which supplied mostly As₂. The plasma was ignited and stabilized with an arsenic overpressure and with the arsenic cap still on the wafer. The wafer was then ramped quickly to GaAs growth temperature, the gallium shutter opened, and the wafer was cooled for GaNAs growth, all under 15x arsenic overpressure. (Recall from Section 4.11 that the GaNAs should be grown with V/III ratio of 3–4 due to the low growth temperature [161].) Once the gallium shutter was opened, 200nm of non-intentionally-doped GaAs was grown for the bottom waveguide. While this GaAs layer was being grown, the wafer was cooled and stabilized at 455°C for the dilute nitride layers. The quantum well consisted of 22nm of GaN_{0.025}As_{0.975} on either side of a 7.5nm Ga_{0.62}In_{0.38}N_{0.023}As_{0.95}Sb_{0.027} well. The GaNAs and GaInNAsSb were grown at 455°C with 15x and 20x arsenic overpressures, respectively. Another 200nm of undoped GaAs was grown at oxide blowoff temperature, then the wafer was cooled and arsenic-capped for transfer back to System 4 for the top AlGaAs cladding. The top cladding was doped p-type using carbon tetrabromide, at $5 \times 10^{17}/\text{cm}^3$ and $3 \times 10^{18}/\text{cm}^3$, with a 5nm GaAs contact layer doped at approximately $1 \times 10^{20}/\text{cm}^3$.

After growth, the wafer was unloaded, cleaved into four quarters, and annealed

under a GaAs proximity cap wafer at 740–800°C. p-type, Ti/Pt/Au ohmic contacts were patterned on top using a lift-off process, as discussed in Section 5.7.1. The contact metal provided the resist for a self-aligned dry etch, which defined ridge waveguides on each sample. The dry etch was performed in the PlasmaQuest, as in Section 5.7.2. The dry etch stopped just before the top GaAs waveguide. For ease in cleaving into laser bars, the samples were thinned to 120 μm by Sarah Zhou at Santur Corp. Au/Ge/Ni/Au was evaporated on the back side for the n-contact, and the samples were annealed at 400°C for 30 seconds to make ohmic contacts. The lasers were then cleaved to various lengths. High-reflection (HR) coatings were applied to one facet for some studies [77], but the devices reported here simply used the cleaved semiconductor facets for mirrors.

5.2.2 Edge Emitting Laser Results

The edge emitting lasers were soldered to a copper block using a low temperature, InSb solder. The copper block was cooled with a thermoelectric cooler controlled by an ILX Lightwave model 3744B laser diode controller. The lasers were driven by an ILX Lightwave model LDP-3840 current source in pulsed mode, or the ILX 3744B for continuous wave (CW) operation. Labview software for data collection was written by L. Goddard, who also made most of the measurements.

The longer wavelengths were reachable by heating the laser, either by an external temperature controller and thermoelectric cooler, or by operating the laser uncooled. The wavelength shifted by 0.58nm/°C, comparable with InGaAs lasers. The L-I curve is shown at the left side of Figure 5.1. For a 20 μm ×2450 μm laser, the CW threshold current density was 1.04kA/cm². This has since been reduced to under 600A/cm², or 450A/cm² in pulsed mode. The right side of Figure 5.1 shows the spectrum from the laser at room temperature, with peak lasing at 1.498 μm .

Continuous-wave (CW) lasing was achieved at a wavelength of 1490–1520nm, much longer than any previously reported CW laser on GaAs at room temperature [21]. Figure 5.2 shows a comparison with other published reports at the time. The lowest thresholds were achieved by under-annealing the lasers, since the growth

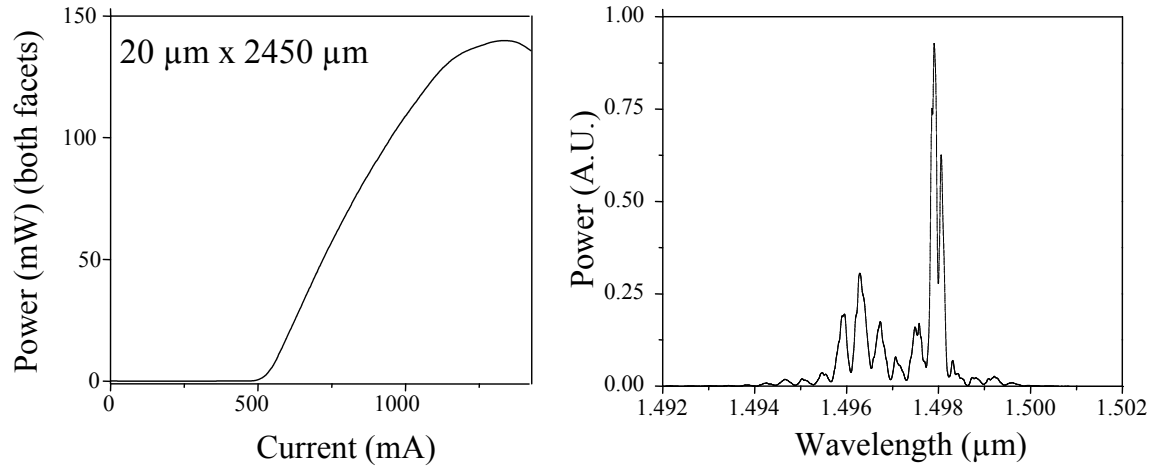


Figure 5.1: L-I curve and lasing emission spectrum for GaInNAsSb edge emitting laser. (Plots courtesy S. Bank.)

of the top AlGaAs cladding, approximately 1 hour at 580°C, partially anneals the GaInNAsSb. Because these lasers were mounted epitaxial-side up, the TEC was not very efficient at cooling the laser. Better results are expected by mounting the lasers epi-side down on an aluminum nitride or diamond heat spreader.

The gain of the laser as a function of current and wavelength are shown in Figure 5.3. This shows the onset of lasing (the point at which gain exceeds loss, including mirror loss) at about 0.8kA/cm², and a gain of over 1400/cm at a threshold current density of 2.0kA/cm², 2.5× threshold. The wavelength, gain, and threshold current density are important design parameters for the VCSELs, as will be described in Section 5.4.

To find the optimal mirror structure for VCSELs based on these edge emitters, we begin with the total current supplied to the laser above threshold:[40]

$$I = J_v A L_a + I_P + I_P \alpha_i L / \ln(1/R), \quad I_P \equiv \frac{q P_o}{h \nu \eta_i F}, \quad (5.1)$$

where P_o is power out, I_p is injected current, J_v is threshold current per unit volume, F is the fraction of total light output that comes from the output facet (=1 if only one exit), α_i is the internal cavity loss (excluding mirrors) per unit length, L is the cavity length, and $R = r_1 r_2$ is the combined reflectivity of the two mirrors. The first

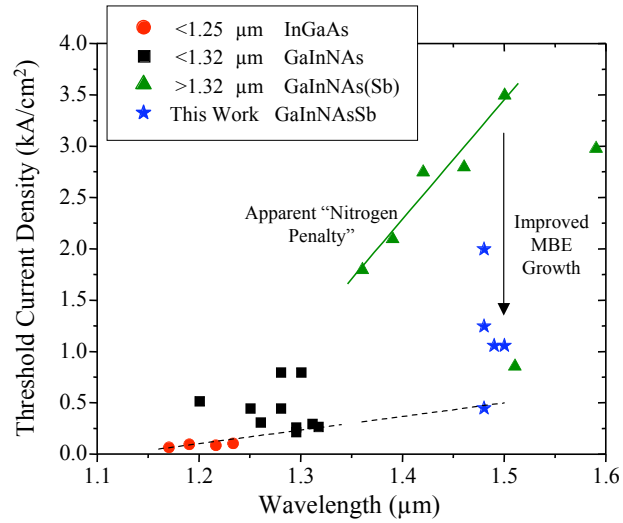


Figure 5.2: Laser threshold current density vs. wavelength for long-wavelength lasers on GaAs. (Plot courtesy S. Bank.)

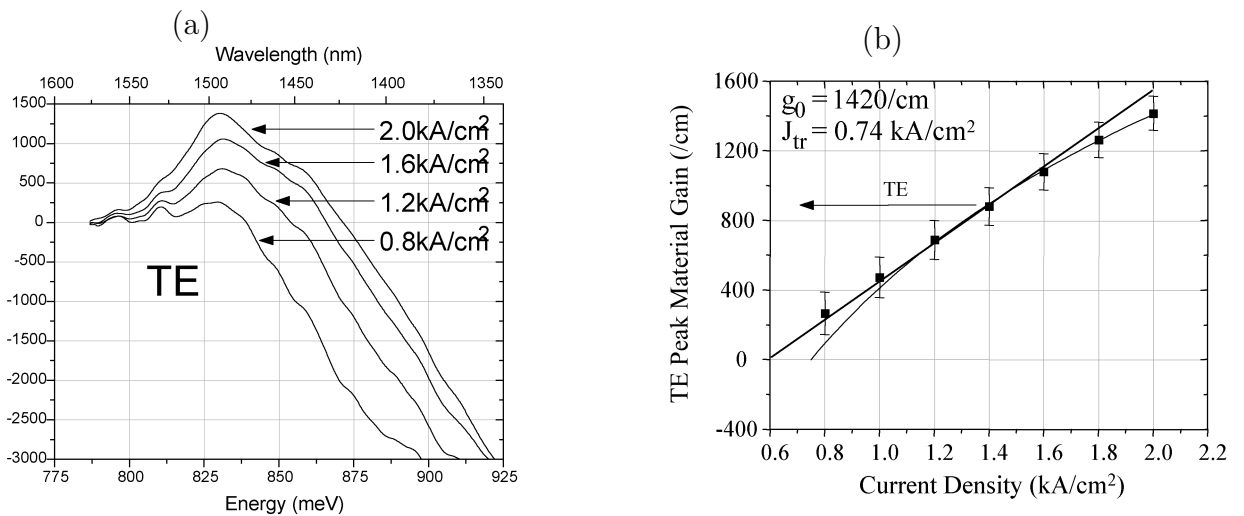


Figure 5.3: (a) Edge emitting laser gain spectrum vs. wavelength. (b) Gain vs. current. (Plots by L. Goddard.)

term represents the current that is required to drive the material to transparency (inversion) and overcome scattering and mirror loss. The second term represents the amount of current that actually gets injected into the quantum well, rather than carriers that bypass it by some leakage path or undergo ballistic transport over the top of the well and recombine on the other side. The injected current is what contributes to lasing. The third term includes the effect of cavity losses, because some fraction of the current that does get injected to the quantum well is lost to optical scattering, etc. Equation 5.1 can be rewritten as follows:

$$I = \left\{ \left(\frac{J_v}{g} \frac{A}{\Gamma_{\text{enh}} \Gamma_{xy}} \ln\left(\frac{1}{R}\right) + I_p \right) \right\} \left(1 + \frac{\alpha_i L}{\ln 1/R} \right) \quad (5.2)$$

Γ_{xy} is the overlap between the optical mode and the electrically-pumped gain region. It is fairly close to 1 for oxide-confined VCSELs, but must be calculated for proton-implanted VCSELs, which have a much larger optical mode. Γ_{enh} is the standing wave enhancement factor, and represents the fact the standing electric field at certain places in a folded cavity can be up to twice as large as a ring cavity, due to constructive interference. If a very narrow quantum well is placed at the peak of the standing wave, $\Gamma_{\text{enh}} = 2$, otherwise it must be calculated from

$$\Gamma_{\text{enh}} = 1 + \sin(\beta La) / \beta La \quad (5.3)$$

where βLa is the width of the overlap between the QW and the standing wave, measured in wavelengths times π . For multiple quantum well VCSELs, an equivalent βLa must be calculated, since the quantum wells are distributed at different physical locations within the standing wave.

By taking the derivative of Eqn. 5.2 with respect to some variable and setting it to zero, we can minimize the current with respect to that variable. The two parameters that are most relevant to VCSEL design are the optimal number of quantum wells, and the ideal reflectance of the mirrors, i.e. the thickness of the DBR mirrors.

$$\# \text{ wells}|_{\text{opt}} = \frac{\alpha_i L + \ln 1/R}{\Gamma_{\text{enh}} \Gamma_{xy} g_{\text{opt}} L} \quad (5.4)$$

$$R|_{\text{opt}} = \exp \left\{ - \sqrt{I_p \alpha_i L \frac{\Gamma_{\text{enh}} \Gamma_{xy}}{A} / \frac{J_v}{g_{\text{min}}}} \right\} \quad (5.5)$$

The lifetime of the edge emitting lasers was less than 100 hours, sometimes much less. But this is not surprising given the uncoated facets and sidewalls of the device. AlGaAs oxidizes progressively in air, particularly with heat, and this degrades the laser over time. We believe that the lifetime issue is a matter of processing rather than fundamental materials limitations. Several groups have demonstrated thousand-plus hours of laser operation under severe conditions [67]. Lasers with 8500 hours of operation were presented by Aoki [219], and lasers with projected lifetimes of 148 years mean time between failure have also recently been reported by Optical Communication Products (OCP) [138].

5.3 VCSELS: Vertical Cavity Surface Emitting Lasers

Unlike edge emitting lasers, which by definition emit light in the plane of the semiconductor, vertical-cavity surface-emitting lasers (VCSELS) emit light vertically, as shown in Figure 5.4. The VCSEL is constructed by placing one or more light emitting quantum wells between two distributed Bragg reflectors (DBRs) which serve as the laser mirrors. Each DBR is made from repeated pairs of alternating materials, such as GaAs and AlAs. Light circulates vertically through the cavity and is amplified with each pass through the QW. Because each QW is so thin, typically just 5-10nm, the mirrors must be very highly reflective so the light passes through the QWs many times before escaping through a mirror as the laser emission. The top DBR in a top emitting VCSEL, such as in the figure, will often have a reflectivity of 99.5% or better. The bottom DBR may have a nominal reflectivity of 99.99%, where the loss is mostly due to free carrier absorption, rather than than transmission.

Vertical cavity surface emitting lasers (VCSELS) are are of great commercial interest for optical networking and dense, fast interconnects. Vertical emission off the chip allows the VCSELS to be integrated directly with conventional GaAs or InP electronic circuits, or to be bonded to silicon for direct integration with CMOS, without losing

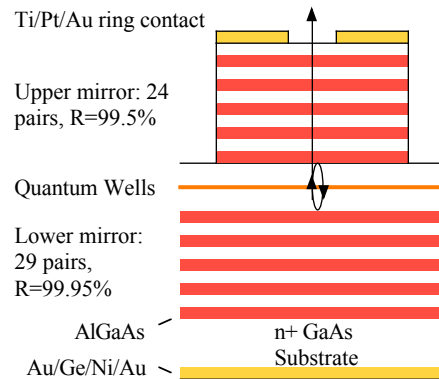


Figure 5.4: Simplified structure of a top-emitting VCSEL. Light is emitted through the hole in top ring contact.

significant real estate on the chip. Typical VCSEL mesas range from $8\text{-}30\mu\text{m}$ in diameter. Vertical emission allows all of the devices on a wafer to be tested before being packaged, which greatly reduces manufacturing overhead costs. Vertical emission also allows simpler alignment into either polymer waveguides on a circuitboard, or into optical fiber for metro-area and campus-area networks. VCSELs emit a circular beam, which greatly simplifies the coupling into optical fiber, since no cylindrical lenses are required to reshape the beam. And VCSELs can be grown in 1D and 2D arrays, which may someday prove to be important for high-density data transfer, particularly for chip-to-chip interconnects. Furthermore, VCSELs have a very small cavity volume, typically a few dozen cubic microns, so they can often operate with threshold currents less than 1mA , making them more compatible with CMOS. The distributed Bragg reflector (DBR) mirrors offer greater immunity to feedback and a higher degree of temperature stability compared to edge emitting lasers. In contrast to edge emitting lasers, which are easy to grow but difficult to test or package, VCSELs are easy to test and package, but they can be quite difficult to grow, especially with a new material system.

What VCSELs have particularly lacked, until recently, was the ability to emit light at an appropriate wavelength for fiber communication. The best mirrors (distributed Bragg reflectors, or DBRs) could only be grown on GaAs substrates. Even when dielectric or air gap DBRs were available, GaAs substrates and GaAs/AlGaAs DBRs

were generally preferred for VCSELs because GaAs is an effective thermal conductor, which means the VCSELs can operate without special cooling requirements. And AlGaAs DBRs also offer a stable and selective oxide for making current apertures. But GaAs-compatible materials could only emit light in the red and very near infrared, from 0.7-1 μ m. Fiber communication typically requires wavelengths from 1.3-1.6 μ m where absorption in the fiber is a minimum. A number of alternative approaches have been tried in recent years, including AlGaInAs alloys on InP,[220] InGaAs grown on InP and then flip-chip bonded between conventional DBRs,[221] InAs quantum dots on GaAs,[30, 222] extremely strained InGaAs,[24] and lattice-matched DBRs on InP using either InAlGaAs/InAlAs[27] or AlGaAsSb [223]. All of these techniques have been improved in recent years, but still lack the simplicity, reliability, and manufacturing advantages of a one-step, monolithic growth of a VCSEL with GaAs/AlGaAs DBRs. Dilute nitrides such as GaInNAs(Sb) can provide a GaAs-based active region for VCSELs with GaAs/AlGaAs DBRs.

The situation changed when Kondow reported the first use of nitrogen in InGaAs, extending the wavelength of emission farther into the infrared [11]. A flurry of activity with GaInNAs followed, leading to VCSELs that were optically pumped for 1.27 μ m emission,[13] and electrically pumped for 1.2 μ m[224] and 1.3 μ m [225]. The focus of this thesis was the demonstration of the first GaAs-based VCSEL beyond 1.31 μ m, at 1.46 μ m, which will be described in detail later in this chapter. The following section will describe the overall design of VCSELs, particularly for GaInNAs and GaInNAsSb.

5.4 Introduction to VCSEL Design

5.4.1 What makes a great VCSEL

The ideal VCSEL would have high output power at a stable, desirable wavelength, operate with a single transverse mode, with low voltage and low threshold current density, and be able to operate at tens of gigahertz with a single polarization over a

wide temperature range. Polarization control can be provided by growing on a high-order substrate [226, 227], or by processing the VCSEL into a rectangular or elliptical mesa [228]. Both of these are beyond the scope of this work, although GaInNAs luminescence from high index substrates has been reported. [190] The wavelength of a VCSEL increases with temperature, since the bandgap of the semiconductor decreases, but this is somewhat pinned by the wavelength of the DBRs. It is possible to extend the range of lasing temperatures by intentionally detuning the cavity toward the infrared, so it is closer to resonance at higher temperatures.

The transverse mode requirement is for efficient coupling to single-mode optical fiber for long distance communications and networking. It also reduces noise from chaotic mode-hopping. Single-mode operation can be achieved with a small, proton-implanted [48, 49] or oxide [229, 230] aperture, shown in Figure 5.5, or by making the mesa very small, typically 6–8 μm in diameter. Small sizes, with smaller device capacitance, are also advantageous for high speed modulation. But these small sizes reduce the total power available, and increase diffraction losses from the sidewalls and oxide aperture. Transverse modes can also be controlled by using a very long cavity with properly curved mirrors [50, 231], but this is much more complicated than the single, monolithic growths presented here.

To design and grow VCSELs that meet the remaining goals requires several key ingredients. Some of these are important to edge emitting lasers as well, and have already been mentioned in the previous section. For example, nearly all semiconductor lasers require very high material quality, with few defects, which will efficiently emit light. The role of plasma damage, oxygen contamination, and antimony have already been mentioned in prior chapters. Also, several material and device parameters can be extracted from edge emitting lasers grown from the desired material. These parameters include lasing wavelength, threshold current density, and gain per unit length, and were discussed in Section 5.2.2. The key ingredients that are specifically important for VCSELs include QW material, wavelength, accurate layer thicknesses and refractive indices, a cavity correction, low-resistance DBRs, and low thermal impedance. These will be discussed below.

The choice of quantum wells and barriers is determined primarily by the desired

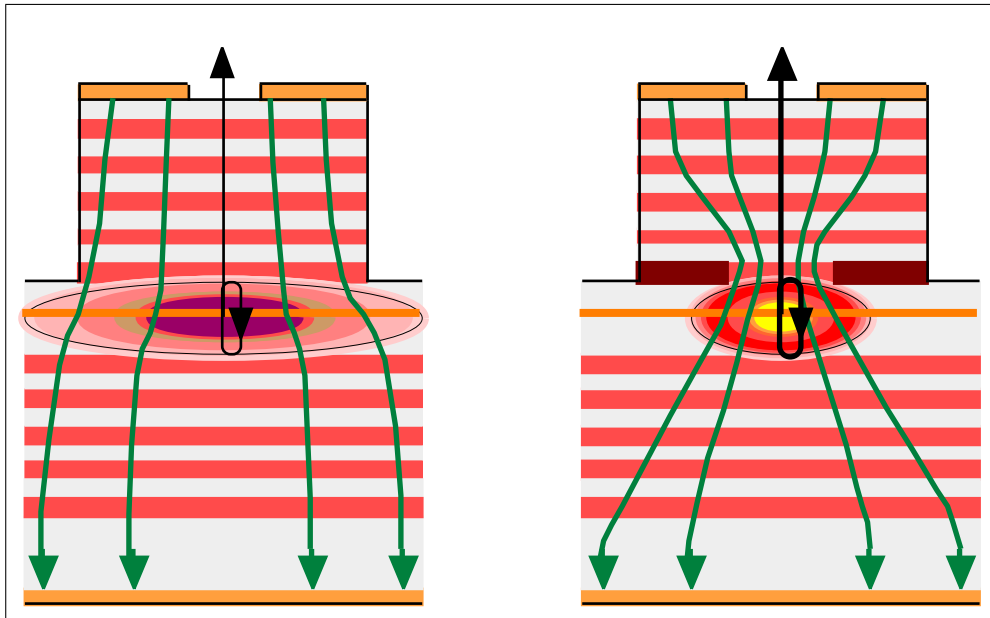


Figure 5.5: VCSEL oxide aperture increases current density, leading to higher power output.

wavelength and the availability of a suitable materials system. As discussed in Section 2.4, it is difficult to reach wavelengths beyond $1.1\mu\text{m}$ on GaAs using only GaNAs in the quantum well, or beyond $1.2\mu\text{m}$ using only InGaAs, or beyond $1.3\mu\text{m}$ using only GaInNAs. By using GaInNAsSb quantum wells with GaNAs barriers, lasers have been demonstrated at $1.55\mu\text{m}$ and longer [21, 23, 149].

The next most important factor in VCSEL design is the thicknesses of the various layers, beginning with the cavity. Because of the short distance between the mirrors, it is critically important that the cavity be the correct optical thickness. There must be an integer number of half-wavelengths in one round trip between the mirrors for the VCSEL to lase. Since these are wavelengths within the material, rather than in free space, the refractive index must be known.

5.4.2 AlGaAs refractive index

Correct selection of the layer thicknesses in the VCSEL requires accurate refractive index data for GaAs and AlGaAs. Although Adachi's method [232, 233] is almost

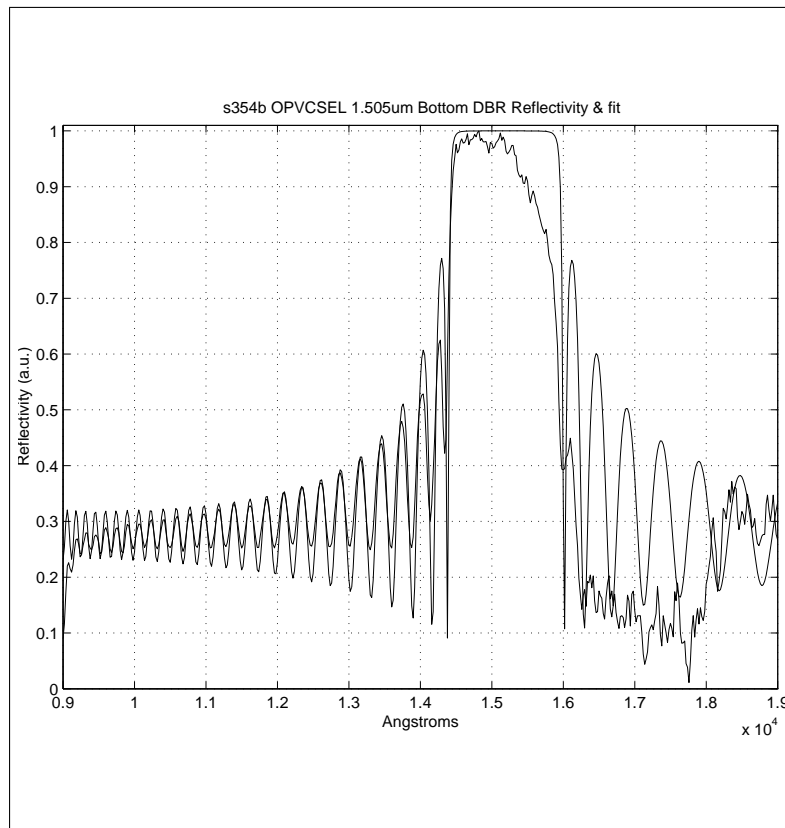


Figure 5.6: DBR reflectivity modeled accurately with refractive indices from Gehrsitz over all wavelengths of interest. The deviation above $1.6\mu\text{m}$ is due to system response.

universally used for GaAs and AlGaAs refractive indices, and is generally quite accurate near the bandgap, its accuracy decreases in the near infrared. Gehrsitz [234] reported an improvement in measurement accuracy using grating coupling into an antiguided waveguide. The empirical model of the refractive index from $1\text{-}3\mu\text{m}$ is in good agreement with experimental data from Deri [235]. We have also found excellent fit of this model with experiment, as shown in Figure 5.6. Gehrsitz' semiempirical model offers an added feature in terms of being able to predict the refractive index at elevated temperatures, up to 150°C or so. It should be noted that doping will change the refractive index, so some slight correction may be necessary. Growth of a calibration sample of a desired doping of GaAs or AlGaAs can fix the actual refractive index and eliminate possible errors between theory and practice.

5.4.3 GaInNAs refractive index

The refractive index of GaNAs is fairly straightforward to model, with only one parameter (Group III composition), and has been reproduced in Figure 5.7 [236]. GaInNAs, with two parameters, is more complicated. An early measurement of the absorption spectra of GaInNAs was made by Kondow's group at Hitachi,[237] and shows an increasing refractive index with increasing nitrogen mole fraction, but it is unclear to what extent material quality may have interfered with their measurement. The only major recent study of the refractive index of GaInNAs appears to be Leibiger, Šik, and coworkers, using MOVPE grown material [236, 238]. (The refractive index plot from Šik's earlier paper appears to have suffered a publishing misprint in the axes.) Unfortunately, their work suffers from poor material quality, as evidenced by the lack of an exciton peak, as well as a slow absorption edge, so it offers at best an approximation to the refractive index of GaInNAs of any composition. No systematic studies of GaInNAsSb refractive index have been reported to date, so the refractive index for GaInNAsSb quantum wells can only be estimated from GaInNAs at correspondingly shorter wavelengths. Small errors in the GaInNAsSb refractive index should be negligible for cavity thickness, since the GaInNAsSb QWs constitute only 22nm of total thickness. Errors in the GaNAs refractive index would be significant, since the total GaNAs thickness of 88nm represents more than a half-wavelength.

One method of guaranteeing the correct cavity thickness is to stop the growth after a few top DBR pairs, cool the wafer to room temperature (or lasing temperature), and measure the reflectivity spectrum using a white light source [43]. Any error in the cavity length can be detected by matching the reflectivity spectrum to a simulation [239]. If the cavity is too short or too long, the subsequent layer of the DBR can be made longer or shorter, respectively, to “pull” the cavity mode in the correct direction [43]. The use of a cavity correction at the beginning of the top DBR can save a growth even if the sources have drifted somewhat from the intended growth rates, or if there was some error in the refractive index of the GaInNAs(Sb) or GaNAs.

Unfortunately, the presence of an arsenic cap (Section 4.8) leads to an error in the measured reflectivity spectrum, as shown in Figure 5.8. This means that the wafers must not have an arsenic cap when the reflectivity spectrum is measured. This is not

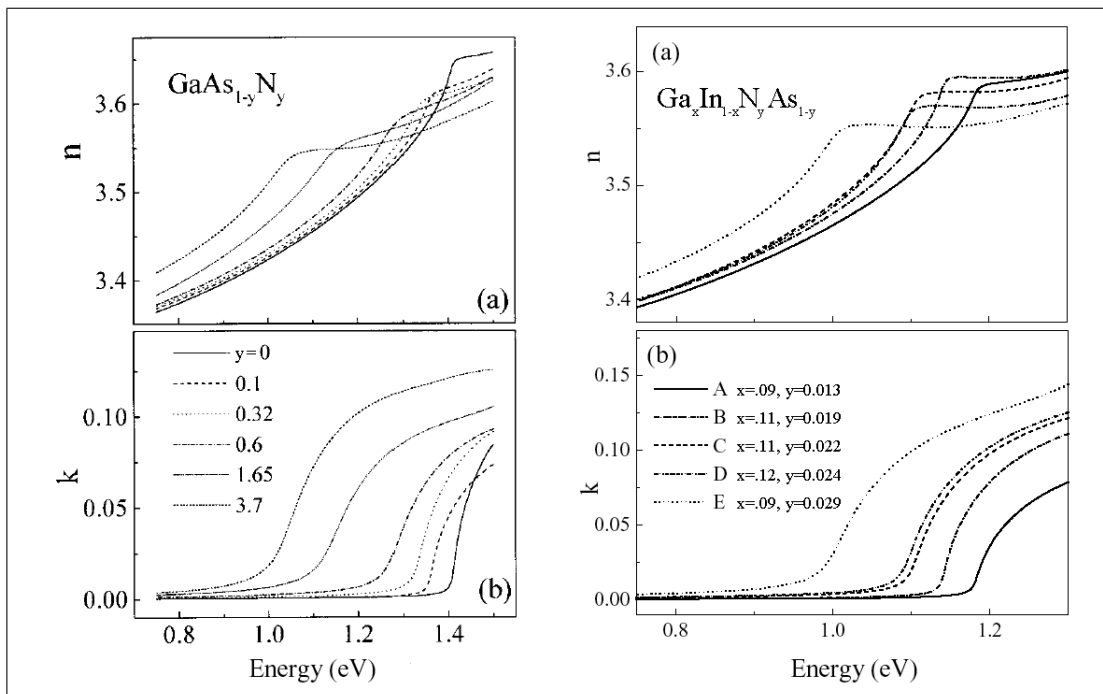


Figure 5.7: Refractive index and absorption coefficients $N = n + ik$ for GaNAs (left) and GaInNAs (right). (From Leibiger et al.)

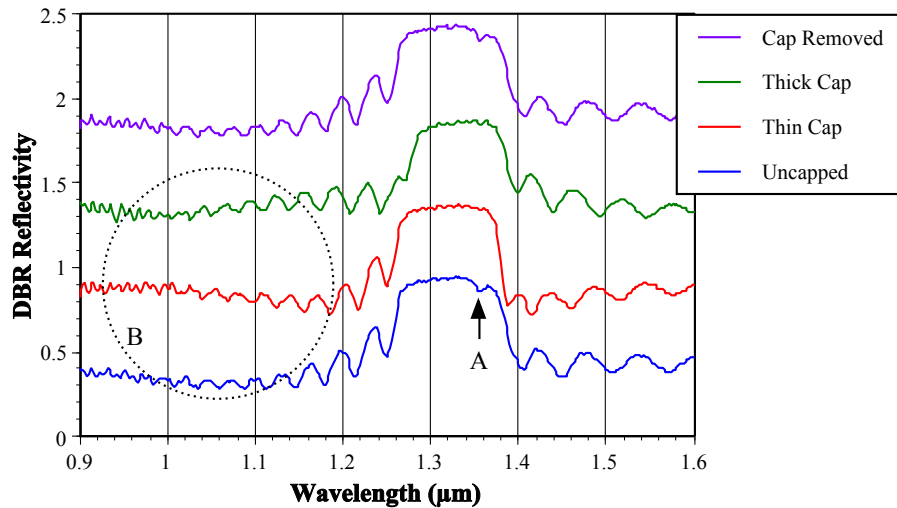


Figure 5.8: Arsenic cap leads to reflectivity error. Note missing dip at A and the change in the overall envelope at B, plus the overall shift to longer wavelengths. Original spectrum is restored when the cap is evaporated (top plot). Plots have been offset for clarity.

such a bad thing for the cavity correction, which is performed after the quantum wells and cavity are finished. But measurements of the bottom DBR add several steps to the growth, since the wafer must be recapped before igniting the plasma. It is also critical that GaAs or AlAs calibration growths be arsenic-free on the surface. This should be verified by verifying RHEED surface reconstruction just before the wafer is unloaded from the MBE growth chamber.

5.4.4 Electrical and Thermal Impedance of DBRs

The last of the special DBR layers is the phase matching layer at the top surface. At the surface of the VCSEL, the top contact can be used as part of the top mirror, even for a top-emitting VCSEL, where the ring contact or patterned surface can be used to suppress higher order transverse modes [47]. But metals are lossy reflectors with a complex refractive index, so they introduce some phase delay in the incident wave. The top surface of the DBR, then, needs to be phase matched to the gold.

Because DBRs have less contrast in refractive index at $1.5\mu\text{m}$ than they do at

1.0 μm , more mirror pairs are required to provide a given reflectance. But adding mirror pairs increases optical loss, and worse, Joule heating from increased resistance. It is therefore quite important for long wavelength lasers that the DBR be optimized for low resistance. Yechuri (at Honeywell) has provided a straightforward method of optimizing DBR band structure for minimal electrical resistance[240, 241] using graded regions at each interface, as well as careful doping. Growth of these graded regions is fairly straightforward to perform by MOCVD, because variable gas flows are available, but MBE offers only discrete shutter operations. The usual solution is to perform step grading and/or digital alloying, in which a shutter is opened and closed with a $\sim 2\text{nm}$ period and successively longer or shorter duty cycles. Particular attention should be paid to the p-doped DBR, because free carrier absorption is worse for holes than electrons, and the absorption increases at longer wavelengths, roughly increasing with the square of the wavelength in the mid-ir region. By performing digital alloying with at least one intermediate step, using multiple group III sources, a reasonable approximation to the Yechuri method above can be made, and with a reasonable number of total shutter operations.

For the VCSELs presented here, it was decided to take a very conservative approach. Free carrier absorption can be a significant problem in a VCSEL, particularly at longer wavelengths, so for these VCSELs, the doping of the DBRs was kept very low. This led to a high series resistance, as will be discussed later. The doping profile of the DBRs was not optimized, which also contributed to the series resistance.

Each interface in the DBRs was graded from GaAs to AlAs or AlGaAs, or vice versa, by a combination of digital alloying and step grading. This grading was in order to avoid large barriers to electrons or holes at each interface. The step profile is shown in Figure 5.9. The n-DBR simply had one step grading of 2nm of 47% AlGaAs. It was thought that the high doping in the n-DBR, as well as the wide area of the substrate, would sufficiently reduce the resistance of the DBR.

Although most of the layers in each DBR are exactly one-quarter of a wavelength in thickness, there are three exceptions. The first is the optional cavity correction layer mentioned in Section 5.4.3. The second is an oxide confinement layer. Holonyak's group discovered that high-aluminum AlGaAs layers, when exposed to

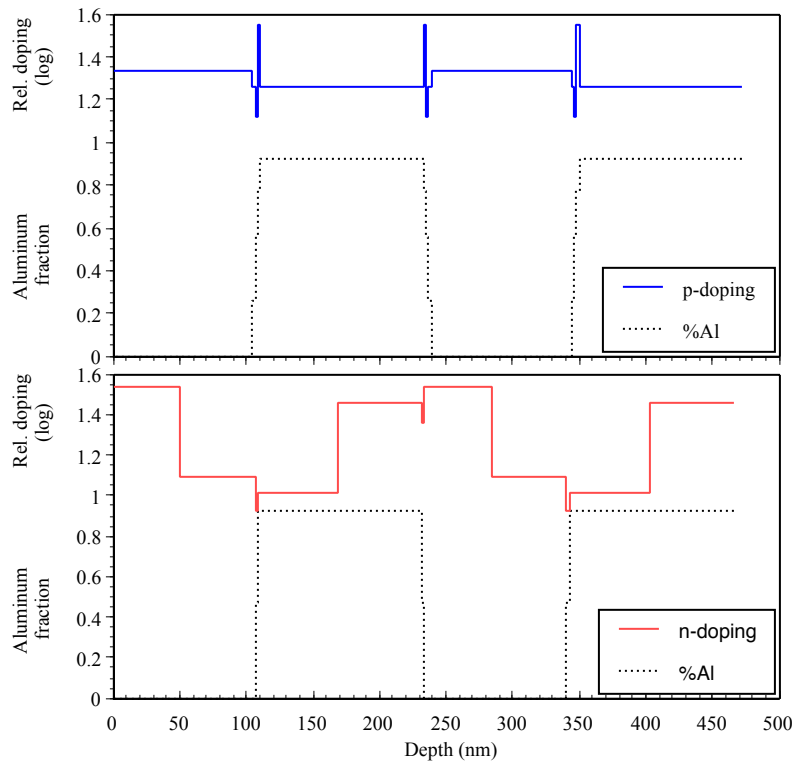


Figure 5.9: Graded DBR profile.

steam at temperatures from 300-400°C, will oxidize in a controllable and mechanically robust fashion [242, 243]. By oxidizing one layer of a VCSEL by several microns, an aperture is formed, restricting current to the center of the mesa, which increases the current density and prevents carriers from recombining along the sidewalls of the mesa [229, 230]. The oxidized layer also presents a lower refractive index than the original AlGaAs, which helps confine the optical mode and keep it from the (possibly rough) sidewalls of the mesa and from the hard aperture of the top metal contact. Very high aluminum mole fraction or very fast oxidation rates can lead to peeling of the AlO_x from the rest of the layers, so conservative oxidation rates ($\sim 1\mu\text{m}/\text{min}$) generally lead to higher reliability. In ordinary VCSELs, an oxide aperture would be placed both above and below the QWs to prevent current spreading. But dilute nitride lasers appear to suffer from reliability issues when the mesa is etched all the way through the QW. Although oxide confined VCSELs have occasionally met with disfavor in industry due to reliability issues, oxide confinement is still very important for GaInNAs(Sb) VCSELs due to the high current densities. The gain of GaInNAs(Sb) at longer wavelengths is somewhat poor, and DBRs are more lossy and have lower index contrast, so higher current densities are required to overcome these losses.

The electrical resistance is not the only issue in a DBR. Because the DBR is so thick, and because it sits between the QWs and the substrate or heat sink, the thermal impedance of the DBR is significant as well. The temperature of the QW will generally be higher than in an edge emitting laser with the same QW design, which may change the operating wavelength, leading to a gain/cavity mismatch. This leads to a decrease in output power, and aggravates the heat-related drop in internal quantum efficiency. Generally the best results are produced by mounting bottom-emitting VCSELs with the epitaxial side (top side) down on a heat sink, but reasonable top emitters can also be made. Binary materials such as GaAs and AlAs tend to have better thermal conductivity than alloys, which in turn are significantly better than dielectric DBRs. The worst case thermal impedance is an air gap DBR; thick heat spreading layers are necessary for such devices to lase at all [244]. Ideally, the DBRs should be made with as few pairs as possible and highly doped, which reduces both thermal impedance and ohmic heating from electrical resistance. For VCSELs formed by etching a mesa,

etching through the cavity increases the thermal impedance, although this may be offset by the increased quantum efficiency from having a second oxide aperture below the QWs. Early devices also showed poor lifetime when the quantum well was etched through, possibly due to nitrogen outdiffusion. Planarization can also help remove heat from the VCSEL mesa and may help with device reliability by protecting the DBRs from oxidation.

5.5 Growth Considerations

One of the major difficulties in growing VCSELs is the need for stable and reliable fluxes from each source. If one of the gallium cells drifts by just 4%, the error in the DBR will be sufficiently high (up to 30nm at $1.5\mu\text{m}$) that the VCSEL will not lase. These drifts were common with earlier types of cells in MBE chambers, which had wide open trumpet-shaped crucibles. SUMO cells from Veeco (formerly EPI or Applied Epi) have a constriction at the neck of the cell that isolates the cell from the surrounding MBE chamber. They also have a two-zone heating system, so the temperature at the base of the cell can be controlled independently from the tip. Although we had been assured by Veeco that the cells were stable with just single-zone heating, they were not stable enough for VCSEL growth. By establishing a fixed, 150°C difference between the tip and base of the gallium cells, the SUMO cells were made much more stable for long periods of time. They also were found to converge to their final flux output much faster, and with much less variation, as shown in Figure 5.10. The standard deviation in the flux measurement was reduced from 7.7×10^{-9} to 2.7×10^{-9} Torr. However, 150°C was not quite sufficient to keep material from accumulating around the lip of the crucible, so recent growths have used 180°C , or better still, a fixed fraction of the cell temperature (e.g. 16%).

The aluminum cells, one SUMO and one trumpet-style, were operated with heat only applied to the base. This is to avoid destruction to the cell. Aluminum wets pyrolytic boron nitride (PBN), so it can creep up the cell walls and overflow, shorting out the heater filament and permanently destroying the cell.¹ Dual-zone heating of

¹This is true even with the extended lip of a SUMO cell. Our first SUMO was slightly overfilled

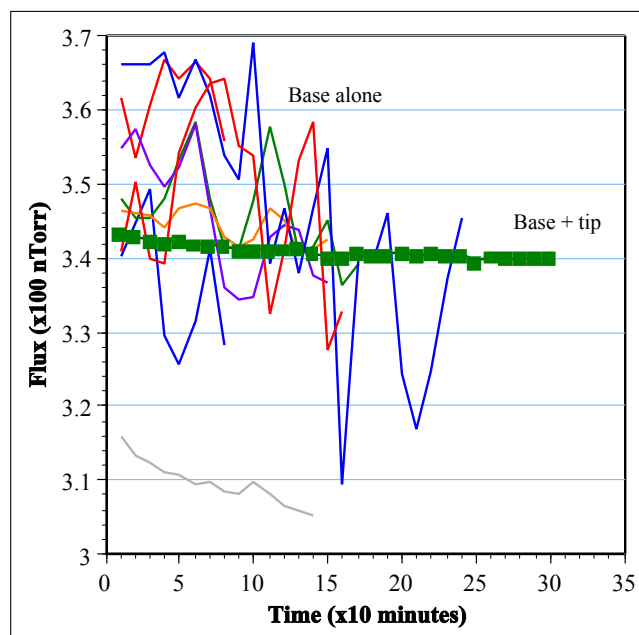


Figure 5.10: Gallium flux from SUMO cell is much more stable when both base and tip are under the control of separate Eurotherm controllers. Controlling the base alone leads to flux variability.

the aluminum cell may provide a more uniform growth rate across the wafer, but stability did not appear to be an issue with single-zone heating.

To assure the correct thicknesses of the layers in the VCSEL, several growth calibrations were made immediately before growth, with the sources at their final temperatures. For each of the aluminum sources on System 4, a 1000nm AlAs layer was grown on GaAs after a 300nm buffer. The normal incidence, white light reflectivity spectrum of the wafer was taken and matched to simulation by the thin-film solver “mff.” The wafer was reinserted into System 4, and another 1000nm of GaAs was grown on top, and the reflectivity and simulation were repeated to calibrate the two gallium sources. The subsequent error in remaining DBRs was estimated to be less than 1% over the course of 3 days. This affirmed the use of a fixed difference between the base and tip temperatures of the SUMO cells.

by a former student, and the creeping aluminum destroyed the cell within 2 months after it was installed.

5.6 Growth of VCSELS for 1.5 μ m Emission

The Stanford GaInNAsSb VCSELS were grown before the corresponding edge emitting lasers had been fully tested. The VCSELS were designed rather conservatively, as hard numbers for gain had not yet been established. In addition, long wavelength lasers tend to suffer from Auger recombination and low quantum efficiency, conditions that could be improved by cooling, so the VCSELS were designed to operate at temperature of 0°C or below. This meant that the VCSELS were intended to lase at a wavelength near 1.470 μ m, while the edge emitting lasers lased at 1.495 μ m at room temperature. This is consistent with the 0.6nm/°C shift in the edge emitting lasers, and similar to the usual shift with temperature in InGaAs lasers. A PL sample was grown immediately before the VCSEL QWs to ensure that the wavelength of emission would be correct. The sample was immediately unloaded from the chamber, then annealed at 760°C for 1min. PL showed peak emission at 1.508 μ m, far longer than the 1.465 μ m from amplified spontaneous emission, and also longer than the 1.463 μ m from the original PL sample on which these growths were based. The longer wavelength from the PL sample is attributed to excessive plasma damage during that particular growth, since the plasma needed to be ignited several times, without an arsenic cap. We have established through other experiments that plasma damage causes a shift to longer wavelengths, even though it decreases nitrogen composition [245]. There may also have been an uncontrolled increase in antimony flux from our unvalved Sb cracker: the desired Sb flux was 1.11×10^{-7} Torr but remained constant at 1.0×10^{-7} Torr even after the temperature was raised several times, but we suspect the actual Sb flux then rose soon after the growth began. However, even a 10% change in Sb flux is expected to cause only 2nm of wavelength shift [246].

The VCSELS consisted of a bottom mirror, cavity, and top mirror, all epitaxially grown on n-doped GaAs. The bottom mirror was composed of 29 alternating pairs of silicon-doped Al_{0.92}Ga_{0.08}As and GaAs for the distributed Bragg reflector (DBR). The cavity was a one-wavelength (1λ) thick layer of GaAs, designed for 1.485 μ m, with three quantum wells (QWs) at the center of the cavity. The QWs were based on the edge emitting lasers, which operated at wavelengths from 1.49-1.51 μ m. The QWs

were 7nm $\text{Ga}_{0.62}\text{In}_{0.38}\text{N}_{0.016}\text{As}_{0.958}\text{Sb}_{0.026}$ with 20nm GaNAs barriers below, between, and above the QWs. The composition reported here was determined from calculations based on work by K. Volz using SIMS, XRD, RBS, and NRA-RBS [99]. The top DBR was p-doped with carbon, and 24 pairs thick. A thin, digital alloy of 98% aluminum was included as part of the second AlGaAs layer from the cavity for use as the oxide confinement layer. Growth details were similar to Section 5.2.1, including two-chamber growth, use of an arsenic cap while the plasma was ignited (Section 4.8), and ion deflection plates on the plasma source (Section 4.7.1). Nitrogen was supplied by an SVT Associates rf plasma cell at 300W and 0.5sccm with a 4-hole aperture of unknown conductance. The Sb flux was 1.15×10^{-7} Torr, and the arsenic overpressure was 20 times the Group-III flux in the quantum wells and 15 times elsewhere. Plasma conditions were optimized to minimize plasma damage during growth [180, 182, 203]. A conventional liftoff process was used to define metal rings for the top contacts, and top and bottom metal were deposited by e-beam evaporation in the Innotec.

The bottom DBR was grown in System 4, which contains two aluminum cells and two gallium cells. This allowed straightforward growth of step-graded interfaces. There is also growing consensus that growing AlGaAs separate from nitrogen-containing layers may improve the material quality, although there have been striking exceptions [149, 23].

After the growth of the cavity, the wafer was cooled to room temperature, and the reflectivity spectrum was taken using a white light source. The spectrum and fit are shown in Figure 5.11. In this case, the spectrum showed that the cavity would need to be extended by 17.3nm for a round-trip phase of exactly π radians. To make this determination, first the lower DBR was verified to be centered at the desired wavelength of 1480nm. Then the simulation was performed to determine the actual layer thicknesses, and the phase of reflection at 1480nm. The phase was only 2.05 radians, but should have been π radians, so an additional thickness of

$$a = \frac{\lambda}{4n} \times \left(\frac{\pi - 2.05}{\pi} \right) \quad (5.6)$$

was needed.

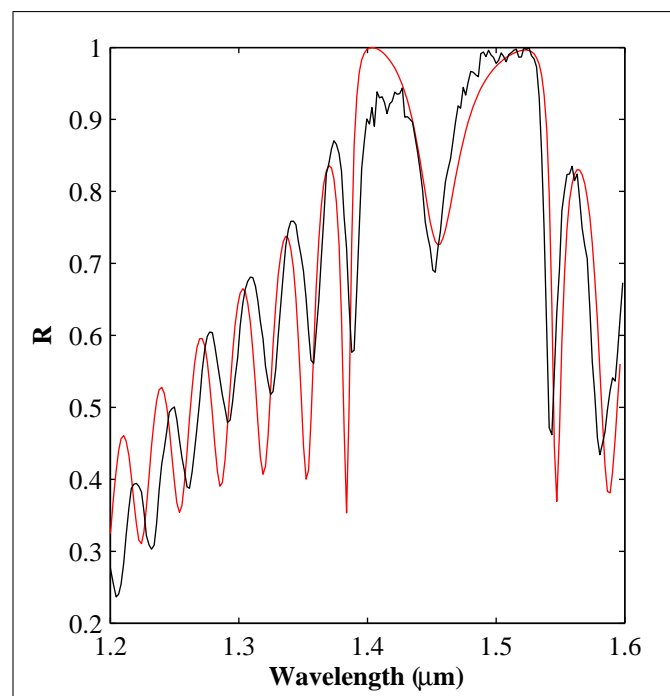


Figure 5.11: VCSEL (n540) reflectivity spectrum from bottom DBR with cavity and two top DBR pairs. Fit from simulation is shown in pale.

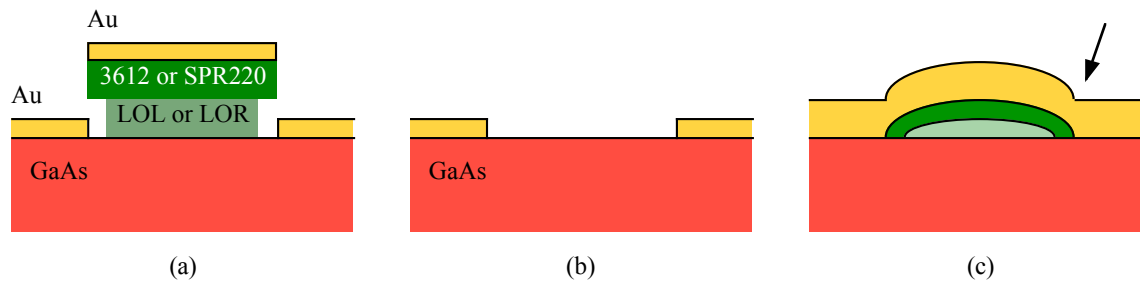


Figure 5.12: (a) Proper structure of several possible bilayer resists for liftoff, after exposure, development, and the evaporation of metal. Undercut prevents continuous metal. (b) Desired result after liftoff. (c) Thicker metal and rounded (burned) resist prevent liftoff solvents from reaching resist layers (arrow).

5.7 VCSEL Processing

5.7.1 Lift-off process

The fabrication process for VCSELs was similar to the edge emitting lasers: growth, top-side lithography with a single mask step, metallization and liftoff, backside metallization, a dry etch, and a contact anneal. A bilayer resist was patterned with conventional photolithography on the Karl Suss. The bilayer resist was undercut by several microns to help with the lift-off process, as shown in Figure 5.12(a). A top metal contact was deposited by e-beam evaporation in the Innotec. The top contact was Ti/Pt/Au, with thicknesses of 40nm, 40nm, and 400nm, respectively.

The actual processing steps—which are not recommended—were as follows. The bilayer resist was LOL2000, followed by $1\mu\text{m}$ of SPR3612 photoresist. After the soft bake, the resist was exposed in KarlSuss 2. On a processing dummy, the exposure was 1.7sec. The resist was hard-baked, then 40nm Ti, 40nm of Pt, and 400nm of Au were evaporated. Liftoff was successful with this dummy. However, the subsequent dry etch completely removed the gold, so it was decided that the thickness of gold would be increased to 600nm. However, the thickness of the bilayer resist (LOL2000) was not increased accordingly, and the photoresist was mistakenly given a multiple exposure of $4 \times 1.7\text{sec}$ rather than $1 \times 1.7\text{sec}$. The extended exposure caused the photoresist to heat and reflow, as shown in Figure 5.12(c). Also, the extra thickness of gold

completely buried the resist, making it impossible for lift-off solvents to dissolve and remove the resist or the gold above it. These errors in processing significantly affected laser performance, as will be discussed in following sections.

For reference, based on the results of the lithography above, the revised lift-off process is summarized as follows. An adhesion layer of HMDS in the YES oven is unnecessary if the wafer has been sufficiently cleaned. LOR should be used in place of LOL2000 for a thicker bilayer undercut. Either SPR3612 or SPR220-3 may be acceptable for the photoresist layer for the liftoff layer, since these are large features (minimum $6\mu\text{m}$ diameter). The exposure time for SPR3612 is only 1.6 seconds, and only once; the exposure for SPR220-3 is 4×1.7 seconds. The resist is developed in LDD26W until the excess resist was removed, approximately 1 minute. If a top-emitting mask is to be used for bottom-emitting VCSELs, the wafer should be fully developed until the resist from the center of the ring contact is fully dissolved away. This will also increase the diameter of the pad, so the mask should be selected accordingly. After development, the wafer is cleaned and baked again. Rather than using a thick layer of gold, the top metal should be capped with a thin layer that is highly resistant to the dry etch, such as 20nm of Cr. The top metal evaporation would then be 40nm Ti, 40nm Pt, 400nm Au, and perhaps 20nm Cr. After the metal is evaporated, the wafer is immersed in acetone or resist stripper (1165) to dissolve the resist and wash the excess metal away. A spritzer may be useful for removing excess metal. The wafer is then baked dry on a hot plate before dry etching to prevent trace solvents from outgassing into the PlasmaQuest.

For top-emitting VCSELs, another mask step must be used to deposit a thick photoresist on top of the mesa, such as SPR220-7, in order to protect the exposed semiconductor inside the ring contact. In this case, no adhesion layer or bilayer is used, although the thick resist must be baked especially long to prevent outgassing in the PlasmaQuest.

5.7.2 Dry Etching with PlasmaQuest

The PlasmaQuest plasma etching system was used to perform the dry etching. The PlasmaQuest uses electron cyclotron resonance (ECR) to generate a reactive plasma that etches exposed semiconductor. The recipe used for our processing (Gigi2.rcp: argon, BCl_3 , and Cl_2) etches metals very slowly, and does not etch photoresist. Vertical features were achieved with 200W of ECR power (400W for ignition) and 55W of RF power, at a pressure of 2mTorr.

Uniform etching is critical for GaInNAs VCSELs: if the active region is exposed to air, the laser will rapidly die. On the other hand, if the top DBR is not entirely removed, then larger currents will be needed to overcome the effect of current spreading. Also, the oxide aperture is planted in the second or third DBR pair, and must be exposed in order for the selective oxidation process to succeed. In order to achieve uniform etching in the PlasmaQuest, it is important that the sample be at a uniform temperature. The conventional method of mounting samples using double-sided copper tape led to very nonuniform etching: the edges of each sample were heated by the plasma, and etched up to 30% faster than the sample center—a serious problem when trying to stop within 50nm after etching through more than $5\mu\text{m}$ of DBR. Also, if any copper tape was exposed, the etch rate was affected nearby. Instead, a carrier wafer was made by indium-soldering short rails of silicon in a tight 3" circle onto the requisite PlasmaQuest substrate (a 4" p-type, silicon wafer, with wafer flats at specified positions). Because the samples are cooled by thermal conduction through the back, it is vital that the samples and the carrier wafer be entirely free of dust, debris, solder, and nonuniform metallization, and unscratched. For this reason, it is preferable that the dry etch be done before backside metallization, and that the backside of each wafer be carefully swabbed to remove stray photoresist. The backside cooling helium flow rate should also be at maximum (10), with the wafer chuck set to 10°C or lower, for best uniformity. But colder temperatures tend to etch semiconductor and metal at similar rates. To compensate, for the VCSELs, thicker metal was deposited, but this caused severe problems with liftoff, as discussed in Section 5.7.1. A better solution, using Cr as an etch resistant layer, is being developed. Using these techniques, straight sidewalls and uniform etching are possible, as shown in Figure 5.13.

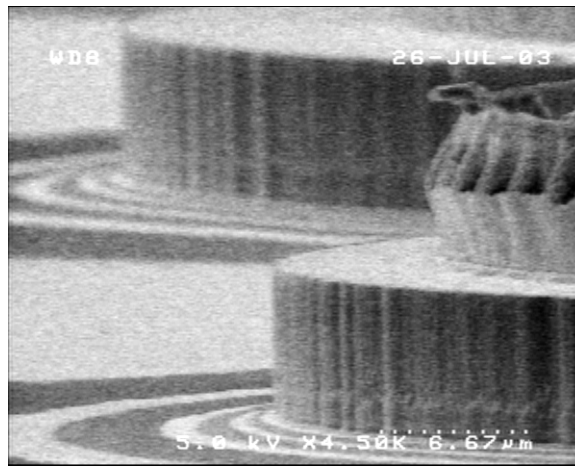


Figure 5.13: Vertical sidewalls after dry etch.

Note the “poofy crown” on top of the mesa due to gold that was resputtered onto the side walls of the SPR220-7 protective resist, before that resist was stripped off. Also note that all of the gold has been removed; the dry etch was insufficiently selective of semiconductor over metal, as discussed in Section 5.7.1.

Thanks to efforts by R. Aldaz and E. Thrush, the PlasmaQuest has an etch monitor similar to that on Drytek 4. A diode laser with wavelength 632–650nm shines at an angle of 70° from normal incidence. As the layers are etched away, the reflectivity of the sample changes with time. For a periodic structure like a DBR, it is straightforward to count oscillations in the reflectivity and determine the etch depth to within a few tens of nanometers. As part of this thesis work, the thin film simulator *mff* was updated to provide a reflectivity profile with etch depth. The expected profile for top-emitting VCSELs is shown in Figure 5.14.

Previous problems with contamination of wafers in the PlasmaQuest were believed to be caused by other pquest users improperly etching PMMA or inappropriate materials, or possibly a memory effect from fluorine. These problems only arose for high-aluminum etches such as VCSELs and ARROWs. The problems went away when the staff partitioned the week to separate III–V etches from all other etches.

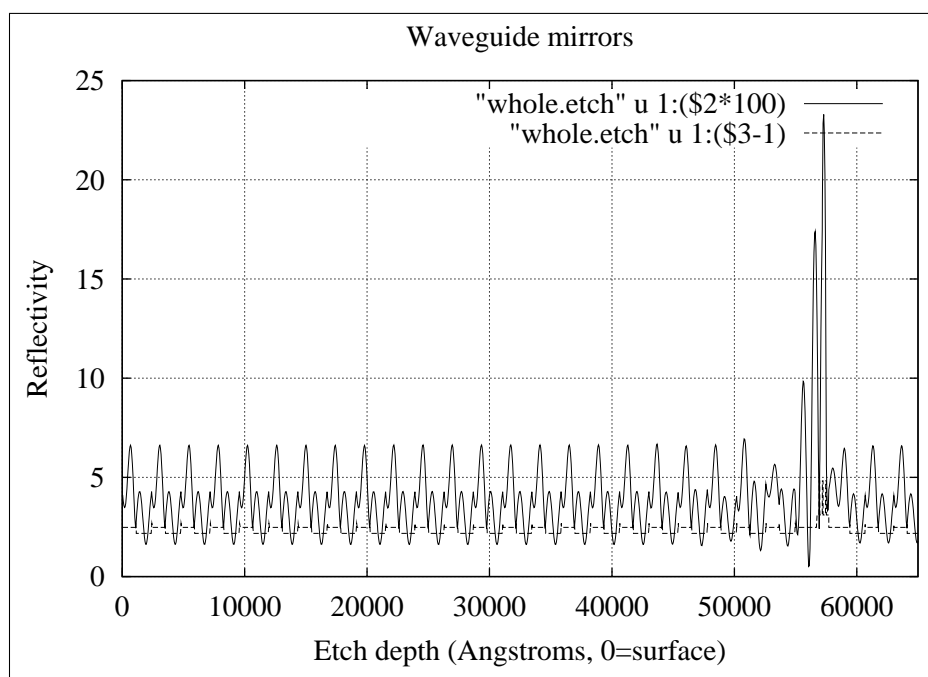


Figure 5.14: Simulated reflectivity vs. depth of dry etch (or time), from updated *mff*.

5.7.3 Recovery from a failed lift-off process

Unfortunately, the liftoff solvents failed to penetrate the metal. Many suggestions were solicited from SNF personnel, and all of these techniques were tried, including an overnight soak in strong solvents (1165 stripper), an acetone spritz (mechanical removal), a hot acetone bath, ultrasound, and even Scotch tape—which peeled off either all the metal or none of it. It became clear that the metal needed to be thinned before the solvents could penetrate it and provide proper metal lift-off. A weak solution of potassium iodide and iodine, which is known to etch gold, was unsuccessful at providing lift-off.

The gold was thinned using aqua regia (1:3 HNO_3 : HCl). This step significantly damaged the metal and the wafer surface: as soon as the etch sufficiently thinned the gold, it attacked the GaAs and AlGaAs underneath, and at a much faster rate. This led to extremely rough sidewalls and surfaces and added significant scattering loss to the VCSELs. Typical etch holes are shown in Figure 5.16. Even with the aqua regia etch, very few mesas smaller than $62\mu\text{m}$ in diameter survived the liftoff process; the

others did not lift off. The gold etch rate was difficult to control, because the aqua regia etch rate increased with time and, perhaps, also with the amount of material dissolved. In the presence of heat or light, nitric acid becomes more corrosive:



This is known as “fuming” nitric acid. The aqua regia solution visibly turned darker with time. New solution was mixed for every etch sample, and the etch rate was calibrated using strips of a dummy silicon wafer with 200nm of gold. This still did not prevent the wafer damage mentioned earlier. Clearly, it is much easier to prevent problems with liftoff and processing, rather than to try to correct them after the metal has been deposited.

5.7.4 Oxide aperture by selective oxidation

After lift-off, the wafer is usually annealed to drive in the Au/Ge eutectic for the n-type contact. For VCSELs, this is unnecessary because of the high-temperature oxidation step that followed, as described on page 150. When AlGaAs is exposed to hot steam at temperatures near 400°C, the aluminum-containing layers will preferentially oxidize. The arsenic is reduced by the hydrogen in the water, forming neutral arsenic and arsine gas, which then escapes from the now-porous material. The remaining aluminum bonds with oxygen from the water. The oxidation rate is constant with time, but varies with temperature and the fraction in the carrier gas, as shown in Figure 5.15(a). [230] Even 2% gallium in AlGaAs can drop the oxidation rate by an order of magnitude. It should be noted that this selectivity based on composition is itself dependent on temperature, as shown in Figure 5.15(b). For temperatures near 400°C, there is not much difference in the oxidation rates of 98% AlGaAs and 92% AlGaAs. This will be significant shortly.

The VCSELs were oxidized in the GaAs oxidation tube, a 6” furnace with pre-heated quartz boat and a bubbler to saturate N₂ with steam at 95°C. The nitrogen flow rate was 20sccm, in high flow mode, at 100% flow (the “argon” knob set to 000). The furnace was 435°C according to its thermocouple. According to Figure 5.15(b),

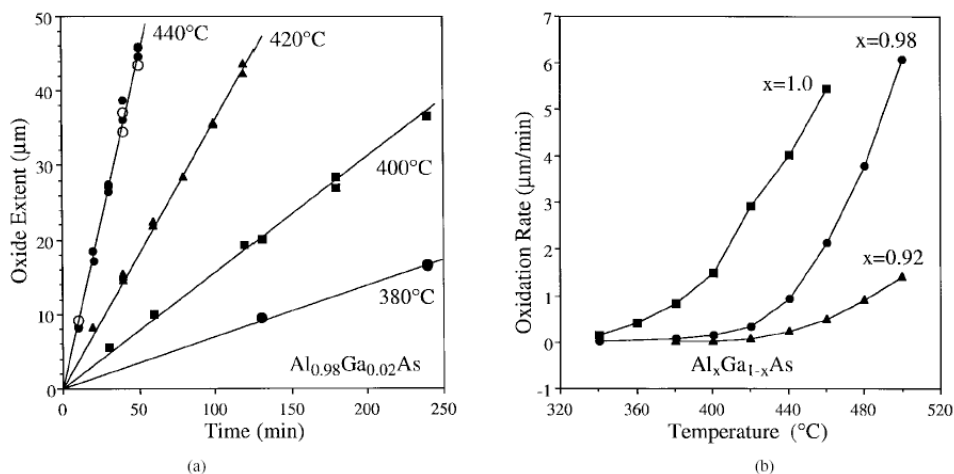


Figure 5.15: Selective oxidation of AlGaAs. (a) Oxide thickness is linear with time but strongly temperature dependent. (b) A small change in composition causes large change in selectivity. From [230].

this should have produced about 4:1 selectivity between the 92% AlGaAs DBR layers and the 98% digital alloy used for the oxidation layer, with an oxidation rate of about $1\mu\text{m}/\text{min}$. Instead, it was found that no oxidation occurred during the first 10 minutes, then the oxidation rate was about $0.2\mu\text{m}/\text{min}$. Also, the entire stack of AlGaAs layers in the DBR oxidized at the same rate as the nominally-selective oxidation layer, as shown in Figure 5.16.

The fact that the oxidation was non-selective disagrees with Ref. [230] and calls into question the whole point of doing selective oxidation. There are two likely causes of the disparity between this and published results. First, the oxidation furnace may have been significantly cooler than the thermocouple reported. This would explain the low oxidation rates in general. Unfortunately, because all of the processing dummies and practice DBRs had been irreparably damaged during the lift-off recovery, along with many of the VCSEL samples, it was not possible to try the oxidation with higher temperatures.

Second, it is believed that the selective oxidation layer was too thin. The high-aluminum, selective oxidation layer was not freestanding, but was part of a thicker AlGaAs layer with lower aluminum content. This was an intentional design strategy,

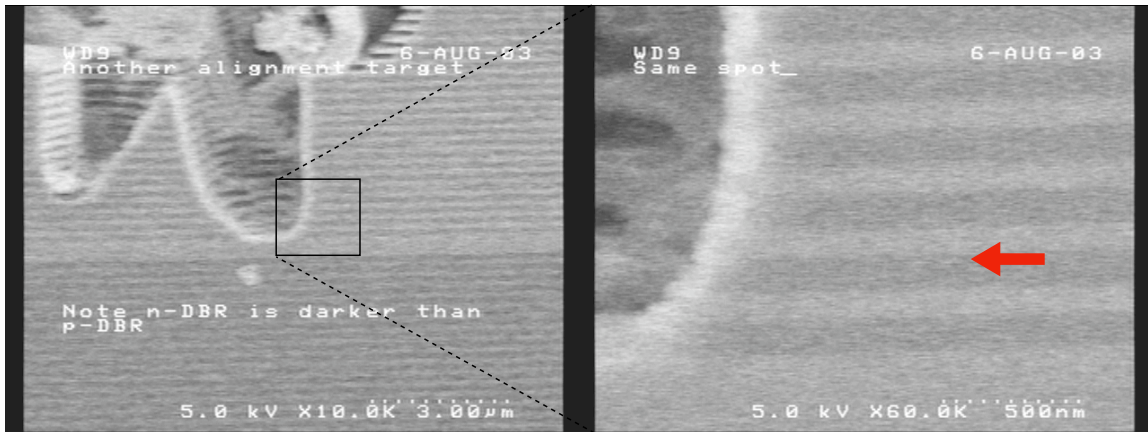


Figure 5.16: Left: damage due to aqua regia etch. Right: oxidation front (at arrow) barely visible, uniform through all AlGaAs layers in DBR.

as it should have formed a wedge-shaped oxidation front, which would result in a softer optical aperture and lower diffraction losses. However, it is believed that the low-aluminum AlGaAs served as a sink for incoming oxygen, slowing the oxidation front. In order to provide a truly selective oxide aperture, therefore, the selective layer must be thick enough to supply not only itself with oxygen, but also the neighboring, low-aluminum layer. This should be taken into account when designing the DBR, as it will change the overall optical thickness of the layer.

Because the oxidation was not selective, the top DBR oxidized uniformly about $10\mu\text{m}$ inwards. This added optical scattering losses and series resistance to the top DBR. On the other hand, no oxide delamination was apparent in any of the devices.

5.8 VCSEL Results

The VCSELs were mounted epi-side-up on a copper chuck for testing. Since the top-emitting VCSELs had been designed to operate at cold temperatures (i.e. a shorter cavity and shorter wavelengths), the testing station was modified to be able to cool below 0°C . The chuck temperature was cooled by a two-stage thermoelectric cooler (TEC), with the first stage driven by a constant current source and the second stage controlled with a feedback loop by the temperature controlling portion of an

ILX LDP-3744B laser diode controller. The TEC was mounted to a Koolance brand, water-cooled copper block, 1" square, cooled by a recirculating chiller at 5°C. A special low-temperature thermocouple, ILX model #521, was used, accurate to -40°C. The testing station was surrounded with plastic and purged with dry nitrogen gas in order to prevent condensation of water on the sample below the dew point ($\sim 10^\circ\text{C}$). The copper stage could then be cooled to temperatures as low as -33°C.

The testing station consisted of a Bausch and Lomb optical stereomicroscope on a Cascade Microtech probe station designed for 6" wafers. One of the microscope objectives was replaced with a ThorLabs $f=8\text{mm}$ C240TM-C collimating lens, a $f=11\text{mm}$ C220TM-C focusing lens, and a $62.5\mu\text{m}$ multimode fiber, allowing the use of fiber-coupled instruments listed below for measuring the power or spectrum of the VCSELs. An ILX LDP-3840 pulse generator with a custom sampling circuit was used to drive the VCSELs for pulsed measurements. Voltage and current pulses were measured using an Agilent Infinium 4-channel oscilloscope. Pulsed optical measurements were made using a ThorLabs PDA400 amplified photodetector, which was mounted in place of another of the microscope objectives. An HP 8153A lightwave multimeter was used to measure the fiber-coupled power from the devices. an HP 70951B optical spectrum analyzer (OSA) was used to measure the fiber-coupled spectrum. The collection efficiency of the fiber stage was not calculated, but was known to be no more than 47%, and probably much lower. Therefore, the total VCSEL power was probably significantly higher than the values reported below. The pulse driver circuitry had been optimized for low resistance, edge-emitting lasers, so there was poor impedance matching with the high-resistance VCSELs. This led to a slow rise time and strong overshoot with each pulse.

Despite the difficulties mentioned in previous sections, the VCSELs lased in pulsed mode when cooled to a chuck temperature of -10°C . Figure 5.17 shows the multimode fiber coupled optical spectrum at 500mA and 800mA of peak current, showing the onset of stimulated emission. For this measurement, the VCSELs were not bonded or soldered to the copper chuck, but were merely held in place by a plastic tweezer. The resulting poor thermal conductance led to the high threshold currents shown in the figure. The wavelength of lasing, $1.46\mu\text{m}$, is the longest reported wavelength

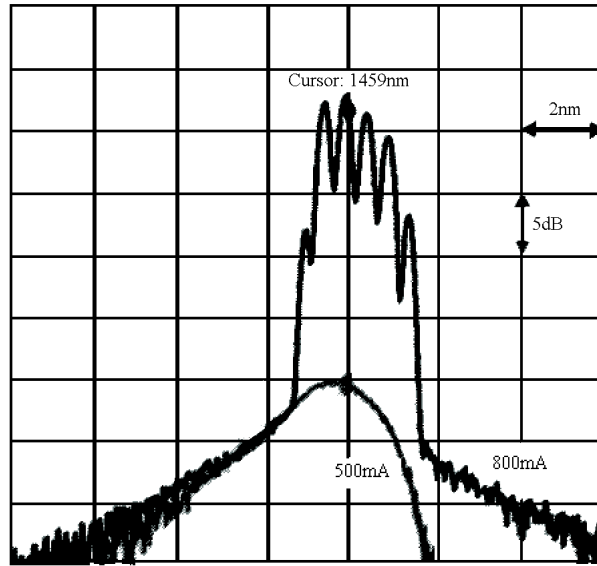


Figure 5.17: Multimode fiber-coupled spectrum of VCSEL pulsed at 500mA (lower curve) and 800mA (upper curve), showing onset of stimulated emission and multiple transverse modes above threshold.

from a GaAs-based VCSEL, far beyond the previously reported $1.32\mu\text{m}$ VCSELs with quantum dots [30, 247], InGaAs [24], or GaInNAs [248].

Multiple transverse modes were visible above threshold, due to the large $66\mu\text{m}$ current aperture size of the VCSELs. The VCSELs QWs were identical to the single quantum well from the equivalent CW $1.49\mu\text{m}$ edge emitting lasers. Due to the lower operating temperature and a short cavity, the VCSELs lased at $1.46\mu\text{m}$, a significantly shorter wavelength. Microcavity emission from a similar structure showed that the growth of the top DBR only partially annealed the active region, but an additional rapid thermal anneal was required for peak photoluminescence. A peak power of 0.77mW was achieved (not shown), which was surprisingly high given the problems outlined above.

The VCSELs were pulsed at 0.1% duty cycle, with $2\mu\text{s}$ pulses at a 500Hz repetition rate. The VCSELs lased at $1.458\text{--}1.460\mu\text{m}$ from -10°C down to at least -30°C , which was the limit of the TEC stage. This particular model of current source, the ILX LDP-3840, produces a constant 4mA of DC output power even when set to 0

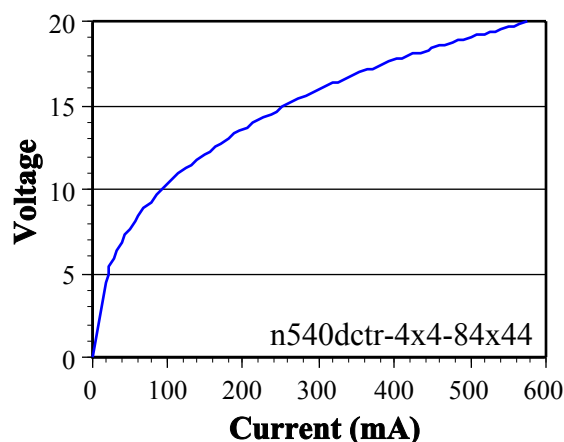


Figure 5.18: Current vs. voltage for VCSELs in pulsed mode.

amps pulsed. Since the point of pulsed measurements is to avoid heating of the device, having such a DC offset greatly reduces the usefulness of the technique. It is not known how much better the VCSELs would operate without this additional DC bias.

The reason the VCSELs did not lase CW, but only in pulsed mode, is clear from Figure 5.18. Not only was the threshold current surprisingly high, but the operating voltages were quite high as well: 20V near threshold. It will be recalled that a high series resistance was expected from the conservative design of the DBRs, with very low doping to avoid free carrier absorption in the DBRs. However, the nonlinear curvature up to high voltages suggests that another mechanism is at work. The doping was not optimized at the heterojunctions, which may have led to some diode-like contribution to the I-V curve. Also, the condition of the metal contacts was in question, since they were excessively annealed (up to 1 hour at 435°C) during the oxidation step. Non-ohmic contacts may have added to the nonlinear voltage characteristic as well.

With heating clearly an issue, the VCSELs were then soldered to the copper chuck, rather than merely held with a plastic clip. The thresholds dropped by approximately a factor of 2. This is evidence that the VCSELs were still heat-limited even in pulsed operation. Several L-I curves for a VCSEL with a 66 μ m diameter aperture are shown in Figure 5.19. The threshold current I_{th} was 229mA (pulsed) at -25°C , 248mA

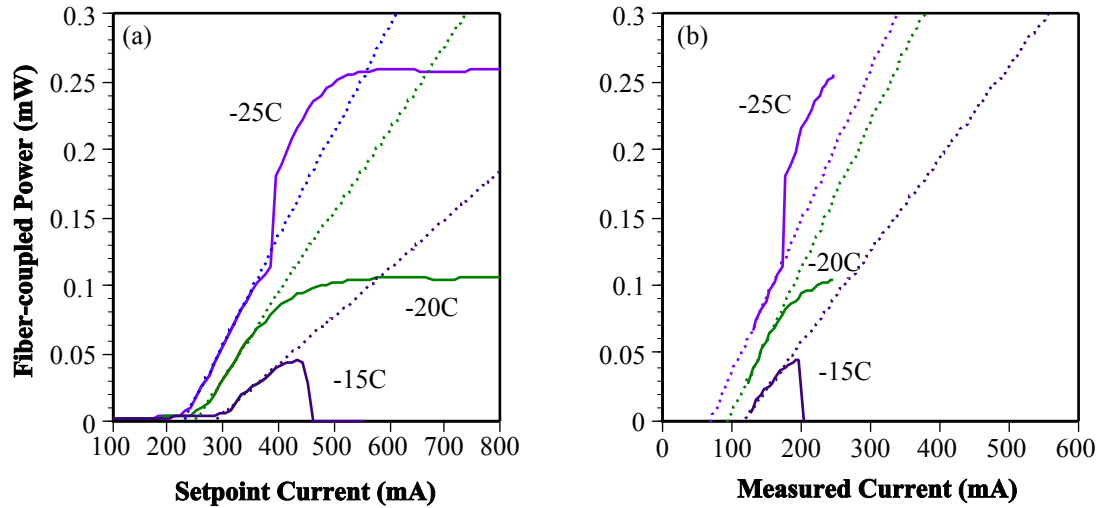


Figure 5.19: Multimode fiber-coupled, pulsed VCSEL output power vs. (a) setpoint current, and (b) measured current, at various temperatures.

at -20°C , and 283mA at -15°C , corresponding to current densities J_{th} of 6.7 , 7.3 , and $8.3\text{kA}/\text{cm}^2$, respectively. The improvement in threshold with better thermal mounting is an indication of excess heating. Attempts to reduce the duty cycle of the VCSELs, to further reduce heating, were unsuccessful. The pulse width needed to be extended² to maintain sufficient signal, but pulses longer than $2.5\mu\text{s}$ led to device failure.

The limits of the current driver were also apparent in the results. The threshold current for each temperature is listed.

The kink in the -25°C curves in Figure 5.19 is explained by overshoot by the current source. The current source and monitoring circuit were designed to be impedance matched to a low-resistance edge emitting laser, and the mismatch with the high-resistance VCSEL led to a slow rise time and an overshoot with each pulse, as mentioned earlier. Also, the current source was operating near its voltage limits. As a result, as the current was increased, the pulses began to overshoot the value of threshold current. A large increase in power resulted when the pulse shape became rounded, as shown schematically in Figure 5.20.

²Slower than the duty cycle was increased, of course.

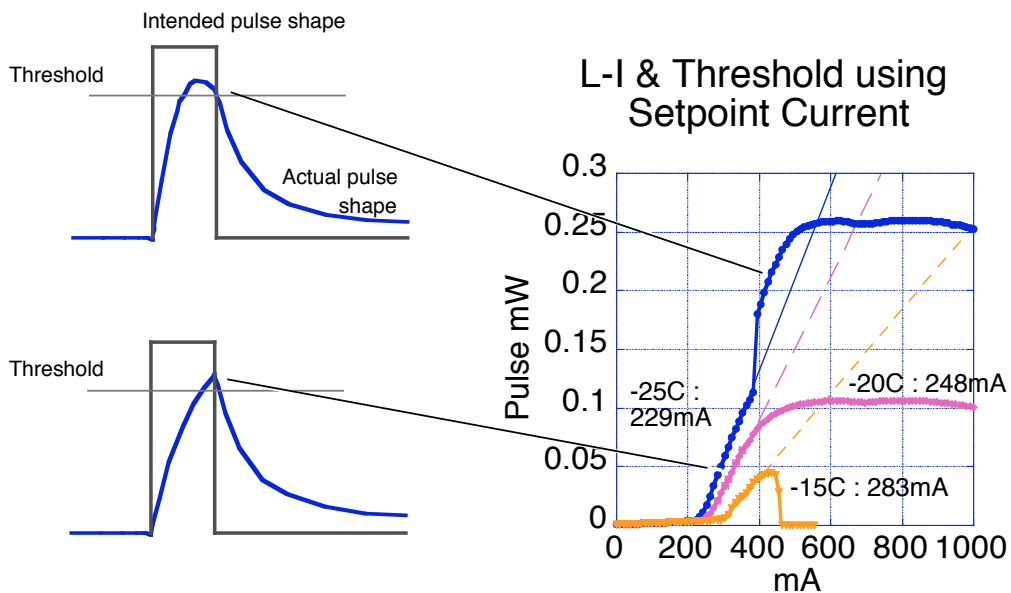


Figure 5.20: Impedance mismatch and limits of pulse driver produce soft turn-on and overshoot.

Table 5.1: VCSEL Threshold Currents with Temperature

	-15°C	-20°C	-25°C
Lower Bound	3.3 kA/cm ²	2.7 kA/cm ²	2.0 kA/cm ²
Upper Bound	8.3 kA/cm ²	7.3 kA/cm ²	6.7 kA/cm ²

With such an unusual pulse shape, it is not clear what the correct measurement of “measured” current should be: integrated current, peak current, integrated current above threshold, etc. The L-I curves all do appear to be linear just above threshold, so the limitations of the current source appear to be problematic only at high voltages and/or currents, and the extraction of threshold current seems to be valid. However, the algorithm used to measure the current—even though it produces a linear L-I curve—may be misled by the non-square pulse shape. Therefore, the thresholds derived from measured current may only represent a lower bound on the actual device thresholds, as shown in Table 5.1.

5.9 Analysis and Summary of VCSEL Results

In summary, GaInNAsSb VCSELs have been demonstrated at $1.46\mu\text{m}$, and there is no reason to believe that they could not reach 1.5 or $1.55\mu\text{m}$, given that CW edge emitting lasers have already been demonstrated beyond $1.5\mu\text{m}$. At these long wavelengths, extra care must be given to optimal DBR design, both electrically and optically. Accurate refractive index data are vital for the design and characterization of the VCSEL structure, as well as for corrections to the cavity during the growth. Heating is another issue, especially with weak gain and thicker DBRs, but this can be minimized by regrowth, planarizing, or careful packaging.

The VCSELs presented here were designed very conservatively, with low doping in the DBRs to avoid free carrier absorption, and with a short cavity that was designed for operation at low temperatures. The VCSELs were grown before the extremely high quality of the CW edge emitting lasers became clear, so in hindsight, a much more aggressive VCSEL design was certainly possible, and probably would have achieved CW lasing at room temperature.

It is believed that shorter pulses, from an impedance-matched current source, would produce better results from these VCSELs. However, the primary focus of this work was on reaching longer wavelengths, and rather than spending additional effort on characterizing the characterization setup itself, so efforts were shifted to future VCSEL growths. The next generation of VCSELs, needless to say, is eagerly anticipated. It seems clear that dilute nitride based VCSELs will soon cover the full range of fiber wavelengths, from 1.2 – $1.6\mu\text{m}$, offering great promise for inexpensive, high bandwidth fiber networking.

Chapter 6

Conclusion

6.1 Summary

This thesis presented several key improvements in the understanding and MBE growth of dilute nitrides such as GaInNAs, culminating in the demonstration of VCSELs at unprecedented long wavelengths on GaAs. The intrinsic properties of dilute nitrides were presented, particularly the small bandgap caused by band anticrossing and several additional, minor effects. The blueshift of the emission wavelength with anneal was examined, as was the increased luminescence after anneal. Defects have been found to play a significant role in the properties of dilute nitrides to date.

To grow good quality material, with few defects, several new techniques were employed. The beam flux ionization gauge in the MBE chamber was used as a remote Langmuir probe to sample the actual ion flux coming from the plasma cell. This ion flux was found to be nonnegligible, and ion deflection plates were employed to remove the ions from the plasma beam. Large voltages on the ion deflection plates made no improvement in the material quality, but moderate voltages, from 18–100V, were found in experiment and theory to be sufficient to remove all measurable ions from the plasma beam. Also, an arsenic capping technique was applied in order to protect the wafer surface from the plasma ignition, and to allow the plasma to reach its final, steady state without exposing the wafer to plasma for an extended period of time. By comparing the effects of ion damage and pre-QW plasma damage, it was

found that defects themselves reduce the bandgap, similar to the redshift from adding nitrogen. Defects also change the amount of nitrogen that gets incorporated into the crystal. It is clear that the role of defects has been overlooked in past materials studies, and those studies are now being repeated with the new, high quality material that we are now able to grow.

The VCSELs presented here were constrained by severe difficulties in processing and by a mirror structure that was not fully optimized. The VCSELs were heat limited, and tested epi-side up, yet they still lased at the design wavelength near $1.46\mu\text{m}$. Simple improvements in the processing and design should allow electrically pumped VCSELs to operate beyond $1.50\mu\text{m}$ and optically pumped VCSELs to operate at even longer wavelengths. Low threshold CW edge emitting lasers have now been demonstrated at $1.52\mu\text{m}$, and pulsed lasers with somewhat higher thresholds at $1.53\mu\text{m}$. It seems clear that monolithic VCSELs will soon be possible at wavelengths up to and including the WDM S band, and possibly the C and L bands as well. It is hoped that these advances will contribute to the development of inexpensive fiber communication networks.

6.2 Future Work

Although a great deal of progress has been made in the understanding of the inherent material properties of dilute nitrides, and in the techniques for growing high quality material, several key requirements remain as tantalizing prospects for the near future. Our DLTS [249] and z-parameter measurements [78] show that a significant number of defects remain in the material even with the improvements provided by this thesis. Further optimization needs to be made of the plasma ignition sequence and the desorption of the arsenic cap. Precise and repeatable temperature control would be extremely helpful for assuring that each growth took place in the small window of acceptable growth parameters; bandgap thermometry has made this possible for undoped wafers, but not yet for doped wafers. An infrared CCD would be very helpful in this regard as well.

Many long wavelength devices are now possible with this material as well. The

foremost of these is the CW, room temperature VCSEL at $1.55\mu\text{m}$ for optical communication. There is also a need for high power (10W) pump lasers at $1.3\text{--}1.5\mu\text{m}$ for solid-state lasers and Raman amplifiers. Ultra fast lasers and modulators, above 10GHz, appear to be possible for $1.5\mu\text{m}$ applications as well. Tunnel junctions based on an Ga(In)AsSb/GaInNAs interface may allow high efficiency multijunction and intracavity-contact VCSELs. Finally, it may be possible to produce direct-emitting lasers in the mid-infrared, from $2\text{--}10\mu\text{m}$, by taking advantage of band bowing on dilute nitrides grown on GaSb or InAs.

Another area of interest is to push to even longer wavelengths with VCSELs. Although edge emitting GaInNAs(Sb) lasers have been demonstrated at $2\mu\text{m}$ on InP [95] and $2.3\mu\text{m}$ on GaSb [96], no VCSELs have been demonstrated at these wavelengths yet. Since gain is likely to be a problem for first-generation VCSELs on these new substrates, an optically-pumped VCSEL test station has been assembled, as shown in Figure 6.1. If the pump beam is at a certain rational fraction of the desired emission wavelength, then the backside DBR can be designed for high reflectivity for both wavelengths, doubling the effectiveness of the pump [250]. Also, optically-pumped VCSELs are much easier to grow and fabricate, since they have much less heating without the electric current, and because there is no need to etch a mesa that would add to thermal isolation; the pump beam can simply be focused to the desired spot size. It is also possible to use dielectric DBRs such as $\text{SiN}_x/\text{SiO}_2$ with optically-pumped VCSELs, since it is not necessary to pass electrical current through the DBR. Infineon has demonstrated antimony-free GaInNAs edge emitting lasers on GaAs that emitted at $1.59\mu\text{m}$, so it may be possible to reach $1.6\mu\text{m}$ with optically-pumped VCSELs.

Finally, there remain several interesting questions that merit further exploration—the answers to which should be considered tenuous in this thesis. For example, it is unclear which parts of the Langmuir probe measurement in Section 4.6 are due to secondary electrons. Is it the current at high V, or its slope, or a more complex contribution? Also, the angle vs. deflection plot in Figure 4.24 is somewhat misleading, because electron current, secondary electrons, and ion current are convoluted together. Finally, it is still unknown what the microscopic mechanism was behind

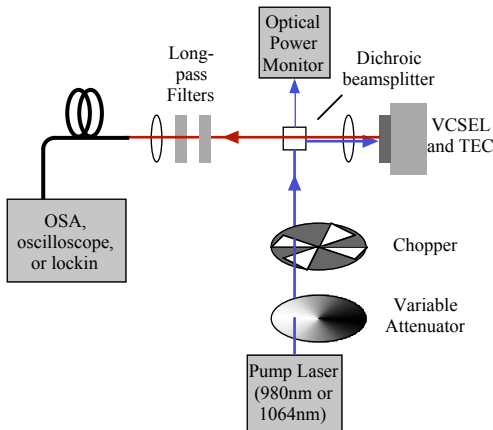


Figure 6.1: Test setup for optically-pumped VCSELs.

the arsenic cap improvement in Section 4.8. Which defects did it get rid of? Was it just surface roughening? If defects cause redshift, why do we sometimes get a sample with blueshift? These questions await the development of further experimental study.

6.3 Other Contributions

A number of other contributions have been made to the lab during the course of this work, including but not limited to the following:

- Replaced the control electronics in the MBE lab, allowing the replacement of the PDP-11 minicomputer with the new Sun workstation. Wayne Martin had done the same for Systems 1 and 2, but the current requirements for Systems 4 and 5 were somewhat different. Maintained all electronics in the lab.
- Rewrote significant sections of the MBE software, especially readflux, euread, and other utilities. The software is able to read and control many more types of instruments, with a modular scheme for future expansion. Several major security holes in the MBE software were also discovered and closed. Maintained all MBE software in the lab.
- Brought up System 4. Installed the carbon tetrabromide source and developed operating procedures for it.

- Improvements to post-growth characterization techniques such as white light reflectivity.
- Maintained and improved the accuracy and interface for the Hall measurement system. Xin Jiang also contributed to the interface.
- Standardized the way we bake out wafers in the load chamber and bakeout chamber. Computer control of load chamber bake lamp. Added logging for forensic examination if something goes wrong with a wafer.
- Designed a folding, telescoping arm for reloading source material without opening the MBE chamber. See Appendix B.1.

Appendix A

Glossary of Abbreviations and Commonly-used Terms

- BFM:** Beam Flux Monitor. An ionization pressure gauge which is used to measure the amount of material (flux) which is coming from one or more cells in an MBE chamber.
- CB:** Conduction band. The energy level of electrons which are free to move in a semiconductor.
- CL:** Cathodoluminescence.
- Crucible:** An open container used for holding hot metals or, in the case of the plasma source, the plasma.
- CW:** Continuous-Wave. The opposite of pulsed or intermittent, as in a laser.
- Dilute Nitride:** GaAs or InGaAs with a small amount of nitrogen replacing up to 5% of the arsenic in the alloy, forming GaNAs or GaInNAs. See also GaInNAs.
- DLTS:** Deep Level Transient Spectroscopy. A characterization technique which measures the defect concentration in a semiconductor as a function of physical depth, as well as the energy levels of the defect levels within the bandgap.
- Epitaxy:** A method of growing semiconductors (and other crystals) one layer of atoms at a time. Each atom lines up with the atom(s) below it in a particular periodic fashion, which depends on the crystal structure of the material.
- GaInNAs:** Gallium indium nitride arsenide. A semiconductor with a small bandgap which emits light in the near infrared.
- GaN:** Gallium Nitride. A semiconductor with a wide bandgap, which emits light in the violet or ultraviolet. Not to be confused with “dilute nitrides” such as GaInNAs.

- ICP:** Inductively Coupled Plasma. One of several methods by which electrical power can be concentrated to create a plasma, by passing RF through a coil.
- IR:** Infrared. Light with a wavelength somewhere beyond the limit of human vision (red, $0.7\mu\text{m}$) toward longer wavelengths (lower energies).
- MBE:** Molecular Beam Epitaxy. A technique for growing very thin layers of very pure semiconductors under ultra-high vacuum. Also known as Mostly Broken Equipment. See Epitaxy.
- MFC:** Mass Flow Controller. A special valve which keeps the gas flow rate constant. Used on the nitrogen plasma cell.
- MOCVD:** A gas-based form of epitaxy. Gases break down at the hot wafer surface, depositing metal atoms.
- PBN:** Pyrolytic Boron Nitride. A white, machinable, nonreactive ceramic. All of the Ga, Al, In, Si, Be, and N crucibles are made from PBN.
- QW:** Quantum Well. A thin (3–20nm) layer of material sandwiched between two layers of larger bandgap. Both electrons and holes can fall into the QW, where they are confined until they either recombine or escape.
- RF:** Radio Frequency. Hundreds of watts of RF power are concentrated, using a coil, to strip electrons from nitrogen gas and generate the plasmas discussed in this thesis.
- RGA:** Residual Gas Analyzer. A mass spectrometer inside the MBE chamber which gives the relative amounts of each type of atom or molecule. Most used when checking for leaks.
- RHEED:** Reflection High-Energy Electron Diffraction. A technique for measuring the wafer surface under high vacuum conditions, such as during MBE growth. RHEED shows surface smoothness, surface reconstruction, and the presence of any amorphous layer such as an arsenic cap.
- Reconstruction:** A repeating pattern of atoms on the surface of an ordered material. The dominant reconstruction for GaAs at growth temperature is (2x4): a rectangle two atoms wide, four atoms long.
- SIMS:** Secondary Ion Mass Spectroscopy. A characterization technique which tells the composition of a wafer as a function of depth.
- UV:** Ultraviolet.
- VB:** Valence band. The energy level of electrons in their lowest-energy state.
- VCSEL:** Vertical-cavity, surface-emitting laser.

Appendix B

Reloading Arm and Electropolishing of Stainless Steel Parts

B.1 Reloading Sources in MBE

John English at the University of California at Santa Barbara has created a tool for reloading a cell of an MBE chamber without opening the growth chamber. This reloading arm is a long, narrow, rigid tray which attaches in place of the nosepiece on the transfer arm. To refill the cell, the transfer tube is vented, and the reloading arm is attached to the transfer arm, with source material placed on the tray. The transfer tube is then closed and pumped down to UHV. The gate valve between the transfer tube and the growth chamber. The transfer arm is extended into the growth chamber, with the reloading arm passing underneath the beam flux gauge and CAR. The reloading arm is aligned with the opening of the cell to be refilled, and the source material is carefully shaken out of the reloading arm into the cell. Fuenzalida has also reported a similar arm, using a bimetallic tweezer, resistively heated, to hold and drop a single pellet of source material.[251]

The advantages of English's technique are that it allows the reloading of one cell without breaking vacuum on the actual growth chamber, and it can hold a large

amount of source material. The main disadvantage is that it still requires breaking vacuum on the transfer tube, thus exposing the cleanest part of the MBE system to atmosphere. Even if the installation of the reloading arm takes place inside a nitrogen-purged glove bag [252], we have found contamination from water vapor still requires a bake, albeit a shorter one. But the transfer tube cannot be baked if the reloading arm is loaded with either gallium or indium, because these elements will melt. This means a long pumpdown must be used on the transfer tube, resulting in a long downtime for the machine. Also, the transfer tube is only pumped by ion pumps, which tend to crack water vapor and release hydrogen, which is not well pumped. Finally, the UCSB design used a long, narrow tray to hold the source material, but this only allows reaching the two lowest sources in the machine. Turning the transfer arm to reach any other sources spills the source material from the tray. It is also quite difficult to refill newer SUMO cells, which have a small neck at the opening.

If a reloading arm could be designed to be loaded on the wafer trolley, many of these difficulties would be avoided. One design which very nearly worked is shown in Figure B.1. The arm consists of two telescoping tubes of stainless steel, with a hinge allowing the tube to fold flat against the trolley, parallel to the face of the transfer arm nosepiece. The inner tube holds the source material and is extended in the growth chamber to reach under the CAR to the lip of the cell. By using a tube rather than a tray, it is possible to reach all of the lower cells in the MBE machine, not just the two middle sources. (With a stiff hinge, the tube can also reach the upper cells. This may not be useful for reloading sources, but could be handy for bending, say, the antimony shutter back in place.) Also, the small diameter of the tube matches the diameter of the SUMO cells, potentially allowing refilling of narrow-necked SUMO cells.

Unfortunately, a single telescoping stage was not sufficient to reach the cells in our Mod-Gen II MBE chamber. With the telescope retracted, the arm must not exceed 6.25in from hinge to tip, or else the tip will run into the sides of the bellows, marked as point "A" in Figure B.1. While this still allows enough length to reach just to the tip of an older, trumpet-style cell, the SUMO cells are mounted farther away from the wafer and, consequently, just barely out of reach of the reloading arm. The reloading

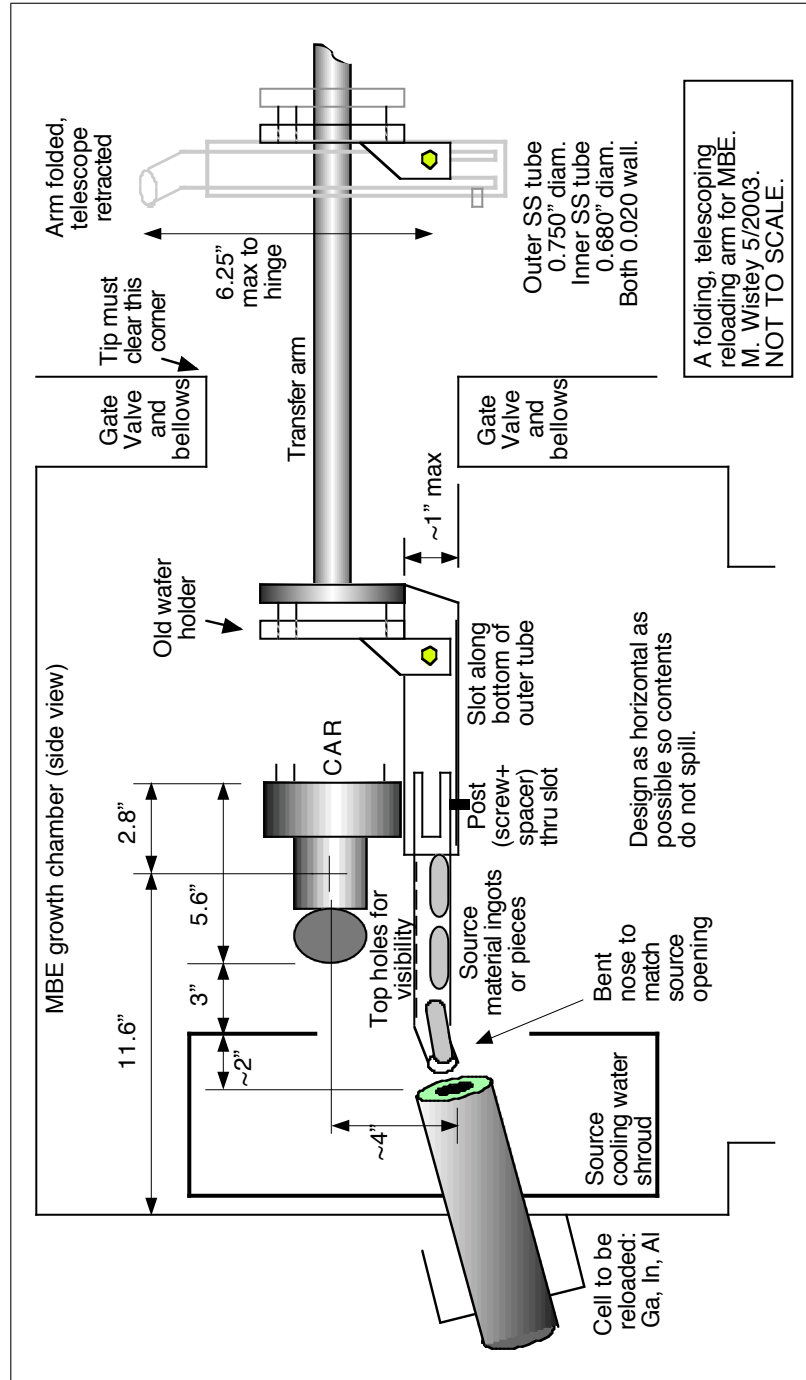


Figure B.1: A retractable reloading arm for refilling MBE cells.

principle was proven using a shorter prototype, which was able to exactly touch the mouth of our aluminum cell, an older trumpet style. This prototype showed good rigidity even with the telescope fully extended. It was also able to reach to the two second-lowest ports on the machine.

System 5 was eventually opened and refilled the conventional way, eliminating the urgency of this project, but the opening was more due to a broken heater more than inherent problems with the technique. With a little more work, all four Group III sources on the MBE machine could be refilled with this technique. There are several possibilities for how to reach the extra 2-4cm to the SUMO cells with a telescoping arm. One would be to add a third, outer tube to the telescope. Another would be to replace or augment the two-stage telescope with a tube which slid along rails.

Although this particular iteration of the reloading arm was not successful, it is still believed that a trolley-loadable reloading arm could prolong an MBE growth campaign indefinitely, or until something major broke. It is hoped that others will pick up where this project left off. The development of a “live” reloading technique would be of great service to the MBE community.

B.2 Electropolishing

Most UHV chambers and large parts are made with stainless steel because it does not outgas in UHV, and it withstands baking at 100°C for short periods. However, machined parts contain many pits and voids due to the machining process, which would lead to virtual leaks due to trapped gases. Also, machined parts are contaminated with heavy oils from cutting tools. In order to introduce new parts to a UHV environment such as an MBE chamber, all stainless steel must first be electropolished. Electropolishing removes trapped oil, passivates the surface (iron and nickel are preferentially etched, leaving unreactive chromium), and removes surface hydrogen. It is also possible to use wrought aluminum and some sand-cast and die-cast aluminum alloys for UHV parts, but electropolishing of aluminum requires perchloric acid and acetic anhydride (in a 2:7 ratio), which is an explosive hazard.[253] Therefore the reloading arm was made with molybdenum or stainless steel parts wherever possible.

In order for electropolishing to be successful, the surface must be extensively cleaned with solvents to remove organic contaminants. For the reloading arm, the parts were soaked in a slightly heated, ultrasonic bath of acetone, then isopropanol, then methanol, then rinsed thoroughly with deionized water. The parts were then soaked briefly in a 50% HNO_3 solution to strip remaining organics, taking care to avoid any droplets of HNO_3 coming in contact with a solvent, which could lead to a fire. A length of 1/4" stainless tubing, longer than the height of the beaker, should be cleaned at the same time, for use as the cathode. This beaker was also thoroughly cleaned with solvents and HNO_3 .

The actual electropolishing is performed as follows. A heavy wire, 12 to 14 gauge, is connected between the positive terminal of a heavy-duty current source, and the sample to be polished, the anode. Another wire is attached between the negative terminal and the cathode. The cathode can be any common metal, but stainless steel tubing avoids contamination issues. The current required for electropolishing is large: more than 10 Amps (100A per square foot of etched material), so the wire must be a heavy gauge. The wires should remain mostly insulated so they cannot accidentally short together outside the beaker. The wires should not be immersed in the acid since they are not ultraclean.

A large, ceramic beaker is filled with a concentrated acid solution of 1:1 sulfuric acid:phosphoric acid, deep enough to cover the sample. If the sample is hollow, such as the tube in the reloading arm, it will need to be electropolished from the inside as well, so it is important to be able to put the cathode inside the sample and repeat the etch. Immerse the sample and the cathode in the acid solution, taking care not to let them touch. Turn up the current slowly, over at least 20 seconds, because there is a delay between the onset of current and the production of gas bubbles (hydrogen). Use enough current that the cathode is bubbling but the etch piece is not; if both are bubbling, turn down the current. A low voltage drop, 2–4V, should appear. Zero volts means your cathode and etch piece have shorted together. Higher voltage (10–30V) either means current is too high (generating too much gas at surfaces) or else the surface of the cathode is dirty and needs cleaning, perhaps just a strong spray of water. The acid solution may turn a bit green, but this is normal.

The I-V curve is supposed to have a flat spot at the ideal etch current density, which occurred just before the onset of massive bubbling. If the solution and parts are clean, nearly all the bubbles will be at the cathode, even at 10A. For the reloading arm, it was not necessary to heat or stir the solution, though those may have helped. The polish worked with either phosphoric or sulfuric acid alone, but a mirror finish required both. The etch is finished when the voltage rises. It may be necessary to remove the sample and cathode, spray with water, and restart the etch. Shake off or blow off excess water before immersing in the acid solution.

The acid is considered hazardous waste and cannot go down the acid sink, since it contains nickel from the stainless steel, a heavy metal poison. It may also contain traces of chromium. Let the acid cool and dispose of it appropriately as hazardous waste.

Appendix C

Publication List

Publications, Conferences, and Invited Talks

1. M. A. Wistey, et al., "Optimization of Photoreceiver Designs," *Proceedings of the National Conf. on Undergraduate Research*, 1994.
2. S. G. B. Spruytte, M. A. Wistey, M. C. Larson, C. W. Coldren, H. Garrett and J. S. Harris, Jr., "1.3 Micron Opto-electronic Devices on GaAs using Group III-Nitride-Arsenides," *Photonics West 2001*, San Jose, California, Proc. SPIE, vol. 4286, pp. 22-33.
3. Vincent Gambin, Wonill Ha, Mark Wistey, Seongsin Kim, and James S. Harris, "GaInNAs Material Properties for Long Wavelength Opto-Electronic Devices," *MRS 2001 Fall Meeting*, H7.1,
4. Ha, W; Gambin, V; Wistey, M; Kim, S; Harris, "High efficiency multiple quantum well GaInNAs/GaNAs ridge-waveguide laser diode operating out to 1.4 μm ," *J. Compound Semiconductors*, 2001; 2002; no.170, p.165-169
5. W. Ha, V. Gambin, M. Wistey, S. Kim, J. S. Harris Jr., "High Efficiency Multiple Quantum Well GaInNAs/GaNAs Ridge-Waveguide Laser Diode Operating up at 1.386 μm ," *Proc. 28th International Symposium on Compound Semiconductors (ISCS)*, Oct. 2001, Tokyo, Japan.
6. V. Gambin, W. Ha, M. Wistey, S. Bank, H. Yuen, S. Kim, J. Harris, "Material Properties for Long Wavelength Opto-Electronic Devices," *Proc. Mat. Res. Soc.*, Vol. 692, Nov. 2001, Boston, Massachusetts.
7. V. Gambin, W. Ha, S. R. Bank, M. A. Wistey, H. B. Yuen, S. Kim, and J. S. Harris Jr., "Nitrogen Incorporation in GaInNAs," *Fall 2001 MRS Meeting*, Boston, MA, November 2001.
8. W. Ha, V. Gambin, M. Wistey, S. Kim, J. S. Harris Jr., "Long wavelength GaInNAs Ridge Waveguide Lasers with GaNAs Barriers," *Proc. 14th IEEE Lasers and Electro-Optics Society (LEOS)*, Nov. 2001, San Diego, CA.
9. W. Ha, V. Gambin, S. Bank, M. Wistey, S. Kim, J. S. Harris Jr., "High Efficiency Multiple Quantum Well GaInNAs/GaNAs Ridge-Waveguide Diode Lasers," *Proc. SPIE Photonics West 2002*, Jan. 2002, San Jose, California.
10. E. Thrush, O. Levi, K. Wang, M. A. Wistey, J. S. Harris, S. J. Smith, "High throughput devices for biochip fluorescent detection," *Proc. SPIE*, v. 4982, pp. 162-169, 2002.
11. W. Ha, V. Gambin, M. Wistey, S. Bank, H. Yuen, S. Kim, J. Harris, "Long Wavelength GaInNAsSb/GaNAsSb Multiple Quantum Well Lasers," *Electron. Lett.*, Vol. 38, No. 6, pp. 277-8, Mar. 2002.
12. W. Ha, V. Gambin, M. A. Wistey, S. R. Bank, H. B. Yuen, S. Kim, and J. S. Harris Jr., "Long Wavelength GaInNAs(Sb) Lasers on GaAs," *Optical Fiber Communications 2002 Meeting*, Anaheim, CA, March 2002.
13. V. Lordi, V. Gambin, W. Ha, S. Bank, J. Harris, "Examination of N Incorporation into GaInNAs," *Proc. MRS*, Vol. 722, Apr., 2002, San Francisco, California.
14. V. Gambin, W. Ha, M. Wistey, S. Bank, H. Yuen, S. Kim, J. Harris, "High Intensity 1.3–1.6 μm Luminescence from MBE Grown GaInNAsSb," *Proc. MRS*, Vol. 722, Apr., 2002, San Francisco, California.
15. J. S. Harris Jr., M. Larson, S. Spruytte, C. Coldren, V. Gambin, W. Ha, M. A. Wistey, H. B. Yuen, S. R. Bank, T. Gugov, "GaInNAs: A New Material in the Quest for Communication Lasers," *Spring 2002 MRS Meeting*, San Francisco, CA, April 2002.
16. W. Ha, V. Gambin, S. Bank, M. Wistey, S. Kim, J. S. Harris Jr., "Long Wavelength GaInNAs(Sb) Lasers on GaAs," *Proc. 14th International Conf. on Indium-Phosphide and Related Materials (IPRM)*, May 2002, Stockholm, Sweden.
17. W. Ha, V. Gambin, M. Wistey, S. Bank, S. Kim, J. Harris, "Multiple Quantum Well GaInNAs/GaNAs Ridge-Waveguide Laser Diodes Operating Out to 1.4 μm ," *IEEE Photon. Technol. Lett.*, Vol. 14, No. 5, May 2002.
18. W. Ha, V. Gambin, S. Bank, M. Wistey, S. Kim, J. S. Harris Jr., "Long Wavelength GaInNAs(Sb) Lasers on GaAs," *Proc. 22nd Conf. on Lasers and Electro-Optics (CLEO)*, May 2002, Long Beach, California.

19. V. Gambin, W. Ha, M. Wistey, S. Bank, H. Yuen, S. Kim, J. Harris, "Long Wavelength, High Efficiency Photoluminescence from MBE Grown GaInNAsSb," *44th Electronic Materials Conf. (EMC)*, June 2002, Santa Barbara, California.
20. W. Ha, V. Gambin, S. Bank, M. Wistey, S. Kim, J. S. Harris Jr., "A 1.5 μm GaInNAs(Sb) Laser Grown on GaAs by MBE," *60th Device Research Conf. (DRC)*, June 2002, Santa Barbara, California.
21. V. Gambin, W. Ha, M. Wistey, S. Bank, H. Yuen, S. Kim, J. Harris, "GaInNAsSb for 1.3-1.6 μm Long-Wavelength Lasers Grown by Molecular Beam Epitaxy," *J. Select. Topics Quantum Electron.*, Vol. 8, No. 4, pp. 795-800, July 2002.
22. V. Gambin, V. Lordi, W. Ha, M. Wistey, K. Volz, S. Bank, H. Yuen, J. Harris, "High Intensity 1.3-1.6 μm Luminescence and Structural Changes on Anneal from MBE Grown (Ga, In)(N,As,Sb)," *12th International Conference on MBE*, Sep. 2002, San Francisco, California.
23. W. Ha, V. Gambin, S. Bank, M. Wistey, H. Yuen, L. Goddard, S. Kim, J. S. Harris Jr., "A 1.5 μm GaInNAs(Sb) Laser Grown on GaAs by MBE," *12th International Conference on MBE*, Sep. 2002, San Francisco, California.
24. K. Volz, V. Gambin, W. Ha, M. Wistey, J. S. Harris, "Structure and composition of (GaIn)(NAsSb)/GaAs multi quantum well structures grown by MBE," *12th International Conference on MBE*, 2002.
25. W. Ha, V. Gambin, S. Bank, M. Wistey, H. Yuen, S. Kim, J. S. Harris Jr., "A 1.5 μm GaInNAs(Sb) Laser Grown on GaAs by MBE," *Proc. 18th IEEE International Semiconductor Laser Conf. (ISLC)*, Sep. 2002, Garmisch, Germany.
26. W. Ha, V. Gambin, M. Wistey, S. Bank, H. Yuen, S. Kim, J. Harris, "Long Wavelength GaInNAs(Sb) Lasers on GaAs," *J. Quantum Electron.*, Vol. 38, No. 9, pp. 1260-7, Sep. 2002.
27. V. Gambin, V. Lordi, W. Ha, M. Wistey, T. Takizawa, K. Uno, S. Friedrich, J. S. Harris, "Structural changes on annealing of MBE grown (Ga, In) (N, As) as measured by X-ray absorption fine structure," *Journal of Crystal Growth*, Apr. 2003, v.251, no.1-4, p.408-411.
28. S. Bank, W. Ha, V. Gambin, M. Wistey, H. Yuen, L. Goddard, J. S. Harris, "1.5- μm GaInNAs(Sb) Lasers Grown on GaAs by MBE," *Journal of Crystal Growth*, v. 251, pp. 367-371, 2003.
29. K. Volz, V. Gambin, W. Ha, M. A. Wistey, H. Yuen, S. Bank, J. S. Harris, "The role of Sb in the MBE growth of (GaIn)(NAsSb)," *Journal of Crystal Growth*, v. 251, pp. 360-366, 2003.
30. E. Thrush, O. Levi, K. Wang, M. A. Wistey, J. S. Harris, "Integrated semiconductor fluorescent detection system for biochip and biomedical applications," *Proc. SPIE*, v. 4626, pp. 289-297, 2003.
31. Hyunsoo Yang, A. Khalili, M. Wistey, S. Bank, Homan Yuen, J. Harris, D. Falquier, B. Moslehi, "Long wavelength GaInNAs(Sb) in-line fiber photodetector on GaAs," *Conference on Lasers and Electro-Optics (CLEO)*, June 2003.
32. H. B. Yuen, S. R. Bank, M. A. Wistey, A. Moto, J. S. Harris, "An Investigation of GaNAs(Sb) for Strain Compensated Active Regions at 1.3 and 1.55 μm ," *Electronic Materials Conf. (EMC)*, June 2003, Salt Lake City, Utah.
33. H. B. Yuen, S. R. Bank, M. A. Wistey, W. Ha, V. Gambin, A. Moto, J. S. Harris Jr., "Analysis of Material Properties of GaNAs(Sb) Grown by MBE," *Electronic Materials Conf. (EMC)*, June 2003, Salt Lake City, Utah.
34. S. R. Bank, H. B. Yuen, W. Ha, V. F. Gambin, M. A. Wistey, J. S. Harris, "Strong Photoluminescence Enhancement of 1.3 μm GaInNAs Active Layers by Introduction of Antimony," *45th Electronic Materials Conf. (EMC)*, June 2003, Salt Lake City, Utah.
35. S. R. Bank, M. A. Wistey, H. B. Yuen, L. L. Goddard, J. S. Harris, "Low Threshold, CW, Room Temperature 1.49 μm GaAs-Based Lasers," *61st Device Research Conf. (DRC)*, Late News, June 2003, Salt Lake City, Utah.
36. S. R. Bank, M. A. Wistey, H. B. Yuen, L. L. Goddard, J. S. Harris, "Low Threshold, CW, Room Temperature 1.49 μm GaAs-Based Lasers," *30th International Symposium on Compound Semiconductors (ISCS)*, Aug. 2003, San Diego, California.
37. S. R. Bank, M. A. Wistey, H. B. Yuen, L. L. Goddard, J. S. Harris, "A Low Threshold CW GaInNAsSb/GaAs Laser at 1.49 μm ," *Electron. Lett.*, vol. 39, pp. 1445-6, Oct. 2, 2003.
38. M. A. Wistey, S. R. Bank, H. B. Yuen, L. L. Goddard, J. S. Harris, "Real-Time Ion Count from Nitrogen Plasma Source," *2003 North American Conf. on Molecular Beam Epitaxy (NAMBE)*, P2-9, Oct. 2003.
39. M. A. Wistey, S. R. Bank, H. B. Yuen, L. L. Goddard, J. S. Harris, "GaInNAs(Sb) VCSELs at 1460nm," *2003 North American Conf. on Molecular Beam Epitaxy (NAMBE)*, Oct. 2003.
40. H. B. Yuen, V. Lordi, S. R. Bank, M. A. Wistey, J. S. Harris Jr., and A. Moto, "Analysis of Material Properties of GaNAs(Sb) Grown by MBE," *Fall 2003 MRS Meeting*, Boston, MA, December 2003.
41. M. A. Wistey, S. R. Bank, H. B. Yuen, L. L. Goddard, J. S. Harris, "Monolithic, GaInNAsSb VCSELs at 1460nm on GaAs by MBE," *Electronics Letters*, 39, pp. 1822-3, Dec. 12, 2003.
42. S. R. Bank, M. A. Wistey, H. B. Yuen, L. L. Goddard, J. S. Harris, "Progress Towards High Power 1.5 μm GaInNAsSb/GaAs Lasers for Raman Amplifiers," *2004 Optical Fiber Communication Conf. (OFC)*, Feb. 2004, Los Angeles, California.
43. V. Lordi, H. B. Yuen, S. R. Bank, M. A. Wistey, and J. S. Harris Jr., "Electroabsorption Properties of GaInNAs(Sb) Quantum Wells at 1300-1600 nm," *Spring 2004 MRS Meeting*, San Francisco, CA, April 2004.
44. L. L. Goddard, S. R. Bank, M. A. Wistey, H. B. Yuen, J. S. Harris, "Measurements of Intrinsic Properties of High Power CW Single Quantum Well GaInNAsSb/GaAs Lasers at 1.5 μm ," *2004 Conf. on Lasers and Electro-Optics (CLEO)*, May 2004, San Francisco, California.
45. S. R. Bank, L. L. Goddard, M. A. Wistey, H. B. Yuen, J. S. Harris, "The Temperature Sensitivity of 1.5 μm GaInNAsSb Lasers on GaAs," *2004 Conf. on Lasers and Electro-Optics (CLEO)*, San Francisco, California, May 2004.
46. S. R. Bank, M. A. Wistey, L. L. Goddard, H. B. Yuen, J. S. Harris, "Low Threshold, Continuous Wave, 1.5 μm GaInNAsSb Lasers Grown on GaAs," *IEEE Journal of Quantum Electronics*, vol. 40, no. 6, pp. 656-664, June 2004.
47. M. A. Wistey, S. R. Bank, H. B. Yuen, L. L. Goddard, J. S. Harris, "GaInNAs(Sb) vertical-cavity surface-emitting lasers at 1.46 μm ," *J. Vac. Sci. Tech.-B*, 22, no. 3, pp. 1562-1564, May/June 2004.
48. M. A. Wistey, "GaInNAs on GaAs: Fiber optics lasers for the masses," *Lockheed Martin Advanced Technology Center Colloquium*, Feb. 5, 2004.

49. M. A. Wistey, S. R. Bank, H. B. Yuen, L. L. Goddard, J. S. Harris, "GaInNAsSb/GaNAs VCSELs at 1.46 μ m," *2004 Conf. on Lasers and Electro-Optics (CLEO)*, May 2004, San Francisco, California.
50. J. S. Harris, Jr., M. Wistey, S. Bank, L. Goddard, V. Lordi, H. Bae, H. Yuen, "Long-Wavelength Dilute Nitride-Antimonide Lasers," Chapter 17 in *Dilute Nitride (III-N-V) Semiconductors: Physics and Technology*, M. Henini, editor. Taylor & Francis, 2004.
51. J. S. Harris, Jr., H. Yuen, M. Wistey, S. Bank, V. Lordi, T. Gugov, H. Bae, L. Goddard, "MBE Growth and Characterization of Long Wavelength Dilute Nitride III-V Alloys," Chapter 1 in *Dilute Nitride (III-N-V) Semiconductors: Physics and Technology*, M. Henini, editor. Taylor & Francis, 2004.
52. T. Gugov, V. Gambin, M. Wistey, H. Yuen, S. Bank, J. S. Harris, "Use of transmission electron microscopy in the characterization of GaInNAs(Sb) quantum well structures grown by molecular beam epitaxy," *J. Vac. Sci. Tech.-B*, 22, no. 3, pp. 1588-1592, May/June 2004.
53. J.-X. Fu, S. R. Bank, M. A. Wistey, H. B. Yuen, J. S. Harris, "Solid-source molecular-beam epitaxy growth of GaInNAsSb/InGaAs single quantum well on InP with photoluminescence peak wavelength at 2.04 μ m," *J. Vac. Sci. Tech.-B*, 22, no. 3, pp. 1463-1467, May/June 2004.
54. A. Khalili, M. A. Wistey, J. S. Harris Jr., "Side-coupled in-line fiber-semiconductor laser," *Proc. SPIE*, v. 5355, p. 159, 2004.
55. Tihomir Gugov, Mark Wistey, Homan Yuen, Seth Bank, James S. Harris Jr., "Structural characterization of molecular beam epitaxy grown GaInNAs and GaInNAsSb quantum wells by transmission electron microscopy," *Spring 2004 MRS Meeting*, San Francisco, CA, April 2004.
56. H. B. Yuen, S. R. Bank, M. A. Wistey, H. Bae, J. S. Harris Jr., and A. Moto, "Effects of N₂ Flow on GaInNAs Grown by a RF Plasma cell in MBE," *Spring 2004 MRS Meeting*, San Francisco, CA, April 2004.
57. S. R. Bank, V. Lordi, M. A. Wistey, H. B. Yuen, and J. S. Harris, "Temperature Dependent Behavior of GaInNAs(Sb) Alloys Grown on GaAs," *46th Electronic Materials Conf.*, Notre Dame, June 2004.
58. S. R. Bank, M. A. Wistey, H. B. Yuen, L. L. Goddard, and J. S. Harris, "The role and suppression of carrier leakage in 1.5 μ m GaInNAsSb/GaAs lasers," *62nd Device Research Conf. (DRC)*, June 2004, Notre Dame.
59. M. A. Wistey, S. R. Bank, H. B. Yuen, V. F. Gambin, and J. S. Harris, "Low-Voltage Deflection Plates Reduce Plasma Damage in MBE Dilute Nitride Growth," *46th Electronic Materials Conf.*, Notre Dame, 2004.
60. S. R. Bank, M. A. Wistey, L. L. Goddard, H. B. Yuen, H. P. Bae, and J. S. Harris, "High Performance 1.5- μ m GaInNAsSb Lasers Grown on GaAs," *Electron. Lett.*, Vol. 40, No. 19, pp. 1186-1187, 16 Sep 2004.
61. H. B. Yuen, M. A. Wistey, S. R. Bank, Hopil Bae, A. Moto, and J. S. Harris, "An investigation of nitrogen flow variation into an rf plasma cell on plasma properties and GaInNAs(Sb) grown by molecular beam epitaxy," *North American Conf. on Molecular Beam Epitaxy (NAMBE)*, Banff, Canada, Oct. 2004.
62. M. A. Wistey, S. R. Bank, H. B. Yuen, Hopil Bae, and J. S. Harris, "Nitrogen Plasma Optimization for High Quality Dilute Nitrides," *International Conf. on Molecular Beam Epitaxy*, Edinburgh, Scotland, 2004.
63. S. R. Bank, M. A. Wistey, H. B. Yuen, V. Lordi, V. F. Gambin, and J. S. Harris Jr., "Effects of Antimony and Ion Damage on Carrier Localization in MBE-Grown GaInNAs," *2004 North American Conf. on Molecular Beam Epitaxy (NAMBE)*, Banff, Canada, Oct. 2004.
64. S. R. Bank, M. A. Wistey, H. B. Yuen, L. L. Goddard, H. P. Bae, and J. S. Harris Jr., "MBE Growth of Low-Threshold CW GaInNAsSb Lasers at 1.5 μ m," *2004 North American Conf. on Molecular Beam Epitaxy (NAMBE)*, Banff, Canada, Oct. 2004.
65. M. A. Wistey, S. R. Bank, H. B. Yuen, Lynford Goddard, Tihomir Gugov, and J. S. Harris, "Protecting wafer surface during GaInNAs plasma ignition by use of an arsenic cap," *2004 North American Conf. on Molecular Beam Epitaxy (NAMBE)*, Banff, Canada, Oct. 2004.
66. L. L. Goddard, S. R. Bank, M. A. Wistey, H. B. Yuen, H. P. Bae, J. S. Harris, "Reduced monomolecular recombination in GaInNAsSb/GaAs lasers at 1.5 μ m," *LEOS 2004*.
67. H. B. Yuen, S. R. Bank, M. A. Wistey, J. S. Harris Jr., and A. Moto, "Comparison of GaNAsSb and GaNAs as Quantum Well Barriers for GaInNAsSb Optoelectronic Devices Operating at 1.3-1.55 μ m," *J. Appl. Phys.*, Vol. 96, No. 11, 1 Dec. 2004.
68. H.B. Yuen, M.J. Seong, S. Yoon, R. Kudrawiec, S.R. Bank, M.A. Wistey, J. Misciewicz, A. Mascarenhas, and J.S. Harris Jr., "Improved Optical Quality from Indium-Free GaNAsSb in the Dilute Sb (\approx 3%) Limit," *Fall 2004 MRS Meeting*, Boston, MA, December 2004.
69. D. Gollub, M. Kamp, A. Forchel, J. Seufert, S. R. Bank, M. A. Wistey, H. B. Yuen, L. L. Goddard and J. S. Harris Jr., "Continuous-wave operation of GaInNAsSb distributed feedback lasers at 1.5 μ m," *Electronics Letters*, Vol. 40, No. 23, pp. 1487-1488, 11 Nov 2004.
70. L. L. Goddard, S. R. Bank, M. A. Wistey, H. B. Yuen, J. S. Harris, "High performance GaInNAsSb/GaAs lasers at 1.5 μ m," *Photonics West 2005*, San Jose, CA, 2005.

Pending:

1. S. R. Bank, L. L. Goddard, M. A. Wistey, H. B. Yuen, J. S. Harris, "On the Temperature Sensitivity of 1.5 μ m GaInNAsSb Lasers," submitted to *IEEE Journal of Quantum Electronics*.
2. M. A. Wistey, S. R. Bank, H. B. Yuen, J. S. Harris, "Using beam flux monitor as Langmuir probe for plasma-assisted MBE," submitted to *J. Vac. Sci. Tech.-A*
3. M. A. Wistey, H. B. Yuen, S. R. Bank, J. S. Harris, "Redshift from plasma-related defects in GaInNAs(Sb)," to be submitted to *Appl. Phys. Lett.*

4. M. A. Wistey, S. R. Bank, H. B. Yuen, and J. S. Harris, "Reduced damage during growth of GaInNAs using low voltage ion deflection plates," submitted to *Appl. Phys. Lett.*
5. M. A. Wistey, S. R. Bank, H. B. Yuen, and J. S. Harris, "Nitrogen plasma optimization for high quality dilute nitrides," accepted to *J. Cryst. Growth*
6. M. A. Wistey, S. R. Bank, H. B. Yuen, L. L. Goddard, J. S. Harris, "Protecting wafer during plasma ignition by use of an arsenic cap," submitted to *J. Vac. Sci. Technol.-B*.
7. S. R. Bank, L. L. Goddard, M. A. Wistey, H. B. Yuen, and J. S. Harris, "Effects of Auger Recombination, Carrier Leakage, and Intolerance Band Absorption in 1.5 μm GaInNAsSb Lasers," submitted to *IEEE J. Quantum Electron.*
8. S. R. Bank, M. A. Wistey, H. B. Yuen, V. Lordi, V. F. Gambin, and J. S. Harris Jr., "Effects of Antimony and Ion Damage on Carrier Localization in MBE-Grown GaInNAs," submitted to *J. Vac. Sci. Technol. B*.
9. S. R. Bank, M. A. Wistey, H. B. Yuen, L. L. Goddard, H. P. Bae, and J. S. Harris Jr., "MBE Growth of Low-Threshold CW GaInNAsSb Lasers at 1.5 μm ," submitted to *J. Vac. Sci. Technol. B*.
10. R. Kudrawiec, K. Ryczko, J. Misiewicz, H. B. Yuen, S. R. Bank, M. A. Wistey, H. P. Bae, and J. S. Harris Jr., "The Band Gap Discontinuity in GaNAsSb/GaAs Single Quantum Wells Investigated by Photoreflectance Spectroscopy," submitted to *Appl. Phys. Lett.*
11. L. L. Goddard, S. R. Bank, M. A. Wistey, H. B. Yuen, Z. L. Rao and J. S. Harris Jr., "Recombination, Gain, Band Structure, Efficiency, and Reliability of 1.5 μm GaInNAsSb/GaAs Lasers," submitted to *J. Appl. Phys.*
12. R. Kudrawiec, K. Ryczko, J. Misiewicz, H. B. Yuen, S. R. Bank, M. A. Wistey, H. P. Bae, and J. S. Harris Jr., "Photoreflectance and Photoluminescence Investigations of a Step-Like GaInNAsSb/GaAsN/GaAs Quantum Well Tailored at 1.5 μm : the Energy Level Structure and the Stokes Shift," submitted to *J. Appl. Phys.*
13. R. Kudrawiec, J. Sitarek, J. Misiewicz, S. R. Bank, H. B. Yuen, M. A. Wistey, and J. S. Harris Jr., "Interference Effects in Electromodulation Spectroscopy Applied to GaAs-Based Structures: a Comparison of Photoreflectance and Contactless Electoreflectance," submitted to *J. Appl. Phys.*

Minor posters and presentations:

1. J. S. Harris, Jr., S. G. Spruytte, M. Larson, C. Coldren, V. F. Gambin, M. Wistey and S. Bond, "Low-Voltage Optical Interconnects using GaInNAs," MARCO Workshop, Atlanta, Georgia, Aug. 2000.
2. M. Wistey, W. Ha, C. Coldren, S. G. Spruytte, M. Larson and J. S. Harris, Jr., "Long Wavelength Vertical Cavity Surface Emitting Lasers," CNOM Meeting, Stanford University, Sept. 2000.
3. M. Wistey, V. F. Gambin, S. G. Spruytte, M. Larson, C. Coldren and J. S. Harris, Jr., "Long Wavelength, GaAs-Based VCSELs," LAM Grand Opening, Stanford University, Oct. 2000
4. M. Wistey, V. F. Gambin, S. G. Spruytte, M. Larson, C. Coldren and J. S. Harris, Jr., "Long Wavelength, GaAs-Based VCSELs," CIS AdCom, Stanford University, Oct. 2000
5. J. S. Harris Jr., M. A. Wistey, V. Gambin, W. Ha, T. Gugov, H. B. Yuen, S. R. Bank, "GaInNAs: A New Material in the Race for High Speed, Low Cost, Long Wavelength MAN and LAN Transmitters," SNRC Workshop, Stanford, CA December 2001.

On the lighter side:

1. E. A. Viau and M. Wistey, "The mathematical determination of optimal human population size," *J. Recreational Math.*, Vol. 28, Issue 3, p188-193, AN 9712113463, 1996/7.
2. M. A. Wistey and S. R. Bank, "Molecular Heterodyning: Using Nonlinear Mixing to Convert ^{208}Pb to ^{197}Au ," Stanford EE Research Fair, 1 Apr. 2003.

Bibliography

- [1] J. M. Reifsnider, S. Govindaraju, and A. L. Holmes, “Use of optical emission intensity to characterize an RF plasma source for MBE growth of GaAsN.” *J Cryst Growth*, vol. 243, no. 3/4, pp. 396 – 403, SEP 2002.
- [2] A. R. Kovsh, D. A. Livshits, N. A. Maleev, A. E. Zhukov, V. M. Ustinov, J. S. Wang, R. S. Hsiao, G. Lin, J. Y. Chi, and N. N. Ledentsov, “1.3 micron single lateral mode lasers based on InAs qds and InGaAsN quantum wells,” in *North American Molecular Beam Epitaxy Conference. Oct. 2003, Keystone, Colorado, 2003*.
- [3] M. Weyers, M. Sato, and H. Ando, “Red shift of photoluminescence and absorption in dilute GaAsN alloy layers.” *Jpn J Appl Phys 2*, vol. 31, no. 7A, pp. L853 – 5, JUL 1992.
- [4] S. Sakai, Y. Ueta, and Y. Terauchi, “Band gap energy and band lineup of III–V alloy semiconductors incorporating nitrogen and boron.” *Jpn J Appl Phys 1*, vol. 32, no. 10, pp. 4413 – 17, OCT 1993.
- [5] P. Krispin, S. G. Spruytte, J. S. Harris, and K. H. Ploog, “Electron traps in ga(as,N) layers grown by molecular–beam epitaxy.” *Applied Physics Letters*, vol. 80, no. 12, pp. 2120 – 2, MAR 2002.
- [6] Y. Zhang, B. Fluegel, M. C. Hanna, J. F. Geisz, L. W. Wang, and A. Mascarenhas, “Effects of heavy nitrogen doping in III–V semiconductors – how well does the conventional wisdom hold for the dilute nitrogen “III–V–N alloys”?.” *Physica Status Solidi B*, vol. 240, no. 2, pp. 396 – 403, 2003.

- [7] S. B. Zhang and S. H. Wei, "Nitrogen solubility and induced defect complexes in epitaxial GaAs:N." *Phys Rev Lett*, vol. 86, no. 9, pp. 1789 – 92, FEB 2001.
- [8] M. Kondow, K. Uomi, A. Niwa, T. Kitatani, S. Watahiki, and Y. Yazawa, "GaInNAs: a novel material for long-wavelength-range laser diodes with excellent high-temperature performance." *Jpn J Appl Phys 1*, vol. 35, no. 2B, pp. 1273 – 5, FEB 1996.
- [9] S. Bharatan, K. S. Jones, C. R. Abernathy, S. J. Pearton, F. Ren, P. W. Wisk, and J. R. Lothian, "Structural characterization of GaN and GaAs_xN_{1-x} grown by electron cyclotron resonance-metalorganic molecular beam epitaxy." *J Vac Sci Technol A*, vol. 12, no. 4, pp. 1094 – 1098, JUL-AUG 1994.
- [10] M. Kondow, K. Uomi, K. Hosomi, and T. Mozume, "Gas-source molecular beam epitaxy of GaN_xAs_{1-x} using a N radical as the N source." *Jpn J Appl Phys 2*, vol. 33, no. 8A, pp. L1056 – 8, AUG 1994.
- [11] M. Kondow, T. Kitatani, S. Nakatsuka, M. C. Larson, K. Nakahara, Y. Yazawa, M. Okai, and K. Uomi, "GaInNAs: a novel material for long-wavelength semiconductor lasers." *J Select Topics Quantum Electron*, vol. 3, no. 3, pp. 719 – 30, JUN 1997.
- [12] S. Sato, Y. Osawa, T. Saitoh, and I. Fujimura, "Room-temperature pulsed operation of 1.3 μm GaInNAs/GaAs laser diode." *Electron Lett*, vol. 33, no. 16, pp. 1386 – 7, JUL 1997.
- [13] M. C. Larson, M. Kondow, T. Kitatani, K. Tamura, Y. Yazawa, and M. Okai, "Photopumped lasing at 1.25 μm of GaInNAs-GaAs multiple-quantum-well vertical-cavity surface-emitting lasers." *IEEE Photonics Technol Lett*, vol. 9, no. 12, pp. 1549 – 51, DEC 1997.
- [14] X. Yang, M. J. Jurkovic, J. B. Heroux, and W. I. Wang, "Molecular beam epitaxial growth of InGaAsN:Sb/GaAs quantum wells for long-wavelength semiconductor lasers." *Appl Phys Lett*, vol. 75, no. 2, pp. 178 – 80, JUL 1999.

- [15] M. C. Larson, C. W. Coldren, S. G. Spruytte, H. E. Petersen, and J. S. Harris, "Low-threshold oxide-confined GaInNAs long wavelength vertical cavity lasers." *IEEE Photonics Technol Lett*, vol. 12, no. 12, pp. 1598 – 600, DEC 2000.
- [16] H. Shimizu, K. Kumada, S. Uchiyama, and A. Kasukawa, "High performance CW 1.26 μm GaInNAsSb-SQW and 1.20 μm GaInAsSb-SQW ridge lasers." *Electron Lett*, vol. 36, no. 20, pp. 1701 – 3, SEP 2000.
- [17] —, "High-performance CW 1.26- μm GaInNAsSb-SQW ridge lasers." *J Select Topics Quantum Electron*, vol. 7, no. 2, pp. 355 – 64, MAR-APR 2001.
- [18] M. Fischer, M. Reinhardt, and A. Forchel, "GaInAsN/GaAs laser diodes operating at 1.52 μm ." *Electron Lett*, vol. 36, no. 14, pp. 1208 – 9, JUL 2000.
- [19] W. Ha, V. Gambin, M. Wistey, S. Bank, H. Yuen, S. Kim, and J. S. Harris, "Long wavelength GaInNAsSb/GaNAsSb multiple quantum well lasers." *Electron Lett*, vol. 38, no. 6, pp. 277 – 8, MAR 2002.
- [20] T. Takeuchi, Y. L. Chang, M. Leary, A. Tandon, H. C. Luan, D. Bour, S. Corzine, R. Twist, and M. Tan, "1.3 μm InGaAsN vertical cavity surface emitting lasers grown by MOCVD." *Electron Lett*, vol. 38, no. 23, pp. 1438 – 40, NOV 2002.
- [21] S. R. Bank, M. A. Wistey, H. B. Yuen, L. L. Goddard, W. Ha, and J. S. Harris, "Low-threshold CW GaInNAsSb/GaAs laser at 1.49 μm ." *Electron Lett*, vol. 39, no. 20, pp. 1445 – 6, 2003.
- [22] M. A. Wistey, S. R. Bank, H. B. Yuen, L. L. Goddard, and J. S. Harris, "Monolithic, GaInNAsSb vcsels at 1.46 μm on GaAs by MBE." *Electron Lett*, vol. 39, no. 25, pp. 1822 – 3, 2003.
- [23] R. Averbeck, H. Riechert, *et al.*, "Low threshold InGaAsN/GaAs SQW lasers beyond 1400 nm," in *International Molecular Beam Epitaxy Conference. Edinburgh, Scotland*, 2004.

- [24] P. Sundgren, R. M. von Wurtemberg, J. Berggren, M. Hammar, M. Ghisoni, V. Oscarsson, E. Odling, and J. Malmquist, "High-performance 1.3 μm InGaAs vertical cavity surface emitting lasers." *Electron Lett*, vol. 39, no. 15, pp. 1128 – 9, JUL 2003.
- [25] Nakagawa *et al.*, in *National Fiber Optic Engineers Conference (NFOEC), 2002*, 2002.
- [26] G. Patriarche, F. Jeannes, J. L. Oudar, and F. Glas, "Structure of the GaAs/InP interface obtained by direct wafer bonding optimised for surface emitting optical devices." *J Appl Phys*, vol. 82, no. 10, pp. 4892 – 903, Nov 1997.
- [27] L. Goldstein, C. Fortin, C. Starck, A. Plais, J. Jacquet, J. Boucart, A. Rocher, and C. Poussou, "GaAlAs/GaAs metamorphic bragg mirror for long wavelength vcsels." *Electron Lett*, vol. 34, no. 3, pp. 268 – 70, Feb 1998.
- [28] Y. Qian, Z. H. Zhu, Y. H. Lo, D. L. Huffaker, D. G. Deppe, H. Q. Hou, B. E. Hammons, W. Lin, and Y. K. Tu, "Long wavelength (1.3 μm) vertical-cavity surface-emitting lasers with a wafer-bonded mirror and an oxygen-implanted confinement region." *Appl Phys Lett*, vol. 71, no. 1, pp. 25 – 7, Jul 1997.
- [29] D. L. Huffaker, G. Park, Z. Zou, O. B. Shchekin, and D. G. Deppe, "1.3 μm room-temperature GaAs-based quantum-dot laser." *Appl Phys Lett*, vol. 73, no. 18, pp. 2564 – 6, NOV 1998.
- [30] O. B. Shchekin and D. G. Deppe, "Low-threshold high- T_0 1.3- μm InAs quantum-dot lasers due to p-type modulation doping of the active region," *IEEE Photonics Technol Lett*, vol. 14, no. 9, pp. 1231 – 1233, September 2002.
- [31] J. A. Lott, N. N. Ledentsov, V. M. Ustinov, N. A. Maleev, A. E. Zhukov, A. R. Kovsh, M. V. Maximov, B. V. Volovik, Z. I. Alferov, and D. Bimberg, "InAs-InGaAs quantum dot vcsels on GaAs substrates emitting at 1.3 μm ." *Electron Lett*, vol. 36, no. 16, pp. 1384 – 5, AUG 2000.

- [32] N. Yamamoto, K. Akahane, S. Gozu, and N. Ohtani, "Over 1.3 μm CW laser emission from InGaSb quantum-dot vertical-cavity surface-emitting laser on GaAs substrate." *Electron Lett*, vol. 40, no. 18, pp. 1120 – 1, Sep 2004.
- [33] V. M. Ustinov, A. Y. Egorov, V. A. Odnoblyudov, N. V. Kryzhanovskaya, Y. G. Musikhin, A. F. Tsatsul'nikov, and Z. I. Alferov, "InAs/InGaAsN quantum dots emitting at 1.55 μm grown by molecular beam epitaxy." *J Cryst Growth*, vol. 251, no. 1/4, pp. 388 – 91, APR 2003.
- [34] S. Makino, T. Miyamoto, M. Ohta, T. Kageyama, Y. Ikenaga, F. Koyama, and K. Iga, "Growth characteristics of GaInNAs/GaAs quantum dots by chemical beam epitaxy." *J Cryst Growth*, vol. 251, no. 1/4, pp. 372 – 7, APR 2003.
- [35] S. G. Spruytte, "MBE growth of nitride-arsenides for long wavelength optoelectronics," Ph.D. dissertation, Leland Stanford Junior University, Department of Materials Science and Engineering, Stanford, CA, 94305 USA, 2001.
- [36] R. F. Pierret, Ed., *Modular Series on Solid State Devices*. Addison-Wesley, 1982.
- [37] D. A. B. Miller, EE 243 course reader, Stanford University.
- [38] "Britney spears guide to semiconductor physics," <http://britneyspears.ac/lasers.htm>.
- [39] A. Siegman, *Lasers*. University Science Books, 1986.
- [40] L. A. Coldren and S. W. Corzine, *Diode Lasers and Photonic Integrated Circuits*. Wiley-Interscience, 1995.
- [41] S. L. Chuang, *Physics of Optoelectronic Devices*. Wiley-Interscience, 1995.
- [42] C. W. Wilmsen, Ed., *Vertical Cavity Surface Emitting Lasers*. Cambridge University Press, 2001.

- [43] K. L. Bacher, “Improvements toward high–efficiency vertical–cavity surface–emitting lasers,” Ph.D. dissertation, Leland Stanford Junior University, Department of Electrical Engineering, Stanford, CA, 94305 USA, June 1995.
- [44] V. Lordi, H. B. Yuen, S. R. Bank, and J. S. Harris, “Quantum–confined stark effect of GaInNAs(sb) quantum wells at 1300–1600 nm.” *Appl Phys Lett*, vol. 85, no. 6, pp. 902 – 4, AUG 2004.
- [45] M. A. Hadley, G. C. Wilson, K. Y. Lau, and J. S. Smith, “High single–transverse–mode output from external–cavity surface–emitting laser diodes.” *Appl Phys Lett*, vol. 63, no. 12, pp. 1607 – 9, SEP 1993.
- [46] S.-H. Park, Y. Park, H. Kim, H. Jeon, S. M. Hwang, J. K. Lee, S. H. Nam, B. C. Koh, J. Y. Sohn, and D. S. Kim, “Microlensed vertical–cavity surface–emitting laser for stable single fundamental mode operation.” *Applied Physics Letters*, vol. 80, no. 2, pp. 183 – 5, 2002.
- [47] H. J. Unold, S. W. Z. Mahmoud, R. Jager, M. Grabherr, R. Michalzik, and K. J. Ebeling, “Large–area single–mode vcsels and the self–aligned surface relief.” *J Select Topics Quantum Electron*, vol. 7, no. 2, pp. 386 – 92, March/April 2001.
- [48] M. Orenstein, A. C. Vonlehmen, C. Changhasnain, N. G. Stoffel, J. P. Harbison, L. T. Florez, E. Clausen, and J. E. Jewell, “Vertical–cavity surface–emitting InGaAs/GaAs lasers with planar lateral definition.” *Appl Phys Lett*, vol. 56, no. 24, pp. 2384 – 6, JUN 1990.
- [49] K. Tai, R. J. Fischer, K. W. Wang, S. N. G. Chu, and A. Y. Cho, “Use of implant isolation for fabrication of vertical cavity surface–emitting laser diodes.” *Electron Lett*, vol. 25, no. 24, pp. 1644 – 5, Nov 1989.
- [50] H. J. Unold, S. W. Z. Mahmoud, R. Jager, M. Kicherer, M. C. Riedl, and K. J. Ebeling, “Improving single–mode VCSEL performance by introducing a long monolithic cavity.” *IEEE Photonics Technol Lett*, vol. 12, no. 8, pp. 939 – 41, Oct 2000.

- [51] M. Achtenhagen, A. A. Hardy, and E. Kapon, "Design of distributed bragg reflector structures for transverse-mode discrimination in vertical-cavity surface-emitting lasers." *J Lightwave Tech*, vol. 22, no. 8, pp. 1962 – 7, August 2004.
- [52] S. Sato, Y. Osawa, T. Saitoh, and I. Fujimura, "Long-wavelength GaInNAs epitaxial growth and its application for 1.3 μm laser diodes." in *LEOS '97. 10th Annual Meeting IEEE Lasers and Electro-Optics Society 1997 Annual Meeting, 10-13 Nov. 1997, San Francisco, CA, USA*. New York, NY, USA : IEEE, 1996, 1996, pp. 321 – 2 vol.2.
- [53] C. W. Tu, W. G. Bi, H. P. Xin, Y. Ma, J. P. Zhang, L. W. Wang, and S. T. Ho, "III-N-V: a novel material system for lasers with good high-temperature characteristics." *Proc SPIE*, vol. 3284, pp. 190 – 6, 1998, see J Vac Sci Tech-B 2005.
- [54] W. Li, M. Pessa, T. Ahlgren, and J. Decker, "Origin of improved luminescence efficiency after annealing of ga(in)nas materials grown by molecular-beam epitaxy." *Applied Physics Letters*, vol. 79, no. 8, pp. 1094 – 6, 2001.
- [55] J. V. Thordson, O. Zsebok, U. Sodervall, and T. G. Andersson, "Surface morphology and structure of GaN_xAs_{1-x}," *MRS Internet J Nitride Sem Res*, vol. 2, no. 8, pp. CP1 – &, 1997.
- [56] N. Tansu, J. Y. Yeh, and L. J. Mawst, "Low-threshold 1317-nm InGaAsN quantum-well lasers with GaAsN barriers." *Appl Phys Lett*, vol. 83, no. 13, pp. 2512 – 14, SEP 2003.
- [57] K. Volz, S. Nau, B. Kunert, S. Reinhard, and W. Stolz, "C incorporation in (GaIn)(nas) and its dependence on growth conditions and influence on lasing characteristics," in *European Materials Research Society (E-MRS) Spring Meeting, 24 May 2004, Strasbourg, France*.
- [58] M. A. Herman and H. Sitter, *Molecular Beam Epitaxy: Fundamentals and Current Status*. Springer-Verlag, 1997.

- [59] V. F. Gambin, “Long wavelength luminescence from GaInNAsSb on GaAs,” Ph.D. dissertation, Leland Stanford Junior University, Solid State Photonics Laboratory, Stanford, California, 94305, USA, Nov 2002.
- [60] A. Roshko, T. E. Harvey, S. Y. Lehman, R. P. Mirin, K. A. Bertness, and B. L. Hyland, “InGaAs quantum dot distributions and their dependence on GaAs buffer layer morphology,” in *North American Molecular Beam Epitaxy Conference. Oct. 2004, Banff, Canada, 2004*, proceedings expected in JVST-B 2005.
- [61] A. E. Zhukov, R. Zhao, P. Specht, V. M. Ustinov, A. Anders, and E. R. Weber, “MBE growth of (In)GaAsN on GaAs using a constricted DC plasma source.” *Semicond Sci Technol*, vol. 16, no. 5, pp. 413 – 19, MAY 2001.
- [62] W. C. Hughes, W. H. Rowland, M. A. L. Johnson, S. Fujita, J. W. Cook, Jr., J. F. Schetzina, J. Ren, and J. A. Edmond, “Molecular beam epitaxy growth and properties of GaN films on GaN/SiC substrates.” *J Vac Sci Technol B*, vol. 13, no. 4, pp. 1571 – 7, 1995.
- [63] F. J. Grunthaner, R. Bicknell-Tassius, P. Deelman, P. J. Grunthaner, C. Bryson, E. Snyder, J. L. Giuliani, J. P. Apruzese, and P. Kepple, “Ultrahigh vacuum arc-jet nitrogen source for selected energy epitaxy of group III nitrides by molecular beam epitaxy.” *J Vac Sci Technol A*, vol. 16, no. 3, pp. 1615 – 20, MAY-JUN 1998.
- [64] R. P. Vaudo, Z. Yu, J. W. Cook, and J. F. Schetzina, “Atomic–nitrogen production in a radiofrequency plasma source,” *Opt Lett*, vol. 18, no. 21, pp. 1843 – 1845, NOV 1993, for nitrogen plasmas in ZnSe growth, see references therein.
- [65] I. A. Buyanova, W. M. Chen, and B. Monemar, “Electronic properties of ga(in)nas alloys,” *MRS Internet J Nitride Sem Res*, vol. 6, no. 2, pp. 1 – 19, 2001.
- [66] J. S. Harris, “GaInNAs long–wavelength lasers: progress and challenges,” *Semicond Sci Technol*, vol. 17, no. 8, pp. 880 – 91, AUG 2002.

- [67] H. Riechert, A. Ramakrishnan, and G. Steinle, “Development of InGaAsN-based 1.3 μm vcsels.” *Semicond Sci Technol*, vol. 17, no. 8, pp. 892 – 7, AUG 2002.
- [68] J. S. Harris, Jr., H. Yuen, M. Wistey, S. Bank, V. Lordi, T. Gugov, H. Bae, and L. Goddard, *MBE Growth and Characterization of Long Wavelength Dilute Nitride III–V Alloys*. Taylor & Francis, 2004, ch. 1.
- [69] J. S. Harris, Jr., M. Wistey, S. Bank, L. Goddard, V. Lordi, H. Bae, and H. Yuen, *Long–Wavelength Dilute Nitride–Antimonide Lasers*. Taylor & Francis, 2004, ch. 17.
- [70] W. Shan, W. Walukiewicz, J. W. Ager, E. E. Haller, J. F. Geisz, D. J. Friedman, J. M. Olson, and S. R. Kurtz, “Band anticrossing in GaInNAs alloys.” *Phys Rev Lett*, vol. 82, no. 6, pp. 1221 – 4, FEB 1999.
- [71] S. G. Spruytte, C. W. Coldren, A. F. Marshall, M. C. Larson, and J. S. Harris, “MBE growth of nitride–arsenide materials for long wavelength optoelectronics,” *MRS Internet J Nitride Sem Res*, vol. 5, pp. U407 – U412, 2000.
- [72] W. H. Ha, “Long wavelength GaInNAs and GaInNAsSb lasers on GaAs,” Ph.D. dissertation, Leland Stanford Junior University, Solid State Photonics Laboratory, Stanford, California, 94305, USA, Dec 2002.
- [73] T. Kitatani, K. Nakahara, M. Kondow, K. Uomi, and T. Tanaka, “A 1.3– μm GaInNAs/GaAs single–quantum–well laser diode with a high characteristic temperature over 200 K.” *Jpn J Appl Phys 2*, vol. 39, no. 2A, pp. L86 – 7, FEB 2000.
- [74] V. Lordi, V. Gambin, S. Friedrich, T. Funk, T. Takizawa, K. Uno, and J. S. Harris, “Nearest–neighbor configuration in (GaIn)(nas) probed by x–ray absorption spectroscopy.” *Physical Review Letters*, vol. 90, no. 14, pp. 145 505 – 4, APR 2003.

- [75] J. B. Heroux, X. Yang, and W. I. Wang, "Photoreflectance spectroscopy of strained (In)GaAsN/GaAs multiple quantum wells." *J Appl Phys*, vol. 92, no. 8, pp. 4361 – 6, OCT 2002.
- [76] G. Mussler, L. Daweritz, K. H. Ploog, J. W. Tomm, and V. Talalaev, "Optimized annealing conditions identified by analysis of radiative recombination in dilute GaAsN." *Appl Phys Lett*, vol. 83, no. 7, pp. 1343 – 5, AUG 2003.
- [77] S. R. Bank, M. A. Wistey, L. L. Goddard, H. B. Yuen, V. Lordi, and J. S. Harris, "Low-threshold continuous-wave 1.5- μm GaInNAsSb lasers grown on GaAs." *IEEE J Quantum Electron*, vol. 40, no. 6, pp. 656 – 64, JUN 2004.
- [78] L. L. Goddard, S. R. Bank, M. A. Wistey, H. B. Yuen, Z. L. Rao, and J. S. Harris, Jr., "Recombination, gain, band structure, efficiency, and reliability of 1.5 μm GaInNAsSb/GaAs lasers," *Journal of Applied Physics*, Submitted for publication.
- [79] R. Kudrawiec, K. Ryczko, J. Misiewicz, H. B. Yuen, S. R. Bank, M. A. Wistey, H. P. Bae, and J. S. Harris, Jr., "Photoreflectance and photoluminescence investigations of a step-like GaInNAsSb/GaAsN/GaAs quantum well tailored at 1.5 μm : the energy level structure and the Stokes shift," *J. Appl. Phys.*, submitted for publication, submitted for publication.
- [80] S. G. Spruytte, M. C. Larson, W. Wampler, C. W. Coldren, and J. S. Harris, "Molecular beam epitaxial growth of group III-nitride-arsenides for long wavelength optoelectronics." in *2000 IEEE International Symposium on Compound Semiconductors Proceedings of the IEEE Twenty-Seventh International Symposium on Compound Semiconductors, 2-5 Oct. 2000, Monterey, CA, USA*. Piscataway, NJ, USA : IEEE, 2000, 2000, pp. 61 – 6.
- [81] M. Fischer, D. Gollub, M. Reinhardt, M. Kamp, and A. Forchel, "GaInNAs for GaAs based lasers for the 1.3 to 1.5 μm range." *J Cryst Growth*, vol. 251, no. 1/4, pp. 353 – 9, APR 2003.

- [82] M. Reason, H. A. McKay, W. Ye, S. Hanson, R. S. Goldman, and V. Rotberg, “Mechanisms of nitrogen incorporation in GaAsN alloys,” *Appl Phys Lett*, vol. 85, no. 10, pp. 1692 – 1694, Sep 2004.
- [83] C. Skierbiszewski, S. P. Lepkowski, P. Perlin, T. Suski, W. Jantsch, and J. Geisz, “Effective mass and conduction band dispersion of GaAsN/GaAs quantum wells.” *Physica E*, vol. 13, no. 2/4, pp. 1078 – 81, March 2002.
- [84] G. Bisognin, D. D. Salvador, C. Mattevi, M. Berti, A. V. Drigo, G. Ciatto, L. Grenouillet, P. Duvaut, P. Gilet, and H. Mariette, “Determination of lattice parameter and of N lattice location in $\text{In}_x\text{Ga}_{1-x}\text{N}_y\text{As}_{1-y}/\text{GaAs}$ and $\text{GaN}_y\text{As}_{1-y}/\text{GaAs}$ epilayers.” *J Appl Phys*, vol. 95, no. 1, pp. 48 – 56, Jan 2004.
- [85] S. G. Spruytte, C. W. Coldren, J. S. Harris, W. Wampler, P. Krispin, K. Ploog, and M. C. Larson, “Incorporation of nitrogen in nitride–arsenides: Origin of improved luminescence efficiency after anneal.” *J Appl Phys*, vol. 89, no. 8, pp. 4401 – 6, APR 2001.
- [86] W. Li, M. Pessa, and J. Likonen, “Lattice parameter in GaNAs epilayers on GaAs: Deviation from Vegard’s law,” *APPLIED PHYSICS LETTERS*, vol. 78, no. 19, pp. 2864 – 2866, MAY 2001.
- [87] K. Uesugi, N. Morooka, and I. Suemune, “Reexamination of N composition dependence of coherently grown GaNAs band gap energy with high–resolution X–ray diffraction mapping measurements.” *Appl Phys Lett*, vol. 74, no. 9, pp. 1254 – 6, MAR 1999.
- [88] W. J. Fan, S. F. Yoon, W. K. Cheah, W. K. Loke, T. K. Ng, S. Z. Wang, R. Liu, and A. Wee, “Determination of nitrogen composition in $\text{GaN}_x\text{As}_{1-x}$ epilayer on GaAs.” *J Cryst Growth*, vol. 268, no. 3/4, pp. 470 – 4, Aug 2004.
- [89] T. Gugov, M. Wistey, H. Yuen, S. Bank, and J. S. Harris, Jr., “Structural characterization of molecular beam epitaxy grown GaInNAs and GaInNAsSb

- quantum wells by transmission electron microscopy,” in *Spring 2004 MRS Meeting, San Francisco, CA, April 2004*, 2004.
- [90] K. Volz *et al.*, unpublished.
- [91] X. Yang, M. J. Jurkovic, J. B. Heroux, and W. I. Wang, “Low threshold InGaAsN/GaAs single quantum well lasers grown by molecular beam epitaxy using sb surfactant.” *Electron Lett*, vol. 35, no. 13, pp. 1082 – 3, JUN 1999.
- [92] J. B. Heroux, X. Yang, and W. I. Wang, “Quantum confined stark effect in GaInNAs/GaAs multiple quantum wells.” *IEE Proc Optoelectronics*, vol. 150, no. 1, pp. 92 – 5, FEB 2003.
- [93] N. Grandjean, J. Massies, and V. H. Etgens, “Delayed relaxation by surfactant action in highly strained III–V semiconductor epitaxial layers.” *Phys Rev Lett*, vol. 69, no. 5, pp. 796 – 9, AUG 1992.
- [94] E. C. Young, S. Tixier, T. Tiedje, S. Francoeur, N. Zangenberg, D. Beaton, and S. E. Webster, “Enhanced nitrogen incorporation and improved electronic properties in dilute GaN_xAs_{1-x} grown with a bi surfactant,” in *North American Molecular Beam Epitaxy Conference. Oct. 2004, Banff, Canada*, 2004.
- [95] J. X. Fu, S. R. Bank, M. A. Wistey, H. B. Yuen, and J. S. Harris, “Solid–source molecular–beam epitaxy growth of GaInNAsSb/InGaAs single quantum well on InP with photoluminescence peak wavelength at 2.04 μm ,” *J Vac Sci Technol B*, vol. 22, no. 3, pp. 1463 – 1467, MAY-JUN 2004.
- [96] W. Li, J. B. Heroux, and W. I. Wang, “InGaAsSbN: a dilute nitride compound for midinfrared optoelectronic devices.” *Journal of Applied Physics*, vol. 94, no. 7, pp. 4248 – 50, OCT 2003.
- [97] H. B. Yuen *et al.*, unpublished.
- [98] G. B. Stringfellow, *Organometallic Vapor–Phase Epitaxy: Theory and Practice*. Academic Press, 1989.

- [99] K. Volz, V. Gambin, W. Ha, M. A. Wistey, H. Yuen, S. Bank, and J. S. Harris, “The role of sb in the MBE growth of (GaIn)(NAsSb).” *J Cryst Growth*, vol. 251, no. 1/4, pp. 360 – 6, APR 2003.
- [100] J. C. Harmand, G. Ungaro, L. Largeau, and G. L. Roux, “Comparison of nitrogen incorporation in molecular–beam epitaxy of GaAsN, GaInAsN, and GaAsSbN.” *Appl Phys Lett*, vol. 77, no. 16, pp. 2482 – 4, OCT 2000.
- [101] T. Suda, Y. Kangawa, K. Nakamura, and T. Ito, “An empirical potential approach to structural stability of $\text{GaN}_x\text{As}_{1-x}$.” *J Cryst Growth*, vol. 258, no. 3/4, pp. 277 – 82, NOV 2003.
- [102] I. A. Buyanova, W. M. Chen, G. Pozina, J. P. Bergman, B. Monemar, H. P. Xin, and C. W. Tu, “Mechanism for low–temperature photoluminescence in GaNAs/GaAs structures grown by molecular–beam epitaxy.” *Appl Phys Lett*, vol. 75, no. 4, pp. 501 – 3, JUL 1999.
- [103] Y. Zhang, A. Mascarenhas, H. P. Xin, and C. W. Tu, “Formation of an impurity band and its quantum confinement in heavily doped GaAs:N.” *Phys Rev B*, vol. 61, no. 11, pp. 7479 – 82, MAR 2000.
- [104] H. Gruning, L. Chen, T. Hartmann, P. J. Klar, W. Heimbrodt, F. Hohnsdorf, J. Koch, and W. Stolz, “Optical spectroscopic studies of N–related bands in $\text{ga}(\text{N},\text{as})$.” *Phys Stat Sol B*, vol. 215, no. 1, pp. 39 – 45, SEP 1999.
- [105] P. J. Klar, H. Gruning, W. Heimbrodt, J. Koch, F. Hohnsdorf, W. Stolz, P. M. A. Vicente, and J. Camassel, “From N isoelectronic impurities to N–induced bands in the $\text{GaN}_x\text{As}_{1-x}$ alloy.” *Appl Phys Lett*, vol. 76, no. 23, pp. 3439 – 41, 2000.
- [106] H. P. Hjalmarson, P. Vogl, D. J. Wolford, and J. D. Dow, “Theory of substitutional deep traps in covalent semiconductors.” *Phys Rev Lett*, vol. 44, no. 12, pp. 810 – 13, 1980.

- [107] D. J. Wolford, J. A. Bradley, K. Fry, and J. Thompson, “Nitrogen isoelectronic trap in GaAs.” in *Proceedings of the 17th International Conference on the Physics of Semiconductors.; San Francisco, CA, USA.* New York, NY, USA : Springer-Verlag, 1985, 1985, pp. 627 – 630.
- [108] J. Endicott, A. Patane, J. Ibanez, L. Eaves, M. Bissiri, M. Hopkinson, R. Airey, and G. Hill, “Magnetotunneling spectroscopy of dilute Ga(AsN) quantum wells.” *Phys Rev Lett*, vol. 91, no. 12, pp. 126 802 – 4, SEP 2003.
- [109] J. D. Perkins, A. Mascarenhas, Y. Zhang, J. F. Geisz, D. J. Friedman, J. M. Olson, and S. R. Kurtz, “Nitrogen-activated transitions, level repulsion, and band gap reduction in GaAs_{1-x}N_x with x>0.03.” *Phys Rev Lett*, vol. 82, no. 16, pp. 3312 – 15, APR 1999.
- [110] P. J. Klar, H. Gruning, W. Heimbrodt, G. Weiser, J. Koch, K. Volz, W. Stolz, S. W. Koch, S. Tomic, S. A. Choulis, T. J. C. Hosea, E. P. O’Reilly, M. Hofmann, J. Hader, and J. V. Moloney, “Interband transitions of quantum wells and device structures containing Ga(N, As) and (Ga, In)(N, As).” *Semicond Sci Technol*, vol. 17, no. 8, pp. 830 – 42, AUG 2002.
- [111] I. Vurgaftman and J. R. Meyer, “Band parameters for nitrogen-containing semiconductors.” *J Appl Phys*, vol. 94, no. 6, pp. 3675 – 96, SEP 2003.
- [112] B. A. Weinstein, S. R. Stambach, T. M. Ritter, J. O. Maclean, and D. J. Wallis, “Evidence for selective delocalization of N-pair states in dilute GaAs_{1-x}N_x,” *Phys Rev B*, vol. 68, no. 3, pp. 035 336 –, JUL 2003.
- [113] S. Francoeur, M. J. Seong, M. C. Hanna, J. F. Geisz, A. Mascarenhas, H. P. Xin, and C. W. Tu, “Origin of the nitrogen-induced optical transitions in GaAs_{1-x}N_x,” *Phys Rev B*, vol. 68, no. 7, pp. 075 207 –, AUG 2003.
- [114] A. J. Ptak, S. Kurtz, M. H. Weber, and K. G. Lynn, “Positron annihilation study of vacancies in GaInNAs.” *J Vac Sci Technol B*, vol. 22, no. 3, pp. 1584 – 7, MAY-JUN 2004.

- [115] S. B. Zhang and S. H. Wei, “Nitrogen solubility and induced defect complexes in epitaxial GaAs:N.” *Physical Review Letters*, vol. 86, no. 9, pp. 1789 – 92, FEB 2001.
- [116] Z. Pan, T. Miyamoto, D. Schlenker, F. Koyama, and K. Iga, “Quality improvement of GaInNAs/GaAs quantum wells grown by MOCVD using tertiarybutylarsine.” in *1998 International Conference on Indium Phosphide and Related Materials, 11-15 May 1998, Tsukuba, Japan*. New York, NY, USA : IEEE, 1998, 1998, pp. 135 – 8.
- [117] T. Kageyama, T. Miyamoto, S. Makino, F. Koyama, and K. Iga, “Thermal annealing of GaInNAs/GaAs quantum wells grown by chemical beam epitaxy and its effect on photoluminescence.” *Jpn J Appl Phys 2*, vol. 38, no. 3B, pp. L298 – 300, MAR 1999.
- [118] P. Krispin, V. Gambin, J. S. Harris, and K. H. Ploog, “Nitrogen-related electron traps in Ga(As,N) layers ($x = 3\%$ N),” *Journal of Applied Physics*, vol. 93, no. 10, pp. 6095 – 6099, MAY 2003.
- [119] P. Krispin, S. G. Spruytte, J. S. Harris, and K. H. Ploog, “Origin and annealing of deep-level defects in p-type GaAs/Ga(As,N)/GaAs heterostructures grown by molecular beam epitaxy.” *Journal of Applied Physics*, vol. 89, no. 11, pp. 6294 – 2, JUN 2001.
- [120] —, “Deep-level defects in MBE-grown Ga(As,N) layers.” *Physica B*, vol. 308/310, pp. 870 – 3, DEC 2001.
- [121] M. Ramsteiner, D. S. Jiang, J. S. Harris, and K. H. Ploog, “Nonradiative recombination centers in Ga(As,N) and their annealing behavior studied by Raman spectroscopy.” *Appl Phys Lett*, vol. 84, no. 11, pp. 1859 – 61, MAR 2004.
- [122] G. Mussler, J. M. Chauveau, A. Trampert, M. Ramsteiner, L. Daweritz, and K. H. Ploog, “Nitrogen-dependent optimum annealing temperature of Ga(As,N).” *J Cryst Growth*, vol. 267, no. 1/2, pp. 60 – 6, JUN 2004.

- [123] P. J. Klar, H. Gruning, J. Koch, S. Schafer, K. Volz, W. Stolz, W. Heimbrodtt, A. M. K. Saadi, A. Lindsay, and E. P. O'Reilly, "(ga, in)(N, as)–fine structure of the band gap due to nearest–neighbor configurations of the isovalent nitrogen." *Phys Rev B*, vol. 64, no. 12, pp. 121 203 – 4, SEP 2001.
- [124] S. A. Choulis, T. J. C. Hosea, P. J. Klar, M. Hofmann, and W. Stolz, "Influence of varying N–environments on the properties of (GaIn)(nas) vertical–cavity surface–emitting lasers." *Applied Physics Letters*, vol. 79, no. 26, pp. 4277 – 9, DEC 2001.
- [125] S. Shirakata, M. Kondow, and T. Kitatani, "Optical properties of GaInNAs/GaAs prepared by molecular beam epitaxy." *J Phys Chem Sol*, vol. 64, no. 9/10, pp. 1533 – 7, SEP-OCT 2003.
- [126] S. Kurtz, J. Webb, L. Gedvilas, D. Friedman, J. Geisz, J. Olson, R. King, D. Joslin, and N. Karam, "Structural changes during annealing of GaInAsN." *Applied Physics Letters*, vol. 78, no. 6, pp. 748 – 50, FEB 2001.
- [127] S. G. Spruytte, C. W. Coldren, M. C. Larson, and J. S. Harris, "Incorporation of nitrogen in group III–nitrides–arsenides grown by molecular beam epitaxy (MBE)," in *2000 International Semiconducting and Insulating Materials Conference (SIMC) XI, Canberra, ACT, Australia, 2000*.
- [128] G. Bosker, N. A. Stolwijk, J. V. Thordson, U. Sodervall, and T. G. Andersson, "Diffusion of nitrogen from a buried doping layer in gallium arsenide revealing the prominent role of as interstitials." *Phys Rev Lett*, vol. 81, no. 16, pp. 3443 – 6, OCT 1998.
- [129] L. H. Li, G. Patriarche, A. Lemaitre, L. Largeau, L. Travers, and J. C. Harmand, "Comparison of GaInNAs/GaAs and GaInNAs/GaNAs/GaAs quantum wells emitting over 1.3 μm wavelength." *J Cryst Growth*, vol. 251, no. 1/4, pp. 403 – 7, APR 2003.
- [130] L. H. Li, Z. Pan, W. Zhang, Y. W. Lin, X. Y. Wang, R. H. Wu, and W. K. Ge, "Effect of ion–induced damage on GaNAs/GaAs quantum wells grown by

- plasma-assisted molecular beam epitaxy.” *Journal of Crystal Growth*, vol. 223, no. 1/2, pp. 140 – 4, FEB 2001.
- [131] J. S. Harris, J. W. Mayer, F. H. Eisen, J. D. Haskell, B. Welch, and R. D. Pashley, “Influence of implantation temperature and surface protection on tellurium implantation in GaAs.” *Applied Physics Letters*, vol. 21, no. 12, pp. 601 – 3, 1972.
- [132] R. Macaluso, H. D. Sun, M. D. Dawson, F. Robert, A. C. Bryce, J. H. Marsh, and H. Riechert, “Selective modification of band gap in GaInNAs/GaAs structures by quantum-well intermixing.” *Appl Phys Lett*, vol. 82, no. 24, pp. 4259 – 61, JUN 2003.
- [133] O. M. Khreis, W. P. Gillin, and K. P. Homewood, “Interdiffusion: a probe of vacancy diffusion in III–V materials.” *Phys Rev B*, vol. 55, no. 23, pp. 15 813 – 18, JUN 1997.
- [134] A. Ohmae, N. Matsumoto, M. Kawabe, and Y. Okada, “Effects of atomic hydrogen on the growth of ga(in)nas by RF-molecular beam epitaxy.” *Phys Stat Sol C*, no. 1, pp. 175 – 8, 2002.
- [135] A. Janotti, S. H. Wei, S. B. Zhang, S. Kurtz, and C. G. V. de Walle, “Interactions between nitrogen, hydrogen, and gallium vacancies in GaAs_{1-x}N_x alloys,” *Phys Rev B*, vol. 67, no. 16, pp. 161 201 –, APR 2003.
- [136] J. Toivonen, T. Hakkarainen, M. Sopanen, H. Lipsanen, J. Oila, and K. Saari-
nen, “Observation of defect complexes containing ga vacancies in GaAsN.” *Appl Phys Lett*, vol. 82, no. 1, pp. 40 – 2, JAN 2003.
- [137] S. Kurtz, J. F. Geisz, D. J. Friedman, W. K. Metzger, R. R. King, and N. H. Karam, “Annealing-induced-type conversion of GaInNAs.” *J Appl Phys*, vol. 95, no. 5, pp. 2505 – 8, MAR 2004.
- [138] D. W. Kisker, L. M. F. Chirovsky, R. L. Naone, J. M. V. Hove, J. M. Rossler, M. Adamcyk, N. Wasinger, J. G. Beltran, and D. Galt, “1.3 μm VCSEL production issues,” *Proc SPIE*, vol. 5364, pp. 146 – 157, 2004 2004.

- [139] P. Andre, J. Ondet, G. Bouchard, and A. Lefort, “Optical emission spectroscopy, thermodynamical and thermal disequilibrium aspects in an inductively coupled plasma torch. experimental applications to N₂–O₂ mixtures.” *J Phys D-Appl Phys*, vol. 32, no. 8, pp. 920 – 9, APR 1999.
- [140] H. Carrere, A. Arnoult, A. Ricard, and E. Bedel-Pereira, “RF plasma investigations for plasma–assisted MBE growth of (ga,in)(as,N) materials.” *J Cryst Growth*, vol. 243, no. 2, pp. 295 – 301, AUG 2002.
- [141] C. H. Fischer and P. Bhattacharya, “Photoluminescence and deep levels in lattice–matched InGaAsN/GaAs,” *J Appl Phys*, vol. 96, no. 8, pp. 4176 – 4180, Oct 2004.
- [142] J. C. Zolper, M. E. Sherwin, A. G. Baca, and R. P. Schneider, “Evidence of a thermally stable carbon–nitrogen deep level in carbon–doped, nitrogen–implanted, GaAs and AlGaAs.” *J Electron Mater*, vol. 24, no. 1, pp. 21 – 4, JAN 1995.
- [143] A. Polimeni, G. B. H. von Hogersthal, M. Bissiri, M. Capizzi, A. Frova, M. Fischer, M. Reinhardt, and A. Forchel, “Role of hydrogen in III–N–V compound semiconductors.” *Semicond Sci Technol*, vol. 17, no. 8, pp. 797 – 802, AUG 2002.
- [144] I. A. Buyanova, M. Izadifard, W. M. Chen, A. Polimeni, M. Capizzi, H. P. Xin, and C. W. Tu, “Hydrogen–induced improvements in optical quality of GaNAs alloys.” *Appl Phys Lett*, vol. 82, no. 21, pp. 3662 – 4, May 2003.
- [145] G. Leibiger, V. Gottschalch, N. Razek, A. Schindler, and M. Schubert, “Hydrogen implantation in InGaNAs studied by spectroscopic ellipsometry,” *Thin Solid Films*, vol. 455-56, pp. 231 – 234, MAY 2004.
- [146] L. Geelhaar, H. Riechert, *et al.*, “Improvement of the optical quality of InGaAsN quantum wells by annealing under H₂–atmosphere,” in *International Molecular Beam Epitaxy Conference. Edinburgh, Scotland, 2004.*

- [147] A. Janotti, S. B. Zhang, S. H. Wei, and C. G. V. de Walle, “Effects of hydrogen on the electronic properties of dilute GaAsN alloys.” *Phys Rev Lett*, vol. 89, no. 8, pp. 086403 – 1, AUG 2002.
- [148] G. Bruno, “Reactivity and control of III–V surfaces for passivation and schottky barrier formation,” *Applied Surface Science*, vol. 235, no. 3, pp. 239 – 248, Aug 2004.
- [149] J. A. Gupta, G. I. Sproule, X. Wu, G. C. Aers, and Z. R. Wasilewski, “1.55 μm GaInNAs(Sb)/GaNAs double quantum wells with bright and narrow photoluminescence,” in *North American Molecular Beam Epitaxy Conference. Oct. 2004, Banff, Canada, 2004*.
- [150] R. Hartmann, private communication.
- [151] D. Schlenker, Z. Pan, T. Miyamoto, F. Koyama, and K. Iga, “Effect of surface quality on overgrowth of highly strained GaInAs/GaAs quantum wells and improvement by a strained buffer layer.” *Jpn J Appl Phys 1*, vol. 38, no. 9A, pp. 5023 – 7, 1999.
- [152] H. Kroemer and H. Okamoto, “Some design considerations for multi–quantum–well lasers.” *Jpn J Appl Phys 1*, vol. 23, no. 8, pp. 970 – 974, Aug 1984.
- [153] M. Kawaguchi, E. Gouardes, D. Schlenker, T. Kondo, T. Miyamoto, F. Koyama, and K. Iga, “Low threshold current density operation of GaInNAs quantum well lasers grown by metalorganic chemical vapour deposition.” *Electron Lett*, vol. 36, no. 21, pp. 1776 – 7, OCT 2000.
- [154] T. Takeuchi, Y. L. Chang, M. Leary, D. Mars, H. C. Luan, S. D. Roh, L. M. Mantese, Y. K. Song, A. Tandon, R. Twist, S. Belov, D. Bour, and M. Tan, “Al gettering for InGaAsN in metalorganic chemical vapor deposition,” *Jpn J Appl Phys 2*, vol. 43, no. 8 B, pp. L1085 – L1087, Aug 2004.
- [155] P. Sundgren, C. Asplund, K. Baskar, and M. Hammar, “Morphological instability of GaInNAs quantum wells on Al-containing layers grown by metalorganic vapor–phase epitaxy.” *Appl Phys Lett*, vol. 82, no. 15, pp. 2431 – 3, APR 2003.

- [156] J. Hashimoto, K. Koyama, T. Katsuyama, Y. Iguchi, T. Yamada, S. Takagishi, M. Ito, and A. Ishida, "1.3 μm traveling-wave GaInNAs semiconductor optical amplifier," *Jpn J Appl Phys 1*, vol. 43, no. 6A, pp. 3419 – 3423, JUN 2004.
- [157] M. C. Larson, "Microelectromechanical wavelength-tunable vertical-cavity light-emitters and lasers," Ph.D. dissertation, Leland Stanford Junior University, Department of Electrical Engineering, Stanford, CA, 94305 USA, May 1996.
- [158] R. Fehse, S. Tomic, A. R. Adams, S. J. Sweeney, E. P. O'Reilly, A. Andreev, and H. Riechert, "A quantitative study of radiative, auger, and defect related recombination processes in 1.3- μm GaInNAs-based quantum-well lasers." *J Select Topics Quantum Electron*, vol. 8, no. 4, pp. 801 – 10, JUL-AUG 2002.
- [159] C. W. Coldren, S. G. Spruytte, J. S. Harris, and M. C. Larson, "Group III nitride-arsenide long wavelength lasers grown by elemental source molecular beam epitaxy," *J Vac Sci Technol B*, vol. 18, no. 3, pp. 1480 – 1483, MAY-JUN 2000.
- [160] P. Krispin, V. Gambin, J. S. Harris, and K. H. Ploog, "Ga(as,N) layers in the dilute N limit studied by depth-resolved capacitance spectroscopy." *Applied Physics Letters*, vol. 81, no. 21, pp. 3987 – 9, NOV 2002.
- [161] S. R. Bank, M. A. Wistey, H. B. Yuen, V. Lordi, V. F. Gambin, and J. S. Harris, Jr., "Effects of antimony and ion damage on carrier localization in MBE-grown GaInNAs," in *North American Molecular Beam Epitaxy Conference. Oct. 2004, Banff, Canada*, 2004.
- [162] V. Kirchner, H. Heinke, U. Birkle, S. Einfeldt, D. Hommel, H. Selke, and P. L. Ryder, "Ion-induced crystal damage during plasma-assisted MBE growth of GaN layers." *Phys Rev B*, vol. 58, no. 23, pp. 15 749 – 55, DEC 1998.
- [163] T. Kageyama, T. Miyamoto, S. Makino, F. Koyama, and K. Iga, "Optical quality of GaNAs and GaInNAs and its dependence on RF cell condition in

- chemical beam epitaxy.” *J Cryst Growth*, vol. 209, no. 2/3, pp. 350 – 4, FEB 2000.
- [164] J. Glanz, “The pervasive plasma state,” 1996, American Physical Society, Division of Plasma Physics, <http://www.apsdpp.org/plasma.brochure>.
- [165] M. M. Oye, private communication.
- [166] Y. Aoyagi, K. Shinmura, K. Kawasaki, T. Tanaka, K. Gamo, S. Namba, and I. Nakamoto, “Molecular layer etching of GaAs.” *Appl Phys Lett*, vol. 60, no. 8, pp. 968 – 70, FEB 1992.
- [167] N. Newman, “The energetics of the GaN MBE reaction: a case study of metastable growth.” *J Cryst Growth*, vol. 178, no. 1/2, pp. 102 – 12, June 1997.
- [168] A. J. Ptak, “Growth kinetics and doping of gallium nitride grown by rf-plasma assisted molecular beam epitaxy,” Ph.D. dissertation, West Virginia University, Department of Physics, Morgantown, WV, USA, 2001.
- [169] Z. Y. Fan and N. Newman, “Precise control of atomic nitrogen production in an electron cyclotron resonance plasma using N₂/noble gas mixtures.” *Appl Phys Lett*, vol. 73, no. 4, pp. 456 – 8, 1998.
- [170] R. J. Molnar, R. Singh, and T. D. Moustakas, “Operation of a compact electron cyclotron resonance source for the growth of gallium nitride by molecular beam epitaxy (ECR-MBE).” *J Electron Mater*, vol. 24, no. 4, pp. 275 – 81, APR 1995.
- [171] M. Schiller and W. Kulisch, “Plasma properties at the transition from remote to direct plasma.” *Surf Coat Technol*, vol. 98, no. 1/3, pp. 1590 – 9, JAN 1998.
- [172] A. Ohtani, K. S. Stevens, and R. Beresford, “Microstructure and photoluminescence of GaN grown on si(111) by plasma-assisted molecular beam epitaxy.” *Appl Phys Lett*, vol. 65, no. 1, pp. 61 – 3, JUL 1994.
- [173] A. Kovsh, private communication.

- [174] A. Lofthus and P. H. Krupenie, "The spectrum of molecular nitrogen," *J Phys Chem Ref Data*, vol. 6, no. 1, pp. 113 – 307, 1977, <http://www.nist.gov/srd/PDF%20files/jpcrd93.pdf>.
- [175] A. V. Blant, O. H. Hughes, T. S. Cheng, S. V. Novikov, and C. T. Foxon, "Nitrogen species from radio frequency plasma sources used for molecular beam epitaxy growth of GaN." *Plasma Sourc Sci Tech*, vol. 9, no. 1, pp. 12 – 17, FEB 2000.
- [176] J. D. MacKenzie, L. Abbaschian, C. R. Abernathy, S. M. Donovan, S. J. Pearton, P. C. Chow, and J. VanHove, "Plasma characteristics and the growth of group III–nitrides by metalorganic molecular beam epitaxy." *J Electron Mater*, vol. 26, no. 11, pp. 1266 – 9, NOV 1997.
- [177] D. Voulot, R. W. McCullough, W. R. Thompson, D. Burns, J. Geddes, G. J. Cosimini, E. Nelson, P. P. Chow, and J. Klaassen, "Determination of the atomic nitrogen flux from a radio frequency plasma nitride source for molecular beam epitaxy systems." *J Vac Sci Technol A*, vol. 16, no. 6, pp. 3434 – 7, NOV-DEC 1998.
- [178] M. A. Pinault and E. Tournie, "Influence of alloy stability on the photoluminescence properties of GaAsN/GaAs quantum wells grown by molecular beam epitaxy." *Applied Physics Letters*, vol. 79, no. 21, pp. 3404 – 6, NOV 2001.
- [179] G. J. Collins, eE 576 Lecture 10 course notes, Colorado State University.
- [180] M. A. Wistey, S. R. Bank, H. B. Yuen, H. Bae, and J. S. Harris, Jr., "Nitrogen plasma optimization for high quality dilute nitrides," *J Cryst Growth*, 2005.
- [181] D. Mars, private communication.
- [182] M. A. Wistey, S. R. Bank, H. B. Yuen, and J. S. Harris, "Protecting wafer surface during plasma ignition using an arsenic cap," *Journal of Vacuum Science and Technology B*, Submitted for publication.

- [183] R. J. Molnar and T. D. Moustakas, "Growth of gallium nitride by electron-cyclotron resonance plasma-assisted molecular-beam epitaxy: the role of charged species." *J Appl Phys*, vol. 76, no. 8, pp. 4587 – 95, OCT 1994.
- [184] O. Scientific, "Oxford scientific atom source (RF plasma) brochure," http://www.oxsci.com/guides/pdf/RF_Plasma_Source.pdf.
- [185] P. R. I. Cabarrocas, P. Morin, V. Chu, J. P. Conde, J. Z. Liu, H. R. Park, and S. Wagner, "Optoelectronic properties of hydrogenated amorphous-silicon films deposited under negative substrate bias," *J Appl Phys*, vol. 69, no. 5, pp. 2942 – 2950, MAR 1991.
- [186] U. Birkle, C. Thomas, M. Fehrer, S. Einfeldt, H. Heinke, and D. Hommel, "Influence of activated nitrogen on plasma assisted MBE growth of GaN." *Mater Sci Forum*, vol. 264/268, pp. 1193 – 1196, 1998.
- [187] A. P. Young, L. J. Brillson, Y. Naoi, and C. W. Tu, "The effect of nitrogen ion damage on the optical and electrical properties of MBE GaN grown on MOCVD GaN/sapphire templates," *MRS Internet J Nitride Sem Res*, vol. 5, pp. U679 – U684, 2000.
- [188] T. H. Myers, M. R. Millecchia, A. J. Ptak, K. S. Ziemer, and C. D. Stinespring, "Influence of active nitrogen species on high temperature limitations for (0001-) GaN growth by rf plasma-assisted molecular beam epitaxy." *J Vac Sci Technol B*, vol. 17, no. 4, pp. 1654 – 8, 1999.
- [189] J. Hopwood, C. R. Guarnieri, S. J. Whitehair, and J. J. Cuomo, "Langmuir probe measurements of a radio frequency induction plasma." *J Vac Sci Technol A*, vol. 11, no. 1, pp. 152 – 6, JAN-FEB 1993.
- [190] J. Miguel-Sanchez, A. Guzman, and E. Munoz, "Role of N ions in the optical and morphological properties of InGaAsN quantum wells for 1.3–1.5 μm applications." *Appl. Phys. Lett.*, vol. 85, no. 11, pp. 1940 – 2, SEP 2004.

- [191] M. A. Wistey, S. R. Bank, H. B. Yuen, and J. S. Harris, "Real-time ion count from nitrogen plasma source," in *North American Molecular Beam Epitaxy Conference. P2-9, Oct. 2003, Keystone, Colorado, 2003*.
- [192] J. V. Scanlan and M. B. Hopkins, "Langmuir probe measurements of the electron energy distribution function in radio-frequency plasmas." *J Vac Sci Technol A*, vol. 10, no. 4, pp. 1207 – 1211, 1992.
- [193] E. A. Edelberg, A. Perry, N. Benjamin, and E. S. Aydil, "Energy distribution of ions bombarding biased electrodes in high density plasma reactors." *J Vac Sci Technol A*, vol. 17, no. 2, pp. 506 – 16, MAR-APR 1999.
- [194] A. P. Paranjpe, J. P. McVittie, and S. A. Self, "A tuned langmuir probe for measurements in RF glow discharges." *J Appl Phys*, vol. 67, no. 11, pp. 6718 – 27, JUN 1990.
- [195] J.-S. Chang, "The inadequate reference electrode, a widespread source of error in plasma probe measurements," *J. Phys. D*, vol. 6, no. 14, pp. 1674 – 83, 1973.
- [196] J. G. Laframboise, Univ. of Toronto, Inst. Aerospace Studies, Tech. Rep. 100, June 1966.
- [197] R. M. Clements, "Plasma diagnostics with electric probes." *J Vac Sci Technol*, vol. 15, no. 2, pp. 193 – 8, 1978.
- [198] T. Y. Fishkova and E. V. Shpak, "Fringing fields of plane-parallel and wedge-shaped deflecting systems." *Pis'ma v Zhurnal Tekhnicheskoi Fizika*, vol. 19, no. 13/14, pp. 87 – 90, 1993.
- [199] H. F. Liu, C. S. Peng, J. Likonen, T. Jouhti, S. Karirinne, J. Konttinen, and M. Pessa, "Influence of nitride and oxide cap layers upon the annealing of 1.3 μm GaInNAs/GaAs quantum wells." *J Appl Phys*, vol. 95, no. 8, pp. 4102 – 4, APR 2004.

- [200] A. J. Ptak, S. W. Johnston, S. Kurtz, D. J. Friedman, and W. K. Metzger, "A comparison of MBE- and MOCVD-grown GaInNAs." *J Cryst Growth*, vol. 251, no. 1/4, pp. 392 – 8, APR 2003.
- [201] S. Z. Wang, S. F. Yoon, and W. K. Loke, "Effects of surface nitridation during nitrogen plasma ignition on optical quality of GaInAsN grown by solid source molecular beam epitaxy." *J Appl Phys*, vol. 94, no. 4, pp. 2662 – 6, AUG 2003.
- [202] S. P. Kowalczyk, D. L. Miller, J. R. Waldrop, P. G. Newman, and R. W. Grant, "Protection of molecular beam epitaxy grown $\text{Al}_x\text{Ga}_{1-x}\text{As}$ epilayers during ambient transfer." *J Vac Sci Technol*, vol. 19, no. 2, pp. 255 – 6, 1981.
- [203] M. A. Wistey, S. R. Bank, H. B. Yuen, and J. S. Harris, "Low voltage deflection plates reduce GaInNAs plasma damage," *Applied Physics Letters*, submitted for publication.
- [204] S. R. Bank, M. A. Wistey, H. B. Yuen, V. Lordi, V. F. Gambin, and J. S. Harris, Jr., "Effects of antimony and ion damage on carrier localization in MBE-grown GaInNAs," *J Vac Sci Technol B*, submitted for publication.
- [205] K. Nakashima and K. Tateno, "Structural characterization of GaInNAs/GaAs double quantum well structures." *J Appl Phys*, vol. 95, no. 7, pp. 3443 – 52, APR 2004.
- [206] R. Kudrawiec, G. Sek, J. Misiewicz, L. H. Li, and J. C. Harmand, "Experimental investigation of the C-MN matrix element in the band anticrossing model for GaAsN and GaInAsN layers," *Sol St Comm*, vol. 129, no. 6, pp. 353 – 357, FEB 2004.
- [207] P. Krispin, S. G. Spruytte, J. S. Harris, and K. H. Ploog, "Admittance dispersion of n-type GaAs/ga(as, N)/GaAs heterostructures grown by molecular beam epitaxy." *Journal of Applied Physics*, vol. 90, no. 5, pp. 2405 – 10, SEP 2001.

- [208] N. Gerhardt, M. R. Hofmann, and W. W. Ruhle, "Optical spectroscopy of 1.3 μm (GaIn)(NAs)/GaAs lasers." *IEE Proc Optoelectronics*, vol. 150, no. 1, pp. 45 – 8, FEB 2003.
- [209] X. G. Sun, S. L. Wang, J. S. Hsu, R. Sidhu, X. G. G. Zheng, X. W. Li, J. C. Campbell, and A. L. Holmes, "GaAsSb: A novel material for near infrared photodetectors on GaAs substrates," *IEEE Journal on Selected Topics in Quantum Electronics*, vol. 8, no. 4, pp. 817 – 822, July/August 2002.
- [210] G. Solomon, private communication.
- [211] K. J. Kuhn and G. A. Pubanz, "Variation in GaAs surface oxide desorption temperature as a function of shuttered aluminum oven temperature." *J Vac Sci Technol A*, vol. 7, no. 6, pp. 3265 – 8, NOV-DEC 1989.
- [212] E. S. Hellman and J. S. Harris, "Infrared transmission spectroscopy of GaAs during molecular beam epitaxy." *J Cryst Growth*, vol. 81, no. 1/4, pp. 38 – 42, FEB 1987.
- [213] Z. Z. Wang, S. L. Kwan, T. P. Pearsall, J. L. Booth, B. T. Beard, and S. R. Johnson, "Real-time, noninvasive temperature control of wafer processing based on diffusive reflectance spectroscopy," *J Vac Sci Technol B*, vol. 15, no. 1, pp. 116 – 121, Jan-Feb 1997.
- [214] K. Ma, Ph.D. dissertation, Leland Stanford Junior University, Stanford, CA, 94305, USA, 2005.
- [215] H. Ott, *Noise Reduction Techniques in Electronic Systems*. Wiley-Interscience, 1988.
- [216] R. Kudrawiec, P. Sitarek, J. Misiewicz, S. R. Bank, H. B. Yuen, M. A. Wistey, and J. S. Harris, Jr., "Interference effects in electromodulation spectroscopy applied to GaAs-based structures: a comparison of photoreflectance and contactless electroreflectance," *J. Appl. Phys.*, submitted for publication, submitted for publication.

- [217] R. Kudrawiec, K. Ryczko, J. Misiewicz, H. B. Yuen, S. R. Bank, M. A. Wistey, H. P. Bae, and J. S. Harris, Jr., "The band gap discontinuity in GaNAsSb/GaAs single quantum wells investigated by photoreflectance spectroscopy," *Appl. Phys. Lett.*, submitted for publication, submitted for publication.
- [218] H. B. Yuen, Ph.D. dissertation, Leland Stanford Junior University, Department of Materials Science and Engineering, Stanford, CA, 94305 USA, 2005.
- [219] A. Aoki, M. Kondow, T. Kitatani, S. Nakatsuka, M. Kudo, and S. Tsuji, "Reliable uncooled 10-gbit/s operation of GaInNAs-SQW laser." in *2002 IEEE 18th International Semiconductor Laser Conference. Conference Digest, 29 Sept.-3 Oct. 2002, Garmisch, Germany*. Piscataway, NJ, USA : IEEE, 2002, 2002, pp. 63 – 4.
- [220] C.-E. Zah, R. Bhat, B. Pathak, F. Favire, W. Lin, M. C. Wang, N. C. Andreadakis, D. M. Hwang, M. A. Koza, T.-P. Lee, Z. Wang, D. Darby, D. Flanders, and J. JamesHsieh, "High-performance uncooled 1.3 μ m Al_xGa_yIn_{1-x-y}As/InP strained-layer quantum-well lasers for subscriber loop applications," *IEEE J Quantum Electron*, vol. 30, no. 2, pp. 511 – 523, Feb 1994.
- [221] Y. Qian, Z. H. Zhu, Y. H. Lo, H. Q. Hou, M. C. Wang, and W. Lin, "1.3- μ m vertical-cavity surface-emitting lasers with double-bonded GaAs-AlAs bragg mirrors." *IEEE Photonics Technology Letters*, vol. 9, no. 1, pp. 8 – 10, Jan 1997.
- [222] N. Ledentsov, D. Bimberg, V. M. Ustinov, Z. I. Alferov, and J. A. Lott, "Quantum dots for VCSEL applications at $\lambda = 1.3 \mu\text{m}$," *Physica E: Low-Dimensional Systems and Nanostructures*, vol. 13, no. 2-4, pp. 871 – 875, March 2002.
- [223] T. Asano, D. Feezell, R. Koda, M. H. M. Reddy, D. A. Buell, A. S. Huntington, E. Hall, S. Nakagawa, and L. A. Coldren, "InP-based all-epitaxial 1.3- μ m vcsels with selectively etched AlInAs apertures and sb-based dbars." *IEEE Photonics Technol Lett*, vol. 15, no. 10, pp. 1333 – 5, October 2003.

- [224] C. W. Coldren, M. C. Larson, S. G. Spruytte, and J. S. Harris, “1200 nm GaAs-based vertical cavity lasers employing GaInNAs multiquantum well active regions.” *Electron Lett*, vol. 36, no. 11, pp. 951 – 2, 2000.
- [225] K. D. Choquette, J. F. Klem, A. J. Fischer, O. Blum, A. A. Allerman, I. J. Fritz, S. R. Kurtz, W. G. Breiland, R. Sieg, K. M. Geib, J. W. Scott, and R. L. Naone, “Room temperature continuous wave InGaAsN quantum well vertical-cavity lasers emitting at 1.3 μm .” *Electron Lett*, vol. 36, no. 16, pp. 1388 – 90, AUG 2000.
- [226] D. Sun, E. Towe, P. H. Ostdiek, J. W. Grantham, and G. J. Vansuch, “Polarization control of vertical-cavity surface-emitting lasers through use of an anisotropic gain distribution in [110]-oriented strained quantum-well structures,” *J Select Topics Quantum Electron*, vol. 1, no. 2, pp. 674 – 680, Jun 1995.
- [227] M. Takahashi, P. Vaccaro, K. Fujita, T. Watanabe, T. Mukaihara, F. Koyama, and K. Iga, “An InGaAs-GaAs vertical-cavity surface-emitting laser grown on GaAs(311)A substrate having low threshold and stable polarization.” *IEEE Photonics Technol Lett*, vol. 8, no. 6, pp. 737 – 9, June 1996.
- [228] T. Yoshikawa, H. Kosaka, M. Kajita, K. Kurihara, Y. Sugimoto, and K. Kasahara, “Alternately perpendicular polarisation in chequer-pattern matrix arrays of vcsels.” *Electron Lett*, vol. 31, no. 18, pp. 1573 – 4, Aug 1995.
- [229] D. L. Huffaker, J. Shin, H. Deng, C. C. Lin, D. G. Deppe, and B. G. Streetman, “Improved mode stability in low threshold single quantum well native-oxide defined vertical-cavity lasers.” *Appl Phys Lett*, vol. 65, no. 21, pp. 2642 – 4, NOV 1994.
- [230] K. D. Choquette, K. M. Geib, C. I. H. Ashby, R. D. Twesten, O. Blum, H. Q. Hou, D. M. Follstaedt, B. E. Hammons, D. Mathes, and R. Hull, “Advances in selective wet oxidation of AlGaAs alloys.” *J Select Topics Quantum Electron*, vol. 3, no. 3, pp. 916 – 26, JUN 1997.

- [231] R. I. Aldaz, M. W. Wiemer, D. A. B. Miller, and J. S. Harris, “Monolithically–integrated long vertical cavity surface emitting laser incorporating a concave micromirror on a glass substrate,” *Opt Express*, vol. 12, no. 17, pp. 3967 – 3971, August 2004.
- [232] S. Ozaki and S. Adachi, “Spectroscopic ellipsometry and thermorefectance of GaAs,” *J Appl Phys*, vol. 78, no. 5, pp. 3380 – 6, SEP 1995.
- [233] S. Adachi, “Model dielectric constants of GaP, GaAs, GaSb, InP, InAs, and InSb.” *Phys Rev B*, vol. 35, no. 14, pp. 7454 – 63, MAY 1987.
- [234] S. Gehrsitz, F. K. Reinhart, C. Gourgon, N. Herres, A. Vonlanthen, and H. Sigg, “The refractive index of $\text{al}_x\text{ga}_{1-x}$ as below the band gap: Accurate determination and empirical modeling.” *J Appl Phys*, vol. 87, no. 11, pp. 7825 – 37, JUN 2000.
- [235] R. J. Deri and M. A. Emanuel, “Consistent formula for the refractive index of $\text{al}_x\text{ga}_{1-x}$ as below the band edge.” *J Appl Phys*, vol. 77, no. 9, pp. 4667 – 72, MAY 1995.
- [236] G. Leibiger, V. Gottschalch, and M. Schubert, “Optical functions, phonon properties, and composition of InGaAsN single layers derived from far– and near–infrared spectroscopic ellipsometry.” *J Appl Phys*, vol. 90, no. 12, pp. 5951 – 8, DEC 2001.
- [237] T. Kitatani, M. Kondow, K. Shinoda, Y. Yazawa, and M. Okai, “Characterization of the refractive index of strained GaInNAs layers by spectroscopic ellipsometry,” *Jpn J Appl Phys 1*, vol. 37, no. 3A, pp. 753 – 7, MAR 1998.
- [238] G. Leibiger, V. Gottschalch, G. Benndorf, J. Sik, and M. Schubert, *MOVPE growth, Phonons, Band-to-Band Transitions and Dielectric Functions of InGaAs/GaAs Superlattices and Quantum Wells*. Research Signpost / Transworld Research Network, 2003, ch. 10.
- [239] H. A. MacLeod, *Thin Film Optical Filters*. Institute of Physics Publishing, 2001.

- [240] S. S. Yechuri, T. J. B. Shieh, and R. H. Johnson, "Design of flat-band Al-GaAs heterojunction bragg reflectors." *IEEE Transactions on Electron Devices*, vol. 43, no. 1, pp. 40 – 6, JAN 1996.
- [241] S. S. Villareal and R. H. Johnson, "Assymmetric [sic] distributed bragg reflector for vertical cavity surface emitting lasers," US Patent 20 030 123 513, JUL, 2003.
- [242] J. M. Dallesasse, N. Holonyak, A. R. Sugg, T. A. Richard, and N. Elzein, "Hydrolyzation oxidation of $\text{Al}_x\text{Ga}_{1-x}\text{As}$ -AlAs-GaAs quantum well heterostructures and superlattices." *Appl Phys Lett*, vol. 57, no. 26, pp. 2844 – 6, DEC 1990.
- [243] J. M. Dallesasse and N. Holonyak, "Native-oxide stripe-geometry $\text{Al}_x\text{Ga}_{1-x}\text{As}$ -GaAs quantum well heterostructure lasers." *Appl Phys Lett*, vol. 58, no. 4, pp. 394 – 6, JAN 1991.
- [244] C.-K. Lin, D. P. Bour, J. Zhu, W. H. Perez, M. H. Leary, A. Tandon, S. W. Corzine, and M. R. T. Tan, "High temperature continuous-wave operation of 1.3- and 1.55- μm vcsels with InP/air-gap dbrs." *J Select Topics Quantum Electron*, vol. 9, no. 5, pp. 1415 – 21, 2003.
- [245] M. A. Wistey, S. R. Bank, H. B. Yuen, V. Lordi, and J. S. Harris, "Redshift from plasma-related defects in GaInNAs(sb)," *Applied Physics Letters*, submitted for publication.
- [246] H. Yuen *et al.*, unpublished.
- [247] D. Bimberg and N. Ledentsov, "Quantum dots: lasers and amplifiers." *J Phys C-Solid State*, vol. 15, no. 24, pp. R1063 – 76, Jul 2003.
- [248] J. M. Hopkins, S. A. Smith, C. W. Jeon, H. D. Sun, D. Burns, S. Calvez, M. D. Dawson, T. Jouhti, and M. Pessa, "0.6 W CW GaInNAs vertical external-cavity surface emitting laser operating at 1.32 μm ." *Electron Lett*, vol. 40, no. 1, pp. 30 – 1, 2004.
- [249] S. Johnson, M. A. Wistey, *et al.*, unpublished.

- [250] S. Calvez, D. Burns, and M. D. Dawson, "Optimization of an optically pumped 1.3- μm GaInNAs vertical-cavity surface-emitting laser." *IEEE Photonics Technol Lett*, vol. 14, no. 2, pp. 131 – 3, FEB 2002.
- [251] V. M. Fuenzalida, C. R. Grahmann, and C. Herrera, "A device for recharging evaporation sources in ultrahigh vacuum systems." *Rev Sci Instrument*, vol. 69, no. 8, pp. 3077 – 8, AUG 1998.
- [252] M. M. Oye, J. Ahn, C. Cao, H. Chen, W. Fordyce, D. Gazula, S. Govindaraju, J. Hurst, S. Lipson, D. Lu, J. Reifsnider, O. Shchekin, R. Sidhu, X. Sun, D. Deppe, A. Holmes, Jr., and T. J. Mattord, "Inert gas maintenance for molecular beam epitaxy systems," unpublished.
- [253] L. J. Durney, *Electroplating Engineering Handbook*. Kluwer Academic Publishers, 1984.